
THE UNIVERSITY *of* EDINBURGH

# Tidal Resource Modelling for Sites in the Vicinity of an Island near a Landmass

Alberto Pérez Ortiz


A thesis submitted in partial fulfilment of the requirements for the award on an Engineering Doctorate

The University of Edinburgh

2015

# IDCORE

This thesis is submitted in partial fulfilment of the requirements for the award of an Engineering Doctorate, jointly awarded by the University of Edinburgh, the University of Exeter and the University of Strathclyde. The work presented has been conducted under the industrial supervision of GE Renewable Energy as a project within the Industrial Doctoral Centre for Offshore Renewable Energy.



# Abstract

Before tidal stream energy is exploited, tidal power resource and environmental assessments must be undertaken. This thesis explores limits to power extraction for tidal sites defined by a strait between an island and landmass. Numerical simulations provided by Fluidity are used to analyse power extraction from locations in the strait and around the island for an idealised island-landmass domain and an actual coastal site.

The numerical model is verified by comparing predictions with analytical solutions for inviscid flow past a circular cylinder located in the centre of a channel and in the vicinity of a wall. The model is then validated against laboratory measurements of flow patterns for impulsively-started flow past a submerged circular cylinder, and for flow past a surface-piercing circular cylinder in oscillatory laminar shallow flow. It is demonstrated that the numerical method captures satisfactorily the mechanisms of early wake formation, which indicates the model can be applied to assess tidal stream resource within the coastal geometries considered herein. Finally, the methodology to account for power extraction is satisfactorily verified for bounded and unbounded flows.

Contrary to current practices, results from a parameter study for different idealised coastal sites reveal that the maximum power extracted in the strait is not well approximated by either the power extracted naturally at the seabed or the undisturbed kinetic power. Moreover, an analytical channel model underpredicts the maximum power extracted in the strait due to its inability to account for changes in the driving head resulting from power extraction and flow diversion offshore of the island. An exception is found for islands with large aspect ratios, with the larger dimension extending parallel to the landmass; i.e. the island-landmass geometry approaching that of a channel. In this case, the extracted power is satisfactorily approximated by the power naturally dissipated at the seabed and there is good agreement with the analytical model. The maximum power extracted in the strait is shown to decrease when water depths offshore are greater than in the strait, underlining the importance of fully understanding the wider bathymetry of a given site. A similar conclusion is reached when strait blockage is reduced. The power extraction in the strait is found to be sensitive to both viscosity and seabed friction, and these parameters need to be properly estimated during the setup and calibration of models in order to reduce uncertainty. Power extraction increases when turbines are sited simultaneously both in the strait and offshore.

Tidal power assessment is performed for Rathlin Sound, off the coast of Northern Ireland. Again, no clear relationship is found between maximum power extracted in the strait and

either the power dissipated naturally at the seabed or the undisturbed kinetic power. A similar ratio of power extracted to undisturbed kinetic power is obtained as for the equivalent idealised model. The analytical channel model underpredicts the maximum power extracted. The actual and idealised coastal site models indicate similar responses to changes in seabed friction, and similar reduction in power extraction with decreasing strait blockage.

# Acknowledgements

I would like to thank my main academic supervisor Prof. Alistair Borthwick and my industrial supervisors Paul Vigars and Dr. James McNaughton for all their support, advice and encouragement throughout this project.

I am also grateful to my academic co-supervisors Dr. Helen Smith and Dr. Qing Xiao for their contribution to this project. I would also like to mention Prof. Ian Bryden and Prof. David Ingram for being the main academic supervisors during the first year of this project.

During the almost two years I spent in Edinburgh I had very interesting and challenging tidal discussions with colleagues from the Institute of Energy Systems, with special mention to Dr. John Pescatore, Dr. Abynaya Iyer and Dr. Angus Creech.

This work would not have been possible without the support from the department of Earth Science at Imperial College London and especially from Dr. Alexandros Avdis, Dr. Stephan Kramer and Dr. Matthew Piggott.

I would like to acknowledge Marko Hyensjo and Alec Wilson from Rolls Royce for their contribution during the first year of this project.

I would like to thank my IDCORE colleagues Ampea, Gabriel, Raffaello and Rebecca for those first six months of our EngD spent in Edinburgh and for keeping a good long distance relationship during the following three and a half years.

I would not have completed this project without my family, the weekly calls with my mother and the monthly escape to see them. I want to mention as well my friends from Barcelona, Edinburgh, Bristol, San Juan Island, Thessaloniki, Ha Noi and Trondheim who gave me moral support when I most needed it.

Thanks to Dp Marine Energy Ltd. for providing me access to their measured data.

I acknowledge gratefully IDCORE and GE Renewable Energy for their support.

Funding from the Energy Technologies Institute (ETI) and the RCUK Energy Programme for the Industrial Doctoral Centre for Offshore Renewable Energy (Grant number EP/J500847/1) is gratefully acknowledged.

# Declaration

I declare that this thesis was composed by myself and that the material presented, except where clearly indicated, is my own work. I declare that the work has not been submitted for consideration as part of any other degree or professional qualification.

.....

Alberto Pérez Ortiz

December 2015

# List of Contents

# List of Figures

# List of Tables

# Abbreviations

| Abbreviation | Definition |
|---|---|
| ADCP | Acoustic Doppler current profiler |
| CD | Chart datum |
| CFD | Computational fluid dynamics |
| CFL | Courant-Friedrichs-Lewy |
| CG | Continuous Galerkin |
| DG | Discontinuous Galerkin |
| ES | European shelf |
| FEM | Finite element method |
| FES | Finite element solution |
| GMRES | Generalised minimal residual method |
| GW | Gigawatt |
| GWh | Gigawatt hour |
| LAT | Lowest astronomical tide |
| LES | Large eddy simulation |
| LMADT | Linear momentum actuator disc theory |
| MSL | Mean sea level |
| MW | Megawatt |
| MWh | Megawatt hour |
| RANS | Reynolds averaged Navier Stokes |
| SIF | Significant impact factor |
| SOR | Successive over-relaxation |
| SWE | Shallow water equations |
| TW | Terawatt |
| TWh | Terawatt hour |
| U.K. | United Kingdom |
| U.S.A. | United States of America |
| VORF | Vertical offshore reference frame |
| 1D | One-dimensional |
| 2D | Two-dimensional |
| 3D | Three-dimensional |

# Nomenclature

**Common to Chapters 3-6**

| | | |
|---|---|---|
| $A_f$ | Power extraction area | ($m^2$) |
| $A_S$ | Projected area of the turbine support structure | ($m^2$) |
| $A_T$ | Projected area of the turbine rotor | ($m^2$) |
| $C_d$ | Non-dimensional quadratic bottom friction | (-) |
| $C_D$ | Turbine supporting structure drag coefficient | (-) |
| $C_T$ | Turbine rotor thrust coefficient | (-) |
| $CFL$ | Courant–Friedrichs–Lewy condition | (-) |
| $F_{TOT}$ | Total force exerted by tidal turbines on the flow | (kg $m/s^2$) |
| $g$ | Acceleration due to gravity | ($m/s^2$) |
| $h$ | Total water depth | (m) |
| $k$ | Von Kármán constant | (-) |
| $k_f$ | Enhanced seabed drag due to presence of turbines | (-) |
| $N_T$ | Equivalent number of tidal turbines | (turbines) |
| $t$ | Time | (s) |
| $t^*$ | Non-dimensional time | (-) |
| $T$ | Time period | (s) |
| $u$ | Stream-wise depth-averaged velocity component | (m/s) |
| $\vec{u}$ | Depth-averaged velocity vector | (m/s) |
| $U$ | Stream-wise velocity component | (m/s) |
| $v$ | Transverse depth-averaged velocity component | (m/s) |
| $V$ | Transverse velocity component | (m/s) |
| $x$ | Horizontal coordinate in the stream-wise direction | (m) |
| $y$ | Horizontal coordinate in the transversal direction | (m) |
| $z$ | Bed surface elevation vertically above a fixed vertical datum | (m) |
| $z_o$ | Depth of bottom of the system above a fixed vertical datum | (m) |
| $\delta$ | Free surface elevation above mean sea level | (m) |
| $\nu$ | Fluid kinematic viscosity | ($m^2/s$) |
| $\nu_t$ | Turbulent depth-averaged eddy viscosity | ($m^2/s$) |
| $\mu$ | Fluid dynamic viscosity | ($Ns/m^2$) |
| $\rho$ | Fluid density | ($kg/m^3$) |

**Chapter 3**

| | | |
|---|---|---|
| $C$ | Chezy friction coefficient | (-) |
| $C_w$ | Non-dimensional air-water resistance coefficient | (-) |
| $C_{100}$ | Non-dimensional bottom drag coefficient based on a velocity measured 100 cm above the bottom | (-) |
| $f$ | Coriolis parameter in f-plane approximation | (rad/s) |
| $F_d$ | Force exerted by the seabed | (kg m/s$^2$) |
| $F_D$ | Drag force from the supporting structure of the turbine | (kg m/s$^2$) |
| $F_T$ | Thrust force from the turbine rotor | (kg m/s$^2$) |
| $h_o$ | Still water level | (m) |
| $M$ | Manning friction coefficient | s/m$^{1/3}$ |
| $p_a$ | Atmospheric pressure | (Pa) |
| $P$ | Fluid pressure | (Pa) |
| $T_f$ | Time period used to compute the mean velocity | (s) |
| $U_{100}$ | Flow speed at 100 cm above the seabed | (m/s) |
| $W$ | Vertical velocity component | (m/s) |
| $\theta_{nl}$ | Non-linear relaxation parameter | (-) |
| $\lambda$ | Latitude of the site | (rad) |
| $\sigma$ | Normal viscous stress | (kg/m/s$^2$) |
| $\tau$ | Shear viscous stress | (kg/m/s$^2$) |
| $\tau_b$ | Bottom shear stress | (kg/m/s$^2$) |
| $\tau_w$ | Wind shear stress | (kg/m/s$^2$) |
| $\gamma_f$ | Farm volumetric absorption term | (kg/m$^2$/s) |
| $\varphi$ | Trial function | (-) |
| $\psi$ | Shape function | (-) |
| $\Omega$ | Frequency of earth's rotation | (rad/s) |

**Chapter 4**

| | | |
|---|---|---|
| $a_c$ | Stream-wise distance of symmetrical eddies to surface of cylinder | (m) |
| $a_d$ | Stream-wise coordinate of doublet | (m) |
| $a_f$ | Amplitude of the fluid motion | (m) |
| $a_t$ | Amplitude of the tidal signal | (m) |
| $A$ | Channel cross-sectional area | (m$^2$) |

| | | |
|---|---|---|
| $b$ | Width of the channel | (m) |
| $b_c$ | Transverse distance between symmetrical eddies behind cylinder | (m) |
| $b_d$ | Transverse distance from centre of doublet to wall | (m) |
| $B$ | Width of the numerical domain | (m) |
| $c_o$ | Non-dimensional linear bottom friction | (-) |
| $c_t$ | Non-dimensional linear friction due to presence of turbines | (-) |
| $f_k$ | Fraction of kinetic power extracted from the flow by turbines | (-) |
| $F$ | Opposing force due to natural friction and presence of turbines | ($m/s^2$) |
| $Fr$ | Froude number | (-) |
| $KC$ | Keulegan-Carpenter number | (-) |
| $L$ | Length of the numerical domain | (m) |
| $L_c$ | Closed-wake length of cylinder | (m) |
| $M$ | Manning friction coefficient | $s/m^{1/3}$ |
| $m$ | Strength of source and sink | ($m^2/s$) |
| $N$ | Number of dataset points | (-) |
| $P_e$ | Power extracted from the flow by tidal turbines | (W) |
| $P_{er}$ | Wetted perimeter | (m) |
| $Q$ | Scalar flow | ($m^3/s$) |
| $Q_o$ | Volume flow rate in undisturbed conditions | ($m^3/s$) |
| $R$ | Hydraulic radius of channel | (m) |
| $R_c$ | Cylinder radius | (m) |
| $R_f$ | Radius of circular patch of enhanced bottom friction | (m) |
| $Re$ | Reynolds number | (-) |
| $Re_a$ | Oscillatory Reynolds number | (-) |
| $S$ | Stability parameter for circular cylinders | (-) |
| $u_e$ | Stream-wise velocity at the exit of the channel | (m/s) |
| $U_o$ | Amplitude of the oscillating velocity near the surface | (m/s) |
| $U_\infty$ | Depth-averaged free stream flow speed | (m/s) |
| $\eta$ | Head difference between two ocean basins | (m) |
| $\theta_c$ | Angle of separation of boundary layer at cylinder | (deg) |
| $\lambda$ | Doublet strength | ($m^3/s$) |
| $\tau_{add}$ | Stress due to power extraction by turbines from the flow | ($kg/m/s^2$) |
| $\tau_b$ | Equivalent stress due to seabed bottom friction | ($kg/m/s^2$) |
| $\phi$ | Potential function | ($m^2/s$) |
| $Ø_c$ | Diameter of cylinder | (m) |

| | | |
|---|---|---|
| $\varphi$ | Analytical, experimental and computed variable | (-) |
| $\psi$ | Velocity stream function | ($m^2/s$) |
| $\omega$ | Vertical component of vorticity | ($s^{-1}$) |
| $\omega_t$ | Frequency of the tidal signal | (rad/s) |

**Chapter 5**

| | | |
|---|---|---|
| $a$ | Amplitude of the $M_2$ tidal signal | (m) |
| $a_o$ | Tidal signal ramp-up parameter | (-) |
| $B$ | Width of the numerical domain | (m) |
| $B_f$ | Width of the power extraction area | (m) |
| $B_i$ | Width of the island | (m) |
| $C_P$ | Tidal turbine power coefficient | (-) |
| $CF$ | Capacity factor of tidal farm | (-) |
| $L$ | Length of the numerical domain | (m) |
| $L_f$ | Length of the power extraction area | (m) |
| $L_i$ | Length of the island | (m) |
| $\bar{P}_e$ | Three tidal period averaged power extracted from the flow | (W) |
| $\bar{P}_k$ | Three tidal period averaged kinetic power in the strait | (W) |
| $\bar{P}_{ko}$ | Three tidal period averaged undisturbed kinetic power in the strait | (W) |
| $\bar{P}_k^*$ | Three tidal period percentage decrease in mean strait kinetic power | (%) |
| $P_R$ | Turbine electric power rating | (W) |
| $\bar{P}_S$ | Three tidal period averaged natural seabed power dissipated in the strait | (W) |
| $\bar{P}_T$ | Three tidal period averaged power generated by tidal farm | (W) |
| $\bar{Q}$ | Three tidal period averaged volumetric flow rate | ($m^3/s$) |
| $\bar{Q}_o$ | Three tidal period averaged volumetric flow rate in undisturbed conditions | ($m^3/s$) |
| $s$ | Width of strait between island and landmass | (m) |
| $U_C$ | Tidal turbine cut-in speed | (m/s) |
| $U_o$ | Cross section volumetric flow rate velocity midway along the strait | (m/s) |
| $\bar{U}_o^*$ | Three tidal period percentage decrease in mean strait velocity | (%) |
| $U_R$ | Tidal turbine rated speed | (m/s) |
| $U_z$ | Flow speed on first half of water column above seabed | (m/s) |
| $U_\infty$ | Depth-averaged free stream flow speed | (m/s) |
| $\Gamma$ | Solid/open domain boundary | (-) |

| | | |
|---|---|---|
| $\lambda$ | Wavelength of the $M_2$ tidal signal | (m) |
| $\tau_b$ | Depth integrated bottom shear stress | (kg/m/s$^2$) |
| $\emptyset_i$ | Circular island diameter | (m) |
| $\emptyset_T$ | Tidal turbine rotor diameter | (m) |
| $\omega_t$ | Frequency of the $M_2$ tidal signal | (rad/s) |

**Chapter 6**

| | | |
|---|---|---|
| $a_o$ | Tidal signal ramp-up parameter | (-) |
| $A$ | Normalised free-surface elevation harmonic amplitude | (-) |
| $B_f$ | Width of the power extraction area | (m) |
| $C_{max}$ | Normalised harmonic velocity major ellipse parameter | (-) |
| $C_{min}$ | Normalised harmonic velocity minor ellipse parameter | (-) |
| $CF$ | Capacity factor of tidal farm | (-) |
| $f$ | Coriolis parameter in f-plane approximation | (rad/s) |
| $l$ | Location within transect | (m) |
| $L_f$ | Length of the power extraction area | (m) |
| $L_s$ | Transect length | (m) |
| $\bar{P}_e$ | Three tidal period averaged power extracted from the flow | (W) |
| $\bar{P}_k$ | Three tidal period averaged kinetic power in the strait | (W) |
| $\bar{P}_{ko}$ | Three tidal period averaged undisturbed kinetic power in the strait | (W) |
| $\bar{P}_k^*$ | Three tidal period percentage decrease in mean strait kinetic power | (%) |
| $\bar{P}_S$ | Three tidal period averaged natural seabed power dissipated in the strait | (W) |
| $\bar{P}_T$ | Three tidal period averaged power generated by tidal farm | (W) |
| $\bar{Q}$ | Three tidal period averaged volumetric flow rate | (m$^3$/s) |
| $\bar{Q}_o$ | Three tidal period averaged volumetric flow rate in undisturbed conditions | (m$^3$/s) |
| $\bar{U}_o^*$ | Three tidal period percentage decrease in mean strait velocity | (%) |
| $\theta$ | Normalised harmonic velocity inclination angle | (-) |
| $\lambda$ | Latitude of the site | (rad) |
| $\omega_t$ | Frequency of the $M_2$ tidal signal | (rad/s) |
| $\phi$ | Normalised harmonic phase | (-) |
| $\Omega$ | Frequency of earth's rotation | (rad/s) |

*"A la orilla de la chimenea, a esperar que suba la marea"*

Joaquín Sabina, Física y Química, 1992

# 1. Introduction

The link between carbon emissions and climate change [1], the finiteness and price volatility of fossil fuels [2] [3], and the security of supply and diversification of energy sources are several reasons why over recent decades there has been increasing interest in development of low carbon and renewable energy technologies. Take up of renewable energy in the power sector has been growing fast; it has been forecast that 60 % investment in new power capacity up to 2040 will be spent on renewable energy [4]. Wind, solar and wave are renewable sources characterised by their unpredictable nature, and until an efficient system to store the electricity surplus is available, backup generation (e.g. gas turbines) will be required to supply electricity during the periods when renewable generation is not sufficient to meet the demand. Energy generation from astronomical tides presents the main advantage of being completely predictable, hence facilitating integration within the grid and reducing the need for backup generation capacity. Moreover, tidal energy presents high energy density which limits the footprint of tidal projects compared to other renewable energy sources with lower energy densities.

There are presently two approaches to generate electricity from the tides [5]. First, tidal barrages and lagoons are located at enclosed bays and estuaries where there is a significant tidal range. Tidal barrages are effectively dams which capture the water at high tide and release it when there is sufficient head to generate electricity (e.g. La Rance tidal barrage, north of France). The technology employed has evolved from well proven hydro-electric schemes. However, tidal barrages have high impacts on the environment as they change the tidal cycles inside the bays and alter sediment transport fluxes. Tidal lagoons represent a feasible alternative to tidal barrages as these can be installed offshore and do not close the bay. Second, tidal stream turbines (herein referred as tidal turbines) are hydrokinetic devices that can exploit the locally accelerated currents originating from the combination of sufficient local head difference and the presence of a bathymetric or topographic feature (e.g. island). Tidal turbines have undergone significant development in the past 20 years including laboratory experiments of scaled turbines and tests of MW-scale tidal turbines under real sea conditions; the first pre-commercial arrays are currently under construction, and large tidal arrays are in the design stage.

World energy consumption in 2012 was estimated to be around 17.7 TW [4]. The energy dissipated naturally due to tides worldwide is estimated to be around 2-3 TW [6]. Even if all the energy naturally dissipated was harnessed, which is technically unfeasible, tidal energy would only cover a small fraction of world's energy demand. However, in certain areas of the world tidal energy could contribute significantly to the energy mix. In the U.K., the maximum annual tidal energy yield has been estimated to be between 10.3 TWh and 30.0 TWh [7], compared to the 317.5 TWh electricity demand in the U.K. in 2012 [8], this represents between 3 % and 10 % of the U.K.'s total electricity demand. The tidal current resource of Canada has been estimated to be 42 GW with an equivalent annual energy generation of 365 TWh, which could account for 70 % of Canada's annual electricity consumption [9]. However, the above resource estimates still present high levels of uncertainty.

## 1.1. Motivation

The exploitation of tidal stream energy requires accurate understanding of the tidal resource, the limits to power extraction, and the effects on the environment. Relatively accessible site parameters in the natural state such as the kinetic power or the power dissipated on the seabed [10] have been used to provide an estimate of the tidal resource available for power generation. However, detailed analyses of idealised [11] and actual coastal sites [12] have shown that these parameters may not be good indicators of the tidal resource available for extraction. Typical tidal coastal sites include configurations such as those defined by a channel linking two infinite ocean basins, a channel linking an infinite ocean basin and an enclosed bay, and a headland. According to a survey of tidal sites in the U.K. and U.S.A. carried out by Draper [13], these three types of coastal sites represent around 60 % of the total surveyed sites. Slightly less than 10 % of the surveyed sites are categorised as a strait between an island and a landmass. For certain island and strait geometries, the physical behaviour of the site may approximate that of a channel linking two infinite ocean basins. Moreover, this type of site presents multiple possible layouts of islands and landmass, while also allowing for power extraction both in the strait and offshore side of the island. A sensitivity study would benefit the understanding of the power potential of such coastal sites and enable assessment of the effects of parameters such as island and strait geometry, seabed topography, and power extraction.

## 1.2. Aims and objectives

There is currently a good understanding of the limits to power extraction of the tidal coastal site types categorised as a channel linking two infinite ocean basins, a channel linking an infinite ocean basin and an enclosed bay, and a headland (Figure 1.1). However, there is lack of information on the limits to power extraction in tidal coastal sites defined as an island in the vicinity of a landmass (Figure 1.1).

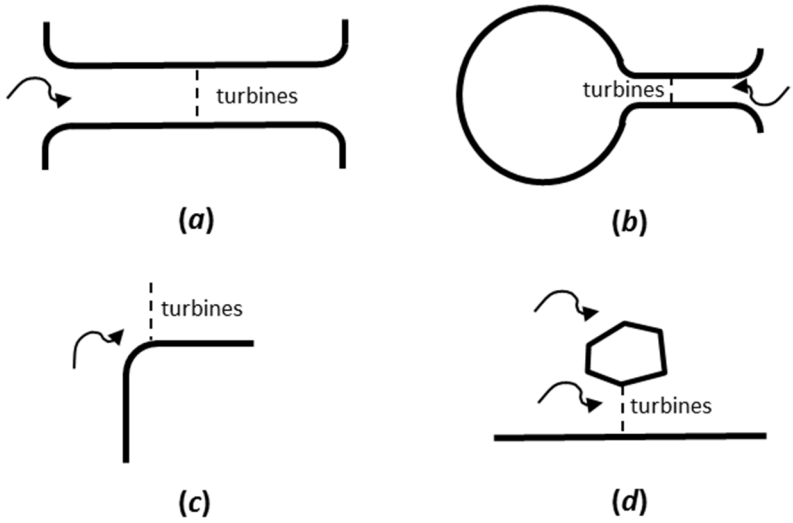


Figure 1.1. Identified tidal coastal sites suitable for tidal power exploitation. (*a*) Channel linking two infinite ocean basins; (*b*) channel linking an infinite ocean basin and an enclosed bay; (*c*) headland; and (*d*) island in the vicinity of a landmass.

The aim of this thesis is therefore to investigate power extraction for idealised and actual cases of tidal turbine arrays located in a tidal flow field surrounding an island in the vicinity of a landmass. The main objectives are:

- To verify and validate a numerical resource assessment methodology for the island-landmass coastal site based on the finite element method code Fluidity.
- To characterise the tidal resource of the island-landmass coastal site by means of a parameter sensitivity study of an idealised version of the coastal site in which coastal geometry features are simplified.
- To assess the validity of the outcomes of the parameter sensitivity study through the tidal resource assessment of an actual coastal site whose geometry and seabed topography conditions can be linked to the idealised coastal site.

## 1.3. Thesis structure

Chapter 2 contains a literature review of the field. The chapter is divided into three parts: first, definitions are provided of tidal resource and assessment techniques; second, a review is given of resource assessments performed for different coastal site types; third, hydrodynamic and resource assessment studies are presented for coastal sites defined as an island in the vicinity of a landmass. Chapter 3 outlines the methodology employed to perform tidal resource assessment. The shallow water equations are derived from the Navier Stokes equations, and parameters relevant to tidal resource assessment are detailed. The numerical scheme is then described. Chapter 4 verifies and validates the methodology that will be employed to assess the resource of the island-landmass coastal site. The physics of the numerical code are validated for flow past submerged and surface piercing circular cylinders. Methodology to account for power extraction is verified for bounded and unbounded flows. Chapter 5 characterises the tidal resource at the island-landmass coastal site by means of a parameter sensitivity study. The sensitivity analysis investigates the effects on the resource estimates of the island and strait geometries, seabed topography, characterisation of the friction and viscous environment, and area and location where power extraction is implemented. Power extraction estimates are compared against analytical models and actual sites when available. Chapter 6 analyses the limits to power extraction in the Rathlin Sound, a coastal site that falls into the category of island in the vicinity of a landmass. Limits to power extraction at the site are assessed and results are compared against the outcomes of the island-landmass study of Chapter 5 and analytical models. Chapter 7 presents the conclusions, summarises the research main findings of this project, and includes some suggestions for further work. The appendix includes a list of conference papers derived from the work included in this thesis.

# 2. Literature review

## 2.1. Introduction

The first multi-megawatt tidal stream energy arrays are planned to become operational in the next ten to twenty years. Accurate estimation of the tidal resource is an important prerequisite for successful implementation of pre-commercial and (subsequent) commercial arrays. This chapter provides a comprehensive overview of the resource assessment techniques currently used and studies of identified tidal coastal site types, with a focus on the coastal site defined by an island near a landmass. This chapter provides a basis for the work presented in Chapters 5 and 6. The chapter is structured in four sections. Section 2.2 examines the various definitions of tidal resource, and techniques currently used in the tidal industry to perform resource assessment. Section 2.3 categorises tidal coastal sites, provides an overview of resource assessment performed for each category and discusses hydrodynamic and resource assessment studies for the case of a coastal site defined by an island near a landmass. Section 2.4 summarises the chapter.

## 2.2. Tidal resource assessment

In the early stages of the tidal stream energy industry, the resource assessment was performed based on local kinetic power, following the wind industry practice [14]. However, tidal current and wind resources differ in the following ways [15]: (1) tides involve potential and kinetic energy, unlike wind which solely involves kinetic energy; and (2) tidal currents are constrained by the seabed, coastlines and the sea surface, thus power extracted cannot be recovered, unlike wind where energy extracted can be recovered through mixing with the atmosphere. Even so, certain aspects applied to the wind industry remain valid when assessing the tidal resource. Common factors limiting the tidal resource available for power extraction [16] [17] [18] [19] include: technical limitations (e.g. current speeds and turbine design); site bathymetry and navigational requirements; environmental restrictions (e.g. unacceptable changes to flow and free surface elevation conditions in the natural state and impacts on marine habitat); economic criteria (e.g. optimum number of turbines and cabling costs); and societal factors (e.g. interactions with fishing industry and local communities).

Black & Veatch Ltd. [20] attempted to account for the technical, economic, environmental and ecological constraints when estimating the extractable resource in U.K. waters by defining a significant impact factor (SIF). Black & Veatch Ltd. calculated the SIF to be 20% of the kinetic power in the natural state. Bryden *et al*. [21] estimated the SIF to be ~ 10%, at which flow speed would reduce under 3% compared to a 6% reduction when 20% of the natural kinetic power is extracted. However, the use of undisturbed kinetic power has been criticised by Garrett and Cummins [11] because it does not represent a valid reference by which to assess power extraction noting the associated flow changes that occur in a channel.

### 2.2.1 Tidal data and long term tidal data prediction

Tidal currents present both potential and kinetic power, and so information on tidal current velocity and sea surface elevation is needed to perform a tidal resource assessment. Tidal diamonds are used by mariners and indicate the direction and speed of tidal currents at the sea surface, and these are included in tidal diamond tables extending 12 hours at intervals of an hour covering both mean spring and neap tides. Information about sea surface elevation is usually obtained from tidal gauges and satellite altimetry. Acoustic Doppler current profilers (ADCP) installed on the seabed or on the bottom of vessels provide measurements of the speed and direction of the currents in the entire water column, which can also be used to estimate the sea surface elevation. Spatial coverage can be achieved by deploying a large number of ADCPs, though this may be economically prohibitive. The limitation of the ADCP's battery life can be extended by means of harmonic analysis [22], whereby the time series of tidal velocities or free surface elevations is decomposed into harmonic components, which then can be used to reproduce the tidal signal at any time interval. For a detailed explanation on harmonic analysis, the reader is referred to [22] and [23]. Whereas the frequency of the harmonic constituents is constant, both amplitude and phase can be altered by local features (e.g. bathymetry). There are 175 tidal constituents including astronomically harmonics and shallow water harmonics (e.g. M4) that arise through interaction with bathymetry. The Rayleigh criterion is used to determine what constituents can be extracted with harmonic analysis based on the time duration of the data record available [22]. For example, 19 years of data are required to resolve all the tidal constituents and 14.7 days are required to determine the principal semidiurnal lunar $M_2$ and solar $S_2$ constituents, whose phase difference is responsible for the spring-neap tidal cycle. Table 2.1 lists the frequency of selected semi-diurnal and diurnal tidal constituents used in Chapter 6. There are several open source tools available to perform harmonic analysis, such as T_Tide [24] used in Chapter 6, Utide [25] and World Currents [23].

| | | | | | | | |
|---|---|---|---|---|---|---|---|
| $K_1$ | 15.0411 | $O_1$ | 13.9430 | $P_1$ | 14.9589 | $Q_1$ | 13.3987 |
| $M_2$ | 28.9841 | $S_2$ | 30.0000 | $N_2$ | 28.4397 | $K_2$ | 30.0821 |

Table 2.1. Frequencies (in degrees per hour) of selected semi-diurnal and diurnal tidal constituents [23].

Tides at a location can be classified according to the amplitudes of the diurnal $K_1$ and $O_1$ and the semi-diurnal $M_2$ and $S_2$ harmonic constituents using the Formzahl number [26], $F_z = (K_1 + O_1)/(M_2 + S_2)$, where the tide is $F_z < 0.25$ semi-diurnal, $0.25 < F_z < 1.5$ mixed semi-diurnal dominant, $1.5 < F_z < 3.0$ mixed diurnal dominant, and $F_z > 3.0$ diurnal. When tides are strongly semi-diurnal, two consecutive tides present currents of similar strength. As tides are more diurnal, there is a significant reduction in the current of one tide per day. Consequently, the local type of tide has direct implications on site resource assessment [27]. Furthermore, from a study of the Orkney Islands in Scotland, Neill *et al*. [28] concluded that the phase between the semi-diurnal lunar constituent $M_2$ and its first harmonic $M_4$ is a valuable indicator of the degree of asymmetry in velocity between flood and ebb. Velocity asymmetry influences site resource assessment; Neill *et al*. found that a degree of 30 % asymmetry in velocity produced a 100 % asymmetry in power density. Tidal asymmetry may also have implications on the site sediment dynamics [29]. Although harmonic analysis can overcome the temporal limitation of data available at a site, it is noted that harmonic analysis alone cannot incorporate changes in the tidal flow due to power extraction.

### 2.2.2 Analytical and numerical models for resource assessment

Analytical and numerical models can overcome the limitations of harmonic analysis because they can account for changes in the flow due to power extraction. Models employed to perform tidal resource assessment are divided into three categories. Analytical one-dimensional (1D) models are used to determine the maximum average power extracted from channels connecting two infinite oceans [11] [15] or an infinite ocean with an enclosed bay [30], based on relatively accessible parameters such as the head amplitude driving the flow, peak flow through the channel, seabed friction and channel dimensions. 1D models assume uniform power extraction and constant seabed and channel geometry. The limitations of analytical 1D models can be overcome with numerical two-dimensional (2D) and three-dimensional (3D) models. 2D models [31] [32] solve the shallow water equations (SWE) (Section 3.2) to compute sea surface elevations and depth-averaged velocities, and use simplified approaches to model power extraction from tidal turbines (Section 3.2.2). 2D

models are computationally efficient and are applied from medium to large-scale domains; however their main disadvantage is that they are unable to capture vertical flow behaviour which may be due to complex seabed profiles. 3D models [33] compute the velocity profile over the entire water column and allow a more detailed representation of power extraction (by carrying out the analysis at the exact rotor position within the water column) thus yielding more accurate resource and environmental assessments. The increase in accuracy comes at a cost of high computational resources and this limits the application of 3D models currently to small and medium-scale domains. A review of the different hydrodynamic modelling approaches, based on the scale of interest, is given by Adcock *et al*. [34]. Furthermore, Vennell *et al.* [35] highlighted that it is not presently feasible to resolve in the same model flow features generated at blade scale of less than a meter and those occurring far from the site at a scale of several kilometres. Moreover, 2D and 3D models can account for other parameters that can influence long term tidal resource assessment such as the interaction between waves and currents or between wind and currents [36] [37], and the interaction with nearby tidal energy developments [38].

Another alternative model used to assess the tidal resource in domains with multiple channels relates the shallow water problem to an electrical circuit analogy, in which the head driving the flow is represented by an alternating voltage, the flow is equal to the electric current and bed friction and turbines are represented using non-linear resistances [13]. This method has been applied by Draper *et al*. [39] to assess the resource of the Pentland Firth, located between north coast of Scotland and the Orkney Islands, and by Cummins [40] to investigate the power potential of a split tidal channel.

## 2.3. Analysis of coastal sites for tidal power extraction

Draper [13] identified in particular four different coastal sites suitable for tidal energy exploitation: strait between two infinite ocean basins; strait between an infinite ocean basin and an enclosed bay; headland; and strait between an island and a semi-infinite landmass. The study of these coastal sites has been performed through three approaches. The first utilises analytical models to represent the main physics of the coastal site; e.g. Garrett and Cummins' [11] (GC2005) analytical model assesses the maximum average power extracted from a channel linking two infinite ocean basins. The second approach models idealised coastal sites and simplifies the coastal geometry features to allow for a parameter sensitivity study; e.g. Draper *et al*. [41] investigated the power potential of an array deployed offshore of an idealised headland and assessed the sensitivity of the power extracted by the array to

changes in the headland geometry. The results from such analysis of an idealised coastal site provide useful guidelines to tidal energy planners during site selection and project pre-feasibility stages. The third approach involves numerical modelling of actual coastal sites, and provides detailed information on local flow dynamics and resource at the site, although the outcomes may not be extrapolated to other coastal sites of the same type; e.g. Blunden and Bahaj [42] used such a method to evaluate the tidal stream resource off Portland Bill, a headland on the south coast of England.

### 2.3.1 Channel connecting two infinite ocean basins

Limits to power extraction, also known as the potential [35], from a channel connecting two infinite ocean basins have been extensively studied from an idealised point of view. Bryden *et al*. [21], [16] and Bryden and Couch [15], [43] assessed the effects of power extraction from a channel on the free surface elevation and velocity profiles along the channel using a 1D quasi-steady analytical channel model (Section 4.9.1). Power extraction is expressed as a percentage of the undisturbed kinetic power, assuming constant channel cross-section. Power extraction is uniform across the channel and the length of the channel over which power extraction is implemented is undefined. Head driving the flow is assumed to be independent of the level of power extraction within the channel. A reduction in the free surface elevation and a consequent increase in flow velocity are predicted downstream of the area of power extraction. However, the increase in power extraction reduces the channel flow velocities compared to the undisturbed case.

GC2005 developed an analytical model to estimate the maximum average power available for extraction based on the head driving the flow, maximum volumetric flow rate through the channel and the phase difference between the driving head and flow in the channel (Section 4.9.2). Maximum average power available is found to be less than the average undisturbed kinetic power through the most constricted cross-section of the channel. Power extraction is uniform across the channel and maximum average power is independent of the location of the tidal array. At maximum power extracted, flow in the channel is reduced to 57.7 % of the flow in undisturbed conditions. The model assumes the head driving the flow is constant and independent of the level of power extraction within the channel. Garrett and Cummins [44] extended the analysis of GC2005 to analyse what fraction of the power of an array blocking completely the channel could be obtained by a partial array, as arrays may not be able to block the entire channel cross-section due to navigational and environmental

constraints. Garrett and Cummins [45] highlight that power maximisation of partial arrays requires numerical modelling.

Vennell [46] extended the model of GC2005 to consider tuning of tidal turbines based on local flow conditions at the channel to optimise power extraction. Power extraction is maximised because the channel cross-section is blocked by the tidal array, and tuned arrays can extract most of the potential of a channel. Tidal array tuning depends on the number of turbines per row, number of rows, channel geometry, seabed friction coefficient, and tidal forcing. When an array consists of different rows, the rows also need to be tuned in the presence of the other rows [47], although in several conditions, optimal tuning is identical or very similar for all rows of turbines. Vennell [48] developed a model to estimate the potential of a channel based on peak undisturbed volumetric flow, seabed drag coefficient, and channel dimensions, and applied it to estimate the potential of the Cook Strait in New Zealand in 15 GW. Plew and Stevens [49] analysed the limits to power extraction and effects on the natural environment for Tory Channel, New Zealand. Plew and Stevens found that the numerical predictions were almost one-third the analytical predictions obtained using the channel model by Vennell [48].

Adcock and Draper [50] expanded the model of GC2005 to consider multiple tidal constituents and their effects on the potential of a channel. The results compared satisfactorily with those from Adcock and Draper's earlier study of the Pentland Firth [51].

Cummins [40] investigated the potential of a split channel using the electric circuit analogy theory and derived analytical expressions for the potential and flow of each section of the channel. Cummins found that the flow reduces to 58 % of its magnitude in undisturbed conditions at maximum power extracted in the impeded sub-channel. Atwater and Lawrence [52] assessed analytically a split channel with a constant head driving the flow independent of the level of power extraction in the channel. Atwater and Lawrence showed that the increased resistance in the impeded sub-channel used to account for the presence of tidal turbines diverted the flow to the free sub-channel and did not decrease total volumetric flow through the channel. Hence, undisturbed kinetic power is not a good indicator of the potential of a split channel. Polagye and Malte [53] and Draper *et al*. [39] carried out further analysis to explore the limits to power extraction in multiple-channel networks.

It should be noted that the coastal sites considered above, that were categorised as a channel linking two infinite ocean basins, could also be categorised as a strait between an island and

landmass or other island-landmass layouts defined in Section 2.3.4. For this reason, Section 2.3.4 includes a wider review of resource assessment of actual sites of this category.

### 2.3.2 Channel connecting an oscillating bay to an infinite ocean basin

The potential of an idealised channel connecting an oscillating bay to an infinite basin has been analysed by Garrett and Cummins [54]. Maximum power available for extraction is reached when tidal range inside the bay is reduced to 74 % of that in undisturbed conditions; and maximum power is not well approximated by the undisturbed kinetic power in the channel. The tidal array is more effective if distributed uniformly across the entrance of the bay. The 1D analytical model by GC2005 used for a channel linking two infinite ocean basins is also valid here after correction of the driving head. The 1D analytical model of Blanchfield *et al*. [30] predicted the maximum average extractable power to be a function of the amplitude of the dominant tidal constituent in the open ocean, the maximum volumetric flow rate, and the amplitude ratio and phase lag between the bay and the open ocean in undisturbed conditions. Numerical results from Draper [13] compare satisfactorily with the analytical model from Blanchfield *et al*. for an isolated bay but the results differ significantly for a bay with two inlet channels. Using a 1D time-dependent numerical model, Polagye *et al*. [55] observed that power extraction leads to a reduction in the volumetric flow rate and kinetic power density in a channel and a reduction in tidal range landward of a tidal array. The magnitude of these effects depends on the rate of power extracted, estuary geometry, tidal regime, and non-linear turbine dynamics, and also cannot be related in any easy way to the fraction of kinetic energy extracted. Vennell's [48] 1D analytical model can also be applied to this type of coastal site and was applied to estimate the potential of the entrance channel to Kaipara Harbour in New Zealand as between 110 MW and 240 MW for a simple channel and channel and lagoon systems respectively.

Karsten *et al*. [56] analysed numerically the Minas Passage in the Bay of Fundy, east coast of Canada, and found that the limit to power extraction is 7 GW, with over 30 % reduction in the volumetric flow rate in the Minas Passage and the tidal amplitude in the Minas Basin. When a 5 % maximum change in the tidal amplitudes is allowed, the power extracted decreases to 2.5 GW. Blanchfield *et al*. [57] used the model by Blanchfield *et al*. [30] to assess the tidal resource of the Masset Sound, located in Haida Gwaii, Canada. When the volumetric flow rate reduced to 58 % of the undisturbed state the maximum power extracted by the array was 79 MW, which reduced to 37 MW if the tidal regime was kept within 90 % of the undisturbed conditions. Kawase and Gedney [58] investigated an ocean-fjord system

and concluded that knowledge of the natural power dissipated on the seabed is important in order to estimate the limits on power extraction for a tidal array deployed in the fjord. Walkington and Burrows [32] found that power extraction depends on the farm spatial layout and that this also affects erosion and sediment transport. Changes in the local flow features and water levels were also assessed by Ahmadian and Falconer [59] and Ahmadian *et al*. [60] in the Severn Estuary and Bristol Channel, south-west of England.

### 2.3.3 Headland

Draper *et al.* [41] analysed the energy potential of a tidal array deployed near an idealised headland and the effect of the array on the environment. Maximum power extracted by the array was not well approximated by either the local undisturbed kinetic power or the power naturally dissipated by the seabed. The undisturbed kinetic power distribution is however useful to determine the best location to deploy a tidal array near a headland. Higher rates of bypass flow were found offshore of the array, where depths were greater, and the bypass flow limited the power extracted by the array. Adcock [61] investigated an idealised headland, obtaining results in agreement with those by Draper *et al.*. Adcock found that extending one or two rows of turbines offshore of the headland led to a higher increase in power extraction than for several rows of turbines close to the headland.

Serhadlıoğlu *et al*. [62] assessed the resource off the Anglesey Skerries, north-west of Wales. They concluded that more power is extracted as turbine arrays are placed closer to the Skerries, power extraction from long rows is greater than from multiple rows, and higher bypass flow occurs offshore of the array than in the region between the array and the Skerries. Results from Serhadlıoğlu *et al*. are in agreement with Draper *et al.* [41]. Blunden and Bahaj [42] analysed the undisturbed hydrodynamics of Portland Bill, however they did not explore the limits to power extraction of the site. Neill *et al*. [63] analysed the effects of power extraction on the sand banks naturally generated from headland eddies and found the maintenance of sand banks could be affected if a 300 MW tidal array were deployed in the vicinity of the headland.

### 2.3.4 Strait between an island and a landmass

A survey of tidal sites in the United Kingdom and North America carried out by Draper [13] revealed that slightly less than 10 % of the coastal sites considered in the survey can be categorised as a strait between an island and a landmass.

This type of coastal site is dominated by two coastal features, namely the strait and the island. A strait is a narrow waterway connecting two large bodies of water (e.g. Strait of Gibraltar connecting the Atlantic Ocean and the Mediterranean Sea). When this narrow water separates two land masses it is referred as a channel (e.g. English Channel separating United Kingdom and France). Vennell [64] analysed the barotropic changes in free surface and velocity along a channel, and distinguished between long, if channel is narrow at a distance 0.2 widths from the ends, and short channels, if channel is wide at a distance 0.2 widths from the ends. Another channel classification was suggested by Vennell *et al*. [35]: large channels are deeper and the undisturbed channel dynamics are dominated by inertia of the flow; and small channels are shallower ones where channel undisturbed dynamics are dominated by natural bottom friction. Vennell defined a channel as non-divergent if transport is the same at every cross-section of the channel; that is, the velocity has the same phase throughout the channel. Vennell found that short channels are non-divergent, an example being the Cook Strait in New Zealand [65].

Flow dynamics around islands have been extensively studied. Aerial observations of island wakes have highlighted the importance of capturing satisfactorily the flow dynamics past an island. Ingram and Chu [66] investigated experimentally the wake behind islands in shallow waters and compared them to aerial observations of the flow around islands in the Rupert Bay, north coast of Quebec (Canada). Ingram and Chu observed that the island wake depends on the stability of the transverse shear layers developed along the two sides of the island. Wolanski *et al*. [67] and Furukawa and Wolanski [68] investigated the island wake in shallow waters generated at Rattray Island, northeast Australia, and concluded that island wakes are very sensitive to the level of detail of the bathymetry near the separation points. Lloyd *et al*. [69] investigated experimentally the mechanisms of wake formation around surface piercing circular islands in oscillatory laminar shallow water flows. Lloyd *et al*. found that the type of oscillatory wake depends on two non-dimensional parameters: the stability parameter, which depends on the bottom friction, island geometry and water depth; and the Keulegan-Carpenter number, which depends on the amplitude and period of the oscillating velocity at the surface. Lloyd and Stansby [70] extended the analysis to conical surface piercing islands and analysed experimentally and numerically the influence of the island side slope angle on the wake. Pingree and Maddock [71] [72] analysed numerically a sloping island and observed the formation of four residual eddies originated from frictional stress on the sloping bathymetry. Couch [73] studied numerically the development of wake eddies from islands through comparison against experimental and observed data.

Under sufficient tidal head to drive the flow, the presence of an island, island-landmass, or a group of islands can increase local current velocities to a point that they can be exploited to generate power. The following is one possible classification of the island-tidal systems (Figure 2.1):

a. Island of similar length and width in the vicinity of a landmass
b. Isolated offshore island
c. Geometrically long island in the vicinity of a landmass
d. Geometrically wide island in the vicinity of a landmass
e. Two isolated offshore islands
f. Isolated offshore multi-island system

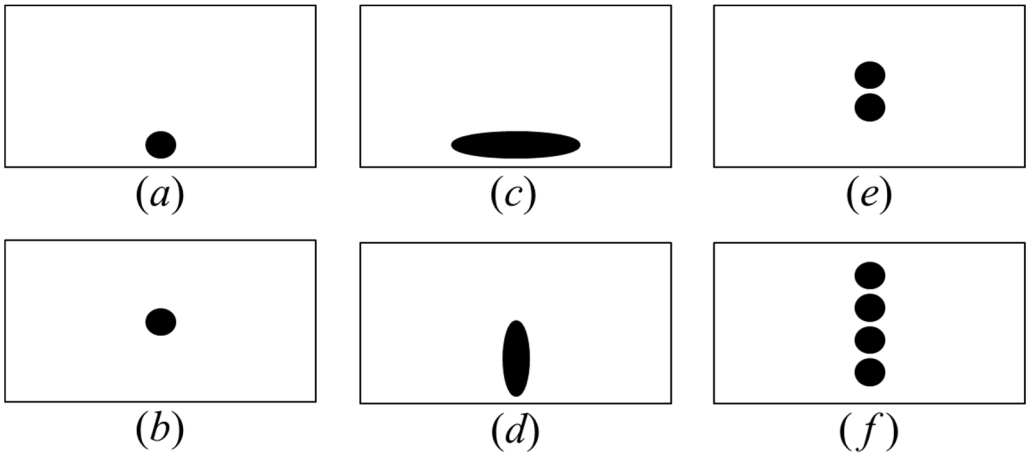


Figure 2.1. Island-tidal system configurations suitable for power exploitation [74].

In his study of a channel linking two infinite ocean basins, Draper [13] analysed numerically a strait between a geometrically long and wide island and a landmass. Draper observed that the maximum averaged power extracted from the strait is not well approximated by the GC2005 channel model mainly due to changes in the driving head induced by power extraction in the strait as the bypass flow offshore off the island was not significant at the island scale analysed. If this difference in head was accounted for, Draper concluded that the GC2005 channel model explains satisfactorily the basic physics of the strait.

Adcock *et al.* [51] assessed numerically the available power in the Pentland Firth, a coastal site that could be categorised as a strait between a geometrically long and wide island and a landmass. Adcock *et al.* found that maximum power extraction in the Pentland Firth is less than half than the predicted value using the GC2005 channel model. Results from Draper *et al*. [12] for the Pentland Firth agree with the power extraction predicted by the GC2005 channel model. The discrepancies between the results obtained by Adcock *et al*. and Draper

*et al*. arise from differences in the methodology used to account for power extraction in their numerical models (Section 3.2.2). Draper *et al*. observed that maximum power extraction in the Pentland Firth does not lead to flow diversion offshore of the Orkney Islands but increases the flow through the sub-channels of the Orkney Islands due to an increase in phase difference. Draper *et al*. also analysed the Inner Sound, a strait between the island of Stroma and the north coast of Scotland which could be categorised as an island of similar length and width in the vicinity of a landmass. Draper *et al*. found the potential of the Inner Sound to be 122 MW if exploited in isolation, and between 108 MW and 320 MW when operated in combination with other arrays in the Pentland Firth. Martin-Short *et al*. [75] analysed the effects of power extraction on the flow regime and sediment transport in the Inner Sound, and found changes in sediment transport for arrays in excess of 85 MW of rated power.

Myers and Bahaj [76] and Bahaj and Myers [77] investigated power generation in the Alderney Race, located between north-east coast of France and the Island of Alderney in the English Channel. An annual energy production of 7.4 TWh is estimated based on the undisturbed conditions, however this figure does not account for changes in the flow due to power extraction. The effects of power extraction on the flow are accounted by Coles *et al*. [78] who estimated the annual electricity generation to be 2.4 TWh for an array blocking the Alderney Race and a maximum average power potential to be 2.3 GW. The effects of power extraction on the environment of the Alderney Race are investigated by Thiébot *et al*. [79] who found that an array of 290 MW produces a 15 % reduction in the mean current velocity compared to undisturbed conditions. Sediment transport between eastern and western part of the Alderney Race is found to be sensitive to the location of the tidal array.

Sutherland *et al*. [31] assessed the limits to power extraction in the Johnstone Strait, located between Vancouver Island and west coast of Canada, a coastal site which could be categorised as a strait between a geometrically long island and a landmass. When flow was not allowed to divert away from the channel, Sutherland *et al*. found that the numerical results were in agreement with the GC2005 channel model.

Blunden *et al*. [80] assessed the resource of the Alas Strait, located between Lombok Island and Sumbawa Island in Indonesia, which could fall into the category of an isolated offshore multi-island system. Power extraction from the flow was accounted by the attenuation of the incident velocity based on the flow direction and the number of rows deep into the array. Annual energy generation was estimated in 330 GWh when turbines were only installed in water depths lower than 40 m and 640 GWh when turbines could also be installed in water

depths up to 80 m. The methodology employed approximated the effects of power extraction on the flow and consequently in the energy yield. However, the analysis was restricted to the Alas Strait and as such it did not consider the effects that power extraction in the Alas Strait could have on the other straits of the multi-island system. Vennell [48] estimated a potential of 15 GW in the Cook Strait in New Zealand, which could fall into the category of two isolated offshore islands.

Chen *et al*. [81] assessed numerically the extracted energy from tidal turbines near Zhaitang Island, located off the east coast of China, a coastal site that could be categorised as an isolated offshore island. Chen *et al*. tested several array configurations of individually represented turbines and observed that turbines closer to the island were producing more power. However Chen *et al*. did not define the limits to power extraction at the coastal site.

Draper *et al*. [39] employed the electric circuit analogy theory to estimate the resource in the Pentland Firth and the Inner Sound, and found that that the maximum average power in the Inner Sound differed by 23 % from the results obtained separately by Draper *et al*. [12]. However, Draper *et al*. [39] did not extend the analysis to the Orkney Islands and offshore to account for bypass flow changes when power is extracted in the Pentland Firth.

## 2.4. Summary

This chapter has summarised the tools currently used to undertake tidal resource assessment, and highlighted the merits and drawbacks of different analytical and numerical models used to estimate the limits to power extraction by tidal arrays and assess the effects on the environment. The available analytical models and numerical studies have been considered for four types of coastal site, following Draper's classification. Coastal sites defined as a channel linking two infinite ocean basins and an infinite ocean basin with an enclosed bay have been extensively studied, and the current analytical models appear to provide a good approximation to the potential of these coastal sites. For headlands, the results from idealised and actual coastal site numerical models appear to be consistent. The coastal site defined as a strait between an island and landmass and alternative layouts is generally analysed as a channel linking two infinite ocean basins, which provides a good approximation to the potential at the site for geometrically long islands in the vicinity of a landmass as discussed by Draper *et al*. and Sutherland *et al*.. However, other island site layouts may exhibit different flow characteristics due to the change in the head driving the flow with power extraction in the strait and bypass flow offshore of the island. Although

flow dynamics around islands have been extensively studied, it is concluded from the literature review that a detailed numerical analysis of this type of coastal site from a resource assessment point of view is required. The analysis should consider the characterisation of the resource based on an idealised site and assess the validity of the outcomes through the analysis of an actual coastal site.

# 3. Methodology

## 3.1. Introduction

Tidal resource assessment of coastal sites through numerical modelling involves prediction of the complex flow dynamics driven by the tidal flow as it interacts with the bed topography of the site and encounters the turbines extracting power from the flow. This chapter presents the SWEs and their implementation applied to tidal resource assessment. The chapter is structured in three sections. Section 3.2 presents the SWEs, their derivation from the three-dimensional Navier Stokes equations, the external equation force terms relevant to tidal applications, and finally summarises the different methodologies to account for power extraction from tidal turbines in SWE models. A discussion is also included on the choice of the SWEs and power extraction methodology. Section 3.3 summarises the fundamentals of the finite element method and describes the main configuration of the numerical model Fluidity used in Chapters 4, 5 and 6 for the various parameter studies. Section 3.4 presents the summary of this chapter.

## 3.2. Shallow water equations

Complex three-dimensional tidal flows can be simplified to a two-dimensional, depth-averaged problem through the use of the shallow water equations (SWE). Shallow water is defined as having a depth at most one tenth of the tidal wavelength, and vertical velocities that are negligible compared to streamwise and transverse velocities [82]. The SWEs are traditionally used in applications such as rivers, and lately have also been employed in tidal resource assessment applications [12]. The SWEs can be either directly derived, or obtained through the depth integration of the continuity and momentum Navier-Stokes equations [83] [84]. Under the assumption of a hydrostatic pressure distribution, depth integration of the Navier-Stokes equations leads to the shallow water equations (Eqs (3.47) - (3.49) in Section 3.2.3).

The Navier-Stokes equations in conservative form are:

$$\frac{\partial U}{\partial x}+\frac{\partial V}{\partial y}+\frac{\partial W}{\partial z}=0 \tag{3.1}$$

$$\frac{\partial U}{\partial t}+\frac{\partial U^2}{\partial x}+\frac{\partial UV}{\partial y}+\frac{\partial UW}{\partial z}=X-\frac{1}{\rho}\frac{\partial P}{\partial x}+\frac{1}{\rho}\left(\frac{\partial \sigma_{xx}}{\partial x}+\frac{\partial \tau_{xy}}{\partial y}+\frac{\partial \tau_{xz}}{\partial z}\right) \tag{3.2}$$

$$\frac{\partial V}{\partial t}+\frac{\partial UV}{\partial x}+\frac{\partial V^2}{\partial y}+\frac{\partial VW}{\partial z}=Y-\frac{1}{\rho}\frac{\partial P}{\partial y}+\frac{1}{\rho}\left(\frac{\partial \tau_{yx}}{\partial x}+\frac{\partial \sigma_{yy}}{\partial y}+\frac{\partial \tau_{yz}}{\partial z}\right) \tag{3.3}$$

$$\frac{\partial W}{\partial t}+\frac{\partial UW}{\partial x}+\frac{\partial VW}{\partial y}+\frac{\partial W^2}{\partial z}=Z-\frac{1}{\rho}\frac{\partial P}{\partial z}+\frac{1}{\rho}\left(\frac{\partial \tau_{zx}}{\partial x}+\frac{\partial \tau_{zy}}{\partial y}+\frac{\partial \sigma_{zz}}{\partial z}\right) \tag{3.4}$$

where $t$ is the time and $x$, $y$ and $z$ are the Cartesian coordinates; $U$, $V$ and $W$ are the simple Cartesian velocity components of the fluid respectively; $X$, $Y$ and $Z$ are external forces; $P$ is the fluid pressure; and $\rho$ is the fluid density (for seawater $\rho$ =1,025 kg/m$^3$). In turbulent flows, such as those occurring in shallow waters, the velocity terms can be separated using the Reynolds decomposition into local mean $\overline{U}$ and fluctuating $U^*$ components [85].

In a time period $T_f$, which is longer than the time scale of the turbulent fluctuations but smaller than the time scale of the main flow features, the velocity components satisfy the following conditions.

$$\overline{U}=\frac{1}{T_f}\int_t^{t+T_f} U\,dt \tag{3.5}$$

$$\overline{U^*}=\frac{1}{T_f}\int_t^{t+T_f} U^*\,dt=0 \tag{3.6}$$

$$U=\overline{U}+U^* \tag{3.7}$$

The Reynolds-decomposed velocity components are substituted into continuity Eq. (3.1) and $x$-direction momentum Eq. (3.2) ($y$ and $z$ momentum equations are changed in a similar way) to obtain the Reynolds-averaged equations:

$$\frac{\partial \overline{U}}{\partial x}+\frac{\partial \overline{V}}{\partial y}+\frac{\partial \overline{W}}{\partial z}=0 \tag{3.8}$$

$$\frac{\partial \overline{U}}{\partial t}+\frac{\partial \overline{U}^2}{\partial x}+\frac{\partial \overline{UV}}{\partial y}+\frac{\partial \overline{UW}}{\partial z}=\overline{X}-\frac{1}{\rho}\frac{\partial \overline{P}}{\partial x}+\frac{1}{\rho}\left(\frac{\partial \overline{\sigma_{xx}}}{\partial x}+\frac{\partial \overline{\tau_{xy}}}{\partial y}+\frac{\partial \overline{\tau_{xz}}}{\partial z}\right) \tag{3.9}$$

The parameters $\bar{\sigma}$ and $\bar{\tau}$ account for effective stress, including normal and shear viscous stresses.

$$\overline{\sigma_{xx}} = 2\mu\frac{\partial\bar{U}}{\partial x} - \rho\overline{U^*U^*} \tag{3.10}$$

$$\overline{\tau_{xy}} = \overline{\tau_{yx}} = \mu\left(\frac{\partial\bar{U}}{\partial y} + \frac{\partial\bar{V}}{\partial x}\right) - \rho\overline{U^*V^*} \tag{3.11}$$

where $\mu$ is the dynamic viscosity ($10^{-3}$ N s/m$^2$ for sea water).

Figure 3.1 shows the shallow water system and the defining parameters. The bottom of the system is defined by a level $z = z_o$, referenced against a vertical datum. The undisturbed total water depth $h = h_o + \delta$ results from the addition of the undisturbed water depth or still water level $h_o$ and the free surface elevation $\delta$. The sea surface is defined as $z = z_o + h$.

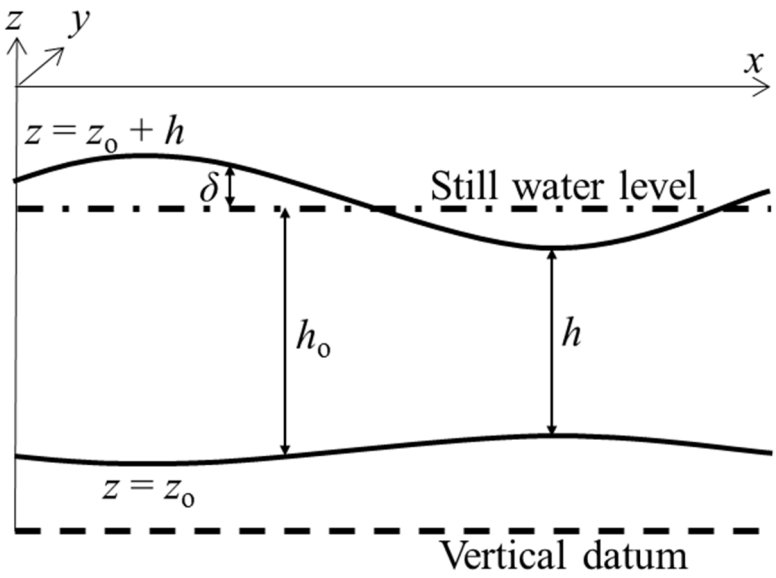


Figure 3.1. Diagram of the shallow water system and the defining parameters.

Derivation of the SWEs is based on two assumptions: hydrostatic pressure and the impermeability of the free surface and sea bed [86]. Pressure is hydrostatic when gravity is counterbalanced by the acceleration induced by pressure. At these conditions, vertical accelerations are negligible. Thus, the pressure $P(x, y, z)$ can be expressed in terms of the weight of the water column:

$$0 = -\frac{1}{\rho}\frac{\partial\bar{P}}{\partial z} - g \tag{3.12}$$

Integrating Eq. (3.12) between $z = z_o$ and the water surface $z = z_o + h$, where $P$ is equal to atmospheric pressure, $p_a$, leads to:

$$P(x, y, z) = p_a - \rho g z_o + \rho g(z_o + h) \tag{3.13}$$

Neglecting the spatial gradient of the atmospheric pressure term, Eq. (3.13) becomes $P = \rho g h$.

Surface and bottom boundaries are impermeable. This boundary condition defines that there is no flow through either boundary, thus particles at either surface remain there. Vertical velocities at sea surface and bottom are computed as follows:

$$W_{z_o+h} = \frac{\partial(z_o+h)}{\partial t} + \bar{U}|_{z_o+h} \frac{\partial(z_o+h)}{\partial x} + \bar{V}|_{z_o+h} \frac{\partial(z_o+h)}{\partial y} \tag{3.14}$$

$$W_{z_o} = \frac{\partial z_o}{\partial t} + \bar{U}|_{z_o} \frac{\partial z_o}{\partial x} + \bar{V}|_{z_o} \frac{\partial z_o}{\partial y} \tag{3.15}$$

The depth-averaged horizontal streamwise $u$ and transverse $v$ velocity components are computed respectively as:

$$u = \frac{1}{h} \int_{z_o}^{z_o+h} \bar{U}\, dz \tag{3.16}$$

$$v = \frac{1}{h} \int_{z_o}^{z_o+h} \bar{V}\, dz \tag{3.17}$$

Finally, the process of derivation of the SWE requires the use of the Leibnitz rule to differentiate an integral with variable boundaries.

$$\frac{\partial}{\partial x} \int_{z_o}^{z_o+h} \bar{U}\, dz = \int_{z_o}^{z_o+h} \frac{\partial \bar{U}}{\partial x} dz + \bar{U}|_{z_o+h} \frac{\partial(z_o + h)}{\partial x} - \bar{U}|_{z_o} \frac{\partial z_o}{\partial x} \tag{3.18}$$

Integrating Eq. (3.1) over the depth and applying the boundary conditions at free surface and seabed shown in Eqs. (3.14) and (3.15) respectively leads to the depth-integrated form of the continuity equation:

$$\frac{\partial \delta}{\partial t} + \frac{\partial}{\partial x}(hu) + \frac{\partial}{\partial y}(hv) = 0 \tag{3.19}$$

The depth-integrated version of the momentum equations is developed by parts. First, the derivative and advection terms of Eq. (3.2) are integrated over the depth and the boundary conditions shown in Eqs. (3.14) and (3.15) are applied, resulting in:

$$\int_{z_o}^{z_o+h}\left(\frac{\partial \bar{U}}{\partial t}+\bar{U}\frac{\partial \bar{U}}{\partial x}+\bar{V}\frac{\partial \bar{U}}{\partial y}+\bar{W}\frac{\partial \bar{U}}{\partial z}\right)dz=\frac{\partial (hu)}{\partial t}+\frac{\partial}{\partial x}(hu^2)+\frac{\partial}{\partial y}(huv) \tag{3.20}$$

Integrating the pressure term in Eq. (3.2) as shown in Eq. (3.13) and assuming no variation of the density along the horizontal plane results in:

$$-\int_{z_o}^{z_o+h}\frac{1}{\rho}\frac{\partial \bar{P}}{\partial x}dz=-gh\frac{\partial (z_o+h)}{\partial x}-\frac{1}{\rho}\frac{\partial p_a}{\partial x} \tag{3.21}$$

For the integration of the viscous terms in Eq. (3.2), the Reynolds stresses are related to the diffusion process using the Boussinesq approximation. The diffusion term is characterised by a turbulent kinematic depth-averaged horizontal eddy viscosity $\nu_t$, which is several orders of magnitude larger than the laminar kinematic viscosity.

$$\frac{1}{\rho}\int_{z_o}^{z_o+h}\left[\frac{\partial \overline{\sigma_{xx}}}{\partial x}+\frac{\partial \overline{\tau_{xy}}}{\partial y}+\frac{\partial \overline{\tau_{xz}}}{\partial z}\right]dz=2\frac{\partial}{\partial x}\left(\nu_t h\frac{\partial u}{\partial x}\right)+\frac{\partial}{\partial y}\left(\nu_t h\left[\frac{\partial u}{\partial y}+\frac{\partial v}{\partial x}\right]\right) \tag{3.22}$$

There are different approaches in the literature to include viscous effects and account for turbulent viscosity and dispersion in the flow dynamics of a shallow coastal model:

- Assume inviscid flow. In this case, the solution can be approximated by potential flow theory [87].
- Use a constant eddy viscosity $\nu_t$ to account for molecular viscosity, turbulent viscosity and dispersion [88]. Some studies have used the eddy viscosity as a parameter to calibrate their hydrodynamic models [89].
- Compute the eddy-viscosity with an empirical turbulence model such as the *k*-$\varepsilon$ or *k*-$\omega$ models which solve additional transport equations for turbulent quantities [90]. Where *k* is the turbulent kinetic energy, $\varepsilon$ is the turbulent dissipation, and $\omega$ is the specific turbulent dissipation rate.

The depth-averaged parabolic eddy viscosity model is based on a perfect balance between the vertical shear stress and the hydrostatic pressure gradient. Under uniform flow conditions, the x-direction momentum equation becomes a balance between vertical shear and pressure gradient [91]. Under the assumption of logarithmic velocity distribution over depth, $\nu_t$ is defined by a parabolic vertical profile, which after integration over depth becomes [92]:

$$\nu_t=\frac{k}{6}(C_d[u^2+v^2])^{1/2}h \tag{3.23}$$

where $k$ = 0.41 is the von Kármán constant, $C_d$ is the non-dimensional bottom drag coefficient and the term $\left[C_d\left(u^2+v^2\right)\right]^{1/2}$ is known as the bed shear velocity.

The depth-averaged parabolic eddy viscosity accounts for the turbulence generated by bed friction, but it does neglect effects of horizontal velocity gradients and it does not account for transport and dissipation processes. It has been used to simulate simple channel flows and to account for turbulence produce by bed friction in more complex models [91].

Wu *et al.* [93] compared this depth-averaged parabolic horizontal eddy viscosity model against the modified mixing length model and three *k-ε* turbulence models. All five turbulence models yielded similar flow velocity distributions when used in simple channel geometry natural rivers. However, all turbulence models provided different simulated secondary flow features around a spur-dyke and in a sudden-expanded flume. Such features are not present in the cases considered in this work and so the depth averaged parabolic eddy viscosity model is considered sufficient to account for turbulence.

### 3.2.1 External forces in the shallow water equations

#### 3.2.1.1 Bed stress

Bottom friction is used to characterise the roughness of the seabed which can be defined by different seabed sediment grain sizes for flat beds or scenarios with bed form. Similarly to viscosity, bottom friction has been used as a calibration parameter when modelling real coastal sites [51] [94].

Bottom friction can be parameterised using a linear or quadratic law. Based on the shear profiles taken from observations at real sites, bottom friction is said to be more realistically modelled using a quadratic law [26]. When using a quadratic drag law, the depth integrated bottom shear stress $\tau_b$ is implemented in the $x$ and $y$ momentum equations as:

$$\tau_{bx} = \rho C_d u(u^2 + v^2)^{1/2} \tag{3.24}$$

$$\tau_{by} = \rho C_d v(u^2 + v^2)^{1/2} \tag{3.25}$$

It is possible to equate the depth integrated shear stress to the vertically resolved shear stress if data of velocity at 100 cm above the bottom $U_{100}$ is available:

$$\tau_b = C_d \rho u^2 = C_{100} \rho U_{100}^2 \tag{3.26}$$

where $C_{100}$ is the bottom drag coefficient based on a velocity measured 100 cm above the bottom.

The above expression can be rearranged as:

$$\frac{C_{100}}{C_d} = \frac{u}{U_{100}} \tag{3.27}$$

Soulsby [95] developed an empirical expression to approximate the velocity profile in the bottom half of the water column:

$$U_z = \left(\frac{z}{0.32h}\right)^{1/7} u \tag{3.28}$$

where $z$ is the location in the water column above the bottom, thus $z = z_o + 1$ m to determine $U_{100}$. The combination of Eqs. (3.27) and (3.28) at $z = z_o + 1$ m leads to the expression:

$$C_d = \left(\frac{1}{0.32h}\right)^{1/7} C_{100} \tag{3.29}$$

Bottom friction is characterised in the literature in terms of the Manning number $M$ and Chezy number $C$, linked to the dimensionless bottom friction as:

$$C_d = \frac{g}{(Mh^{1/6})^2} \tag{3.30}$$

$$C_d = \frac{g}{C^2} \tag{3.31}$$

Table 3.1 presents the bottom drag coefficients derived empirically from field and laboratory data [95] for different bed types and their equivalent non-dimensional friction coefficient, Manning number and Chezy number computed for a water depth $h = 40$ m.

| Bed type | $C_{100}$ | $C_d$ | $M$ | $C$ |
|---|---|---|---|---|
| Mud | 0.0022 | 0.0015 | 43.32 | 80.11 |
| Mud/sand | 0.003 | 0.0021 | 37.10 | 68.61 |
| Silt/sand | 0.0016 | 0.0011 | 50.80 | 93.94 |
| Sand (unrippled) | 0.0026 | 0.0018 | 39.85 | 73.69 |
| Sand (rippled) | 0.0061 | 0.0042 | 26.02 | 48.11 |
| Sand/shell | 0.0024 | 0.0017 | 41.48 | 76.70 |
| Sand/gravel | 0.0024 | 0.0017 | 41.48 | 76.70 |
| Mud/sand/gravel | 0.0024 | 0.0017 | 41.48 | 76.70 |
| Gravel | 0.0047 | 0.0033 | 29.64 | 54.81 |

Table 3.1. Bottom drag coefficients $C_{100}$ for different bed types and their equivalent $C_d$, $M$ and $C$ for water depth $h$ = 40 m [95].

#### 3.2.1.2 Wind stress

Wind stress $\tau_w$ acting on the sea surface is included on the $x$ and $y$ momentum equations of the SWE as [89]:

$$\tau_{wx} = \rho_a C_w U_{10}(U_{10}^2 + V_{10}^2)^{1/2} \tag{3.32}$$

$$\tau_{wy} = \rho_a C_w V_{10}(U_{10}^2 + V_{10}^2)^{1/2} \tag{3.33}$$

where $U_{10}$ and $V_{10}$ are the wind velocity components measured at 10 m height above the sea surface, $\rho_a$ is the air density and $C_w$ is the dimensionless air-water resistance coefficient. Values of $C_w$ are given by Flather [96], obtained from a study of surge prediction in the North-West European continental shelf:

$$C_w = \begin{cases} 0.565 \times 10^{-3} & \text{if } \left(U_{10}^2 + V_{10}^2\right)^{1/2} \leq 5 \\ \left(-0.12 + 0.137\left(U_{10}^2 + V_{10}^2\right)^{1/2}\right) \times 10^{-3} & \text{if } 5 \leq \left(U_{10}^2 + V_{10}^2\right)^{1/2} \leq 19.22 \\ 2.513 \times 10^{-3} & \text{if } \left(U_{10}^2 + V_{10}^2\right)^{1/2} \geq 19.22 \end{cases} \tag{3.34}$$

#### 3.2.1.3 Coriolis

Coriolis forces are negligible in rivers and lakes but are important for large masses of water such as oceans. The depth integration of the Coriolis component is added to the $x$ and $y$ momentum equations as follows:

$$\int_{z_o}^{z_o+h} fv\,dz = fhv \tag{3.35}$$

$$\int_{z_o}^{z_o+h} fu\,dz = fhu \tag{3.36}$$

where $f$ is defined as:

$$f = 2\Omega \sin\lambda \tag{3.37}$$

where $\Omega$ is the rotational frequency of the earth ($2\pi/86164$ rad/s) and $\lambda$ is the latitude of the site; this is called the f-plane approximation. In small domains, the value of $f$ can be considered constant [86].

### 3.2.2 Accounting for the presence of power extraction

This section discusses existing methodologies to model power extraction in SWE models. The methodologies may be categorised as either distributed-drag or individual turbine approaches [35].

#### 3.2.2.1 Distributed drag

This method consists of modifying the aggregated drag farm coefficient at an area in the same range of the equivalent size of the farm footprint. This method of power extraction has been validated experimentally by Coles *et al.* [97] in a flume where power extraction from the flow was modelled using series of porous fences. From the literature it is possible to distinguish two different ways to apply the distributed-drag approach in a SWE model: volumetric momentum sink and enhanced bottom drag.

##### Volumetric momentum sink

In this approach the power extracted from the flow by the turbines due to rotor thrust and support-structure drag is included in the momentum equations as a sink term. The term represents the force exerted on the flow by a turbine averaged over the volume defined by the element area and the local water depth. This method assumes a uniform distribution of

the momentum sink over the farm area and, because it is a two-dimensional approach, also over the water column. In three-dimensional models, as pointed out by Bryden *et al*. [16], a momentum sink can be specified at a particular elevation in the water column allowing for more realistic representation of power extraction from turbines.

This method allows detailed parameterisation of tidal turbines and can include flow dependent drag and thrust curves. The forces exerted by the tidal turbines on the flow can be separated into two components:

- Drag force $F_D$ from the supporting structure of the turbine.
- Thrust force $F_T$ originating from the power extraction from the flow by the turbine rotor.

The total force $F_{TOT}$ from a tidal turbine acting on the flow is expressed as:

$$F_{TOT} = F_D + F_T = \frac{1}{2}\rho A_S C_D |\vec{u}|\vec{u} + \frac{1}{2}\rho A_T C_T |\vec{u}|\vec{u} \tag{3.38}$$

where $A_S$ and $A_T$ are the projected areas of the turbine support structure and rotor respectively; $C_D$ and $C_T$ are the supporting structure drag and rotor thrust coefficients respectively; and $\vec{u}$ is the depth-averaged velocity vector.

The source term $F(\vec{u})$ is considered an external force and included in the momentum equations as:

$$F(\vec{u}) = -\frac{F_{TOT}}{A_f h} \tag{3.39}$$

where $A_f$ is the area where the tidal farm is implemented. The above expression is multiplied by a parameter $N_T$ which accounts for the number of turbines contained in the farm.

For numerical stability, the source term $F(\vec{u})$ is treated implicitly through the addition of a volumetric absorption term $F = \gamma_f \times \vec{u}$ [98], expressed as:

$$\gamma_f = -\frac{N_T(A_S C_D + A_T C_T)|\vec{u}|}{2A_f h} \tag{3.40}$$

This power extraction methodology has been applied in a number of hydrodynamic tidal studies. Neill *et al*. [29] used a 1D model to analyse the effects of power extraction on large-scale sediment dynamics in regions of strong tidal asymmetry and applied it to the Severn estuary (United Kingdom). Ahmadian *et al*. [60] studied the impacts of an array of turbines in the Severn estuary and Bristol channel (United Kingdom) with a 2D hydro-environmental model. Shapiro [33] analysed the effects of power extraction on the circulation at the Celtic Sea with a 3D model. Plew and Stevens [49] applied the same methodology in a 2D model to analyse the effects on the currents of a tidal farm located at the Tory Channel (New

Zealand). Perez-Ortiz *et al*. [88] analysed the electric power generated from a farm in the Inner Sound at the Pentland Firth (United Kingdom) with a 2D model.

### Enhanced bottom drag

In this two-dimensional approach, power extraction by turbines is approximated by an equivalent increase in bottom friction in a given area. Assuming a quadratic seabed drag, the force exerted by the seabed with a non-dimensional seabed-friction coefficient $C_d$ across an area $A_f$ is [31]:

$$F_d = \iint_{A_f} \rho\, C_d |\vec{u}| \vec{u} dA_f \tag{3.41}$$

If tidal turbines are implemented in the area $A_f$, the additional force exerted by tidal turbines on the flow is:

$$F_f = \iint_{A_f} \rho\, k_f |\vec{u}| \vec{u} dA_f \tag{3.42}$$

where $k_f$ is the equivalent seabed friction coefficient due to the presence of turbines in the area $A_f$. The final friction coefficient $C_o$ at the area $A_f$ is the sum of the natural friction coefficient and that accounting for the presence of turbines:

$$C_o = C_d + k_f \tag{3.43}$$

This methodology of power extraction has been employed in two-dimensional models by Karsten *et al*. [56] and Sutherland *et al*. [31] to assess limits to power extraction in the Minas Passage in the Bay of Fundy (Canada) and the Johnstone Strait between the west coast of Canada and Vancouver Island.

If there are $N_T$ turbines in $A_f$, it is possible to determine $k_f$ by equating Eqs. (3.38) and (3.42) as:

$$k_f = \frac{N_T F_{TOT}}{A_f \rho |\vec{u}| \vec{u}} = \frac{N_T (C_T A_T + C_D A_S)}{2A_f} \tag{3.44}$$

The above equivalent horizontal seabed drag coefficient distributes uniformly the force exerted by $N_T$ turbines on the flow across the area $A_f$. If turbine thrust and drag coefficients are velocity dependent, $k_f$ may change across the farm area.

If there is sufficient mesh refinement, both momentum sink and enhanced seabed drag methods permit the specification of a profile of turbine density within the array area.

Yand and Wang [99] compared the methodologies of momentum sink and enhanced seabed drag to account for power extraction against the analytical model of Garrett and Cummins [11]. Both methods gave very similar results in agreement with the predicted values by Garrett and Cummins.

#### 3.2.2.2 Individual turbine

There are currently two approaches used in the SWEs to include power extraction from individual devices: enhanced drag and linear momentum actuator disk theory.

##### Enhanced drag

This approach uses the methodology presented in Section 3.2.2.1 but in this case there are individual areas of drag accounting for each turbine in the array; i.e. $N_T = 1$ and $A_f$ is equal to the footprint of a turbine. This method is computationally more expensive than the distributed drag approach as it requires high levels of mesh refinement to resolve turbulence at turbine and sub-turbine scale. As described by Baston *et al.* [100], here the size of the mesh elements should be small enough to have at least one element per turbine and there should be more than one additional mesh element between turbines to allow for flow diversion around turbines. With sufficient mesh refinement in the turbine wake zone, this approach can account for power lost to mixing behind turbines and the array. Individual power extracted by turbines is computed based on local flow velocity and power from each device is added to compute total array power.

This methodology to represent individual turbines has been used by Funke *et al*. [101] and Divett [102] to optimise the farm layout in a two-dimensional model where turbines were assumed to have constant drag and thrust coefficients. Martin-Short *et al*. [75] included realistic drag and thrust curves to assess the effects of power extraction in sediment transportation at the Inner Sound, a strait between isle of Stroma and north coast of Scotland. Peyrard *et al.* [103] compared the wakes generated from an increase in drag over an element and from a rectangular obstacle and concluded that both wakes were very similar.

The choice of area $A_f$ and the inverse relationship with the local velocity and turbine extracted power have been discussed by Kramer *et al.* [104]. If $A_f$ is large compared to the footprint of the turbine, the additional drag density due to the presence of turbine is small compared to the background bottom drag, and local velocity is close to free stream velocities. On the contrary, small values of $A_f$ mean high turbine drag density and therefore

lower velocities and estimates in the power extracted by the turbine. Kramer *et al.* suggested a non-tested correction methodology for a single turbine based on actuator disc theory (see next section):

$$F_{TOT} = \frac{1}{2}\rho A_T C_T \frac{4}{\left(1+\sqrt{1-\gamma}\right)^2}|\vec{u}|\vec{u} \tag{3.45}$$

where $\gamma$ is defined as:

$$\gamma = C_T \frac{A_T}{\Delta y h} \tag{3.46}$$

and $\Delta y$ is the numerical cell width.

### Linear momentum actuator disc theory

Actuator disk theory provides a simple one-dimensional approach for rotor modelling to compute rotor thrust and extracted power from the flow based on the upstream free stream velocity. This approach, used in wind energy for an isolated turbine [14], was extended by several authors to make it more valid for tidal turbines. Garrett and Cummins [44] looked at a row of tidal turbines in a one-dimensional channel with constant free surface, whilst Whelan *et al.* [105] characterised the flow field around an actuator disk in an open channel with non-uniform free surface profile. Whelan *et al.*'s theory was furthered by Houlsby *et al.*[106] to include downstream mixing (Figure 3.2). Draper *et al.* [107] applied Houlsby *et al.*'s linear momentum actuator disc theory (LMADT) to a depth-averaged numerical model, where three parameters are used to define tidal turbines: the dimensionless change in depth for a given Froude number, defined as the ratio of the flow inertia to the external field; the blockage ratio, defined as the proportion of the channel cross-section occupied by the actuator disk; and a wake induction factor which enables computation of the velocity downstream of the turbine based on the free-stream velocity.

The approach by Draper *et al.* [107] has been used by Draper [13] and Draper *et al.* [41] to characterise the extractable power in idealised coastal sites such as a channel linking two infinite ocean basins, a channel linking an ocean basin and a resonant basin, and a headland. Adcock *et al.* [51] applied this methodology to estimate the extractable power of the Pentland Firth. Serhadlıoğlu *et al.* [62] used LMADT to assess the tidal resource off the Anglesey Skerries in Wales.

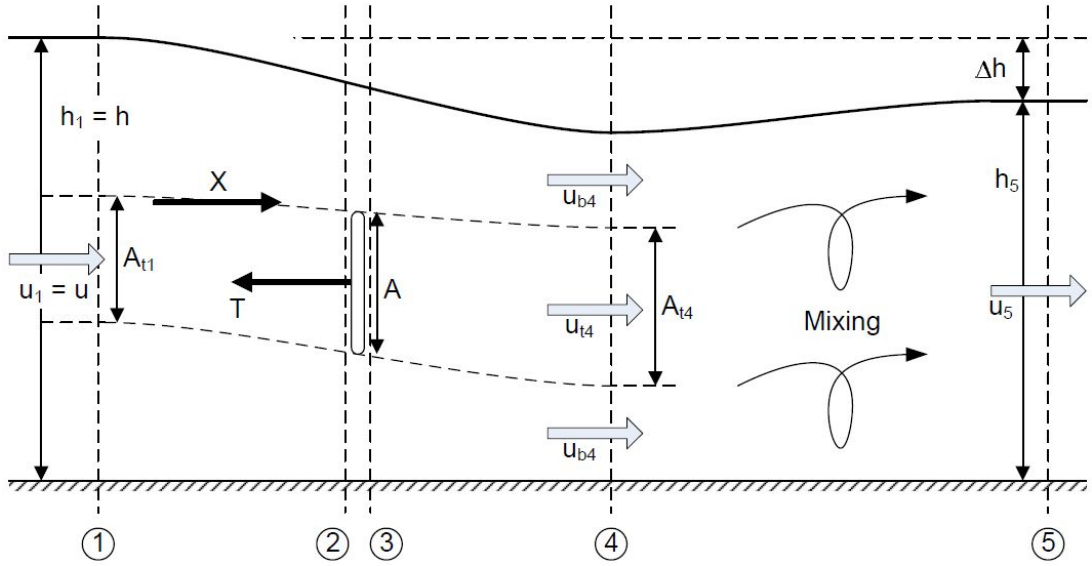


Figure 3.2. LMADT in an open channel flow with non-uniform free surface profile and downstream mixing [106].

#### 3.2.2.3 Discussion on power extraction methodologies

The main advantage of the distributed drag approaches is that they are easily implemented in a numerical model. In the resource characterisation of an idealised headland, Draper [13] showed that when the area with increased distributed drag reduces to a thin strip, both distributed drag and LMADT methods yield similar power extraction figures. Vennell *et al*. [35] concluded that these methods are suitable to estimate the maximum power that can be extracted from a channel, referred to as the channel's potential. However, Vennell *et al*. also highlighted two key disadvantages of the distributed drag approaches:

- Difficulty to link the power extraction levels to the number of turbines required to reach it. The use of realistic drag and thrust curves of isolated turbines can improve the estimation of the number of turbines [49], however they cannot take into account changes to local velocities induced by blockage effects and acceleration of flow bypassing turbines.
- Mixing losses are not accounted for at turbine scale.

Mixing losses and bypass flow acceleration can be captured by representing individually turbines as an increase of drag and applying a correction factor to their footprint as suggested by Kramer *et al.* [104]. However, this method does not take into account partial blockage of the water column and significantly increases the computational requirements as the mesh size should be of the order of the turbine footprint or less.

Draper *et al*. [108] relates the methodology employed to account for power extraction to the mesh size used in the model. When wake length scale is much smaller than the mesh size, it becomes physically realistic to use LMADT to account for power extraction [55]. The use of uniformly distributed enhanced drag is a suitable approach when mesh size is of the order of the turbine wake length [108].

The aim of this study is to understand the limits to power extraction, or the potential, of a site in the vicinity of an island near a landmass. Determining the equivalent number of turbines to the level of power extracted will require individual turbine modelling and this is highly computationally demanding. As such, the distributed drag approach is used as it is considered to provide sufficient accuracy to determine the limits to power extraction.

### 3.2.3 Final equation

Assuming negligible atmospheric pressure gradients (no atmospheric pressure term considered), the non-conservative form of the SWE solved using the finite element numerical code Fluidity [98] are:

$$\frac{\partial \delta}{\partial t} + \frac{\partial}{\partial x}(hu) + \frac{\partial}{\partial y}(hv) = 0 \tag{3.47}$$

$$\frac{\partial}{\partial t}u + u\frac{\partial}{\partial x}u + v\frac{\partial}{\partial y}u = -g\frac{\partial \delta}{\partial x} + fv + \frac{\tau_{wx} - \tau_{bx}}{h\rho} + \nu_t\left[\frac{\partial^2 u}{\partial x^2} + \frac{\partial^2 v}{\partial y^2}\right] \tag{3.48}$$

$$\frac{\partial}{\partial t}v + u\frac{\partial}{\partial x}v + v\frac{\partial}{\partial y}v = -g\frac{\partial \delta}{\partial y} - fu + \frac{\tau_{wy} - \tau_{by}}{h\rho} + \nu_t\left[\frac{\partial^2 u}{\partial x^2} + \frac{\partial^2 v}{\partial y^2}\right] \tag{3.49}$$

When power extraction level $k_f$ by tidal turbines is included, this is added to the parameter $C_d$ in the friction terms $\tau_{bx}$ and $\tau_{by}$ as $C_d + k_f$.

### 3.2.4 Limitations of the shallow water equations

Numerical models based on solution of the SWEs have the following limitations [13] [35] [109] [110]:

- They do not allow for the development of a shear profile due to bottom friction.

- The use of a depth-averaged velocity cannot account for changes in turbine output and wake mixing behind the turbine associated with the rotor position within the water column.
- They only account for lateral turbine bypass flow, i.e. not that above and below the turbine rotor.
- Depth-averaged velocities unable to account properly for turbulence behind turbines and energy dissipated from the flow.
- They are unable to capture secondary flows originating from complex island geometries (e.g. conical islands) which can impact the flow speeds and directions experienced by turbines. This limitation is explained in further detail in Section 4.8.

The above limitations can be overcome by solving the unsteady Navier Stokes equations in a three-dimensional system. However, discretising the water column in multiple layers comes at a high computational cost. In the present study, the characterisation of the limits to power extraction in the strait between an island and landmass is performed with a SWE numerical model, as this presents a reasonable compromise between the accuracy of the solution and the use of computational resources.

## 3.3. Numerical code Fluidity

Fluidity [98] is an open-source computational fluid dynamics (CFD) code developed at Imperial College London able to solve the Navier Stokes equations and SWEs on fully unstructured meshes, that has been extensively used in ocean modelling [111] [112]. Moreover, Martin-Short *et al*. [75] have used the SWE version of Fluidity to model tidal power extraction and assess the effects on flow regime and sediment transportation in the Inner Sound.

Fluidity was selected for use in this project for several key reasons:

- It is open source and in continuous development.
- Multi-scale code capable of modelling from basin to turbine scale.
- Use of advanced finite-element methods (Section 3.3.1).
- Can run on unstructured and structured meshes (Section 3.3.2).
- It is largely scalable (Section 3.3.2).

This section details the main numerical formulation and configuration of Fluidity, for further information the reader is referred to [98], [111], [112], and [113].

### 3.3.1 Numerical schemes: the finite element method

No known analytical solution exists for the SWE in the form of Equations (3.47)-(3.49) and so a numerical scheme is used to approximate the solution. There are three schemes widely used in numerical, coastal models:

- Finite element method (FEM), used in Fluidity [98], TELEMAC [114] and Adcirc [115].
- Finite difference method (FDM) used in Delft3D [116], ROMS [117] and MIKE21 [118].
- Finite volume method (FVM) used in FVCOM [119] and MIKE3 [120]. Note that Fluidity and TELEMAC can also be configured to use this numerical scheme.

Comprehensive overviews of the three methods and their differences are given by Petrila and Trif [121] and Kundu and Cohen [122].

The FEM aims to convert a continuous problem to a discrete problem, which then can be solved numerically. There are two stages in the discretisation of a system of equations using FEM:

- A mesh is created by splitting the domain into a finite number of sub-spaces.
- Finite-dimensional functions are then used to construct the solution at each sub-space.

The mesh and functions create a discrete space in which the continuous solution is projected.

The FEM process is outlined below for a one-dimensional problem [123]. Given the function $y(x)$ in a domain $x \in [x_1 \cdots x_n]$ defined by the following differential equation:

$$\frac{\partial^2 y(x)}{\partial x^2} = c(x) \tag{3.50}$$

With the following boundary conditions $y(x_1) = a$ and $y(x_n) = b$. Equation (3.50) is in so-called strong form as $y(x)$ needs to be twice continuously differentiable. Equation (3.50) is multiplied by a trial function $\varphi(x)$ that satisfies $\varphi(x_1) = \varphi(x_n) = 0$ and integrated over the domain:

$$\int_{x_1}^{x_n} \varphi(x) \frac{\partial^2 y(x)}{\partial x^2} dx = \int_{x_1}^{x_n} \varphi(x) c(x)\, dx \tag{3.51}$$

Which after integration by parts of the left-hand side of the equation results in:

$$\int_{x_1}^{x_n} \frac{\partial \varphi(x)}{\partial x} \frac{\partial y(x)}{\partial x} dx + \int_{x_1}^{x_n} \varphi(x) c(x)\, dx = 0 \tag{3.52}$$

The function $y(x)$ is now continuously differentiable, and so Equation (3.52) is in its in weak form. However, now $\varphi(x)$ must be differentiable.

If the domain based on $x_n$ nodes or degrees of freedom is discretised in $n$ subdomains called elements, the solution of $y(x)$ can be approximated at each subdomain by $\hat{y}$, such as:

$$y(x) = \sum_{i=1}^{n} \psi_i(x)\hat{y_i} \tag{3.53}$$

where $\psi_i$ is the shape function used to interpolate the points within each segment of the domain, typically piecewise polynomials (e.g. constant, linear, quadratic). The value of $\psi_i$ is different on every segment ending in node $i$, and is zero outside these segments. Moreover, the shape function is defined such as $\sum_{i=1}^{n} \psi_i = 1$. Figure 3.3 plots the one-dimension linear and quadratic shape functions on a regular mesh defined such that it is equal to 1 at node $i$ and equal to 0 on the other nodes, this is known as a Lagrange polynomial. In two dimensions, using linear interpolation and triangle elements, the shape function $\psi_i(x, y)$ is written as $ax + by + c$, where $a$, $b$, and $c$ are defined so that $\psi_i$=1 and 0 elsewhere.

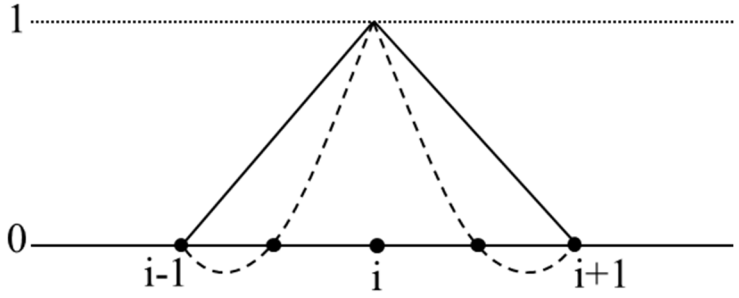


Figure 3.3. Lagrange linear (solid line) and quadratic (dashed line) shape function in one dimension.

Convergence of the solution in FEM is performed by hp-refinement [124]. In h-refinement, convergence is achieved through a reduction in the mesh-element size while the $\psi_i$ polynomial order is kept constant within each element. In p-refinement, the $\psi_i$ polynomial order is increased while mesh element size is kept constant.

Substituting Equation (3.53) into Equation (3.52) results in:

$$\int_{x_1}^{x_n} \frac{\partial\varphi(x)}{\partial x}\frac{\partial\psi(x)}{\partial x}\hat{y}\,dx + \int_{x_1}^{x_n} \varphi(x)c(x)\,dx = 0 \tag{3.54}$$

If the trial function $\varphi(x)$ is defined as:

$$\varphi(x) = \psi(x)\hat{\varphi} \tag{3.55}$$

Where $\hat{\varphi} = [\hat{\varphi}_1 \cdots \hat{\varphi}_n]^T$ are arbitrary values given at the discrete points. Equation (3.54) becomes:

$$\int_{x_1}^{x_n} \frac{\partial(\psi(x)\hat{\varphi})}{\partial x}\frac{\partial\psi(x)}{\partial x}\hat{y}\,dx + \int_{x_1}^{x_n} \psi(x)\hat{\varphi}c(x)\,dx = 0 \tag{3.56}$$

Rewriting Equation (3.56):

$$\hat{\varphi}^T \left( \left( \int_{x_1}^{x_n} \frac{\partial \psi^T(x)}{\partial x} \frac{\partial \psi(x)}{\partial x} dx \right) \hat{y} + \int_{x_1}^{x_n} \psi^T(x) c(x)\, dx \right) = 0 \tag{3.57}$$

Equation (3.57) must hold for all arbitrary values of $\hat{\varphi}$, accordingly:

$$\left( \int_{x_1}^{x_n} \frac{\partial \psi^T(x)}{\partial x} \frac{\partial \psi(x)}{\partial x} dx \right) \hat{y} + \int_{x_1}^{x_n} \psi^T(x) c(x)\, dx = 0 \tag{3.58}$$

Which is a linear system of the form $k\hat{y} = f$, where $k$ and $f$ are respectively:

$$\begin{aligned} k &= \int_{x_1}^{x_n} \frac{\partial \psi^T(x)}{\partial x} \frac{\partial \psi(x)}{\partial x} dx \\ f &= -\int_{x_1}^{x_n} \psi^T(x) c(x)\, dx \end{aligned} \tag{3.59}$$

The linear system can be resolved by adding the known values at the boundary conditions $\hat{y}_1 = a$ and $\hat{y}_n = b$.

Equation (3.58) in continuous space is discretised for each element $e$ between consecutive nodes $x_i$ and $x_j$:

$$\sum_e \left( \int_{x_i}^{x_j} \frac{\partial (\psi^e)^T}{\partial x} \frac{\partial \psi^e(x)}{\partial x} \hat{y}^e\, dx + \int_{x_i}^{x_j} (\psi^e)^T c\, dx \right) = 0 \tag{3.60}$$

If local shape functions and their derivatives are substituted into Equation (3.60), and the sum over all elements is assembled in a global matrix, this results in:

$$k\hat{y} = \sum_e k^e \hat{y}^e = \sum_e f^e = f \tag{3.61}$$

The above has included a simple example of the application of the FEM, a detailed development of FEM applied to the SWE can be found in Hervouet [86] for TELEMAC [114] and in [98] for Fluidity.

In FEM, a Galerkin method is one where the same trial and shape functions are used. If these functions are restricted to polynomials of degree $n \leq N$, these are known as $P_N$ discretisations. In the Continuous Galerkin (CG) discretisation, the polynomials are continuous between elements and boundary nodes are shared between element neighbours (Figure 3.4*a*). When element boundary nodes are not shared between element neighbours this is known as Discontinuous Galerkin (DG) (Figure 3.4*b*).

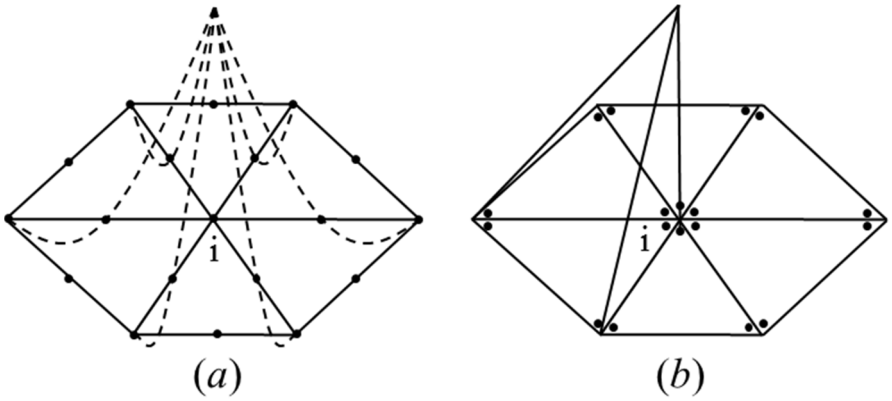


Figure 3.4. Two dimensional (*a*) piecewise quadratic CG and (*b*) piecewise linear DG polynomials. Triangular elements contain six and three nodes in CG and DG discretisations respectively.

In Fluidity [98], the continuous and discontinuous Galerkin methods are available for velocity and the continuous Galerkin for pressure to discretise the momentum equation. Arbitrary degree polynomials $P_N$ can be used for both variables. Several combinations of velocity and pressure element pairs are available. For large scale ocean applications Cotter *et al*. [125] found that the $P_{1\mathrm{DG}}P_2$ ($P_1$ discontinuous Galerkin for velocity and $P_2$ continuous Galerkin for pressure, Figure 3.5) provides excellent geostrophic balance properties [126] when applied to linear SWE and convergence is quadratic with element edge length.

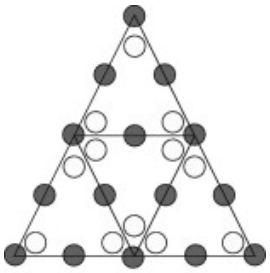

Figure 3.5. Distribution of velocity (white) and pressure (black) nodes in the element pair $P_{1DG}P_2$ in two dimensions. Each element contains three velocity nodes and six nodes for the pressure shared across element boundaries [125].

### 3.3.2 Spatial discretisation

The meshes used in Chapters 4, 5 and 6 are generated with Gmsh [127], a tool capable of generating two and three-dimensional regular and unstructured meshes (Figure 3.6). The inherent flexibility of triangular mesh elements is useful to represent irregular boundaries (e.g. coastal lines). Moreover, the use of unstructured elements allows local increase of mesh resolution minimising the number of elements in the domain and increasing

computational expediency. However, links between unstructured elements require explicit storage, thus increasing computer memory requirements and cost of accessing the data. In regular mesh elements, the area of each element is well defined and suitable for application of uniform terms such as stresses (i.e. power extraction). Furthermore, this reduces the computer requirements as elements' connectivity is implicitly known.

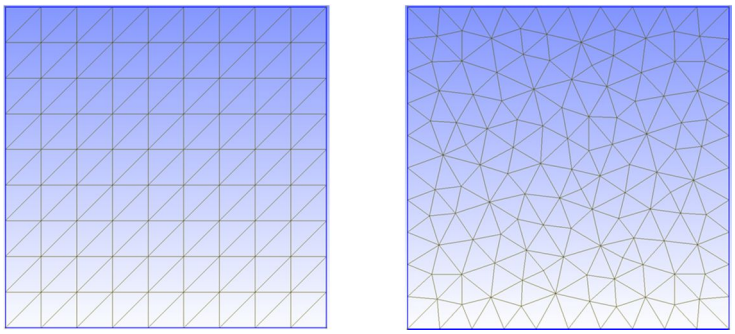

Figure 3.6. Regular biased right isosceles triangles (left) and unstructured triangles (right) mesh types generated with Gmsh [127].

Examples of numerical codes employing unstructured mesh models are TELEMAC [114] and MIKE21 [118]. Delft3D-Flow [116] is a three-dimensional numerical model that is restricted to structured mesh as it uses the finite difference method scheme. In Fluidity [98], both structured and unstructured mesh types are supported.

Moreover, the choice of pair-element is linked to the mesh employed. Two meshes are required when using the $P_{1DG}P_2$ discretisation: a $P_{1DG}$ mesh and a $P_2$ mesh. These two meshes are derived from the Gmsh input mesh, for more details on the mesh derivation process the reader is referred to the Fluidity manual [98].

To increase computational speed, Fluidity is capable of running in parallel using multiple processors. Mesh decomposition involves the division of the mesh in multiple blocks with relatively similar number of elements (Figure 3.7), and each single block is assigned to a processor. There are two types of nodes in each block:

- Owned, where the values of fields on the nodes depend on the solution within the block.
- Non-owned, here the value of fields on the nodes depend on the solution in an adjacent block.

The overlapping regions between mesh blocks contain both the non-owned nodes and nodes visible to adjacent processes.

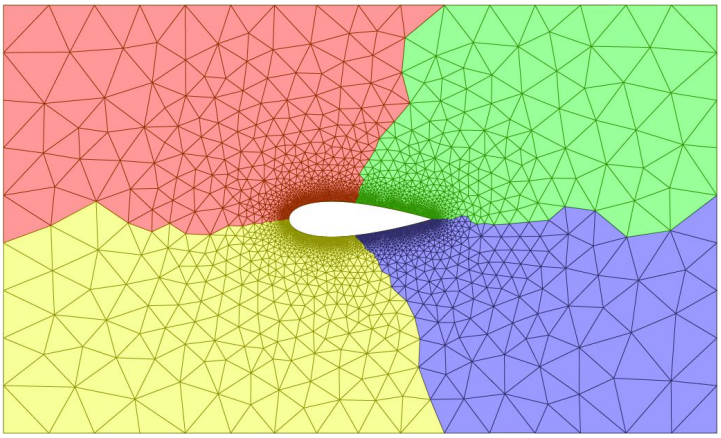

Figure 3.7. Partition of an unstructured mesh around a NACA0025 aerofoil into four blocks (coloured) [98].

### 3.3.3 Temporal discretisation

Fluidity solves the system of non-linear equations with an algorithm based on the non-linear Picard iteration scheme. In this scheme, the best available solution of the variables is used to solve each equation. The process is repeated for a set number of times or until solution convergence is reached [98] [111].

The momentum equation is temporally discretised implicitly using the backward Euler scheme [128].

$$u^{n+1} = u^n + f(t^{n+1}, u^{n+1})\Delta t \tag{3.62}$$

where $n$ and $n + 1$ are the current and next steps respectively, $\Delta t$ is the time step and $f(t^{n+1}, u^{n+1})$ is the function value at step $n + 1$.

The advantage of implicit schemes is that they are unconditionally stable and can handle large time steps albeit at greater computational cost. However, the choice of time step should consider the timescale of the physical process of interest [98]. This increase in numerical stability implies that, contrary to explicit schemes, stability of the numerical solution is insured for higher Courant-Friedrichs-Lewy (*CFL*) numbers [129]. The *CFL* number is defined as the time required $\Delta t$ by a particle to travel across a mesh element of edge length $\Delta x$.

$$CFL = u\frac{\Delta t}{\Delta x} \tag{3.63}$$

Moreover, for dependent variables the solutions at steps $n$ and $n + 1$ might be used. In Fluidity [98], the choice between the two solutions is made using the non-linear relaxation parameter $\theta_{nl} \in [0,1]$ implemented for the depth-averaged stream-wise velocity as:

$$u^{n+\theta_{nl}} = \theta_{nl} u^{n+1} + (1 - \theta_{nl}) u^{n} \tag{3.64}$$

A value of $\theta_{nl} = 1$ is used throughout this thesis.

### 3.3.4 Linear solvers

The discretisation of the solution made in Section 3.3.1 allows setting the problem as a system of linear equations of the form:

$$Aa = b \tag{3.65}$$

where $A$ and $b$ are known and $a$ contains the unknown variables.

In FEM, the derived matrices are sparse because only include base coefficient connecting neighbours, which leads to low use of memory, hence use of iterative methods can be used to solve the system of linear equations. Iterative methods approximate the solution of $a_k$ to the exact solution $a$ by computing at each iteration the residual $r_k$ of the solution as:

$$r_k = b - Aa_k \tag{3.66}$$

The iterative process continues until the residual value falls below a user specified tolerance or the maximum number of iterations is reached.

Several solvers and pre-conditioners are available in Fluidity through the PETSc library [130]. Following Fluidity guidelines [98], this thesis employs a Generalised Minimal Residual Method (GMRES) solver with a Successive Over-Relaxation (SOR) pre-conditioner for the velocity and pressure fields. The tolerance in the error solution and maximum number of iterations are specified to $10^{-7}$ and 1,000 respectively for both fields.

### 3.3.5 Boundary conditions

The boundary conditions represent the known solution of the linear system shown in Eq. (3.65). Throughout this thesis, two main types of boundary conditions are implemented in the SWE domains: solid and open.

Three solid boundary conditions are utilised in this thesis: free-slip condition, also referred as no-normal flow or reflective boundary condition, imposes a zero normal velocity to the boundary as shown in Eq. (3.67) and the tangential velocity is equal to the velocity at the wall; the frictional wall condition also imposes a zero normal velocity and adds an additional frictional force to the momentum equations that is treated numerically and computed as the bottom friction [131]; and a no-slip condition, which imposes a zero normal velocity and a zero tangential velocity at the wall ($u = v = 0$):

$$\vec{u} \cdot \vec{n} = 0 \tag{3.67}$$

where $\vec{n}$ is the outward facing normal vector to the boundary.

Open boundaries can be inlet/outlet velocity or free surface elevation. Inlet/outlet velocity boundaries allow the definition at the inlet sections of a prescribed inlet/outlet flow velocity. Time series of free surface elevations or velocities are commonly used in basin-scale coastal hydrodynamics models and are known as clamped boundaries. Free surface elevation time series are obtained from larger numerical models or observations. For applications in actual coastal sites, databases of harmonic constituents derived from observations are available. The European Shelf Solution from Oregon State University [132] and Finite Element Solution – Global Tide (FES 2012) from Legos [133] are two databases covering the U.K. waters.

The use of clamped boundaries present the main disadvantage that the prescribed time series are based on observations and thus, cannot incorporate reflections (i.e. outgoing waves) originated within the domain by for example tidal power extraction [134]. This problem is believed to have been first detected by Garrett and Greenberg [135] in their study of the Bay of Fundy. Offshore deep water conditions at open boundaries have been used to represent continental shelf domains by Adcock *et al*. [136] for tidal stream power extraction and by Zhou *et al*. [137] for a tidal barrage on the Severn Estuary. The increase of water depth attenuates reflections generated from power extraction to reach the open boundaries, as they are reflected back onto the shelf.

Moreover, when no free surface elevation or velocity value is imposed at the open boundaries, they are defined with a free-stress condition [98], also referred to as "do-nothing boundary condition", in which the derivative of the velocity is set to zero.

The presence of tidal flats in the domain, which are areas that can be submerged or uncovered depending on the tide level, represent a special case of boundary condition. The

solution used in this thesis is to limit the value of water depth to a threshold [98], which is set based on the maximum tidal amplitude observed in the numerical domain. More accurate wetting and drying mechanisms in SWE which are not currently available in Fluidity are discussed by Medeiros and Hagen [138].

## 3.4. Summary

This chapter has described the derivation of the SWEs from the three-dimensional continuity and Navier Stokes equations, noting external forces added to the SWEs which are relevant to tidal site modelling when carrying out a resource assessment. Tidal resource assessment based on the solution of the SWE and three-dimensional Navier-Stokes equations has been discussed. Higher accuracy is achieved with three-dimensional models although at the expense of high computational requirements. SWE models are found to provide a reasonable compromise between accuracy of solution and use of computational resources. The chapter also discussed power extraction methodologies available in SWE models. Here, the distributed drag approach is chosen instead of the more computationally demanding individual turbine representation because the aim of this study is to understand the limits of power extraction in a strait between an island and landmass and how these are affected by local site parameters and not by turbine interactions. The second part of the chapter has outlined the Finite Element Method numerical scheme employed in Fluidity. The numerical configuration of the numerical model Fluidity used in this thesis was explained, including the characteristics of the $P_{1DG}P_2$ element pair, spatial and temporal discretisation employed, linear solvers utilised, and boundary conditions considered.

# 4. Verification and validation of resource assessment methodology

## 4.1. Introduction

Use of a numerical model to simulate a physical domain requires *a priori* verification and validation tests to be undertaken to guarantee the model is mathematically correct and the results are physically relevant. This process ensures that the correctness of the solutions is not disrupted by the numerical error inherent in solving the governing equations or simplifications made when idealising the actual physics. Verification involves comparison between the numerical predictions and analytical solutions of the (usually simplified) mathematical equations on which the model is based. Validation of the numerical model assesses the capability of the model to reproduce correctly the key physics, and is carried out using data obtained from laboratory experiments that resemble the actual conditions. Successful completion of the verification and validation of the numerical model is a necessary prerequisite to application to other domains.

This chapter presents a series of verification and validation tests of the resource assessment methodology employed in Chapter 5 to assess the power that can be extracted from an island-landmass coastal site. Unless otherwise stated, the tests are implemented using the Fluidity shallow water equations solver. This chapter is divided as follows. Section 4.2 presents the verification of Fluidity for steady subcritical open channel flow over a hump. Sections 4.3 and 4.4 verify the mathematics of Fluidity to model the coastal domain of an island and a coastline. Section 4.3 verifies the solution from Fluidity for inviscid flow past a cylinder against potential flow theory [87]. Section 4.4 expands the analysis to include a wall using the method of images. Sections 4.5, 4.6 and 4.7 validate the physics of Fluidity to model the flow past a submerged circular cylinder through comparison against experimental and numerical data. Section 4.5 validates the Fluidity solution for a impulsively started flow past a cylinder at a Reynolds number $Re = 40$ against experimental results from Coutanceau and Bouard [139]. Section 4.6 validates the numerical results obtained from Fluidity for impulsively started unidirectional flow past a cylinder at $Re = 100$ against semi-analytical results obtained by Collins and Dennis [140]. Section 4.7 visually compares the streamlines behind the cylinder at $Re = 5{,}000$ against those experimentally observed by Bouard and Coutanceau [141]. Section 4.8 validates Fluidity for shallow laminar oscillatory flow past a

surface piercing circular cylinder by comparing predictions against experimental measurements by Lloyd *et al.* [69]. Section 4.9 verifies the power extraction methodology implemented in Fluidity against the one-dimensional channel analytical models by Bryden and Couch [15] and Garrett and Cummins [11]. Finally, Section 4.10 expands the verification of the power extraction methodology to two-dimensional domains through comparison against analytical and numerical solutions from Garrett and Cummins [142].

## 4.2. Flow over a hump

Non-uniform bed topography alters the flow velocity and free surface elevation profiles. This test assesses the capability of Fluidity to account for a non-uniform bed. The solution from Fluidity is verified against Bernoulli's equation for a hump along a channel.

In one-dimensional open channel flow, the Froude number is defined as:

$$Fr = \frac{u}{\sqrt{gh}} \tag{4.1}$$

where $u$ is the stream-wise depth-averaged velocity component in m/s, $g$ is the acceleration due to gravity in m/s$^2$ and $h$ is the water depth in m. The Froude number demarks whether the flow regime is subcritical $Fr < 1$, critical, $Fr = 1$, or supercritical $Fr > 1$.

For steady flow over a frictionless hump (Figure 4.1), the changes in free surface elevation and mean flow velocity that occur between an upstream station and one at the crest of the hump can be represented using continuity and Bernoulli's energy equations [143]:

$$u_1 h_1 = u_2 h_2 \tag{4.2}$$

$$\frac{u_1^2}{2g} + h_1 = \frac{u_2^2}{2g} + h_2 + \Delta z \tag{4.3}$$

Replacing $u_2$ in the energy equation leads to a third order polynomial equation with $h_2$ as the unknown, which can be solved using the Newton Raphson method.

$$h_2^3 - \left(\frac{u_1^2}{2g} + h_1 - \Delta z\right) h_2^2 + \frac{u_1^2 h_1^2}{2g} = 0 \tag{4.4}$$

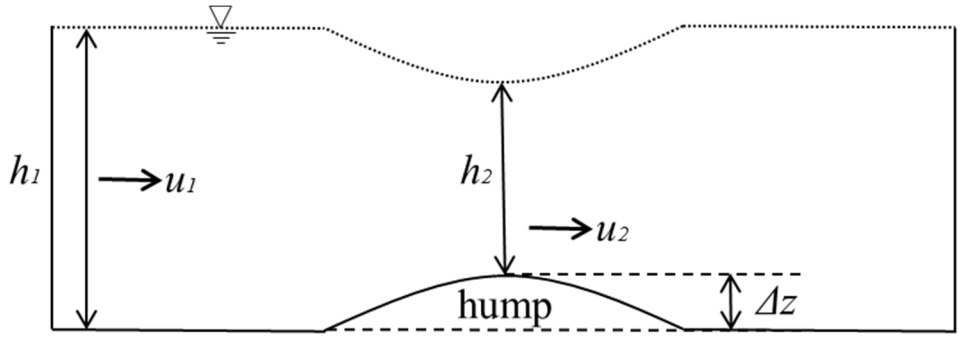


Figure 4.1. Definition sketch of subcritical flow over a hump.

The numerical model consists of a rectangular channel domain with the following geometrical characteristics: Length $L$ = 10,000 m, width $B$ = 1,000 m, downstream water depth $h$ = 40 m. The hump along the channel of height $\Delta z = z_{max}$ = 1m (Figure 4.2) is defined by the following Gaussian distribution:

$$z = z_{max} \exp\left[-\left(\frac{x-\frac{L}{2}}{B}\right)^2\right] \tag{4.5}$$

where $z$ is the bed elevation vertically above a fixed horizontal datum and $x$ is the horizontal coordinate in the stream-wise direction.

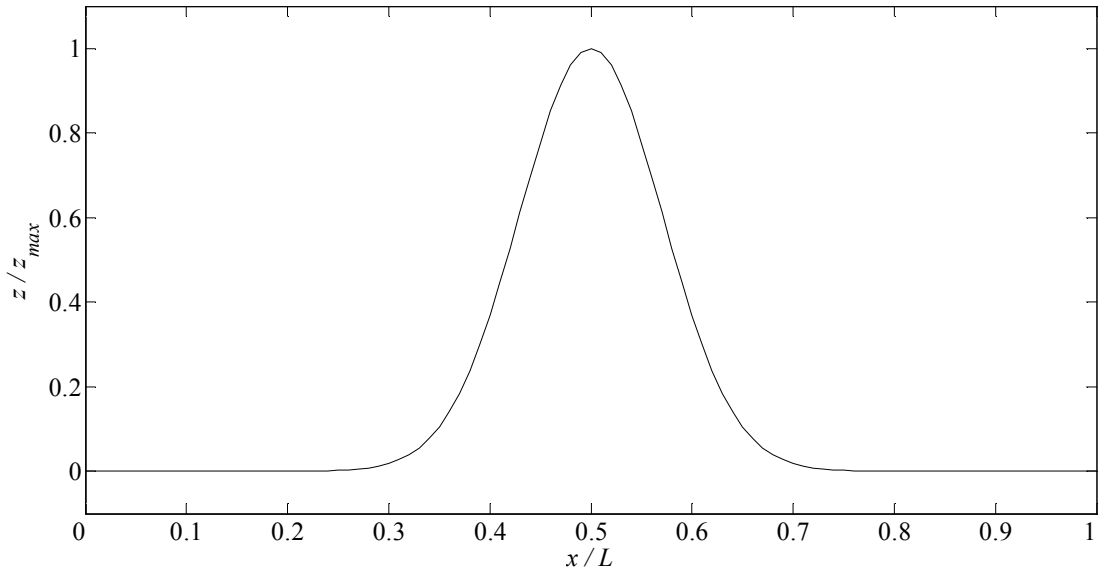


Figure 4.2. Channel bed profile with a Gaussian hump.

The numerical model presents four boundaries in plan. An inlet velocity condition of $u_1 = U_\infty = 3$ m/s in the $x$ direction is prescribed at the west upstream inflow boundary. A zero pressure condition and depth $h_2 = 40$ m is set at the eastern outflow boundary. The north and south boundaries are lateral walls represented using a free-slip condition. The bed and side walls of the channel are frictionless (non-dimensional friction coefficient $C_d = 0$). The kinematic viscosity $v$ is set to zero. The initial velocity mesh field is set to a uniform value $u(x, y) = u_1$ over the entire domain.

An unstructured mesh based on triangular elements is used to discretise spatially the domain. A convergence analysis of the numerical solution of flow over a hump is carried out using five meshes. Table 4.1 lists the set element edge length size and resulting number of mesh elements for the five mesh cases.

| Mesh | Element edge length size (m) | Mesh elements |
|---|---|---|
| 1 | 1,600 | 50 |
| 2 | 800 | 82 |
| 3 | 400 | 230 |
| 4 | 200 | 716 |
| 5 | 100 | 2,852 |

Table 4.1. Element edge length size and number of mesh elements for the five mesh cases analysed.

Figure 4.3 shows the unstructured mesh for Mesh 5 from Table 4.1 with a 100 m element edge length.

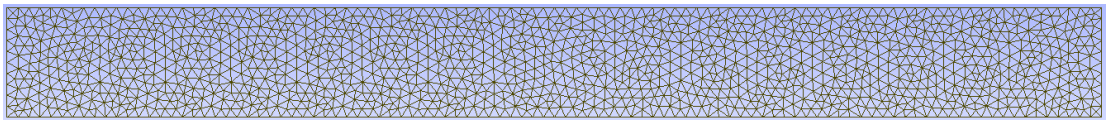

Figure 4.3. Unstructured mesh case 5 with element edge length of 100 m.

Flow conditions are switched on instantaneously. The model is run for a period of time of $90L/u_1 = 300{,}000$ s by which time the velocity values have converged to within $10^{-5}$ m/s.

For the mesh cases analysed, Table 4.2 shows the absolute error in the computation of the free surface elevation and velocity against the values predicted by Bernoulli's equation, computed as:

$$Error = \frac{\sqrt{\sum_{i=1}^{N}\left(\varphi_i^{computed} - \varphi_i^{exact}\right)^2}}{N} \tag{4.6}$$

where $\varphi$ is the variable which error is being analysed and $N$ is the number of dataset points.

| Mesh | Error free surface x $10^{-6}$ (m) | Error velocity x $10^{-6}$ (m/s) |
|---|---|---|
| 1 | 193.3 | 766.9 |
| 2 | 79.4 | 180.4 |
| 3 | 19.5 | 60.2 |
| 4 | 7.1 | 13.9 |
| 5 | 6.1 | 4.5 |

Table 4.2. Absolute error in the numerical free surface and velocity predictions by comparison with the analytical solution from Bernoulli's equation for the five mesh cases considered.

The absolute error of both variables decreases as the number of mesh elements increases. Figure 4.4 and Figure 4.5 compare the analytical and Fluidity-computed free surface $\delta$ and stream-wise depth-averaged velocity $u$ profiles. Solutions are shown in terms of the $x$ coordinate and centred at $y = B/2$.

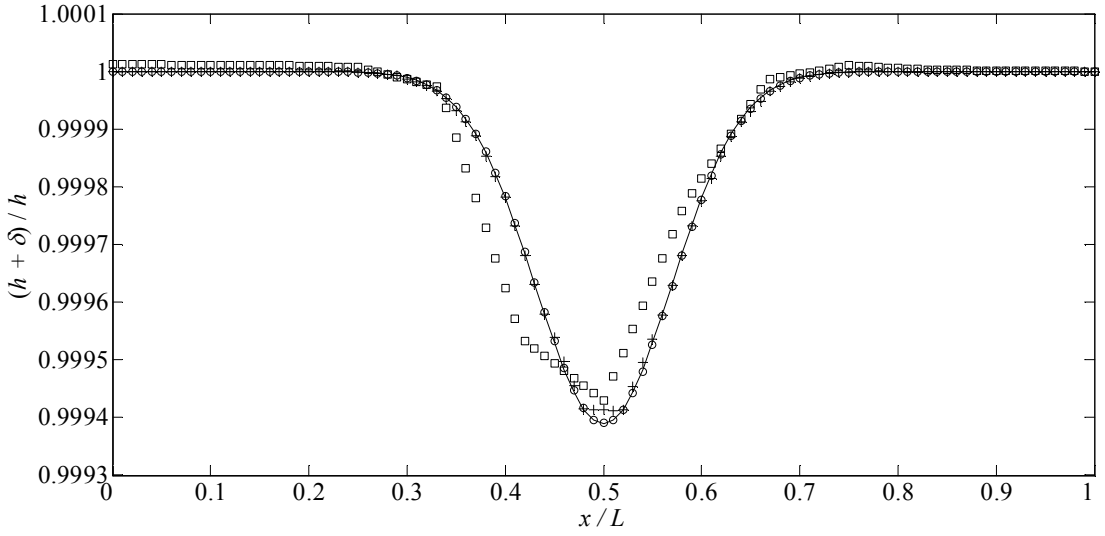


Figure 4.4. Free surface profile for steady flow over a hump: Mesh 1 (square); Mesh 3 (plus sign); Mesh 5 (circle); and analytical solution from Bernoulli's equation (solid line).

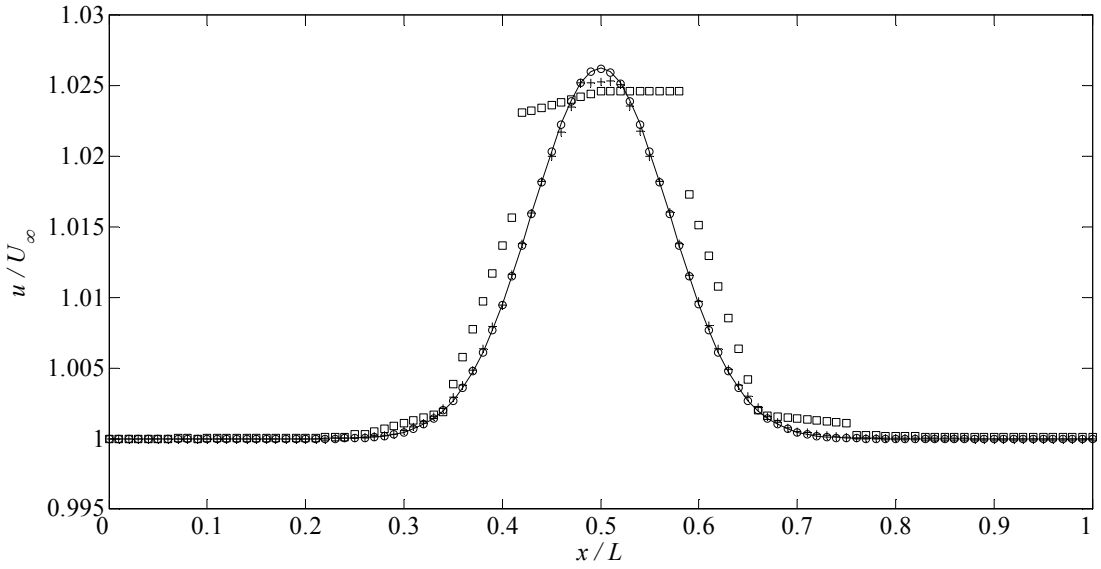


Figure 4.5. Mean flow depth-average stream-wise velocity profile for steady flow over a hump: Mesh 1 (square); Mesh 3 (plus sign); Mesh 5 (circle); and analytical solution from Bernoulli's equation (solid line).

## 4.3. Inviscid flow past a circular cylinder

The flow dynamics around the island are of particular importance for the correct assessment of the resource between the island and the semi-infinite landmass. If the island is considered circular, it can be modelled as a circular cylinder in the shallow water equations. This section verifies the solution obtained using Fluidity against the potential flow solution [87] for flow past a circular cylinder.

Potential flow theory [87] predicts the following velocity stream function $\psi$ for flow past a cylinder centred at the origin in Cartesian coordinates without circulation (Figure 4.6) [143]:

$$\psi = U_\infty y - \frac{U_\infty R_c^2 y}{x^2 + y^2} \tag{4.7}$$

where $U_\infty$ is the free stream velocity and $R_c$ is the radius of the circular cylinder.

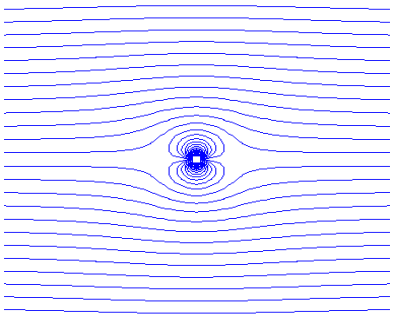

Figure 4.6. Streamlines of flow past a circular cylinder centred at the origin and without circulation.

Likewise, the velocity potential function $\phi$ for flow past a circular cylinder is:

$$\phi = U_\infty x - \frac{U_\infty R_c^2 x}{x^2 + y^2} \tag{4.8}$$

The solution for flow past a circular cylinder centred at the origin is obtained from the combination of a uniform stream in the $x$ direction and the superposition of a source plus an equal sink.

A uniform stream in the $x$ direction $u = U_\infty$ is defined in terms of the stream and velocity potential functions as:

$$u = U_\infty = \frac{\partial \phi}{\partial x} = \frac{\partial \psi}{\partial y} \qquad\qquad v = 0 = \frac{\partial \phi}{\partial y} = -\frac{\partial \psi}{\partial x}$$

Integrating the expression of the velocity in the $x$ direction, the stream function for a uniform stream results in:

$$\psi_{uniform} = U_\infty y \tag{4.9}$$

In the case of a superposition of a source plus and equal sink, a source $+m$ at $(x, y) = (-a_d, 0)$ is combined with a sink of equal strength an opposite sign $-m$, located at $(x, y) = (+a_d, 0)$. In this case, the resulting stream function is:

$$\psi_{doublet} = \psi_{source} + \psi_{sink} = m \tan^{-1} \frac{y}{y + a_d} - m \tan^{-1} \frac{y}{y - a_d} \tag{4.10}$$

The use of trigonometric and logarithmic identities simplifies the above expressions to obtain:

$$\psi_{doublet} = -m \tan^{-1} \frac{2 a_d y}{x^2 + y^2 - a_d^2} \tag{4.11}$$

For small values of $a_d$, this is referred to as a doublet. If the product $2a_dm$, which is the doublet strength, remains constant and is replaced by $\lambda$, the stream function and velocity potential of a doublet can be written in Cartesian coordinates as:

$$\psi_{doublet} = \lim_{n\to\infty}\left(-m\tan^{-1}\frac{2a_dy}{x^2+y^2-a_d^2}\right) = -\frac{2a_dmy}{x^2+y^2} = -\frac{\lambda y}{x^2+y^2} \tag{4.12}$$

Figure 4.7 plots the stream function of a doublet centred at the origin.

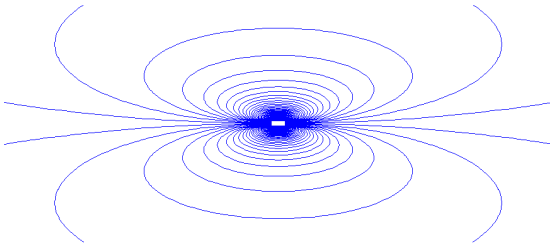

Figure 4.7. Streamlines for a doublet centred at the origin.

The doublet strength $\lambda$ has units of velocity times length squared and can be substituted by the product $U_\infty R_c^2$.

Finally, the stream-wise and transverse velocity components $u$ and $v$ for flow past a circular cylinder are derived from the stream function as:

$$u = \frac{\partial\psi}{\partial y} = U_\infty\left(1 - R_c^2\frac{x^2-y^2}{(x^2+y^2)^2}\right) \tag{4.13}$$

$$v = -\frac{\partial\psi}{\partial x} = \frac{2U_\infty R_c^2 xy}{(x^2+y^2)^2} \tag{4.14}$$

From the above expression, it is possible to determine the stream-wise velocity profile along the $y$ axis centred at $x = 0$ as:

$$u(0,y) = U_\infty\left(1 + \frac{R_c^2}{y^2}\right) \tag{4.15}$$

From the above expression, for a free stream velocity $U_\infty$, the values of the stream-wise velocity at the edges of the cylinder and in the free stream are $2U_\infty$ and $U_\infty$ respectively.

Figure 4.8 shows the domain geometry. A cylinder of diameter $\emptyset_c$ = 2,000 m is centred midway across the domain in the transverse direction. The domain length $L$ and depth $h$ are set to $25\emptyset_c$ and $0.02\emptyset_c$ respectively. The width of the domain $B$ is set such that the ratio of

cylinder diameter to domain width of 0.07. The cylinder is located $10Ø_c$ downstream of western inflow boundary. The selected model dimensions are within the shallow water assumption.

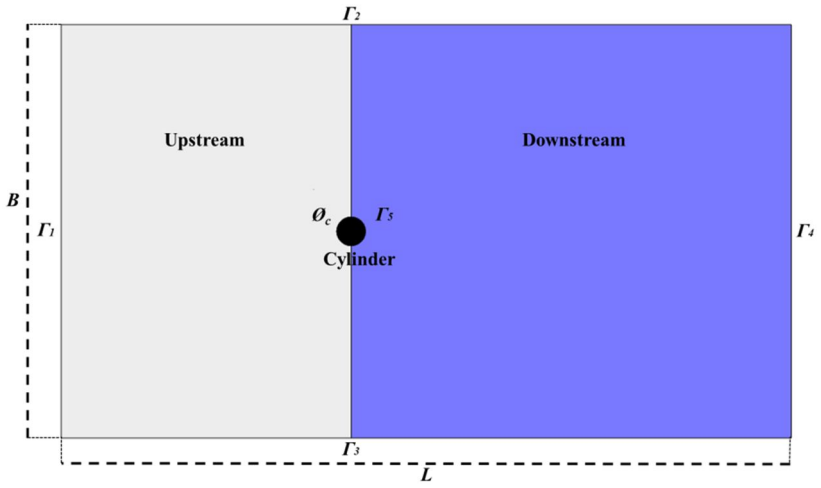


Figure 4.8. Rectangular model geometry of length $L$ and width $B$, containing a cylinder of diameter $Ø_c$, with five boundaries and two mesh regions.

Five boundaries are defined in the model: $\Gamma_1$ is the open inlet boundary at the west end of the domain; $\Gamma_4$ is the open outlet boundary at the east end of the domain; $\Gamma_2$ and $\Gamma_3$ are the north and south lateral wall boundaries; and $\Gamma_5$ is a solid boundary representing the cylinder. The free stream velocity value $U_\infty$ = 2 m/s in the positive $x$ direction is prescribed at $\Gamma_1$. The model is initialised with zero velocity throughout the mesh. The inlet velocity is then ramped up from zero to $U_\infty$ over a time period of $25Ø_c/U_\infty$ s to minimise numerical perturbations at this boundary that could contaminate the simulation. A zero pressure boundary condition is set at the eastern boundary $\Gamma_4$. A free-slip condition is applied to solid boundaries $\Gamma_2$, $\Gamma_3$ and $\Gamma_5$.

An unstructured triangular mesh with variable edge length is used to discretise the domain. Six different meshes are considered in the mesh convergence analysis. The longitudinal position of the cylinder specifies the upstream and downstream mesh regions (Figure 4.8). In addition, a specific element edge length is set at the boundary of the cylinder. Table 4.3 lists the element edge length used for each region in the six mesh cases analysed and the resulting total number of mesh elements. Figure 4.9 shows the mesh 2.

| | Element edge length | | | |
|---|---|---|---|---|
| Mesh | Upstream from cylinder | Downstream from cylinder | Cylinder | Mesh elements |
| 1 | $\emptyset_c$ | $3\emptyset_c/4$ | $\pi\,\emptyset_c/12$ | 1,786 |
| 2 | $\emptyset_c/2$ | $3\emptyset_c/8$ | $\pi\,\emptyset_c/28$ | 7,638 |
| 3 | $\emptyset_c/4$ | $3\emptyset_c/16$ | $\pi\,\emptyset_c/36$ | 31,864 |
| 4 | $\emptyset_c/4$ | $3\emptyset_c/16$ | $\pi\,\emptyset_c/76$ | 41,696 |
| 5 | $\emptyset_c/4$ | $3\emptyset_c/16$ | $\pi\,\emptyset_c/156$ | 52,702 |
| 6 | $\emptyset_c/4$ | $3\emptyset_c/16$ | $\pi\,\emptyset_c/316$ | 68,494 |

Table 4.3. Mesh convergence analysis: element edge lengths and total numbers of mesh elements.

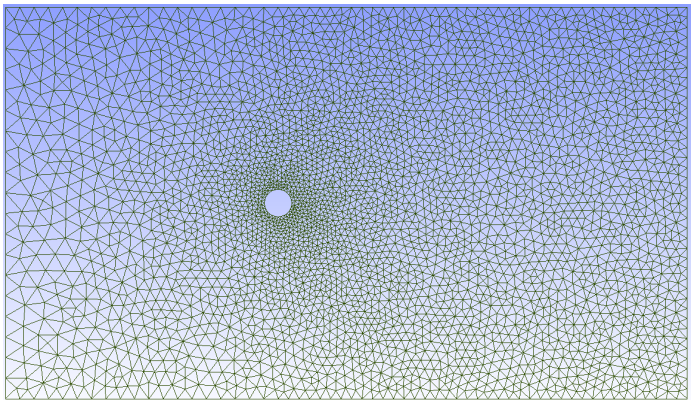

Figure 4.9. Unstructured triangular mesh 2 used to simulate inviscid flow past a cylinder.

The mesh cases listed in Table 4.3 are run in Fluidity in inviscid flow conditions with no drag applied at the domain bed. In each case, the time step is selected according to the *CFL* <1 stability criterion. The solution was considered to converge when variation in the velocity field was in the order of $10^{-3}$ m/s. Solution convergence was reached after a time period of four times the ramping up time period.

Figure 4.10 shows the streamlines for inviscid flow past a circular cylinder, predicted by Fluidity using Mesh 6 (Table 4.3).

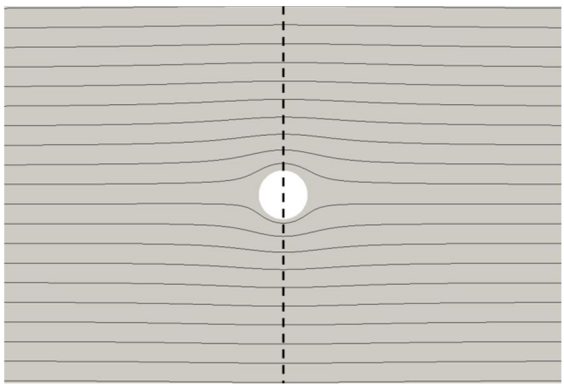

Figure 4.10. Streamlines computed with Fluidity using Mesh 6 for inviscid flow past a cylinder and analysed cross-section at cylinder's centre plane (dashed line).

Table 4.4 lists the absolute error (using Eq. (4.6)) in the predicted stream-wise velocities along the transverse axis at the stream-wise coordinate corresponding to the centre of the cylinder for different numbers of mesh elements. In general, an increase in mesh refinement decreases the difference between the numerical and analytical solutions. For Mesh 3 and above, the mesh is only refined further in the vicinity of the cylinder. This may explain why there is no decrease in the error of the numerical solution between Mesh 3 and Mesh 4. Mesh 5 and Mesh 6 show a significant reduction in the error of the numerical solution compared to the other meshes.

| Mesh | 1 | 2 | 3 | 4 | 5 | 6 |
|---|---|---|---|---|---|---|
| Error [m/s] | 0.0018 | 0.0013 | 0.0011 | 0.0014 | 0.0007 | 0.0006 |

Table 4.4. Absolute error in the computation of stream-wise velocities along the transversal axis at stream-wise coordinate correspondent to the centre of the cylinder in Fluidity against the predicted values by the potential flow theory for the six mesh cases analysed.

Figure 4.11 compares the predicted stream-wise velocity along the transverse axis at cylinder's centre plane (Figure 4.10) using Mesh 6 with the analytical solution. The cylinder is located between $y/Ø_c$ coordinates -0.5 and 0.5. Good agreement is observed between numerical and analytical solutions. The use of a non-structured spatial discretisation scheme may explain the minor asymmetry observed in the stream-wise velocity profile between the north and south sides of the cylinder among other reasons.

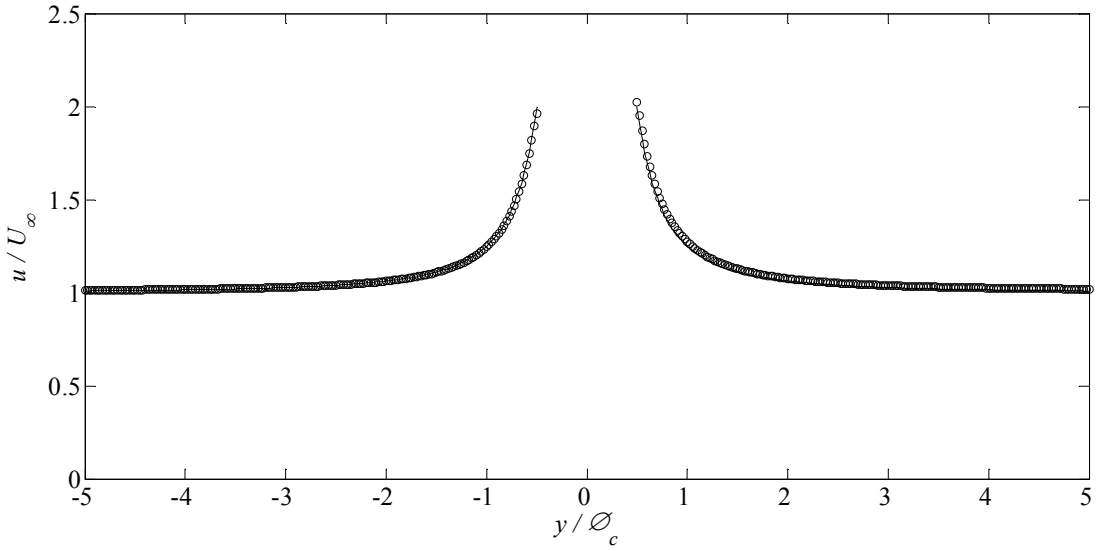


Figure 4.11. Transverse profile of stream-wise velocity at cylinder centre plane for flow past a circular cylinder: Fluidity using Mesh 6 (circle); and analytical solution (solid line).

## 4.4. Inviscid flow past a circular cylinder in the presence of a wall

This section verifies the numerical model for potential flow past a cylinder in the vicinity of a solid wall using the method of images. Here, the effect of a nearby wall on the flow past an object is modelled by inserting a symmetrical mirror image on the opposite side of the wall at an identical offset from the wall. Figure 4.12a shows a doublet representing the cylinder centred at a distance $b_d$ above the virtual wall and a doublet image of equal strength centred at a distance $b_d$ below the virtual wall. The mirror image flattens the streamlines as they approach the virtual wall and transverse velocity components are cancelled out resulting in a plane-surface streamline which resembles a free-slip wall. The resulting stream function from the combination of a uniform flow defined by a velocity component $U_\infty$ in the $x$ direction with two doublets of equal strength $U_\infty R_c^2$ centred at the Cartesian coordinates $(0,b_d)$ and $(0,-b_d)$ is given by (Figure 4.12b):

$$\psi = \psi_{uniformX} + \psi_{doublet} + \psi_{doublet_{image}}$$

$$\psi = U_\infty y - \frac{U_\infty R_c^2 (y - b_d)}{x^2 + (y - b_d)^2} - \frac{U_\infty R_c^2 (y + b_d)}{x^2 + (y + b_d)^2} \tag{4.16}$$

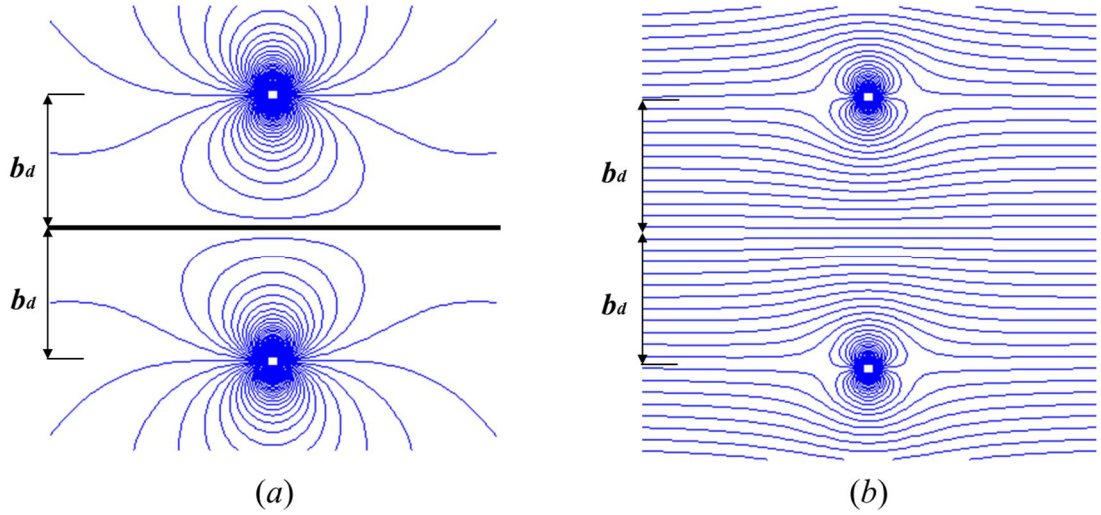


Figure 4.12. (a) Streamlines of two doublets centred at a distance $b_d$ above and below a virtual wall (solid black line). Streamlines are flattened as they get closer to $x$ axis as transverse velocity components are cancelled out. (b) Streamlines of a uniform flow in the $x$ direction combined with two doublets of equal strength positioned at a distance $b_d$ above and below the wall respectively.

From the above stream function, the stream-wise and transverse velocity profiles along the $y$ axis centred at $x = 0$ are as follows:

$$u(0,y) = U_\infty + U_\infty R_c^2 \left( \frac{y^2 + b_d^2 - 2b_d y}{(y - b_d)^4} + \frac{y^2 + b_d^2 + 2b_d y}{(y + b_d)^4} \right) \tag{4.17}$$

$$v(0,y) = 0 \tag{4.18}$$

Figure 4.13 shows the model domain, which has the same length and depth as that used in Section 4.3. The model width is doubled to keep the blockage ratio of the rectangular channel constant at 0.07. The cylinder and its image are centred at a distance $1.5Ø_c$ above and below the mid-transverse section of the rectangular domain and $10Ø_c$ downstream of west domain limit.

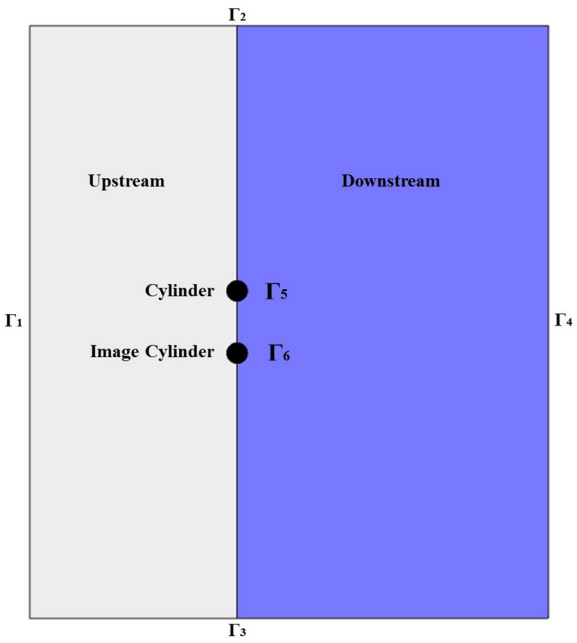


Figure 4.13. Model geometry used to simulate flow past a cylinder near a wall, using Fluidity.

The model has six boundaries. Compared to the model of Section 4.3, the new image cylinder adds a new solid boundary $\Gamma_6$, defined with a free-slip condition. Boundary conditions at inlet and outlet are the same as in Section 4.3. No viscosity or seabed friction is implemented.

A convergence analysis is performed using six unstructured triangular meshes, as listed in Table 4.5. Again there are three mesh regions (Figure 4.13): upstream of the cylinders; downstream of the cylinders; and in the vicinity of the cylinders. Figure 4.14 shows Mesh 1 to model inviscid flow past a cylinder and its image.

| | Element edge length | | | |
|---|---|---|---|---|
| Mesh | Upstream from cylinders | Downstream from cylinders | Cylinders | Mesh elements |
| 1 | $\emptyset_c$ | $3\emptyset_c/4$ | $\pi\,\emptyset_c/12$ | 3,184 |
| 2 | $\emptyset_c/2$ | $3\emptyset_c/8$ | $\pi\,\emptyset_c/28$ | 13,332 |
| 3 | $\emptyset_c/4$ | $3\emptyset_c/16$ | $\pi\,\emptyset_c/36$ | 35,980 |
| 4 | $\emptyset_c/4$ | $3\emptyset_c/16$ | $\pi\,\emptyset_c/76$ | 53,594 |
| 5 | $\emptyset_c/4$ | $3\emptyset_c/16$ | $\pi\,\emptyset_c/156$ | 73,214 |
| 6 | $\emptyset_c/4$ | $3\emptyset_c/16$ | $\pi\,\emptyset_c/316$ | 103,448 |

Table 4.5. Mesh convergence analysis for inviscid flow past a cylinder near a wall: element edge lengths and total numbers of mesh elements.

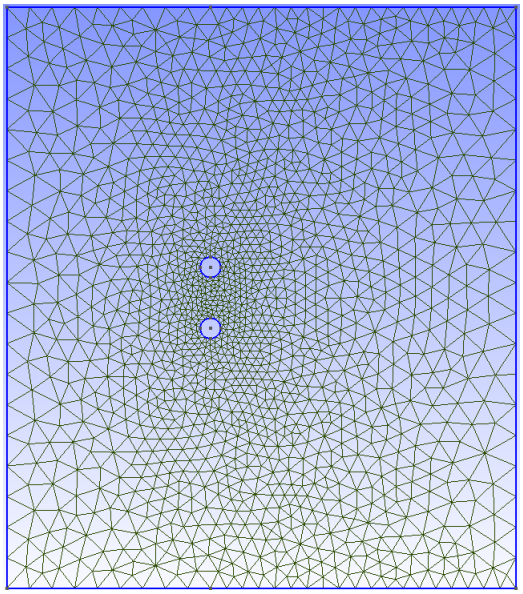

Figure 4.14. Unstructured triangular mesh 1 used to simulate inviscid flow past a cylinder near a wall.

Next we use symmetry to reduce the computational effort. Figure 4.15 shows the geometry of the model, which consists of the upper northern part of the model presented in Figure 4.13, where a physical solid boundary with a free-slip condition is set at the south limit of the rectangular domain to include the presence of a wall. A mesh-convergence analysis was performed using the same six meshes described in Table 4.5.

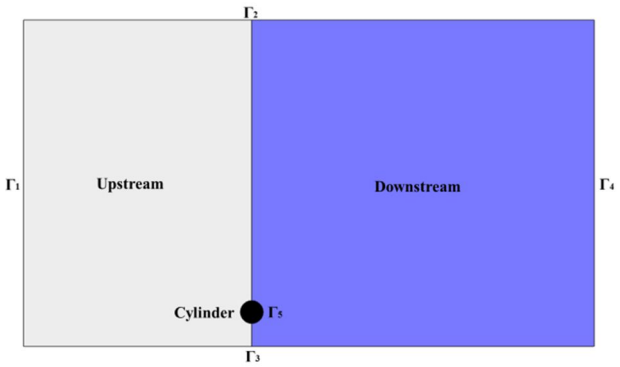


Figure 4.15. Rectangular model geometry with cylinder located near a solid wall, five boundaries and two mesh regions.

Numerical predictions using Fluidity are compared against those predicted by potential theory using the method of images. Figure 4.16 shows the predicted streamlines around the cylinder and its image, using Mesh 6. It can be seen that the streamline equidistant from the centres of the cylinders corresponds to a zero transverse velocity component, resembling the effect of a free-slip boundary.

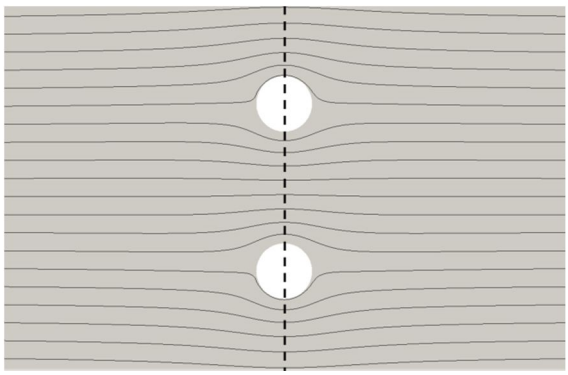

Figure 4.16. Streamlines for inviscid flow past a cylinder and its image computed with Fluidity using Mesh 6. Analysed cross-section at cylinder's centre plane (dashed line).

Table 4.6 lists the absolute root mean squared error (using Eq. (4.6)) in the numerical stream-wise velocity component profile along a transverse line crossing the domain through the centre of the cylinder and its image (Figure 4.16), computed on increasingly fine meshes. As in Section 4.3, the accuracy of the computed solution increases with mesh refinement, and appears converged for Mesh 3 and finer.

| Mesh | 1 | 2 | 3 | 4 | 5 | 6 |
|---|---|---|---|---|---|---|
| Error [m/s] | 0.0018 | 0.0013 | 0.0006 | 0.0005 | 0.0007 | 0.0005 |

Table 4.6. Absolute error in computation of stream-wise velocity component along a transverse line across the domain through the cylinder and image centres using Fluidity, the numerical predictions are compared against the benchmark analytical solution obtained using the method of images for the six mesh cases analysed.

Figure 4.17 plots the predicted and analytical transverse profiles of stream-wise velocity component along a line passing through the centre of the cylinder and its image using Mesh 6. There is good agreement between the two sets of results.

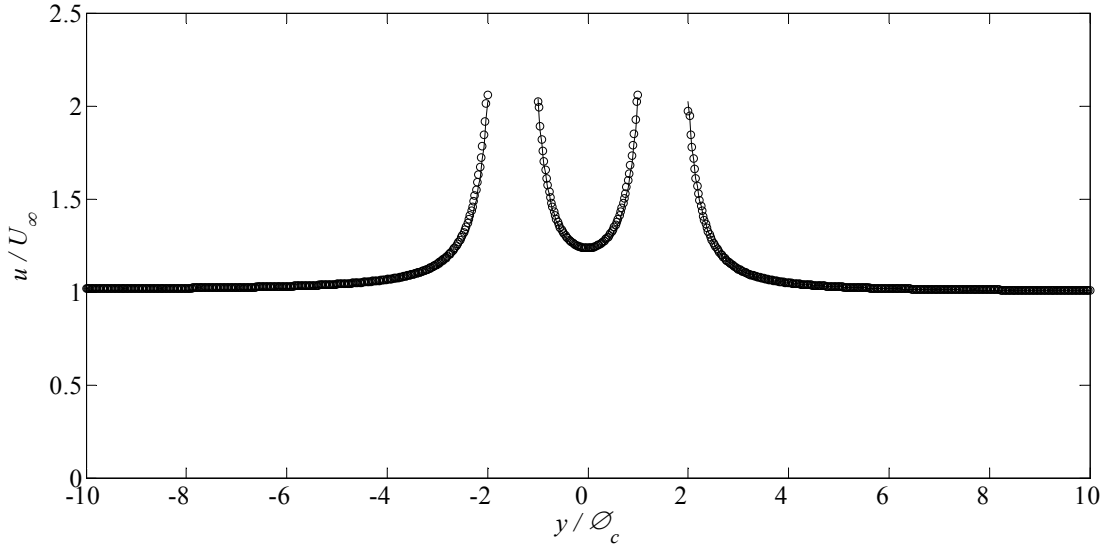


Figure 4.17. Inviscid flow past a cylinder and its image. Comparison between transverse profiles of stream-wise velocity components along a line through the centres of both the cylinder and its image: numerical results obtained using Fluidity on Mesh 6 (circle); and analytical solution using method of images (solid line).

Six spatial discretisation cases based on element edge length values from Table 4.5 are assessed using the numerical model of a cylinder near a solid wall (as illustrated in Figure 4.15). Table 4.7 depicts the absolute errors obtained for the six mesh cases regarding the predicted transverse profiles of stream-wise velocity components along the line passing through the centre of the cylinder and normal to the solid wall. It is clear that mesh refinement reduces the error in computation of the stream-wise velocities.

| Mesh | 1 | 2 | 3 | 4 | 5 | 6 |
|---|---|---|---|---|---|---|
| Error [m/s] | 0.0047 | 0.0024 | 0.0017 | 0.0017 | 0.0005 | 0.0007 |

Table 4.7. Absolute error in predicted transverse profiles of stream-wise velocity component for six meshes using Fluidity for inviscid flow past a cylinder in the vicinity of a wall; the analytical solution is obtained using the method of images.

Figure 4.18 shows the satisfactory agreement between the numerically predicted and analytical transverse profiles of stream-wise velocity through the centre of the cylinder, and normal to the wall, for Mesh 6.

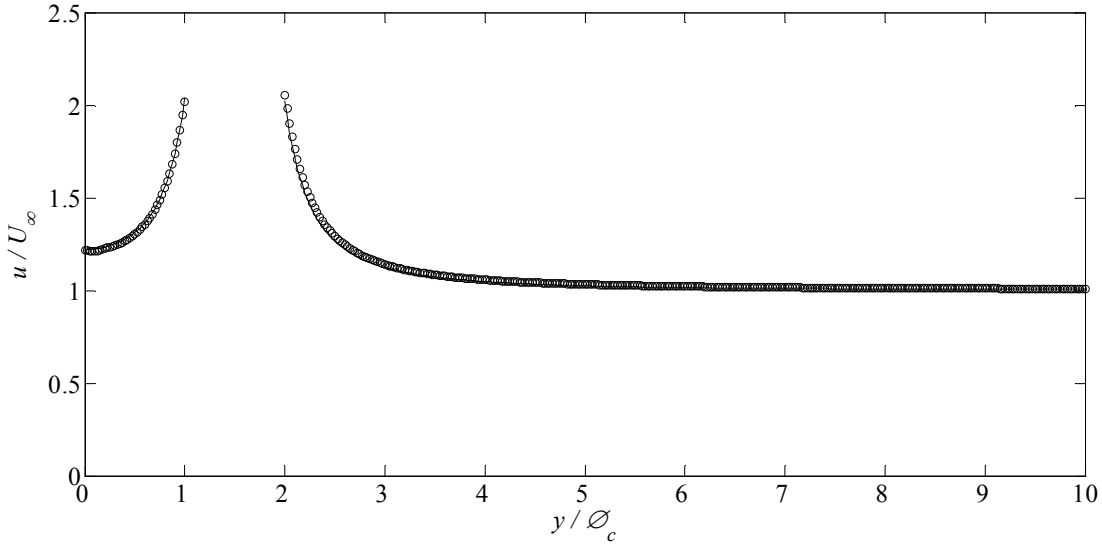


Figure 4.18. Comparison of predicted and analytical transverse profiles of stream-wise velocity component for inviscid flow past a cylinder close to a wall: Mesh 6 (circle); and analytical solution using method of images (solid line).

Both cases have verified that Fluidity correctly solves the mathematical equations used to model inviscid flow past a circular cylinder in the proximity of a nearby wall.

## 4.5. Flow past a circular cylinder at Reynolds number 40

Sections 4.5 to 4.7 focus on validation of Fluidity for viscous flow past a circular cylinder. A primary objective is to confirm that the numerical code is able to capture correctly the wake formation behind the cylinder in unsteady viscous flows. Correct island wake capture formation is important as this may impact on the accuracy of estimates of extractable power from nearby sites.

Coutanceau and Bouard [139] performed experiments in a cylindrical tank where a horizontal axis cylinder was raised vertically at constant speed in order to characterise the unsteady wake of an impulsively started circular cylinder at Reynolds numbers between $Re$ = 20 and $Re$ = 40. The properties of the liquid filling the tank were chosen to obtain a desired range of Reynolds numbers. The experiments assessed the effect of the ratio of cylinder and tank diameter on the results, to account for any blockage effect. A camera was coupled with the cylinder motion in order to capture correctly the flow motion around the cylinder. Wake parameters were determined from analysis of these photographs. Details of the experimental apparatus, visualisation and analysis techniques are given by Coutanceau and Bouard [144].

Coutanceau and Bouard [139] used four parameters to characterise the wake (Figure 4.19): the closed-wake length $L_c$, longitudinal and transversal positions of the vortex centres defined by $a_c$ and $b_c$ respectively, and the angle of separation $\theta_c$.

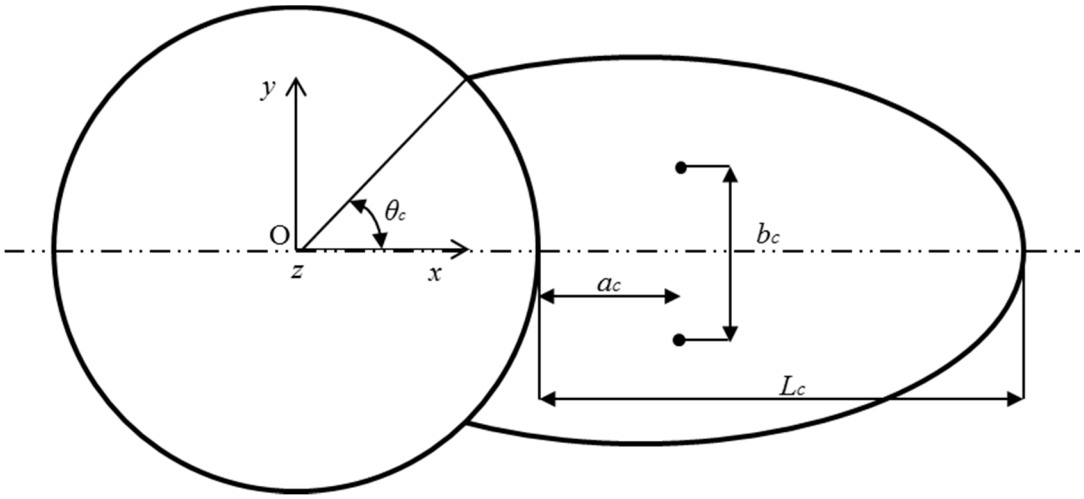


Figure 4.19. Geometric parameters of the closed wake as defined by Coutanceau and Bouard [144]: length of the wake $L_c$, longitudinal $a_c$ and transversal $b_c$ position of vortex centres and angle of separation $\theta_c$.

The non-dimensional time $t^*$ is defined as $t \cdot U_\infty / \varnothing_c$, Table 4.8 summarises the evolution in time of the cylinder wake geometry parameters $L_c/\varnothing_c$, $a_c/\varnothing_c$ and $b_c/\varnothing_c$ and $\theta_c$, observed by Coutanceau and Bouard [139] for a Reynolds number $Re$ = 40 and an aspect ratio of 0.07 between cylinder and tank diameters.

| $t^*$ | 1 | 2 | 3 | 4 | 5 | 6 | 8 | 10 | 12 |
|---|---|---|---|---|---|---|---|---|---|
| $L_c/\varnothing_c$ | 0.36 | 0.74 | 1.11 | 1.41 | 1.62 | 1.79 | 1.94 | 1.96 | 1.96 |
| $a_c/\varnothing_c$ | 0.17 | 0.36 | 0.51 | 0.61 | 0.66 | 0.69 | 0.69 | 0.69 | 0.69 |
| $b_c/\varnothing_c$ | 0.38 | 0.47 | 0.52 | 0.54 | 0.55 | 0.56 | 0.56 | 0.56 | 0.56 |
| $\theta_c$ (deg) | 41.2 | 46.5 | 49.3 | 51.0 | 51.8 | 52.3 | 52.5 | 52.5 | 52.5 |

Table 4.8. Temporal variation of the circular cylinder wake geometry parameters and angle of separation experimentally observed by Coutanceau and Bouard [139] for a Reynolds number $Re$ = 40 and an aspect ratio between cylinder and tank diameters of 0.07.

The rectangular domain is based on that considered in Section 4.3 (Figure 4.8), without modifying the domain width, water depth and cylinder diameter. To model the flow around an impulsively started circular cylinder, the model domain is initialised with a stream-wise velocity $U_\infty$. This creates a numerical reflection in the form of a pressure wave that

originates at the cylinder and travels upstream and downstream from the cylinder. In the absence of an effective dissipation mechanism (e.g. bottom friction) or a transmissive boundary at the west and east limits of the domain, the reflection advects through the domain and returns to the cylinder. For the time-period analysed, this is prevented if the domain length is increased to $200Ø_c$, where the cylinder is centred $80Ø_c$ downstream of the west domain limit.

Six spatial discretisation setups are investigated in the mesh convergence analysis. As in Section 4.3, the domain is divided into three mesh regions: upstream of the cylinder, downstream of the cylinder and cylinder. Table 4.9 presents the mesh edge length set in each domain region and the total number of grid elements for the six meshes considered in the analysis.

| | Element edge length | | | |
|---|---|---|---|---|
| Mesh | Upstream from cylinder | Downstream from cylinder | Cylinder | Mesh elements |
| 1 | $Ø_c$ | $3Ø_c$ /4 | $\pi Ø_c$ /12 | 11,854 |
| 2 | $Ø_c$ /2 | $3Ø_c$ /8 | $\pi Ø_c$ /28 | 12,826 |
| 3 | $Ø_c$ /4 | $3Ø_c$ /16 | $\pi Ø_c$ /36 | 184,072 |
| 4 | $Ø_c$ /4 | $3Ø_c$ /16 | $\pi Ø_c$ /76 | 190,076 |
| 5 | $Ø_c$ /4 | $3Ø_c$ /16 | $\pi Ø_c$ /156 | 197,654 |
| 6 | $Ø_c$ /4 | $3Ø_c$ /16 | $\pi Ø_c$ /316 | 207,322 |

Table 4.9. Six spatial discretisation cases considered in the mesh convergence analysis. Element edge length used in the three mesh regions of the model, and total number of mesh elements.

As in Section 4.3, the model domain has five boundaries (Figure 4.8): A stream-wise inlet velocity $U_\infty$ = 2 m/s condition is set at the west domain limit $\Gamma_1$; a zero pressure condition is set at the east domain limit corresponding to boundary $\Gamma_4$; the north $\Gamma_2$ and south $\Gamma_3$ domain limits are set as solid boundaries with a free-slip condition; finally, a no-slip condition is applied to the cylinder boundary. Kinematic viscosity is specified in the model in order to yield a Reynolds number $Re$ = 40 based on the set values for $U_\infty$ and $Ø_c$. No friction is applied at the bottom or at the walls of the domain. The time step $t$ is chosen for each mesh in order to keep the $CFL$ number below unity. The simulation is run for a time period $T = 12t^*$ in order to match the duration of the experimental data.

Figure 4.20, Figure 4.21, Figure 4.22 and Figure 4.23 compare respectively the temporal variation of the cylinder wake parameters $L_c$, $a_c$, $b_c$ and $\theta_c$ computed by Fluidity on Meshes

1-6 against the experimental observations by Coutanceau and Bouard [139]. Numerical cylinder wake parameters are derived from the flow streamlines at each time step. Mesh convergence is achieved within plotting accuracy for mesh 5. Mesh 4 shows favourable results although for higher values of $t^*$ there is an obvious difference in the $L_c$ values, but this is less important for $a_c$, $b_c$ and $\theta_c$. The numerical solution obtained with Meshes 4-6 are in good agreement with the experimental values.

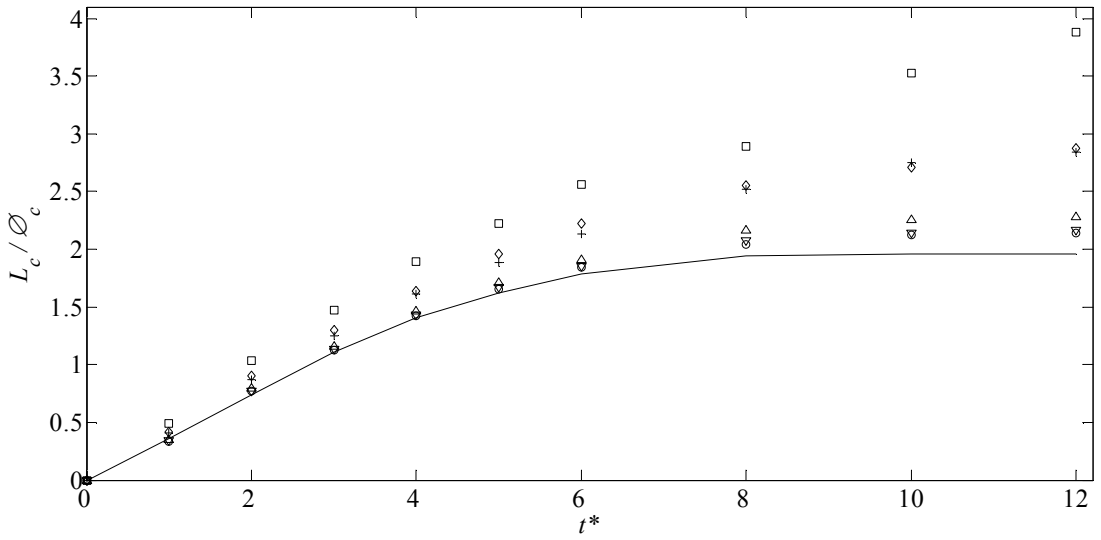


Figure 4.20. Early stage evolution of wake length at $Re$ = 40: experimental results by Coutanceau and Bouard [139] (solid line); Fluidity predictions for Mesh 1 (square), 2 (diamond), 3 (plus sign), 4 (upward-pointing triangle), 5 (downward-pointing triangle) and 6 (circle).

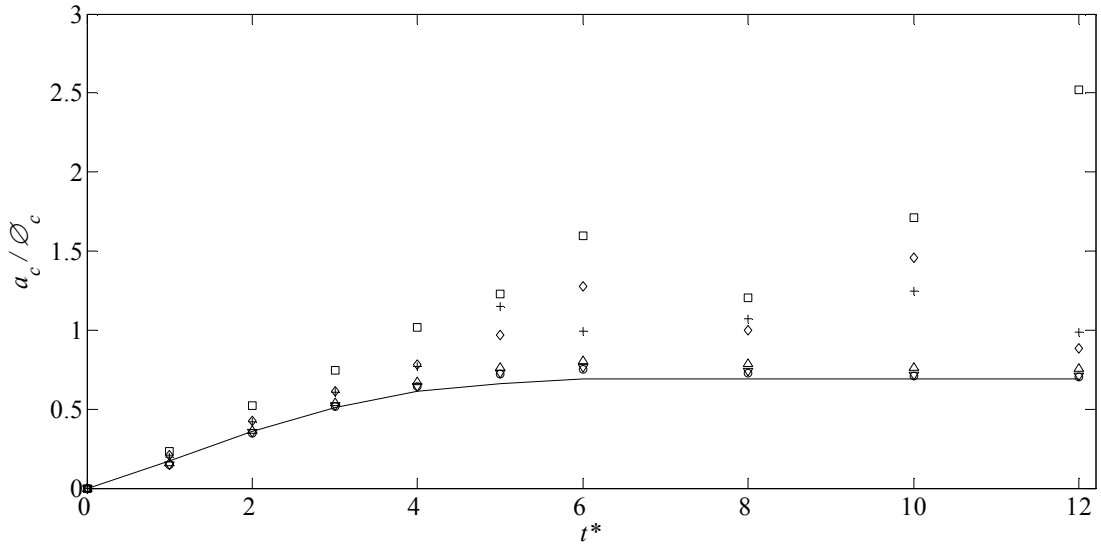


Figure 4.21. Early stage evolution of stream-wise vortex centre distance $a$ at $Re$ = 40: experimental results by Coutanceau and Bouard [139] (solid line); Fluidity predictions for Mesh 1 (square), 2 (diamond), 3 (plus sign), 4 (upward-pointing triangle), 5 (downward-pointing triangle) and 6 (circle).

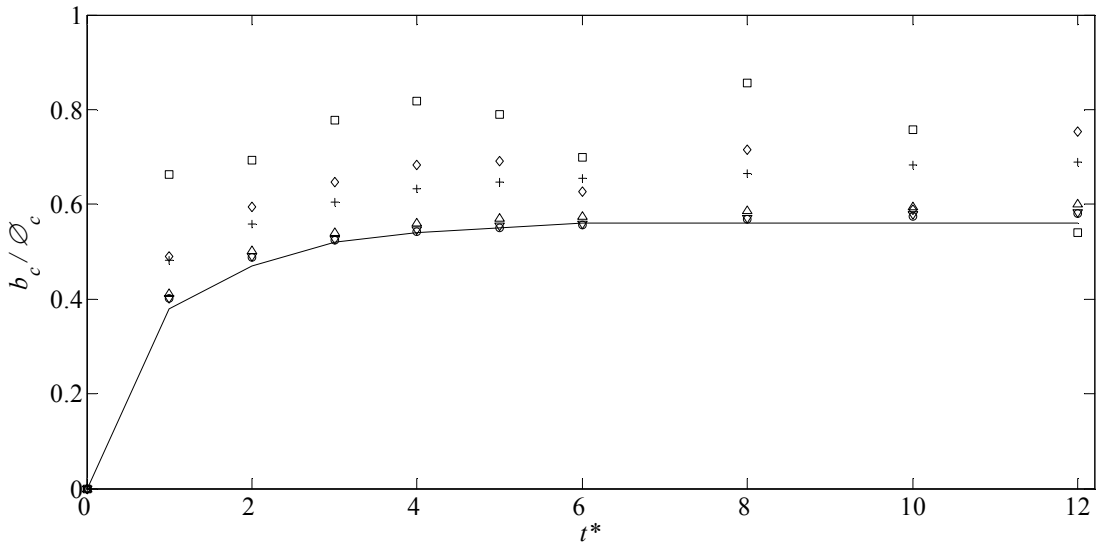


Figure 4.22. Early stage evolution of transverse vortex centre distance $b$ at $Re$ = 40: experimental results by Coutanceau and Bouard [139] (solid line); Fluidity predictions for Mesh 1 (square), 2 (diamond), 3 (plus sign), 4 (upward-pointing triangle), 5 (downward-pointing triangle) and 6 (circle).

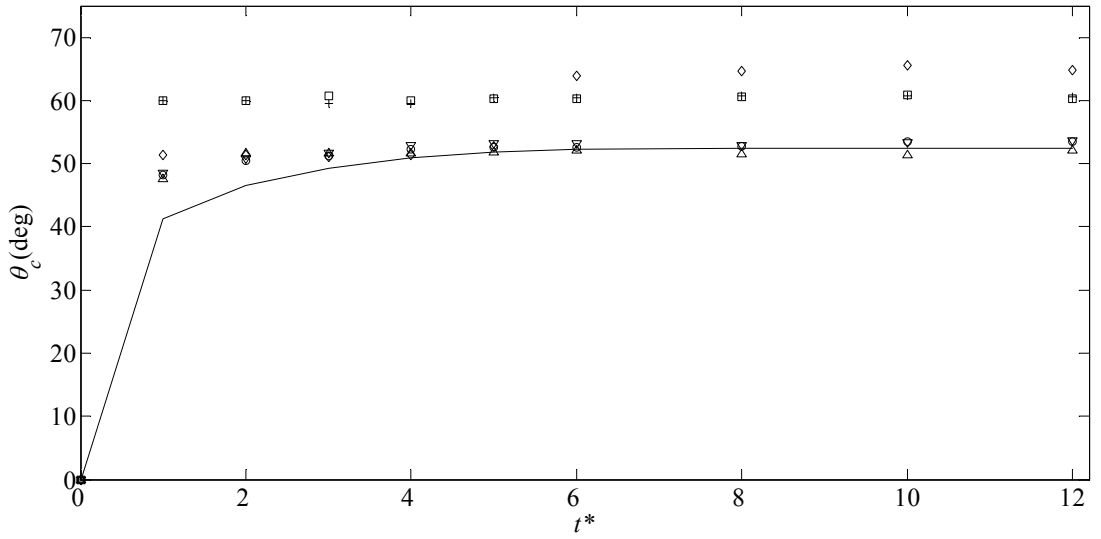


Figure 4.23. Early stage evolution of angle of flow separation at $Re$ = 40: experimental results by Coutanceau and Bouard [139] (solid line); Fluidity predictions for Mesh 1 (square), 2 (diamond), 3 (plus sign), 4 (upward-pointing triangle), 5 (downward-pointing triangle) and 6 (circle).

## 4.6. Flow past a circular cylinder at Reynolds number 100

This case considers the ability of Fluidity to correctly compute the wake length of a circular cylinder for a Reynolds number $Re$ = 100 by comparison to an alternative numerical solution developed by Collins and Dennis [140] who investigated the closed-wake length of an

impulsively-started moving circular cylinder at Reynolds numbers $Re$ = 40, 100 and 500. In their study, Collins and Dennis validated their numerically computed closed-wake lengths at $Re$ = 100 against experimental and numerical data reported by Honji and Taneda [145] and Kawaguti and Jain [146].

Figure 4.24 shows the evolution of the closed-wake length behind an impulsively started circular cylinder for $Re$ = 100 experimentally observed by Honji and Taneda [145] and numerically computed by Kawaguti and Jain [146] and Collins and Dennis [140] integrating the Navier-Stokes equations using the Crank-Nicolson implicit method. Note that compared to the original figure from Collins and Dennis, non-dimensional time is here expressed as $tU_\infty/\emptyset_c$ and closed-wake length is expressed in terms of the cylinder diameter.

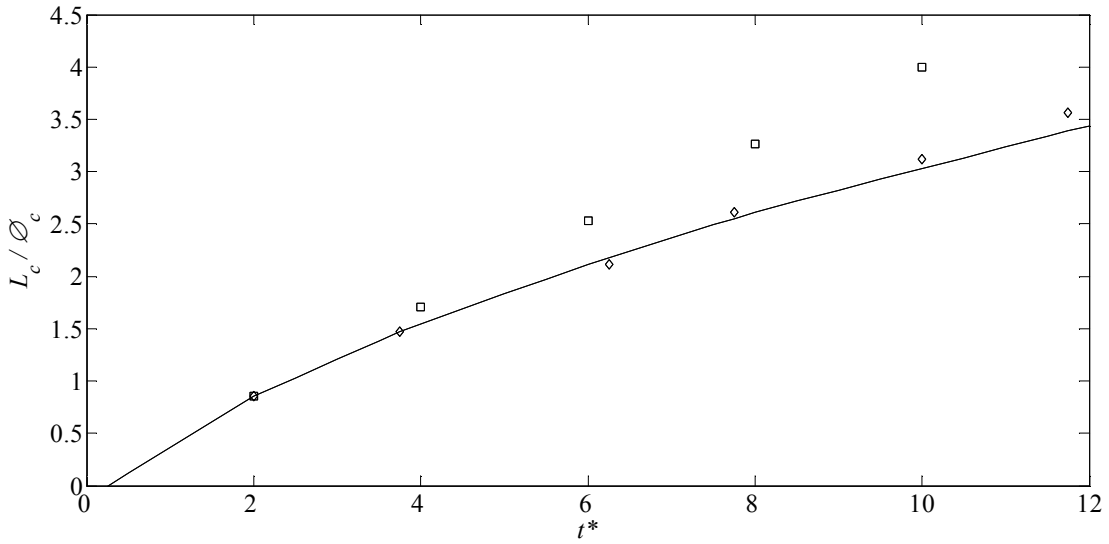


Figure 4.24. Early stage evolution of wake length at $Re$ = 100: numerical results by Collins and Dennis [140] (solid line); numerical predictions by Kawaguti and Jain [146] (square); and experimental observations by Honji and Taneda [145] (diamond).

Following the computational setup described in Section 4.5, Fluidity is used to model the flow past a cylinder at $Re$ = 100. Model geometry, initial and boundary conditions are not modified. A mesh convergence study is carried out based on the meshes shown in Table 4.9. The kinematic viscosity is specified to set the Reynolds number to $Re$ =100. No friction is applied to the bottom and walls of the domain. The time-step chosen is such that the *CFL* number is below unity. The simulation is run for a time period $T = 12t^*$ to match the duration of the numerical data from Collins and Dennis [140]. Figure 4.25 compares the closed wake lengths predicted by Fluidity on Meshes 1-6 with alternative numerical predictions by Collins and Dennis. The results converge as the mesh is progressively

refined, with Meshes 4-6 providing a satisfactory approximation to the numerical solution by Collins and Dennis. Oscillation in the wake length observed for Mesh 1 is caused by lack of mesh refinement which leads to a break in symmetry of the two eddies behind the cylinder.

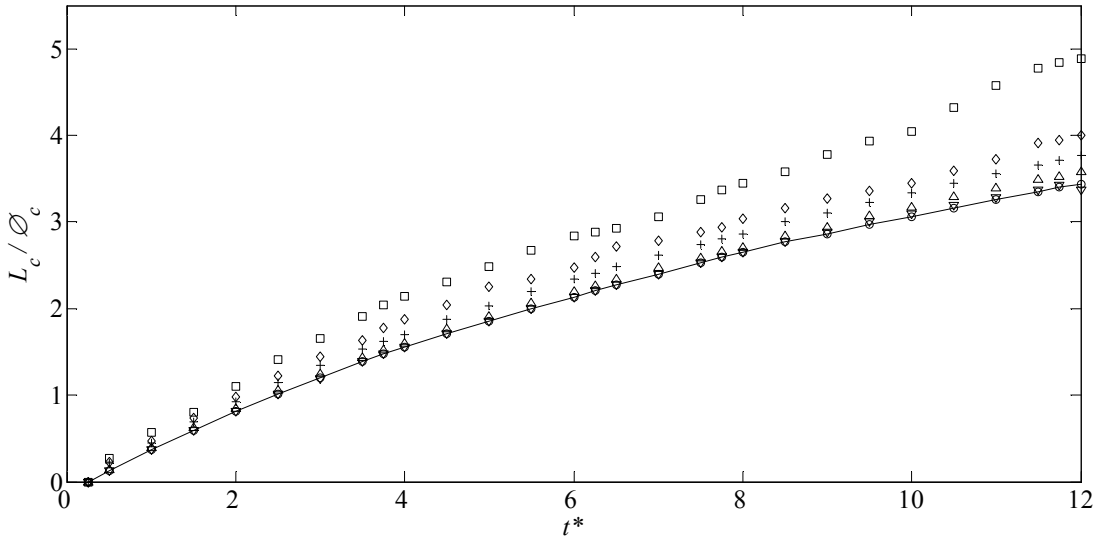


Figure 4.25. Early stage evolution of wake length at $Re$ = 100: numerical results by Collins and Dennis [140] (solid line) and Fluidity predictions for Mesh 1 (square), 2 (diamond), 3 (plus sign), 4 (upward-pointing triangle), 5 (downward-pointing triangle) and 6 (circle).

## 4.7. Flow past a circular cylinder at Reynolds number 5,000

Bouard and Coutanceau [141] investigated the early stages of wake development behind an impulsively started cylinder for a range of Reynolds numbers between 40 and $10^4$. Section 4.5 briefly outlines the experimental technique, which followed that of Coutanceau and Bouard [139]. This section presents a visual comparison of the flow past a cylinder at Reynolds number 5,000 as observed by Bouard and Coutanceau, and predicted by Fluidity. The experiments carried out by Bouard and Coutanceau provides a series of fine resolution photographic plates of the early stages of the flow past a circular cylinder at Reynolds number $Re$ = 5,000. High-quality visualisations produced by Bouard and Coutanceau using reflecting or diffusing solid tracers enabled capture of the streamlines behind the circular cylinder. Bouard and Coutanceau present results for the evolving flow past a cylinder at non-dimensional times $t^*$ 1, 1.5, 2, and 2.5. Figure 4.26 shows the streamlines behind a circular cylinder obtained at $t^*$ 2.5.

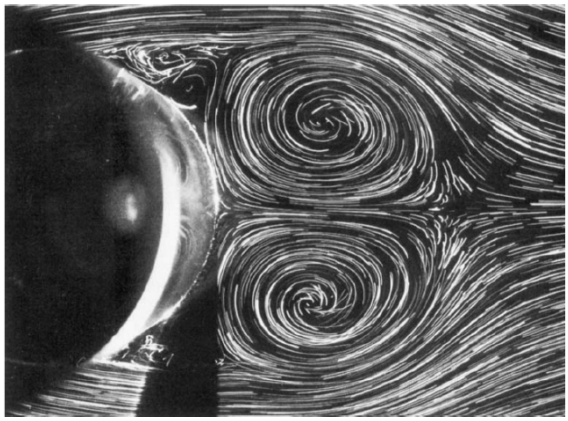

Figure 4.26. Wake behind an impulsively started cylinder at $Re$ = 5000 at $t^*$=2.5 [141].

The numerical model geometry, initial conditions and boundary conditions are the same as for the $Re$ 40 and 100 cases. The value of kinematic viscosity was prescribed, corresponding to a Reynolds number of 5,000. The time step was chosen to keep the $CFL$ number below unity. The simulation was run for a time period of $T = 2.5t^*$ to match the duration of the experimental data. A mesh-convergence study using Meshes 3-6 from Table 4.9 is performed. Figure 4.27 compares the streamlines of flow past a cylinder computed using Fluidity on Meshes 3-6 against the observed streamlines obtained by Bouard and Coutanceau at $t^* = 2.5$. It can be seen that the predicted streamlines on Meshes 4-6 are in close agreement with the experimental observations. The shape and centre location of the symmetrical eddies are satisfactorily approximated by the numerical model. Moreover, for Meshes 4-6 Fluidity reproduces the secondary eddies formed close to the cylinder surface. Again, it is concluded that spatial resolution of Meshes 4 is sufficient to approximate correctly the flow past a cylinder at $Re$ = 5,000.

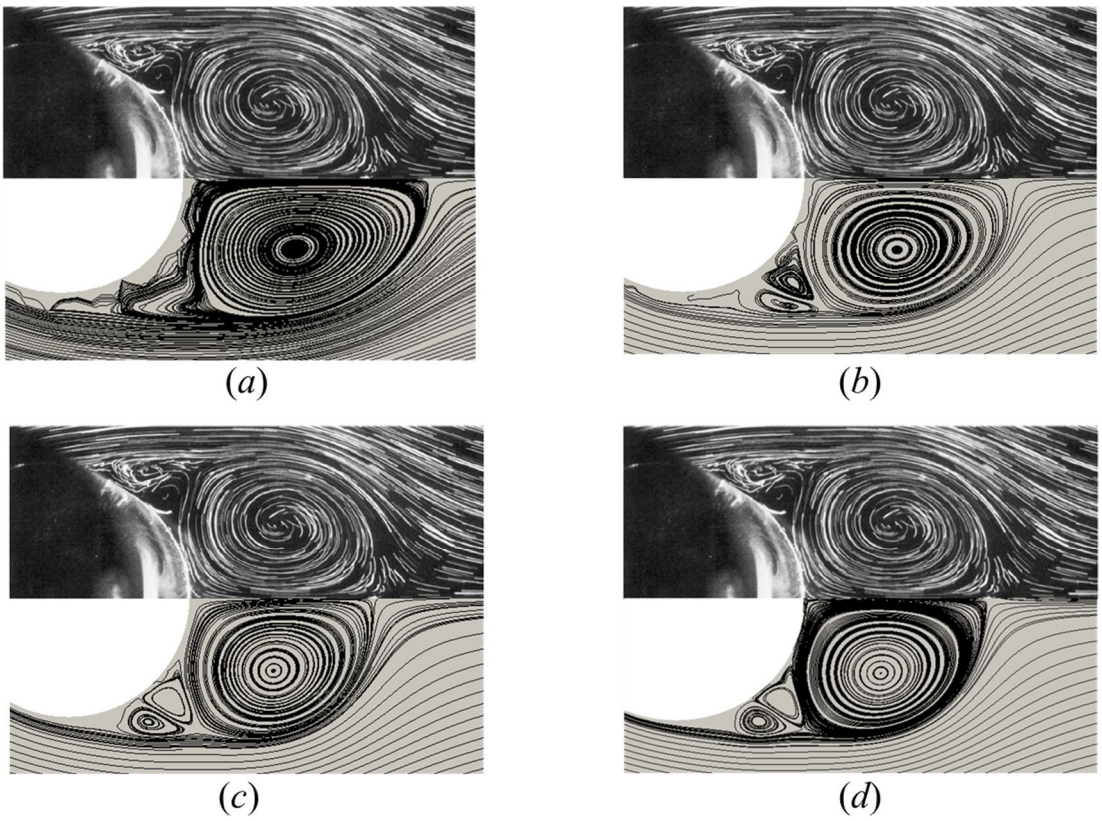


Figure 4.27. Streamlines of flow past a cylinder for $Re$ = 5000 observed by Bouard and Coutanceau [141] (upper subplots) and computed with Fluidity (lower subplots) at $t^*$ = 2.5 computed on Meshes (a) 3, (b) 4, (c) 5 and (d) 6.

Figure 4.28 compares the early stages of the developing flow computed on Mesh 6 against the experimental visualisation by Bouard and Coutanceau [141] at $t^*$ 1, 1.5, 2 and 2.5. It can be seen that the predictions agree well with experimental data and properly reproduce secondary flow phenomena such as the bulge in streamlines (Figure 4.28a) and the consequent isolated secondary eddy (Figure 4.28d).

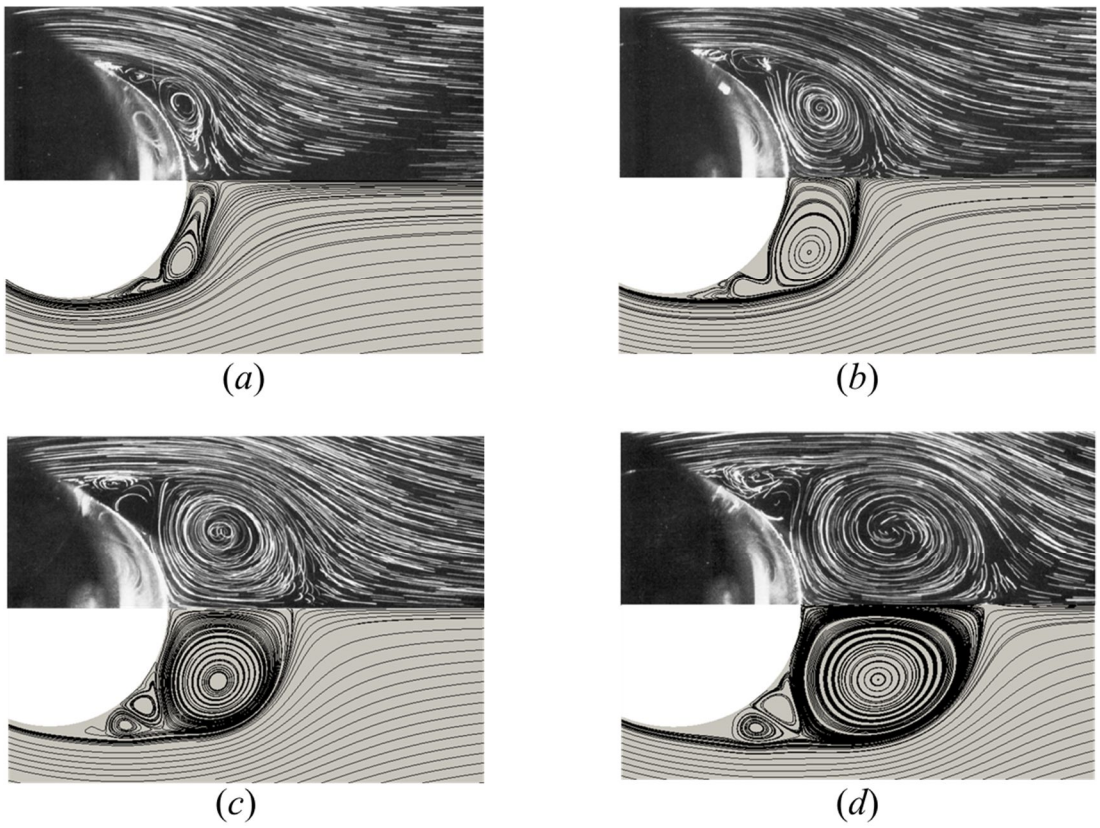


Figure 4.28. Early stage development of streamlines of flow past a cylinder for *Re* = 5,000 observed by Bouard and Coutanceau [141] (upper subplot) and computed with Fluidity (lower subplot) using Mesh 6 for (a) $t^* = 1$, (b) $t^* = 1.5$, (c) $t^* = 2$ and (d) $t^* = 2.5$.

## 4.8. Oscillatory laminar shallow flow past surface piercing circular cylinders

The previous sections examined the capability of Fluidity to model flow past an impulsively started submerged circular cylinder. This section next considers how well Fluidity models flow past circular surface piercing cylinders, including wake formation in oscillatory laminar flows, against the experimental work carried out by Lloyd *et al*. [69].

Lloyd *et al*. [69] investigated the wake formation around cylindrical and conical islands in oscillatory subcritical laminar shallow water flows. Experiments were performed in a shallow-water tidal flume of 11 m length and 3.3 m width. The water depth was altered according to the flow regime tested. Oscillatory current flow was generated using a hydraulic system of four valves and a variable-speed pump. The circular cylinder had diameter of 0.6 m, height of 0.8m, and was placed in the centre of the flume. Lloyd *et al*.

investigated the dependence of the oscillatory shallow wake formation on two non-dimensional parameters: the Keulegan-Carpenter number *KC:*

$$KC = \frac{U_o T}{\emptyset_c} \tag{4.19}$$

where $U_o$ and $T$ are the magnitude and the period of the oscillating velocity near the surface, and the island diameter is taken as the characteristic length for circular objects; and the stability parameter $S$:

$$S = \frac{C_d \emptyset_c}{h} \tag{4.20}$$

which measures the stabilising effect of bed friction relative to the destabilising influence of transverse shear [70]. Lloyd *et al*. [69] noted that wake type also depends on the island-diameter to depth ratio and Reynolds number. Figure 4.29 shows the four types of oscillatory-shallow-water wakes identified by Lloyd *et al*.: (a) symmetric-without-vortex-pairing; (b) symmetric-with-pairing; (c) sinuous-with-pairing; and (d) vortex-shedding. In wake type (a) there is only formation of attached counter-rotating vortices during a half-cycle. Wake type (b) presents the formation in a half-cycle of symmetric vortex pairs and attached counter-rotating vortices. Wake type (c) is similar to type (b) but Lloyd *et al.* define the form as asymmetric sinuous. Finally, wake type (d) represents vortex shedding.

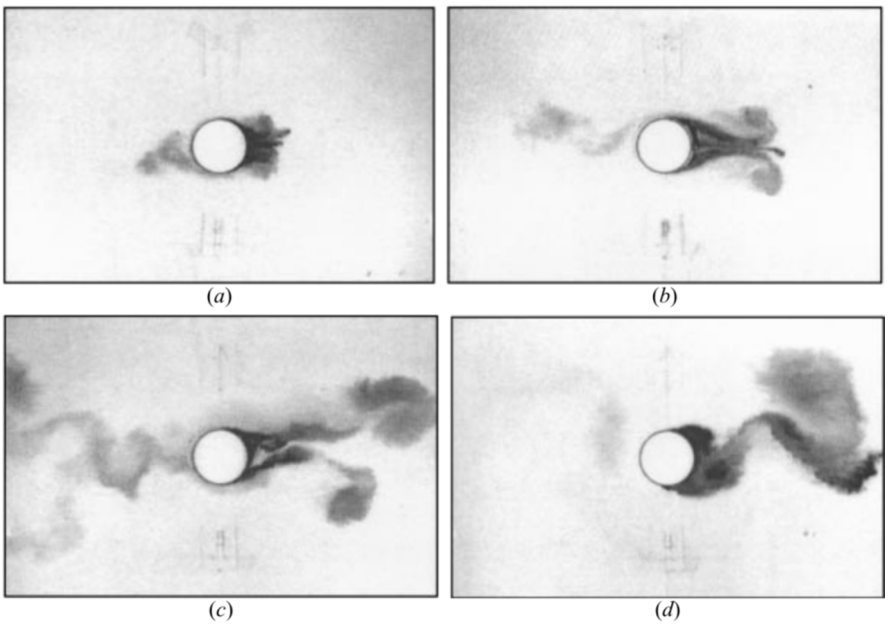


Figure 4.29. Oscillatory shallow water wakes at time $t = T / 4$ for flow from west to east at maximum velocity. (a) symmetric without-pairing; (b) symmetric-with-pairing; (c) sinuous-with-pairing; (d) vortex-shedding [69].

Oscillatory flow in otherwise unbounded flow past a smooth-wall is laminar if the oscillatory Reynolds number $Re_a$ is less than $10^5$. The oscillatory Reynolds number is defined as $Re_a = \rho U_o a_f/\mu$, where $a_f$ is the amplitude of the fluid motion defined as $a_f = U_o T/2\pi$. The boundary layer thickness of the bottom of the tank is computed as $3/4\pi(2a_f\nu/U_o)^2$ [147], and it was found to be smaller than the water depth in the experiments conducted by Lloyd *et al*. [69]. It was assumed that the flume tank had smooth walls and a laminar flow, leading to the calculation of the non-dimensional bottom friction coefficient as $C_d = 2/\sqrt{Re_a}$.

Lloyd *et al*. [69] analysed 20 configurations of *KC*, *S* and $Ø_c/h$ ratios to classify the wake type of a surface piercing circular cylinder in oscillatory laminar flows. Figure 4.30 shows the type of oscillatory-shallow-water wake identified with each of these configurations. Lloyd *et al*. further observed three cases of a wake incorporating vortex shedding and one case for each of the sinuous-with-pairing, symmetric-with-pairing and symmetric-without-pairing wake types. Each case included velocity and vorticity field plots at times $t = T/4$, $T/2$, $5T/8$ and $3T/4$. In addition, Lloyd *et al*.'s work included time history plots of the stream-wise and transverse velocity components at two locations ($x$ , $y$) = (0, 0.45) m and ($x$ , $y$) = (0, -0.45) m for three tidal periods.

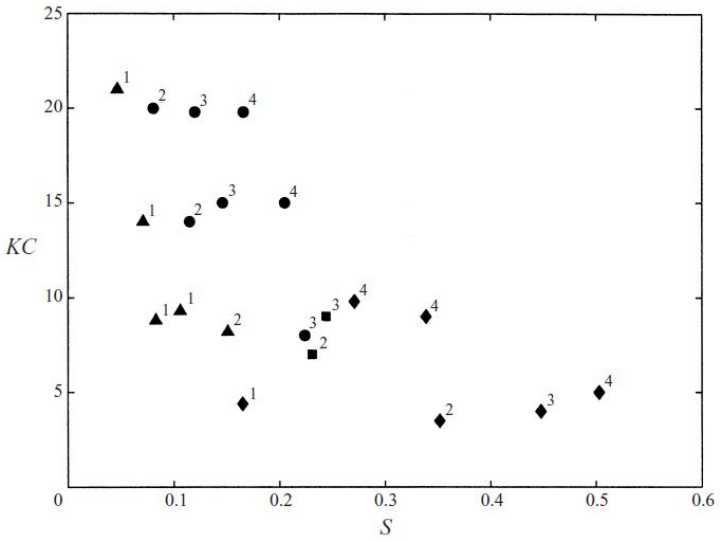


Figure 4.30. Wake type for the circular cylinder tests: symmetric without pairing (diamond); symmetric with pairing (square); sinuous with pairing (circle); vortex shedding (triangle). Symbol superscript indicates the value of $Ø_c$/h: 1, 10,0; 2, 17.6; 3, 24.0; 4, 33.3 [69].

Table 4.10 presents the expected value range for the parameters *KC* and *S* for a 2 km diameter island in an $M_2$ oscillatory tidal flow. A range of 0.5 to 3.0 m/s is considered for the amplitude of the oscillatory tidal flow velocity. A range of seabed-friction coefficients

between 0.001 and 0.005 is considered – in agreement with the coefficient values used to model the Pentland Firth by Baston and Harris [94]. Water depths are taken between 30 and 100 m, consistent with first- and second-generation tidal turbine technologies [148]. Corresponding *KC* and *S* values for realistic islands lie in the ranges of 11-67 and 0.02-0.5, respectively. The majority of *KC*-*S* combinations are off the scales of Figure 4.30. As the tidal-flow period is very large, in all possible cases *KC* is very high. If Figure 4.30 is extrapolated, it is assumed that for large *KC* numbers and *S* between 0.02 and 0.5, vortex shedding and sinuous-with-pairing wake types predominate.

| $T$ (s) | $U_o$ (m/s) | $Ø_c$ (m) | $C_d$ | $h$ (m) | $KC$ | $S$ |
|---|---|---|---|---|---|---|
| 44,700 | 0.5-3.0 | 2,000 | 0.001-0.005 | 30-100 | 11-67 | 0.02-0.5 |

Table 4.10. Geometry and flow conditions in realistic islands and correspondent *KC* and *S* parameters.

Table 4.11 summarises the test conditions described by Lloyd *et al*. [69] for the analysis of the wake type behind a surface piercing circular cylinder, with vortex shedding and sinuous-with-pairing wake types.

| Wake type | Code name in Lloyd *et al*. [69] | $T$ (s) | $U_o$ (m/s) | $h$ (m) | $Ø_c$ (m) | $KC$ | $C_d$ (x$10^{-3}$) | $S$ |
|---|---|---|---|---|---|---|---|---|
| Vortex shedding | CC03 | 140 | 0.040 | 0.060 | 0.60 | 9.3 | 10.592 | 0.106 |
| Sinuous with pairing | CC09 | 120 | 0.070 | 0.034 | 0.60 | 14.0 | 6.538 | 0.115 |

Table 4.11. Experimental test conditions for the wake analysis behind a surface piercing circular cylinder for the vortex shedding and sinuous-with-pairing wake types [69].

Lloyd *et al*. [69] concluded that shallow-water flow modelling with vertical variation is necessary in order to include the effect of the bed boundary-layer thickness (which occupies a smaller scale than the water depth). Moreover, solution of the full three-dimensional Navier-Stokes is required to resolve the bed and wall boundary layers in the vicinity of the cylinder, while including the influence of non-hydrostatic pressure. In a later paper, Stansby [109] concluded that for a conical island, fully three dimensional modelling is necessary to capture correctly the local flow dynamics. Furthermore, Stansby noted that the only case where numerical predictions based on the SWE agrees with those from three-dimensional modelling is when there is prominent vortex shedding behind the circular cylinder.

Here, a rectangular domain is set with identical length and width to the flume used in the experiments by Lloyd *et al*. [69]. The circular cylinder is located at the centre of the domain with Cartesian coordinates $x = 0$ m, $y = 0$ m. The water depth in the model is set to match

the experimental conditions, as described in Table 4.11. Similarly, bottom and wall non-dimensional friction coefficients are defined, also as per Table 4.11. Since the experimental work by Lloyd *et al*. is performed in water, the kinematic viscosity is set as $\nu = 10^{-6}\ m^2\ s^{-1}$. Figure 4.31 shows the unstructured mesh used to spatially discretise the domain. Table 4.12 presents the element edge length of the elements used and total number of elements in the spatial discretisation of the domain. The element edge length is chosen based on the values used to define Mesh 4 in the validation tests of flow past a circular cylinder in Sections 4.5, 4.6 and 4.7. Due to the oscillatory nature of the flow, identical mesh-edge lengths are used upstream and downstream of the cylinder.

| Element edge length | | | |
|---|---|---|---|
| Upstream from cylinder | Downstream from cylinder | Cylinder | Mesh elements |
| $3\varnothing_c$ /16 | $3\varnothing_c$ /16 | $\pi\ \varnothing_c$ /76 | 11,140 |

Table 4.12. Element edge lengths upstream and downstream of the cylinder and at the surface of the cylinder, and total number of mesh elements.

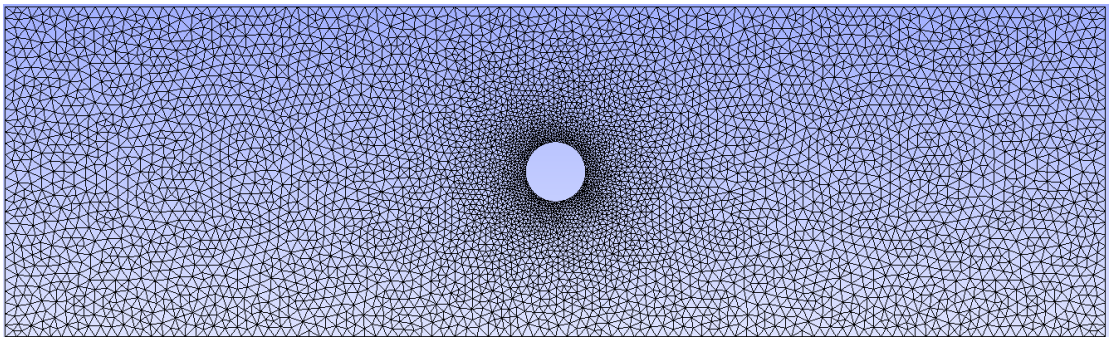

Figure 4.31. Unstructured mesh for domain with circular cylinder at the centre, used in Fluidity to simulate flow past an island in an oscillatory laminar shallow water flow.

The time step is chosen so that the *CFL* number is below unity. A free-slip condition is applied at the north and south boundaries of the domain. A no-slip boundary condition is applied to the surface of the cylinder. To replicate the flow conditions in the laboratory basin used by Lloyd *et al.* [69], a half-wave sine inlet velocity boundary condition of period $T$ = 140 s and amplitude $U_o$ = 0.04 m/s is set at the west and east ends of the rectangular domain (Figure 4.32). For zero inlet velocities at the boundaries, zero pressure and free-stress conditions are also applied.

Stansby [109] observed that numerical models based on the hydrostatic shallow water equations cannot resolve properly the complex flow dynamics past surface-piercing conical islands. To assess the adequacy of the solution of the SWE provided by Fluidity-SWE to

capture the flow past a surface piercing circular cylinder, the vortex shedding wake type case is also run solving the full 3D Navier Stokes equations (Fluidity-3D). In the 3D case, the spatial discretisation in the *x*-*y* plane is identical to the one used in SWE (shown in Figure 4.31). The water column is spatially discretised using 15 sigma layers of uniform vertical size. Thus, in the three-dimensional case, the number of elements in the mesh is approximately 167,100. No turbulence model is used to resolve the power dissipated due to viscous forces at a smaller scale than the grid size.

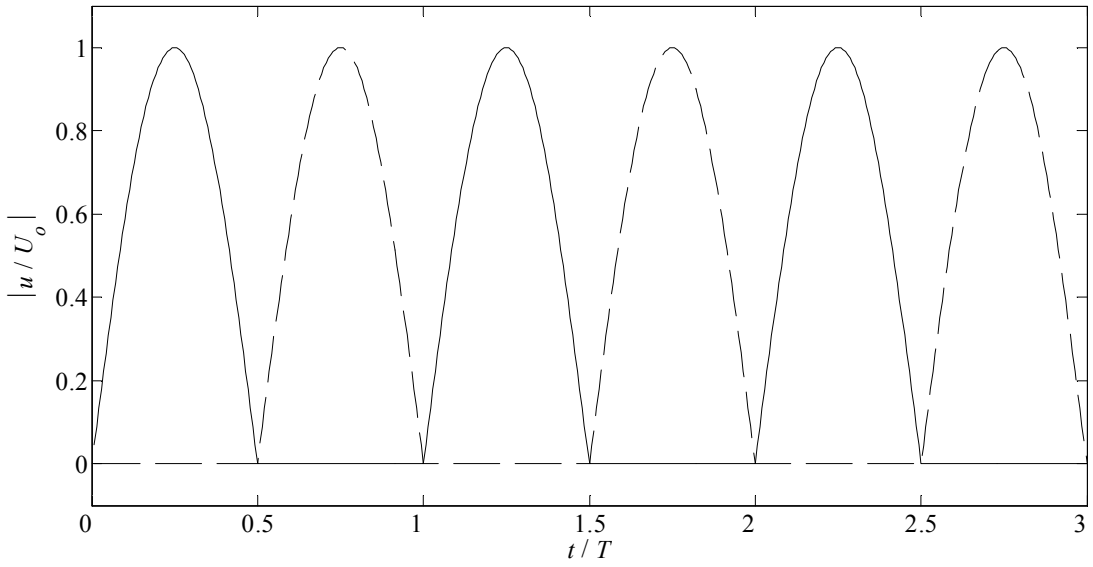


Figure 4.32. Half-wave sine inlet velocity boundary conditions prescribed at the west (solid line) and east (dashed line) ends of the rectangular domain.

Figure 4.33 compares vorticity contour plots obtained experimentally at Keulegan-Carpenter number $KC = 9.3$ by Lloyd *et al*. [69] with those computed using Fluidity-SWE and Fluidity-3D. The vertical component of vorticity is computed as $\omega = \frac{\partial v}{\partial x} - \frac{\partial u}{\partial y}$. Dark-colour vorticity plots in the paper by Lloyd *et al*. correspond to blue-colour vorticity plots in Fluidity and indicate clockwise flow rotation. Light-colour in the paper by Lloyd *et al*. and red-colour in Fluidity indicate anti-clockwise flow rotation. Vorticity contour plots are compared at times $t = T/4$, $T/2$, $5T/8$ and $3T/4$ from the third tidal cycle modelled. In general, the vorticity structures computed with Fluidity-SWE and Fluidity-3D compare reasonably well with those obtained by Lloyd *et al*.. The flow direction around the circular cylinder and local variability in flow rotationality are reasonably well captured by both SWE and 3D. This provides confidence in the capability of Fluidity-SWE to capture the flow dynamics around a surface-piercing circular cylinder in an oscillatory laminar shallow flow.

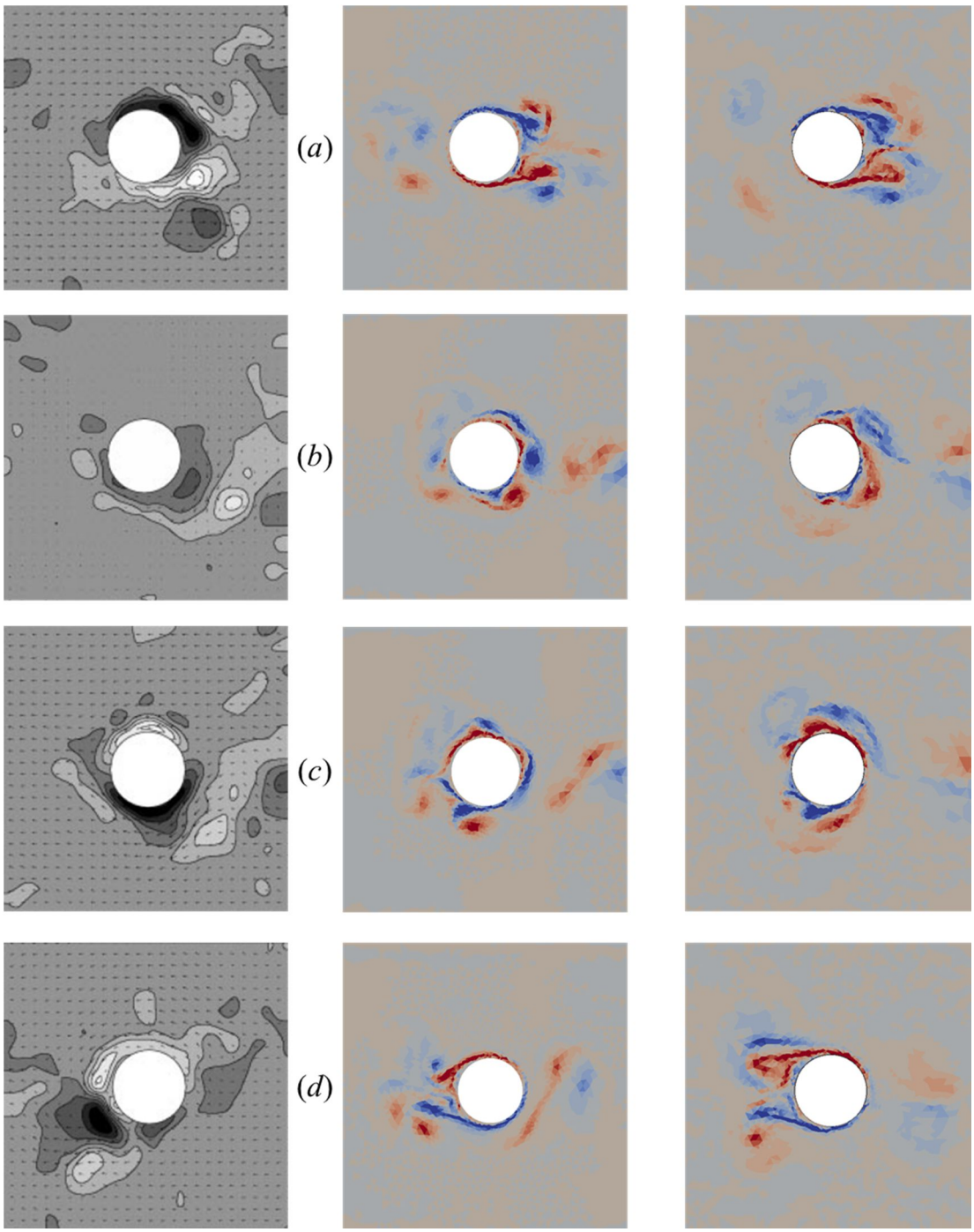


Figure 4.33. Vorticity contour plots for the vortex shedding wake type obtained experimentally by Lloyd *et al.* [69] (left column), generated with Fluidity-SWE (centre column) and generated with Fluidity-3D with 15 sigma layers (right column) for the third tidal period simulated. Dark colour vorticity contour plots in Lloyd *et al.* correspond to blue colour vorticity contour plots in Fluidity. Light colour vorticity contour plots in Lloyd *et al.* correspond to red colour vorticity contour plots in Fluidity. (*a*) $t = T / 4$, (*b*) $t = T / 2$, (*c*) $t = 5T / 8$, (*d*) $t = 3T / 4$.

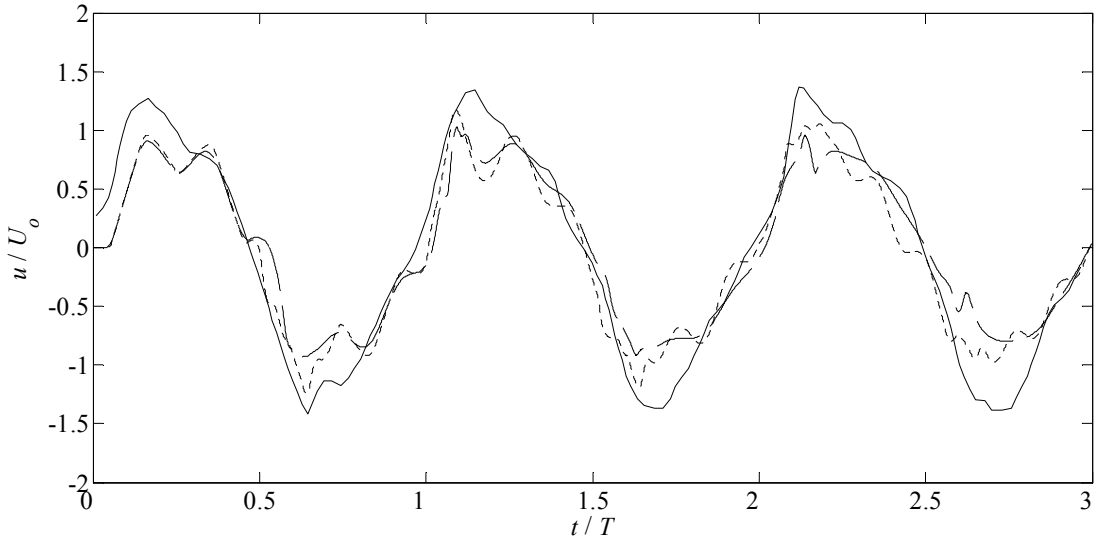


Figure 4.34. Time histories of non-dimensional stream-wise velocity component during 3 tidal periods at $x$ = 0 m and $y$ = 0.45 m at $KC$ = 9.3: experimental data, Lloyd *et al*. [69] (solid line); numerical predictions by Fluidity-SWE (dashed line); and numerical predictions by Fluidity-3D with 15 sigma layers (dotted line).

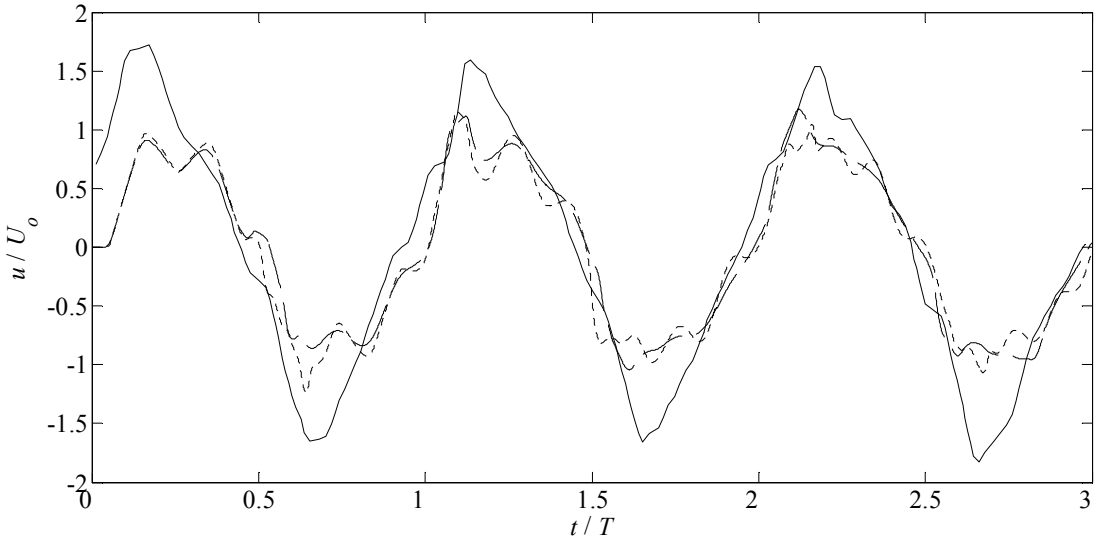


Figure 4.35. Time histories of non-dimensional stream-wise velocity component during 3 tidal periods at $x$ = 0 m and $y$ = -0.45 m at $KC$ = 9.3: experimental data, Lloyd *et al*. [69] (solid line); numerical predictions by Fluidity-SWE (dashed line); and numerical predictions by Fluidity-3D with 15 sigma layers (dotted line).

Time-history plots of the stream-wise velocities at $x = 0$ m, $y = 0.45$ m and $x = 0$ m, $y = -0.45$ m are included in Figure 4.34 and Figure 4.35 respectively. The stream-wise velocities correspond to the depth-averaged and surface velocities from Fluidity-SWE and Fluidity-3D respectively. Range, shape and phase of the velocity time series are satisfactorily reproduced by Fluidity-SWE and Fluidity-3D. From the plots, it is not clear that the Fluidity-3D provides a better approximation to the experimental work than Fluidity-SWE. Certain discrepancies in range and shape between the experimental and numerical solutions may have been influenced by the uncertainty inherent in numerically reproducing the exact experimental conditions.

Figure 4.36 presents vorticity plots at times $t = T/4$, $T/2$, $5T/8$, and $3T/4$ obtained using the Fluidity-SWE solver and experimental data obtained by Lloyd *et al*. [69] at $KC = 14.0$. The predicted and measured vorticity distributions exhibit reasonable agreement.

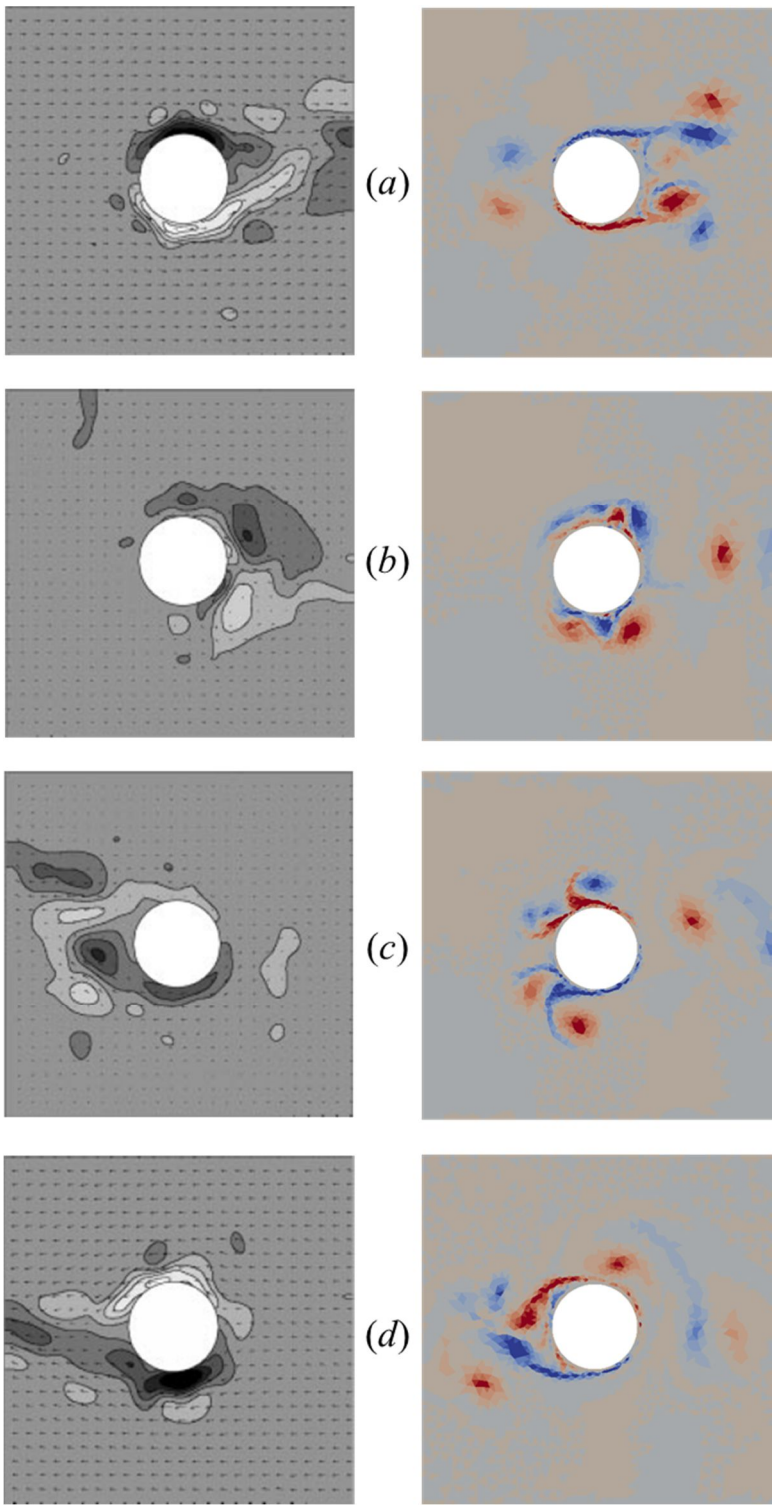


Figure 4.36. Vorticity contour plots for the sinuous wake type obtained by Lloyd *et al*. [69] (left) and generated with Fluidity-SWE for the third tidal period simulated (right). Dark colour vorticity contour plots in Lloyd *et al*. correspond to blue colour vorticity contour plots in Fluidity. Light colour vorticity contour plots in Lloyd *et al*. correspond to red colour vorticity contour plots in Fluidity. (*a*) $t = T / 4$, (*b*) $t = T / 2$, (*c*) $t = 5T / 8$, (*d*) $t = 3T / 4$.

Figure 4.37 and Figure 4.38 plot experimental and predicted stream-wise velocity component time histories at locations ($x$, $y$) = (0, 0.45) m and ($x$, $y$) = (0, -0.45) m in the basin considered by Lloyd *et al*. [69]. Although the velocity range is relatively well reproduced by Fluidity-SWE at both locations, there are some discrepancies in the phase and profile of the velocity time series.

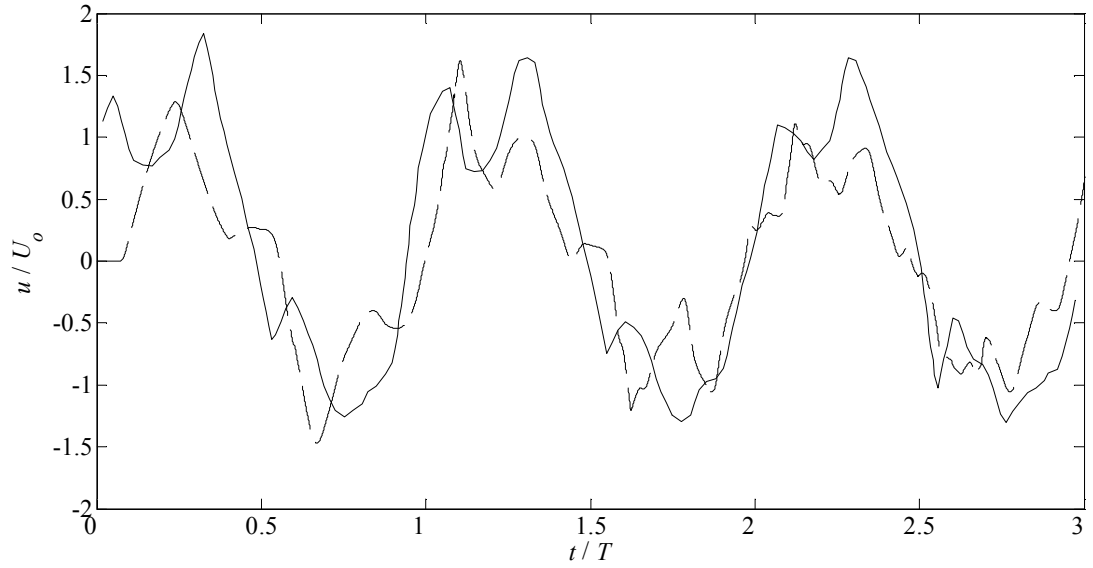


Figure 4.37. Time histories of non-dimensional stream-wise velocity component during 3 tidal periods at $x$ = 0 m and $y$ = 0.45 m at $KC$ = 14.0: experimental data, Lloyd *et al*. [69] (solid line); and numerical predictions by Fluidity-SWE (dashed line).

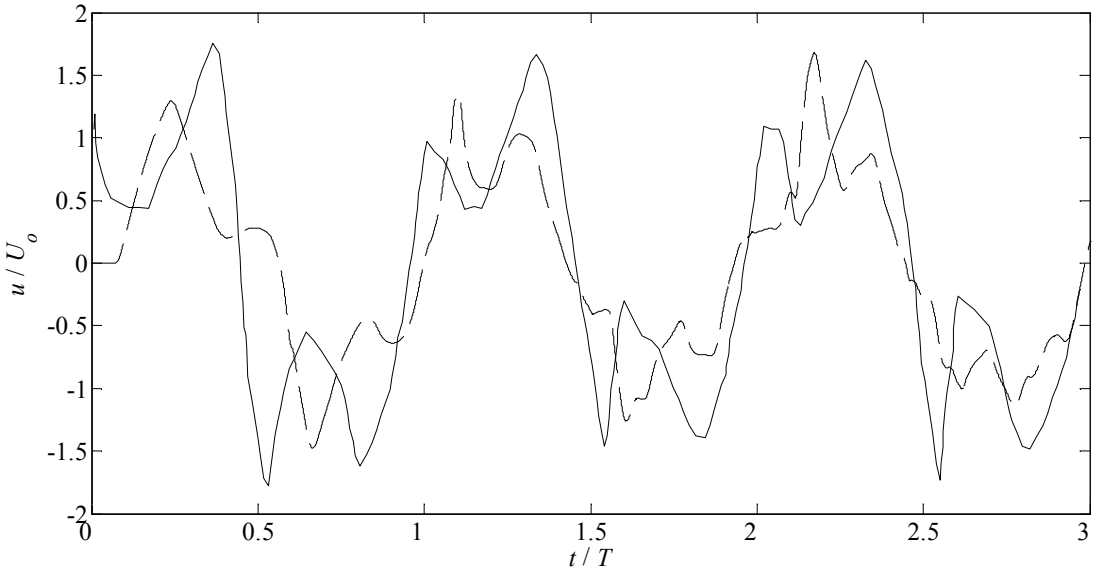


Figure 4.38. Time histories of non-dimensional stream-wise velocity component during 3 tidal periods at $x$ = 0 m and $y$ = -0.45 m at $KC$ = 14.0: experimental data, Lloyd *et al*. [69] (solid line); and numerical predictions by Fluidity-SWE (dashed line).

The above observations accord with those of Stansby [109]. Although the solution of the SWE approximates the flow reasonably well for a vortex shedding wake type, the SWE solver may not provide an accurate model of the flow dynamics of a sinuous wake type. Hence it may be concluded that Fluidity-SWE is capable of modelling oscillatory laminar shallow flows around surface-piercing circular cylinders. However, it may also be necessary to use 3D simulations when modelling the flow dynamics around a surface piercing cylinder for idealised island geometries that lead to a sinuous type of wake.

## 4.9. Power extraction in bounded flow

This section presents verification of the methodology used to estimate power extraction from the flow by the presence of tidal turbines. Verification is performed against two one-dimensional analytical models of power extraction: Bryden and Couch [15]; and Garrett and Cummins [11]. Before presenting the verification tests, the two analytical models are first described separately.

### 4.9.1 The Bryden and Couch model

The model developed by Bryden and Couch [15] (BC2006) computes the water depth and velocity profiles along a hypothetical one-dimensional channel linking two infinite basins. Figure 4.39 is a definition sketch indicating the channel geometry (length, width and depth), and the water head drop along the channel and shear stress due to bed friction. The model assesses the effects of power extraction from the flow on the water depth and velocity profiles along the channel.

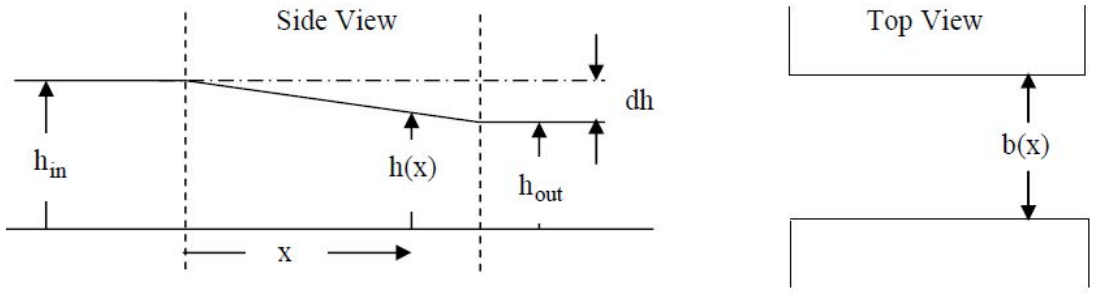


Figure 4.39. Side (left) and top (right) view of a hypothetical channel linking two infinite basins [15].

The momentum of water passing across the channel cross-section area $A$ in an infinitesimal time $\Delta t$ is written as:

$$Momentum = Au^2\rho\Delta t \tag{4.21}$$

where $u$ is the depth-averaged stream-wise velocity component and $\rho$ is the water density. The rate of change of momentum defines the force acting on the mass of water:

$$\frac{D(Momentum)}{Dt} = \frac{\partial}{\partial t}(Au^2\rho)\Delta t + u\frac{\partial}{\partial x}(Au^2\rho)\Delta t \tag{4.22}$$

The change in surface elevation leads to a hydrostatic force per unit area acting on the mass of water expressed as:

$$F_h = -\rho g u \Delta t \frac{\partial h}{\partial x} \tag{4.23}$$

where $g$ is the acceleration due to gravity and $h$ is the local flow depth.
Combining Eqs. (4.22) and (4.23), the momentum equation in a straight channel under steady-state flow conditions including a term to account for energy extraction is written as:

$$u\frac{\partial}{\partial x}(Au^2\rho) = -\rho g u A\frac{\partial h}{\partial x} - uP_{er}(\tau_b + \tau_{add}) \tag{4.24}$$

where $P_{er}$ is the wetted perimeter defined as:

$$P_{er} = b + 2h \tag{4.25}$$

The term $\tau_b$ defines the equivalent frictional stress due to resistance of the seabed and it can be estimated from the following empirical formula:

$$\tau_b = \rho g \frac{Q^2}{b^2h^2}\frac{M^2}{R^{\frac{1}{3}}} \tag{4.26}$$

where $M$ is the Manning friction coeffient and $R$ corresponds to the hydraulic radius of the channel, defined as:

$$R = \frac{bh}{b + 2h} \tag{4.27}$$

The term $\tau_{add}$ is used to represent power extraction from the flow due to the presence of turbine(s). A rate $P_e$ of power extracted from the flow at a stream-wise depth-averaged velocity $u$ adds a retardation force in the flow $F_{TOT}$:

$$F_{TOT} = \frac{P_e}{u} \tag{4.28}$$

The retardation force is converted into a shear stress $\tau_{add}$ as:

$$\tau_{add} = \frac{F_{TOT}}{\Delta x P_{er}} = \frac{P_e}{u \Delta x P_{er}} = \frac{P_e bh}{Q \Delta x P_{er}} \tag{4.29}$$

where $\Delta x$ is the length of the channel where power is extracted by the turbine(s). The power extracted $P_e$ is expressed in terms of the fraction of kinetic power extracted $f_k$ as:

$$P_e = f_k \frac{1}{2} \rho bhu^3 = f_k \frac{1}{2} \rho \frac{Q^3}{b^2 h^2} \tag{4.30}$$

Substituting $P_e$ in Eq. (4.29) results in:

$$\tau_{add} = \frac{1}{2} \frac{f_k \rho Q^2}{\Delta x bh(b + 2h)} \tag{4.31}$$

If conservation of mass $\partial Q / \partial x = 0$ is considered, Eq. (4.24) can be rearranged in terms of the volume flow rate $Q = uA$ as:

$$-\frac{Q^3}{A^3} \frac{\partial A}{\partial x} \rho = -\rho g Q \frac{\partial h}{\partial x} - \frac{Q}{A} P_{er} (\tau_b + \tau_{add}) \tag{4.32}$$

Further manipulation of Eq. (4.32), expressing $A$ in terms of the channel's width $b$ and $h$ leads to:

$$\left(1 - \frac{Q^2}{h^3 b^2 g}\right) \frac{\partial h}{\partial x} = \frac{\partial b_c}{\partial x} \frac{Q^2}{g h^2 b^3} - \frac{1}{\rho g bh} P_{er} (\tau_b + \tau_{add}) \tag{4.33}$$

### 4.9.2 The Garrett and Cummins model

The analytical model derived by Garrett and Cummins [11] (GC2005) assesses the limits to power extraction from a constricted channel linking two infinite ocean basins. The model assumes that the sea elevation at both ends of the channel is not affected by the power extraction within the channel. The equation governing the flow dynamics in a channel of variable cross-section (Figure 4.40) is:

$$\frac{\partial u}{\partial t} + u \frac{\partial u}{\partial x} + g \frac{\partial h}{\partial x} = -F \tag{4.34}$$

where $u$ is the depth-averaged stream-wise flow velocity, $h$ is the depth and $F(x, t)$ represents an opposing force due to natural friction and presence of tidal turbines. If turbines are

deployed filling the entire cross-section of the channel, this term is independent of the cross-sectional position of the turbines.

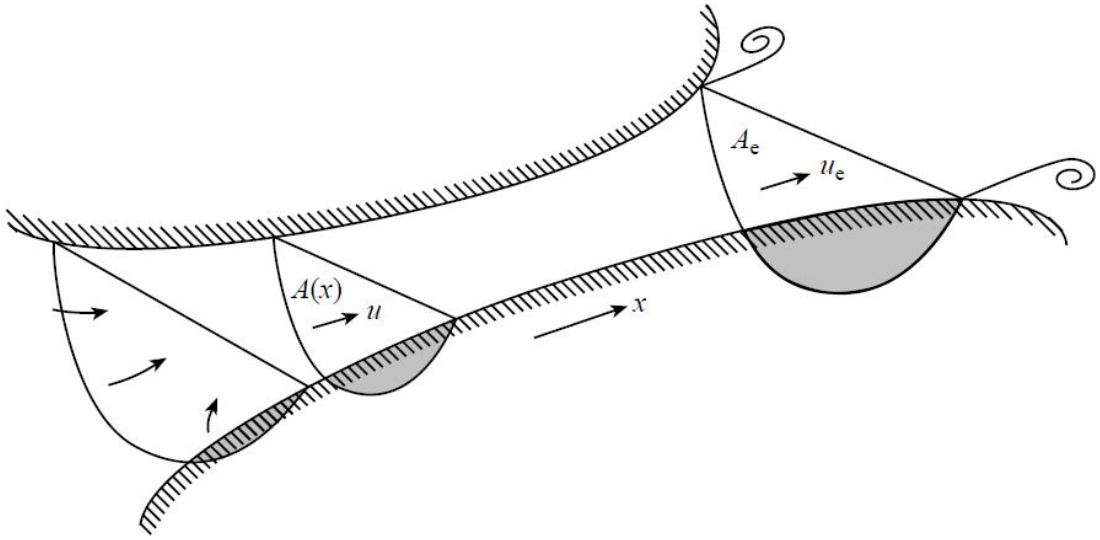


Figure 4.40. Channel connecting two infinite ocean basins with different tidal elevations. Flow velocity $u$ along the channel length $x$ is a function of the channel cross-sectional area $A(x)$. Flow exits the channel at a cross-section area $A_e$ and at a speed $u_e$ [11].

If the length of channel is short compared to the wavelength of the tide, the flux $Au$, where $A$ is the channel cross-sectional area, is independent of $x$ and can be expressed as $Q(t)$. Integrating along the channel, Eq. (4.34) results in:

$$c\frac{dQ}{dt} - g\eta = -\int_0^L F\,dx - \frac{1}{2}u_e|u_e| \tag{4.35}$$

where $c = \int_0^L A^{-1}\,dx$ and $L$ is the length of the channel; $\eta(t)$ is the head difference between the two ocean basins, which is assumed to be independent of the level of extraction $F$ in the channel; and $u_e$ is the velocity at the exit of the channel. Eq. (4.35) accounts for flow separation at the channel exit and associated pressure head loss $1/2\rho u_e^2$. The four terms in Eq. (4.35) account respectively for flow acceleration, sea level difference between the two basins, friction in the channel, and flow separation at the exit of the channel. Provided the natural friction and flow separation terms are small, the flow acceleration is balanced by the sea level difference. The time-dependent head difference is defined as $\eta = a_t \cos\omega_t t$, where $a_t$ and $\omega_t$ are the amplitude and angular frequency of the tidal signal. From Eq. (4.35) the volume flux is $Q = Q_o \sin\omega_t t$, where $Q_o = g a_t (\omega_t c)^{-1}$ and represents the volume flow rate in undisturbed conditions. The average power extracted by the turbines along the channel over a tidal cycle is:

$$P_e = \overline{\int_0^L \rho F Q \, dx} = \rho \overline{Q \int_0^L F \, dx} \tag{4.36}$$

Assuming the drag caused by turbines is linear with respect to the current at any cross-section, Eq. (4.36) may be written as $P_e = \beta \rho \overline{Q^2}$, where $\beta$ is linked to the number of turbines and location along the channel. Then, Eq. (4.35) becomes:

$$c\frac{dQ}{dt} - g a_t \cos \omega_t t = -\beta Q \tag{4.37}$$

The solution of Eq. (4.36) shows that $P_e$ increases initially with $\beta$ but decreases for a high number of turbines as the flow becomes choked. The maximum average power, when $\beta = c\omega_t$, is:

$$P_o = \frac{1}{4}\rho g a_t Q_o \tag{4.38}$$

The maximum average power occurs when the peak flow is reduced to 71 % of the original value and is independent of the cross-section of the channel where extraction is implemented. Assuming the drag caused by turbines is quadratic in current speed, the maximum average power is then 0.97 times the value of $P_o$ found for linear drag.

The effects of natural friction and flow separation at the exit of the channel can be included in the momentum equation by addition of a new term:

$$c\frac{dQ}{dt} - g\eta = -\int_0^L F_{TOT} \, dx - \alpha |Q| Q \tag{4.39}$$

where $\alpha$ includes natural friction and flow separation at the exit of the channel as:

$$\alpha = \int_0^L C_d (hA^2)^{-1} \, dx + \frac{1}{2} A_e^{-2} \tag{4.40}$$

where $A_e$ is the channel cross-sectional area at the exit. In the limit where the acceleration term is unimportant, from Eq. (4.39) it is possible to derive the instantaneous power as:

$$\rho Q \int_0^L F_{TOT} \, dx = \rho Q (g\eta - \alpha |Q| Q) \tag{4.41}$$

Eq. (4.41) has a maximum when $\left(2/3^{3/2}\right)\rho g Q_o \eta$ where $Q_o$ is the volume flux in absence of turbines, expressed as $(g|\eta|/\alpha)^{1/2}$. At this point, the flow is 0.58 of that in the absence of turbines. Averaging Eq. (4.41) over a tidal cycle leads to an average power of:

$$P_1 = 0.21\rho g a_t Q_{max} \tag{4.42}$$

Eq. (4.42) is compared against Eq. (4.38) scaled by 0.97 for the case of quadratic turbine drag, which yields a maximum power of $0.24\rho g a_t Q_o$. This shows that there is only a small variation of the multiplier $\gamma$ from 0.24 to 0.21 (from the case with no background friction to a case where it is dominating). If data in the natural state for head and flux are available, the maximum average power available can be calculated to an accuracy of 10 % using a $\gamma$ = 0.22.

From Eq. (4.41) and the solution of the equation for maximum power extracted, it is possible to derive the following equation:

$$\frac{P_e}{P_{max}} = \left(\frac{3^{3/2}}{2}\right)\left(\frac{Q}{Q_o}\right)\left(1 - \left(\frac{Q}{Q_o}\right)^2\right) \tag{4.43}$$

Using Eq. (4.43), Figure 4.41 plots the ratio of power extracted to maximum power extractable against the ratio of actual to undisturbed volumetric flow rate in a channel connecting two ocean basins. The maximum extractable power $P_{max}$ is achieved when the volume flux is equal to 57.7 % of the undisturbed volume flux.

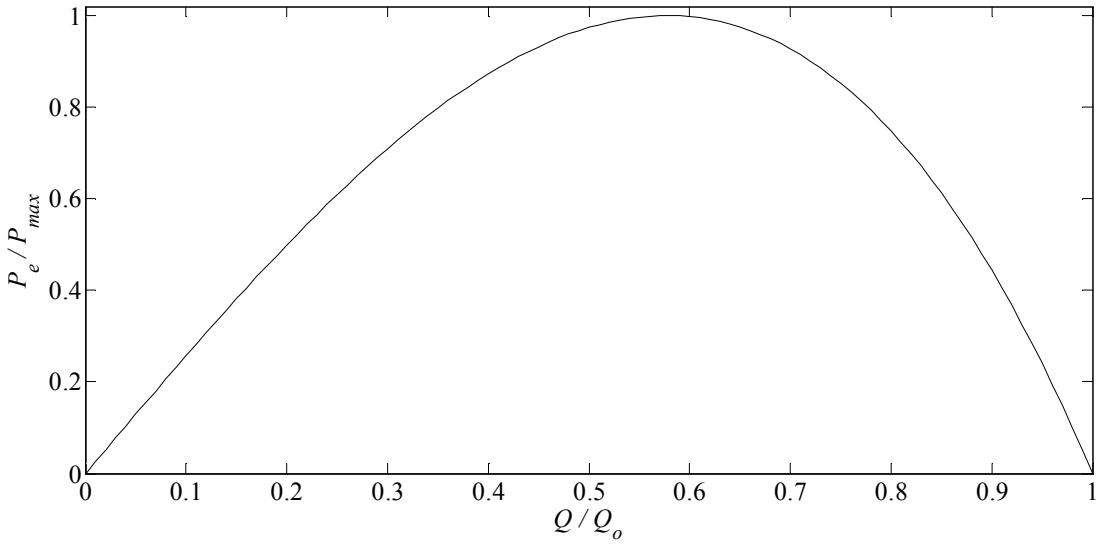


Figure 4.41. Extractable power in a channel connecting two infinite ocean basins predicted by GC2005 as a function of the volume flux through the channel.

### 4.9.3 Numerical model predictions

The Fluidity model has been used to verify the power extraction methodology by comparison against analytical solutions of the BC2006 and GC2005 one-dimensional models. The flow domain is rectangular, with length $L$ = 10,000 m, width $B$ = 2,000 m and water depth $h$ = 40 m. Open boundary conditions are applied at its west and east boundaries, along with a prescribed initial free surface gradient of $0.0125h$ from west to east. The north and south boundaries are solid walls represented by slip conditions with a quadratic drag applied at the walls. A Manning friction coefficient of 0.035 $sm^{-1/3}$ is used to characterise the bed and wall friction.

A regular triangular mesh with element size $0.005L$ in the stream-wise direction and $B$ size in the transverse direction is used (Figure 4.42). Discretisation of the transverse section over one element reduces a two-dimensional problem to one dimension. Power extraction takes place at the longitudinal centre of the channel located at $x \in (0.49L, 0.51L)$ over a length $0.02L$ and across the entire width of the channel $B$. Power extraction is implemented through the distributed drag volumetric momentum sink approach as detailed in Section 3.2.2.

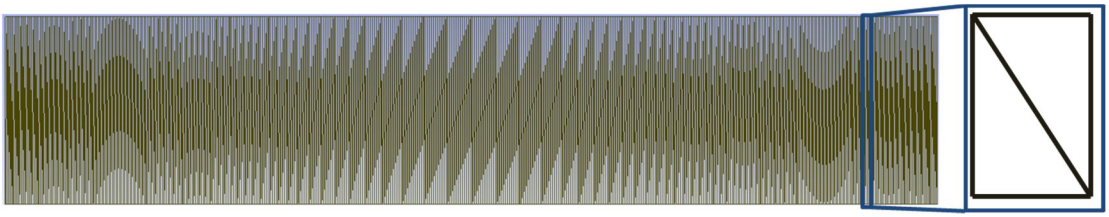

Figure 4.42. Channel mesh with one grid element of size $B$ in the transverse direction and $0.005L$ size grid elements in the stream-wise direction.

This section first compares the results obtained with Fluidity against those predicted by the one-dimensional analytical model by BC2006. Two cases are considered: first in the absence of power extraction, and then with a 10 % kinetic power extraction from the flow. The second part compares the numerically-computed extractable power and reduction of volume flow rate from a channel linking two infinite ocean basins against the predicted values by GC2005.

#### 4.9.3.1 Verification against Bryden and Couch model

First, the Fluidity model (Figure 4.42) is run in the absence of power extraction with the set-up conditions specified in Section 4.9.1. Figure 4.43 and Figure 4.44 compare the

numerically computed profiles of free surface and velocity along the channel computed by Fluidity against those predicted by the one-dimensional analytical model from BC2006. It can be observed that Fluidity predicts correctly the changes in stream-wise free surface and velocity profiles induced by the frictional forces at bottom and sides of the channel.

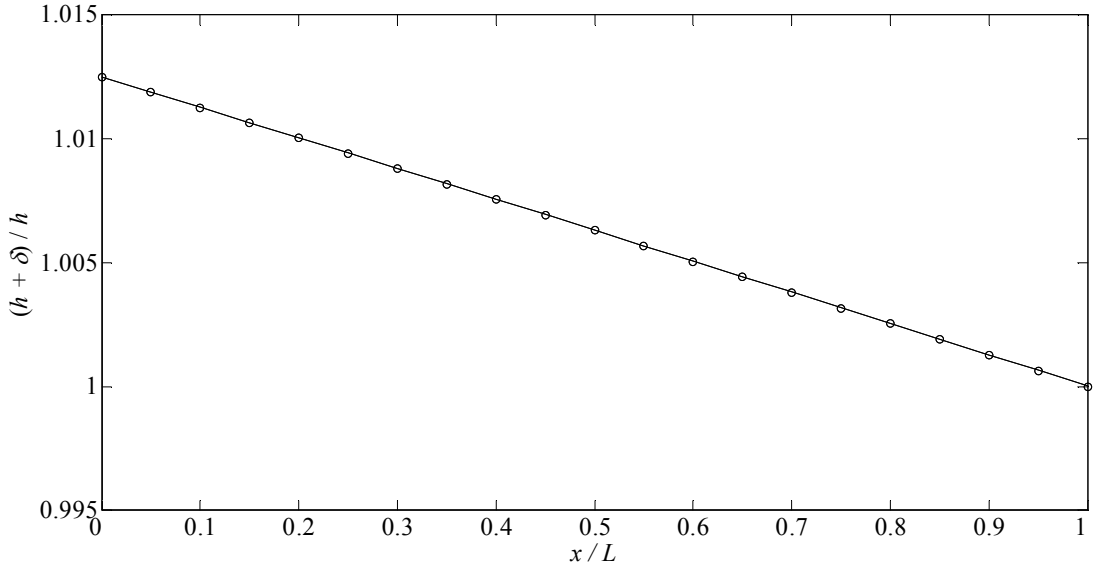


Figure 4.43. Free surface profile along the one-dimensional channel predicted by BC2006 (solid line) and computed with Fluidity (circle).

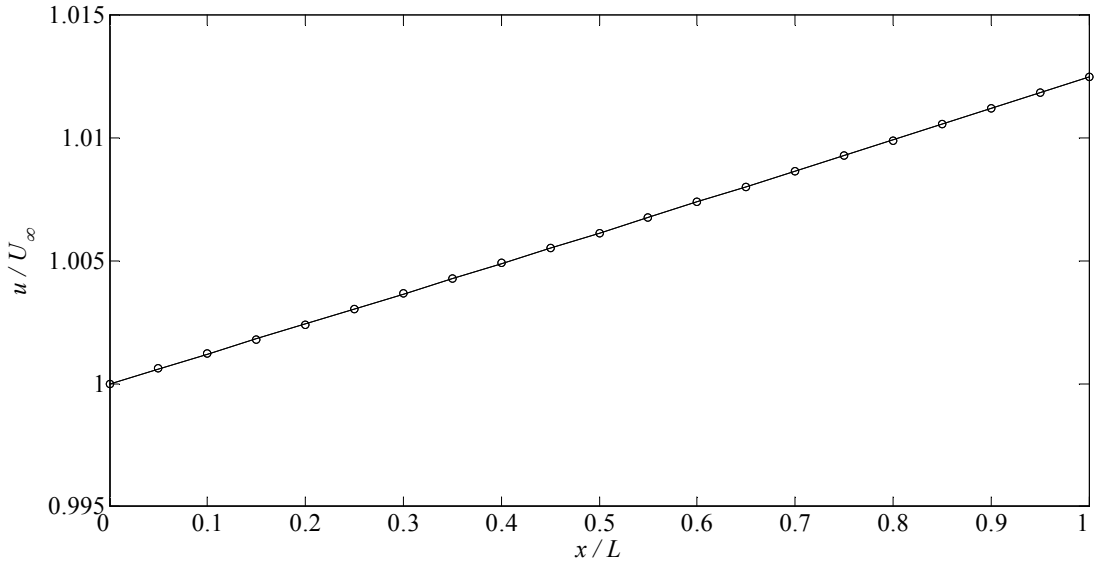


Figure 4.44. Velocity profile along the one-dimensional channel predicted by BC2006 (solid line) and computed with Fluidity (circle).

The BC2006 model is next run considering a 10 % kinetic power fraction extracted from the flow ($f_k$ = 0.1 in Eq. (4.30)). Figure 4.45 and Figure 4.46 compare respectively the predicted free surface and stream-wise velocity profiles along the channel by the BC2006 model and those by Fluidity with power extraction. Good agreement is achieved between the numerical and analytical values.

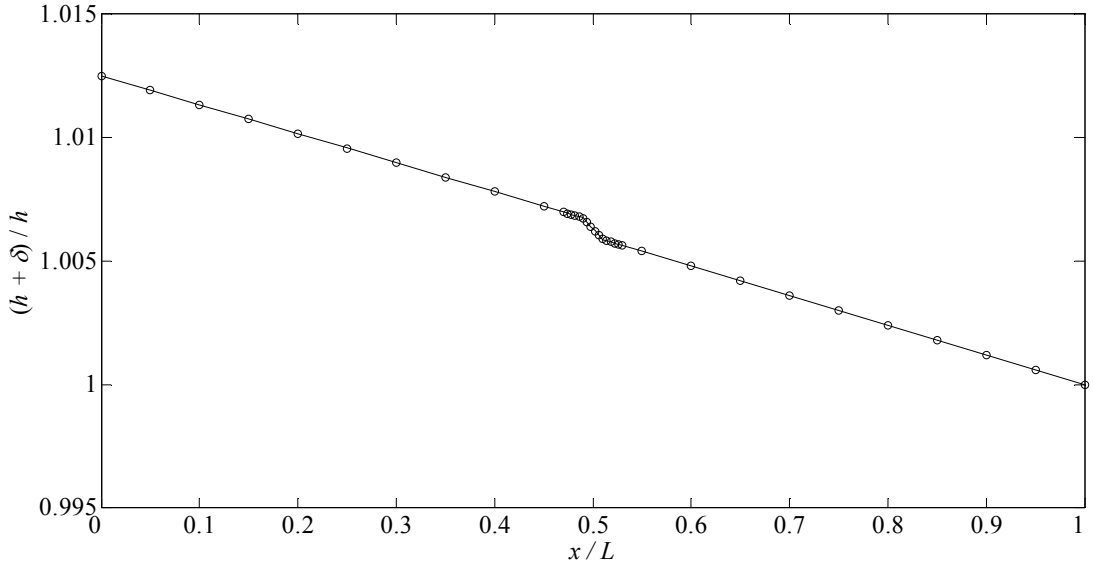


Figure 4.45. Comparison of free surface profile along the channel derived from BC2006 analytical model (solid line) and computed with Fluidity for 10 % of kinetic power extracted from the flow (circle).

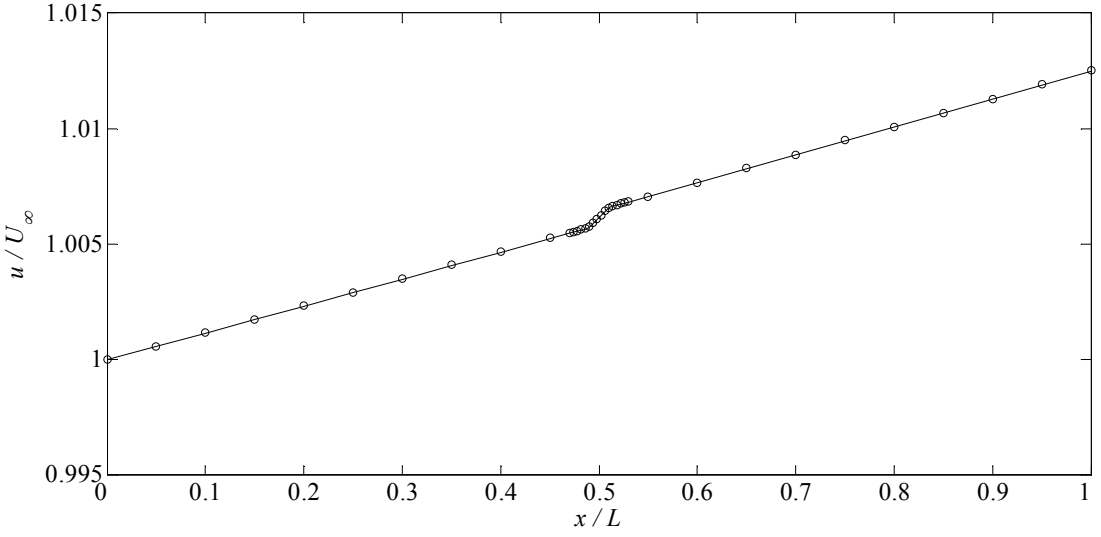


Figure 4.46. Comparison of stream-wise velocity profile along the channel derived from BC2006 analytical model (solid line) and computed with Fluidity for 10 % of kinetic power extracted from the flow (circle).

In addition, the absorption term is converted into an equivalent seabed friction coefficient as described in Section 3.2. This is added to the natural friction coefficient at the area of power extraction $A_f$. The free surface and velocity profiles are identical to those obtained from the addition of an absorption term shown in Figure 4.45 and Figure 4.46.

#### 4.9.3.2 Verification against Garrett and Cummins model

The model presented in Section 4.9.3 is now run in the presence of power extraction at $x \in (0.49L, 0.51L)$ implemented by addition of an absorption term in the momentum equations, which is distributed uniformly and gradually increased. The model is also run with power extraction implemented as an enhanced seabed drag $k_f$ which is added to the natural friction coefficient at the area of power extraction $A_f$. Figure 4.47 plots the extracted power from the channel and volume flux changes against $k_f$ computed as:

$$P_e = \rho \int k_f u^3 \, dA_f \tag{4.44}$$

Maximum extracted power is achieved in both cases when $k_f$ = 1.88 and the volume flux is reduced to 57.7 %, which corresponds to the value predicted by GC2005. Similarities between both approaches in accounting for power extraction were also observed by Zang and Wang [99] for a channel linking a semi-enclosed bay with an infinite ocean basin.

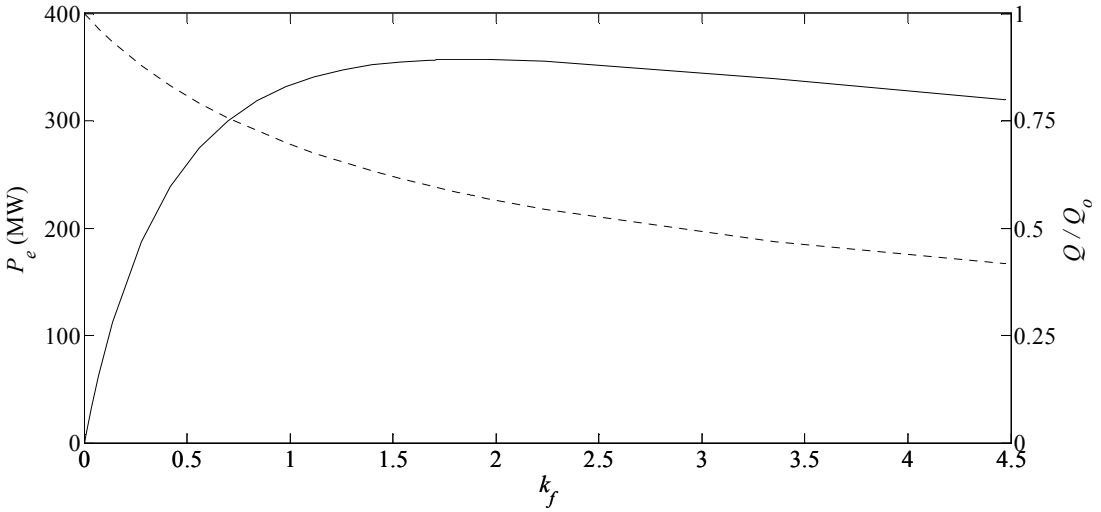


Figure 4.47. Extracted power and changes in volumetric flow rate as a function of the enhanced bottom drag $k_f$ in the area of power extraction. The solid line represents the extracted power (scale on left) and dotted line represents the actual to undisturbed volumetric flow rate (scale on right).

A sensitivity analysis of the power extracted to the area where power extraction is carried out for two arrays of lengths $0.04L$ and $0.004L$ and widths equal to the channel width. In both cases, the maximum extracted power is 357.3 MW and matches the results obtained for an array located between $x$ coordinates $0.49L$ and $0.51L$.

The methodology employed for power extraction does not account for losses due to support structure drag and mixing around tidal turbines [149]. Thus, the present methodology provides an upper limit to power extraction and the power available for turbines for generation will be lower than the peak presented in Figure 4.47.

## 4.10. Power extraction in unbounded flow

Section 4.9 presented verification of the methodology employed to account for power extraction in the numerical model against the one-dimensional analytical models from BC2006 and GC2005. Both analytical models are based on bounded flows through a channel with extraction across the whole cross section of the channel. This section expands the verification carried out in Section 4.9 to power extraction in unbounded flows, where flow can effectively bypass the tidal array.

Garrett and Cummins [142] (GC2013) extended the one-dimensional channel analysis [11] into two-dimensions and investigated the maximum power that can be obtained from a confined circular array of turbines in an unbounded steady tidal flow. GC2013 concluded that the maximum power extracted from the circular array depends on the term that dominates the momentum equations: friction, advective terms or acceleration. GC2013 employed two-dimensional shallow water equations and represented the tidal array by a uniform local increase in bottom friction. GC2013 simplified the two-dimensional shallow water equations approximating the free surface as a rigid lid. This simplification is acceptable when the domain scale is smaller than the wavelength of a tidal signal, that is where variations in free surface $\delta$ are very small compared to the still water level $h_o$.

Under steady flow conditions both acceleration and inertial terms from the shallow water equations may be neglected. A linear bottom friction $c_o$ is implemented over the entire domain except a circle of radius $R_f$ where bottom friction is equal to $c_o + c_t$, where $c_t$ represents the added linear friction due to the presence of the turbines. A far-field current $U_\infty$ in the stream-wise direction is considered.

The power extracted $P_e$ by the tidal turbines is computed as the integral of the fluid inside the circle, turbine drag ($c_t$ times local speed) and local speed.

$$P_e = \rho h_o \pi R_f^2 c_t \frac{4c_o^2 U_\infty^2}{(c_t + 2c_o)^2} \tag{4.45}$$

Maximum $P_e$ is achieved when $c_t = 2c_o$. If the dimensionless parameter $\xi = U_\infty/(c_o R_f)$ is considered, the maximum dissipation in the circular tidal array can be written as:

$$P_{e,max} = \rho h_o R_f^2 c_o U_\infty^2 F(\xi) \tag{4.46}$$

The function $F(\xi)$ is unknown but tends to $\pi / 2$ when $\xi \to 0$. For finite $U_\infty$ and $R_f$, the parameter $\xi$ becomes very large for very small values of $c_o$, and at this limit the maximum power extracted by the array is independent of the value $c_o$. This is possible when $F(\xi)$ and $\xi$ present a linear proportionality. The linear constant of proportionality between $F(\xi)$ and $\xi$ is obtained from the determination of $P_e^*$ in Eq. (4.46) from the numerical solution of the two-dimensional problem.

The setup of the numerical model follows the parameterisation of GC2013. A rectangular domain of length and width $20.5R_f$ is defined, where $R_f$ is the radius of the circular patch of enhanced bottom friction, equal to 1,000 m. The circular tidal array is centred across the domain and one-third downstream from the west boundary. The rectangular domain is defined with inflow/outflow conditions, constant inlet stream-wise velocity $U_\infty = 1$ m/s at the west limit and zero pressure at the east limit. The north and south limits of the domain are set with a free-slip condition. Water depth in the domain is set to $0.01R_f$. The linear bottom friction $c_o$ is defined by the dimensionless parameter $\xi$ as $c_o = U_\infty/\xi R_f$. The flow dynamics in the model are solved using the SWE with free surface.

The numerical model is initialised with flow velocity $U_\infty$ and run until changes in the velocity field reduced to below $10^{-3}$ m/s. GC2013 used a regular grid with 1,025 grid points in both $x$ and $y$ directions, the resulting grid containing more than one million elements. Here a mesh convergence study is carried out to determine the grid resolution that ensures a sufficiently accurate approximation to the solution whilst remaining computationally efficient. The domain is divided into two mesh regions: inside and outside of the tidal array. Table 4.13 includes the three mesh cases considered, their element-edge length and total number of mesh elements.

| | Element edge length | | |
|---|---|---|---|
| Mesh | Circular tidal array | Rectangular domain | Mesh elements |
| 1 | $\frac{\pi R_f}{50}$ | $\frac{20.5R_f}{25}$ | 6,594 |
| 2 | $\frac{\pi R_f}{100}$ | $\frac{20.5R_f}{25}$ | 14,908 |
| 3 | $\frac{\pi R_f}{200}$ | $\frac{20.5R_f}{25}$ | 43,020 |

Table 4.13. Three spatial discretisation cases considered in the mesh convergence analysis of the GC2013 model element edge length used in the two mesh regions of the model, and total number of mesh elements.

Figure 4.48, Figure 4.49 and Figure 4.50 plot the domain cross-sectional non-dimensional stream-wise velocity component profiles at the entrance ($x = -R_f$), centre ($x = 0$) and exit ($x = R_f$) of the circular array.

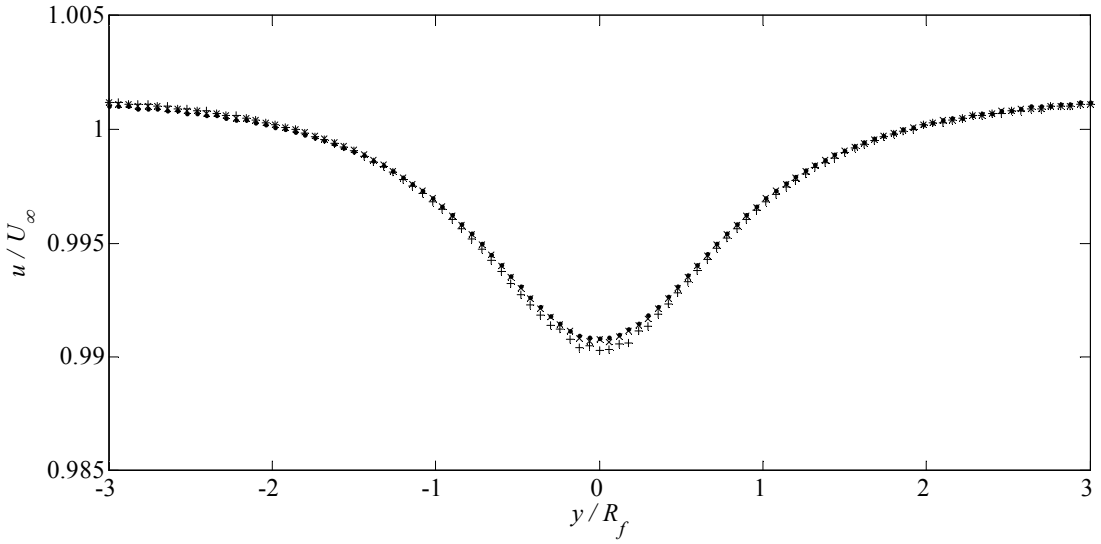


Figure 4.48. Transverse profiles of non-dimensional stream-wise velocity at the entrance of the circular array from Mesh 1 (plus sign), Mesh 2 (cross), and Mesh 3 (point).

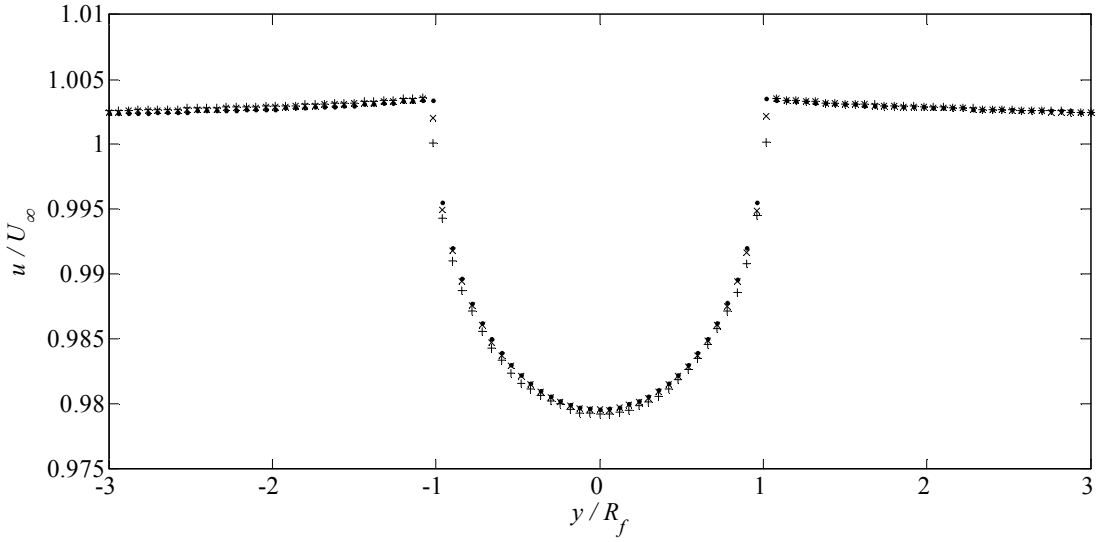


Figure 4.49. Transverse profiles of non-dimensional stream-wise velocity at the centre of the circular array from Mesh 1 (plus sign), Mesh 2 (cross) and Mesh 3 (point).

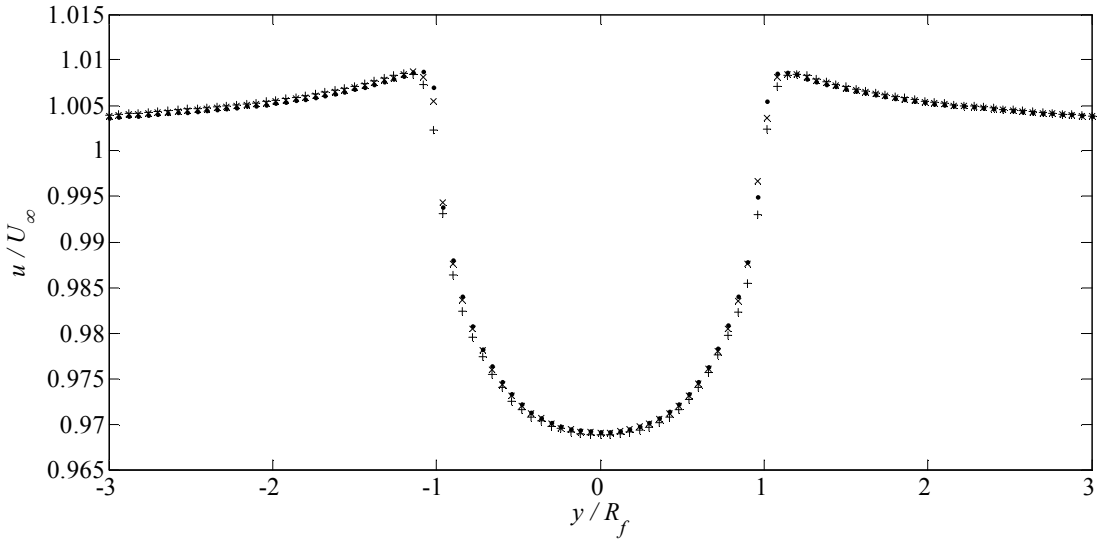


Figure 4.50. Transverse profiles of non-dimensional stream-wise velocity at the exit of the circular array from Mesh 1 (plus sign), Mesh 2 (cross) and Mesh 3 (point).

Solution convergence is reached for Meshes 2 and 3, and so Mesh 2, depicted in Figure 4.51, is chosen to discretise spatially the domain.

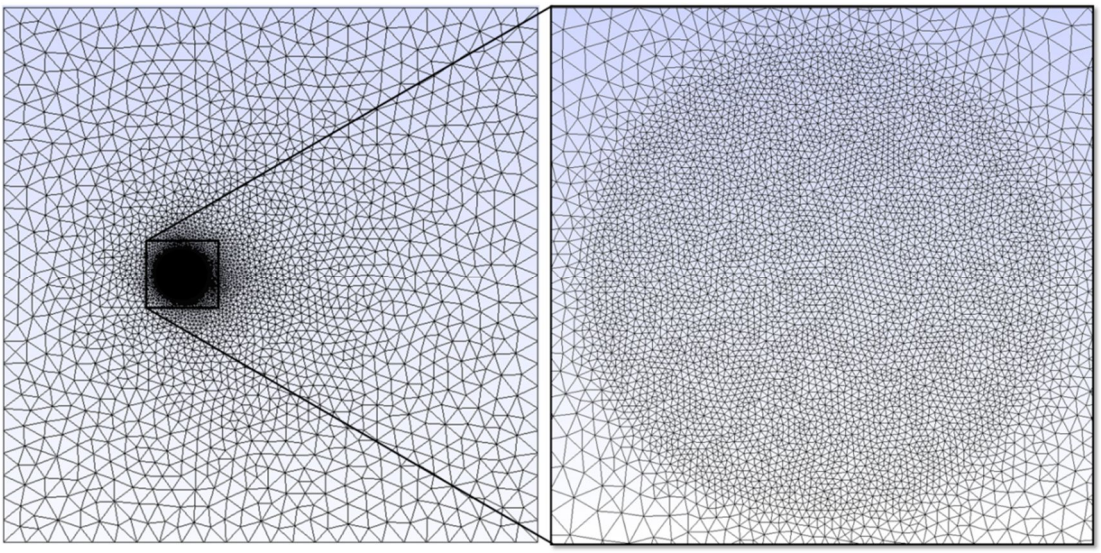

Figure 4.51. Unstructured spatial discretisation of the GC2013 domain on Mesh 2: full domain (left); and circular farm area (right).

$F(\xi)$ is determined from Eq. (4.46) for $\xi$ = 0.5, 1, 2, 4, 10, 15 and 20. For each $\xi$ case, the constant of proportionality $\alpha$ between $c_o$ and $c_t$ is gradually increased from 0.5 to 20 to determine the maximum ratio between power dissipated by the tidal array and power naturally dissipated by bottom friction in the circular area in the absence of the array.

The power dissipated by the tidal array is computed as follows:

$$P_e = \rho h \int c_t \, (u^2 + v^2) \, dA_f \tag{4.47}$$

where $h$ is the total water depth. The function $F(\xi)$ numerically computed with Fluidity is plotted in Figure 4.52 and compared against the linear fit $F(\xi) = 1.6 + 0.7\xi$ derived by GC2013 as a fit to their numerical results. The Fluidity computed $F(\xi)$ values agree reasonably well with those obtained by GC2013. The slight differences can be explained by the assumption of rigid lid in the shallow water equations considered by GC2013, while here the shallow water equations are solved considering a free water surface.

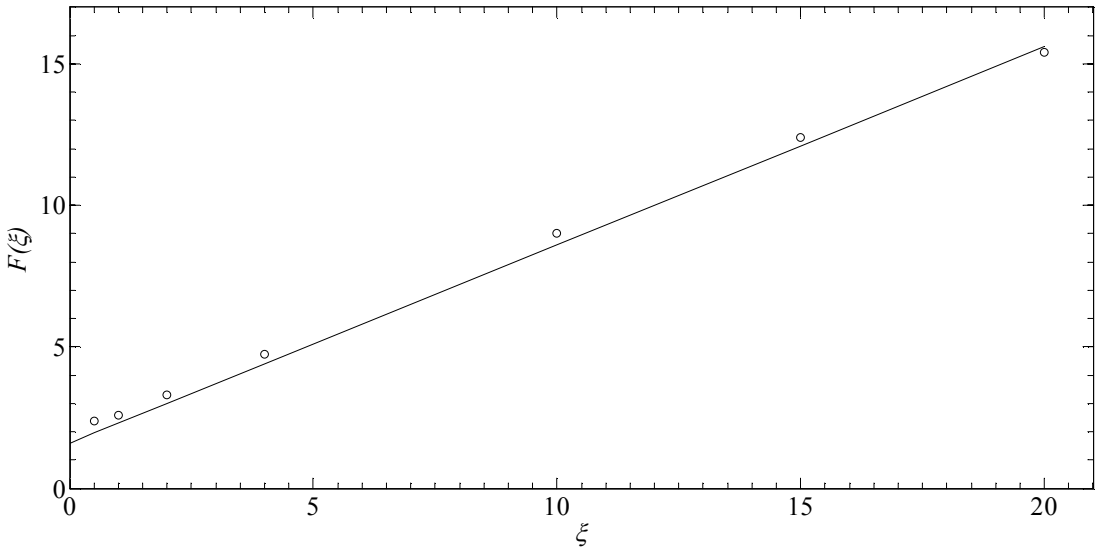


Figure 4.52. Function $F(\xi)$ numerically computed by GC2013 (solid line) and by Fluidity (circle).

Figure 4.53 shows the vorticity plot and streamlines in the wake of the circular array computed with Fluidity at maximum ratio of power extraction for $\xi = 20$. Both plots agree reasonably well with those derived by GC2013. An increase in mesh resolution is required to resolve the vorticity structures behind the circular array.

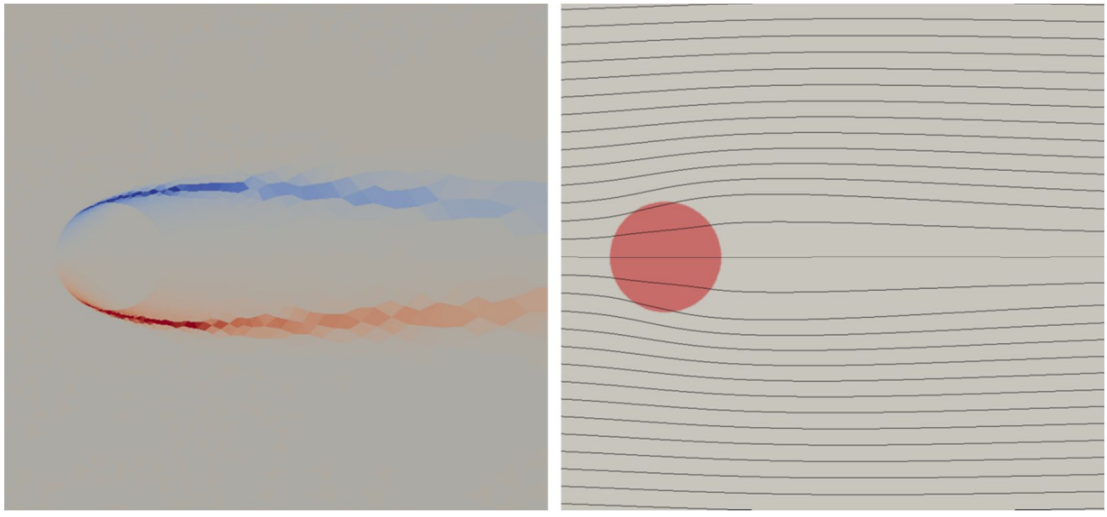

Figure 4.53. Vorticity plot (left) and streamlines (right) in the wake of the area with enhanced drag computed with Fluidity at maximum power extracted with $\xi = 20$.

## 4.11. Summary

This chapter has presented the results of verification and validation tests concerning the capability of Fluidity to model representative flows, leading to tidal resource assessment for a strait between an island and a landmass using the finite element method numerical code Fluidity.

Section 4.2 verified that Fluidity effectively accounts for local changes in flow depth against the analytical solution of flow over a submerged hump. After completion of mesh convergence tests, Sections 4.3 and 4.4 verified that Fluidity's solution is in agreement with potential flow theory for inviscid flow past a circular cylinder in the centre of a wide channel and in the vicinity of a wall. Through the modification of the kinematic viscosity, Sections 4.5, 4.6 and 4.7 satisfactorily validated the physics modelled in Fluidity to simulate impulsively-started flow past a submerged circular cylinder at Reynolds numbers 40, 100 and 5,000. It was found that Fluidity correctly modelled the mechanisms of early stage wake formation for $Re$ = 40 and $Re$ = 100. Section 4.7 included a visual comparison of streamlines behind a circular cylinder at $Re$ = 5,000 against high resolution laboratory flow visualisations. Section 4.8 validated Fluidity-SWE for flow past a surface-piercing circular cylinder in oscillatory laminar shallow flow. Predictions by Fluidity-SWE for a vortex shedding wake and a sinuous wake with pairing were validated against experimental data. The vortex-shedding wake case was also modelled by solving the unsteady 3D Navier Stokes equations and results are in good agreement with those from Fluidity-SWE. Section 4.9 satisfactorily verified the power extraction methodology in bounded flows implemented in Fluidity against two one-dimensional analytical models. Section 4.10 extended the verification of the power extraction methodology to unbounded flows. After a process of mesh convergence, the power extraction methodology was adequately verified in two-dimensional domains against analytical and numerical solutions.

The next chapter uses the present numerical methodology to characterise the tidal resource in a strait between a strait and a landmass.

# 5. Tidal resource in strait between island and landmass

## 5.1. Introduction

This chapter presents the results obtained from the numerical analysis of the idealised site defined as an island in the vicinity of a landmass based on the resource assessment methodology verified and validated in Chapter 4. The present chapter analyses the sensitivity of the extracted power in the coastal site and site flow dynamics to: the island, strait geometry and relative position of island with respect to landmass (Figure 2.1); boundary condition at the island and landmass; bathymetry in strait and offshore of the island; eddy viscosity; bed friction; and the power extraction parameterisation and location. The effect of the island geometry on the limit to power extraction is assessed against the analytical predictions of a channel linking two infinite ocean basins by GC2005. This chapter is structured in three sections. Section 5.2 details the set-up of the numerical model of the coastal site. Section 5.3 presents the results of the sensitivity analysis carried out for the strait between and island and landmass. Section 5.4 summarises the conclusions derived from the analysis of this type of coastal site.

## 5.2. Setup of numerical model

This section presents the parameterisation and mesh convergence of the numerical model of the island in the vicinity of a landmass.

### 5.2.1 Geometry and parameterisation of the model

Figure 5.1 shows the model geometry used in the numerical assessment of the island in the vicinity of a landmass, hereby referred as the island-landmass system. The rectangular domain is defined by a length $L$ and width $B$. The width of the domain $B$ is chosen so that it enables the free-stream velocity $U_\infty$ to be attained at the north boundary, far from the island. The island geometry is elliptical with length $L_i$ and width $B_i$. The island is centred midway along the domain in the stream-wise direction. The parameter $s$ defines the width of the strait.

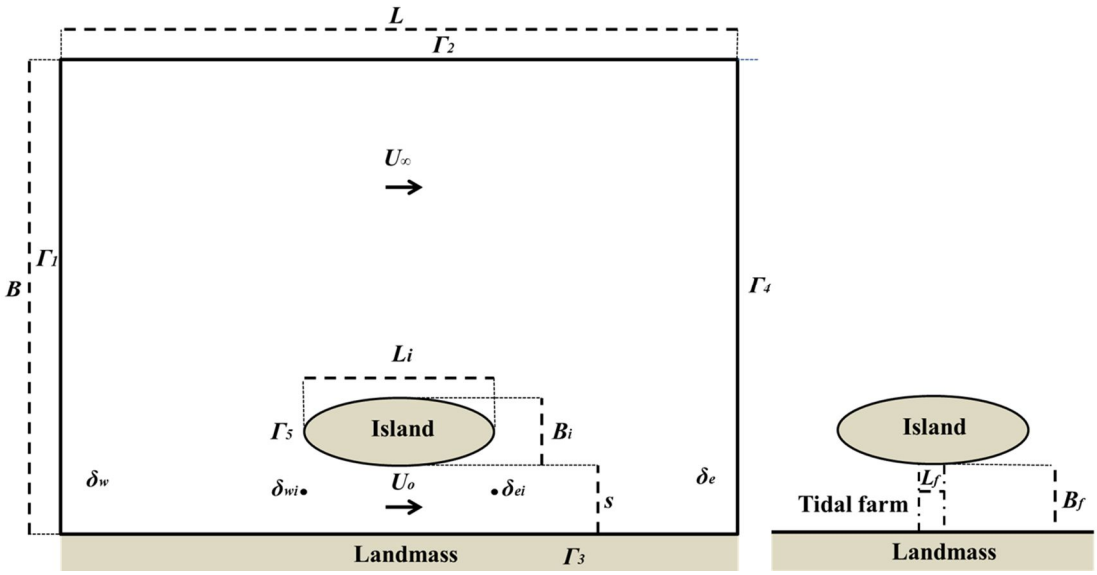


Figure 5.1. Definition sketch for a strait between island and landmass, a) model geometry and tidal parameters; and b) geometry and location of the tidal farm.

The domain encompasses five boundaries: open west and east boundaries $\Gamma_1$ and $\Gamma_4$; solid north and south boundaries $\Gamma_2$ and $\Gamma_3$, the latter representing the landmass; and a solid boundary $\Gamma_5$ which represents the island. The strait is defined by boundaries $\Gamma_3$ and $\Gamma_5$. The variable $U_o$ defines the cross section flow velocity midway along the strait. The water surface elevations at boundaries $\Gamma_1$ and $\Gamma_4$ are denoted by $\delta_w$ and $\delta_e$. The water surface elevations at the west and east ends of the strait are denoted by $\delta_{wi}$ and $\delta_{ei}$. The area of power extraction, herein referred as the tidal farm, is located at the narrowest part of the strait, and has a plan-form geometry defined by a length $L_f$ and width $B_f$.

Figure 5.2 shows the water depth contours throughout the domain. Unless otherwise stated, the water depth $h$ in the domain is fixed at 40 m in the stream-wise direction between cross sections located $0.36L$ upstream and downstream of the centre of the island. The water depth is linearly increased from $h$ to $75h$ in the stream-wise direction from cross sections located $0.36L$ to $0.43L$ upstream and downstream of the island's centre. In the remaining part of the domain, the water depth is kept at $75h$. Offshore deep water conditions at open boundaries have been used to represent continental shelf domains (Section 3.3.5).


Figure 5.2. Water depth contours in the island landmass domain.

A zero surface elevation condition is set at $\Gamma_4$. The surface elevation at $\Gamma_1$ is set to an $M_2$ tidal constituent:

$$\delta_w = a_o a \sin(\omega_t t) \tag{5.1}$$

where $a$ and $\omega_t$ is the amplitude and frequency of the $M_2$ tidal wave (3 m and 1.41 x $10^{-4}$ rad/s respectively). As in Section 4.3, in order to minimise the formation of numerical perturbations at $\Gamma_1$ that will propagate through the domain during the simulation, the tidal signal is ramped up in the first two tidal cycles with the parameter $a_o$:

$$a_o = 0.5\left(1 - \cos\left(\frac{\omega_t t}{4}\right)\right) \tag{5.2}$$

A free-slip condition is applied at the north solid boundary $\Gamma_2$ so as not to affect flow dynamics past the island, and to allow a free-stream velocity to be achieved north of the island. The landmass $\Gamma_3$ and island $\Gamma_5$ are allocated the same boundary conditions: either free-slip or no-slip. The use of a free-slip boundary condition at the island and coastline reduces the scale of complexity of the analysis and enables the characterisation of the strait resource based on a parameter sensitivity study. However, Section 4.8 showed that in order to capture the wake of a surface piercing circular cylinder, representing an island, a no-slip boundary is necessary. It should be noted however that the geometries of real islands differ from a perfectly circular shape and can lead to completely different flow dynamics. Unless otherwise stated, the seabed friction is characterised by the dimensionless coefficient $C_d$ = 0.0025. When modelling real coastal sites, seabed friction is generally employed as a calibration parameter [51]. The value chosen in this study is commonly used in coastal modelling [48] and lies within the range of friction coefficients assessed for the Pentland Firth between 0.001 and 0.005 [94].

Turbulence is modelled using the depth averaged parabolic eddy viscosity empirical model [92] (Section 3.2). Other parameters that could impact on the resource estimates, such as Coriolis force, pressure, wind or wave conditions, are not included in the numerical model as these are considered to be site-dependent. The time step is chosen accordingly to limit the *CFL* number to within O(1).

### 5.2.2 Spatial discretisation of the numerical model

A mesh convergence analysis is carried out with a circular island ($L_i = B_i = Ø_i$) and strait width $s = L_i$ for the free-slip and no-slip scenarios under steady state conditions with the flow travelling from west to east of the domain. Mesh independence is sought through studying six cases with varying mesh-edge lengths, described in Section 4.3, and presented in Table 5.1. Due to the oscillatory nature of tidal flows, to be investigated later, identical mesh edge lengths are used upstream and downstream of the island. A different mesh edge length is defined at the north of the rectangular domain, where an increase in the spatial resolution does not impact the resource assessment in the strait.

| | Element edge length | | | | |
|---|---|---|---|---|---|
| Mesh | South domain upstream and downstream from island | | Island | North domain | Mesh elements |
| | $> 2Ø_i$ | $\leq 2Ø_i$ | | | |
| 1 | $\pi Ø_i /6$ | $\pi Ø_i /6$ | $\pi Ø_i /12$ | $\pi Ø_i$ | 3,902 |
| 2 | $\pi Ø_i /6$ | $\pi Ø_i /6$ | $\pi Ø_i /28$ | $\pi Ø_i$ | 6,156 |
| 3 | $\pi Ø_i /17$ | $\pi Ø_i /28$ | $\pi Ø_i /36$ | $\pi Ø_i$ | 9,968 |
| 4 | $\pi Ø_i /17$ | $\pi Ø_i /36$ | $\pi Ø_i /76$ | $\pi Ø_i$ | 13,658 |
| 5 | $\pi Ø_i /17$ | $\pi Ø_i /76$ | $\pi Ø_i /156$ | $\pi Ø_i$ | 27,498 |
| 6 | $\pi Ø_i /17$ | $\pi Ø_i /156$ | $\pi Ø_i /316$ | $\pi Ø_i$ | 62,526 |

Table 5.1. Six spatial discretisation cases considered in the mesh convergence analysis. Element edge length used in the three mesh regions of the model, and total number of mesh elements.

Mesh convergence is carried out for the free-slip and no-slip scenarios through the analysis of the stream-wise velocity profile at four cross sections through the domain, which are defined in Figure 5.3. Meshes 1 and 2 are not included in the analysis because results from Section 4.3 showed that their resolution was insufficient to resolve the flow dynamics past a cylinder.

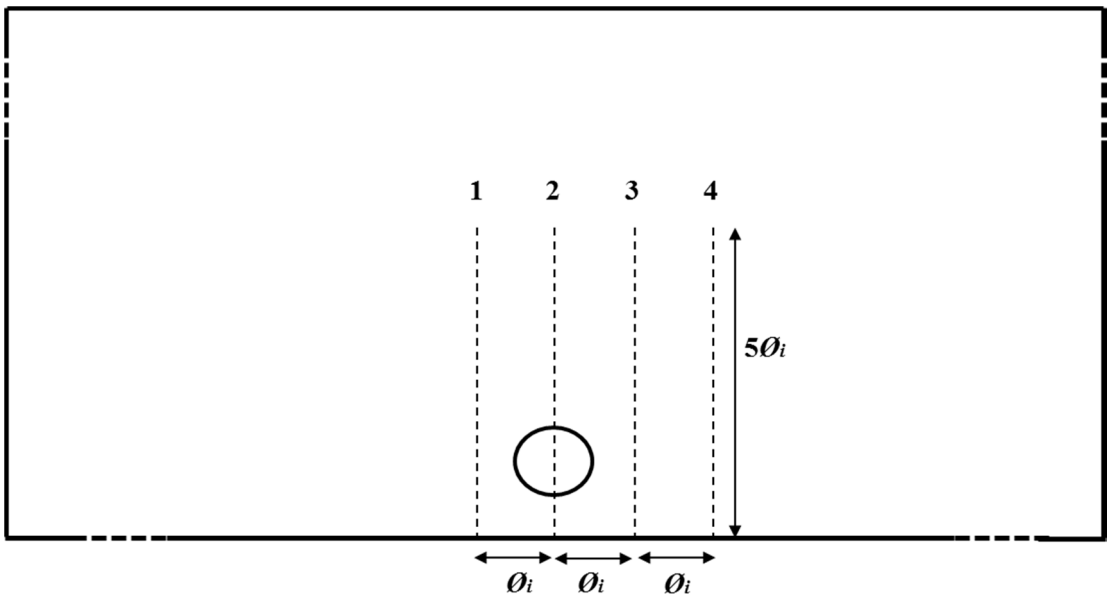


Figure 5.3. Four domain cross-sections of length $5Ø_i$ north of landmass used in mesh convergence analysis.

As in Section 4.5, non-dimensional time $t^*$ is defined as $t \cdot U_\infty / Ø_i$. Following Section 4.3, the solution was considered to converge when the temporal variation from one time step to the next in the velocity field fell below $10^{-3}$ m/s. The stream-wise velocity is extracted at $t^* = 44$, when the solution was fully converged. Cross-sectional stream-wise velocity profiles for the free-slip scenario at sections 1-4 are presented in Figure 5.4, Figure 5.5, Figure 5.6 and Figure 5.7 respectively. From the plots, it is possible to observe that mesh independence is achieved for Mesh 4, in accordance with the conclusions in Section 4.3.

For the no-slip scenario, Figure 5.8 and Figure 5.9 show the stream-wise velocity profile at cross sections 2 and 4 respectively. At section 2 in the strait, mesh convergence is again achieved using Mesh 4. However, Figure 5.9 shows that convergence of the velocity field on cross section 4 has not been achieved and a further increase in mesh resolution is required to resolve the wake behind the island. Although the wake behind the island is not accurately captured in the no-slip scenario, the results from the validation test of flow past a surface piercing circular cylinder in Section 4.8 show that Mesh 4 is able to capture the main flow features around the island.

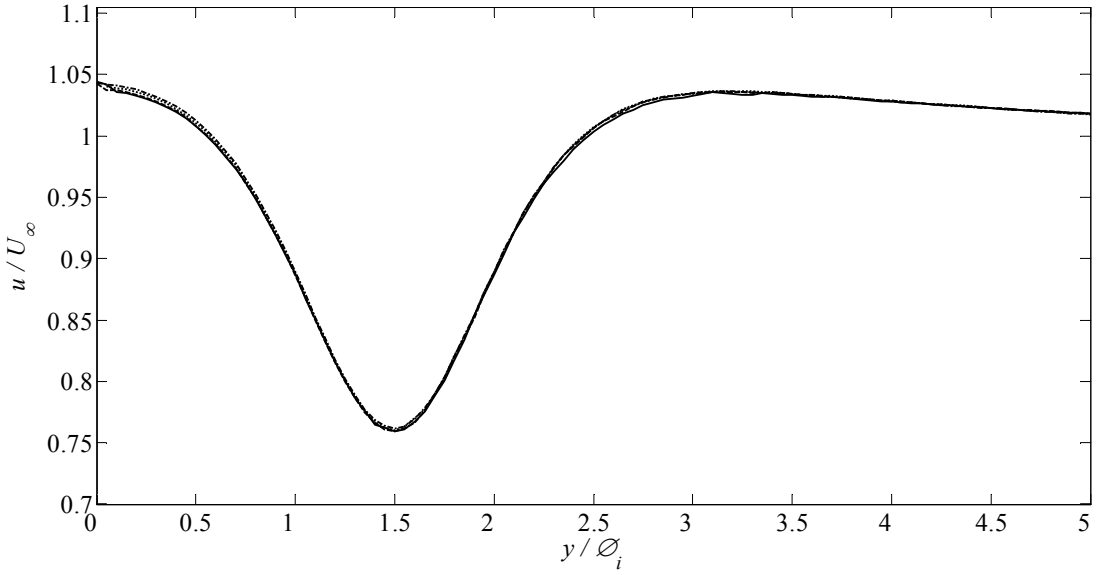


Figure 5.4. Stream-wise flow velocity profile at cross-section 1, one diameter upstream from the centre of the circular island. The model is run with free-slip boundary conditions at island and coastline. Fluidity predictions for Mesh 3 (solid line), 4 (dashed line), 5 (dotted line) and 6 (dash-dot line).

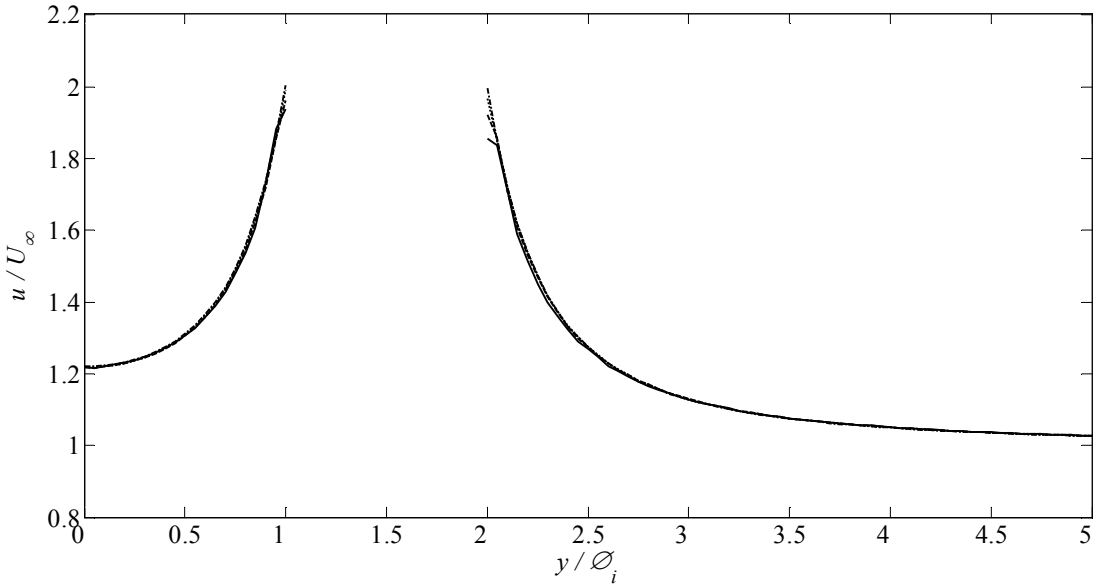


Figure 5.5. Stream-wise flow velocity profile along cross section 2, at the stream-wise centre of the strait. The model is run with free-slip boundary conditions at island and coastline. Fluidity predictions for Mesh 3 (solid line), 4 (dashed line), 5 (dotted line) and 6 (dash-dot line).

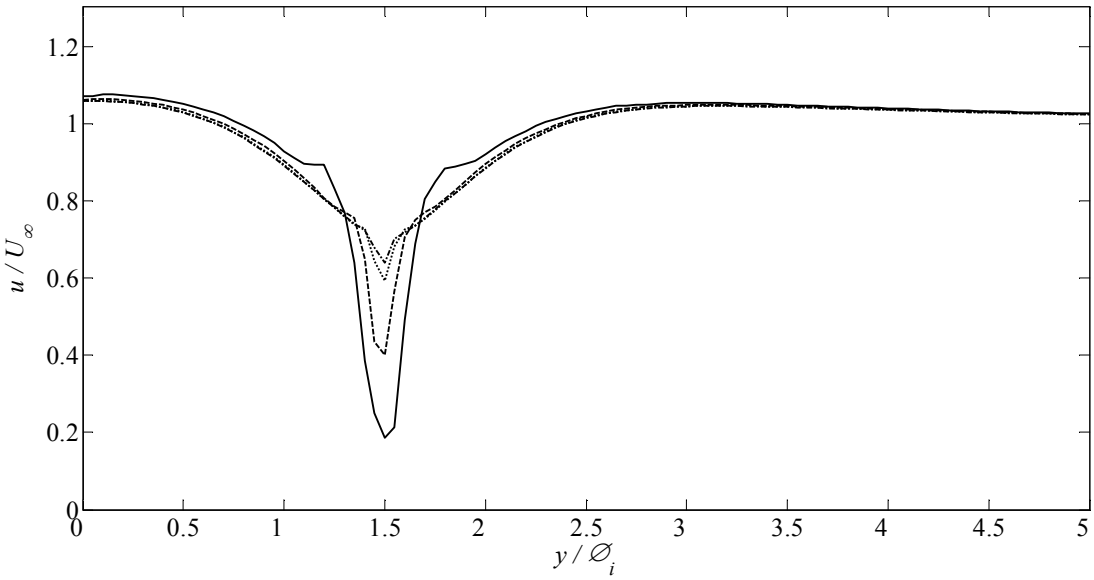


Figure 5.6. Stream-wise flow velocity profile at cross section 3, one diameter downstream from the centre of the circular island. The model is run with free-slip boundary conditions at island and coastline. Fluidity predictions for Mesh 3 (solid line), 4 (dashed line), 5 (dotted line) and 6 (dash-dot line).

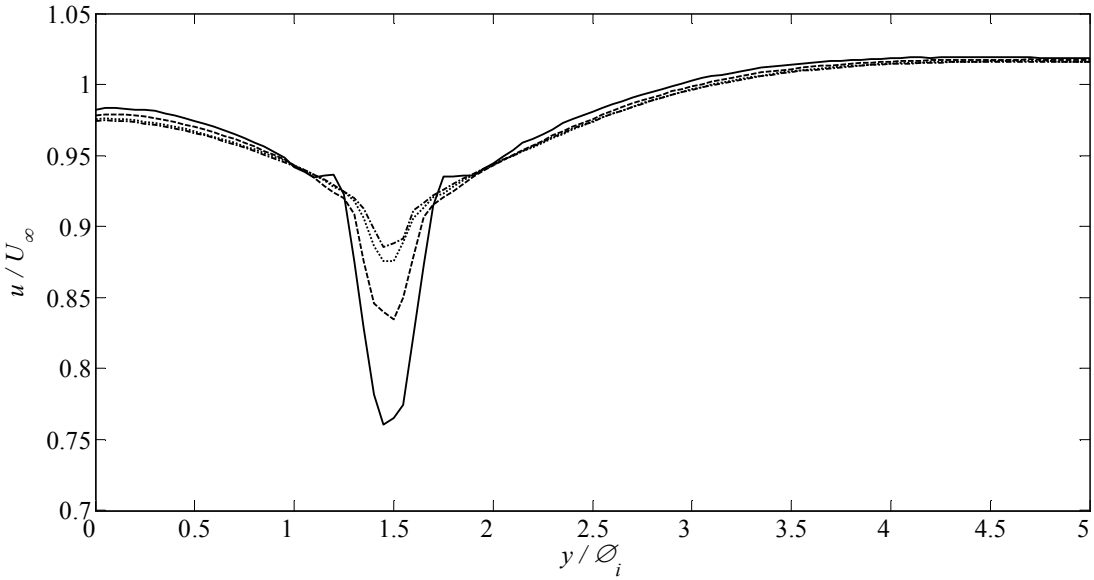


Figure 5.7. Stream-wise flow velocity profile at cross section 4,two diameters downstream from the centre of the circular island. The model is run with free-slip boundary conditions at island and coastline. Fluidity predictions for Mesh 3 (solid line), 4 (dashed line), 5 (dotted line) and 6 (dash-dot line).

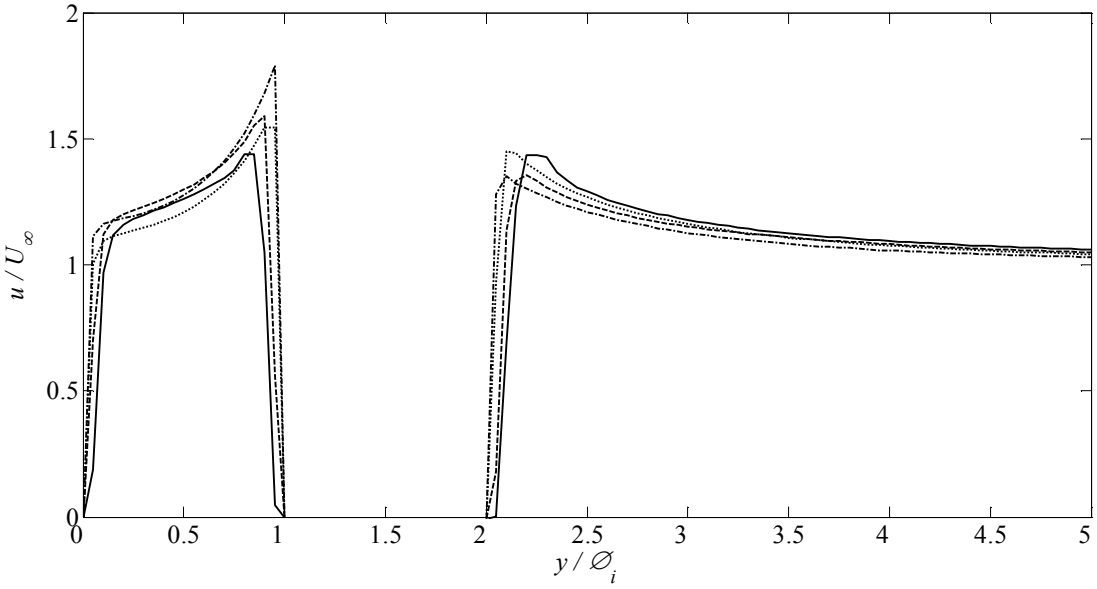


Figure 5.8. Stream-wise flow velocity profile at cross section 2, at the stream-wise centre of the strait. The model is run with no-slip boundary conditions at island and coastline. Fluidity predictions for Mesh 3 (solid line), 4 (dashed line), 5 (dotted line) and 6 (dash-dot line).

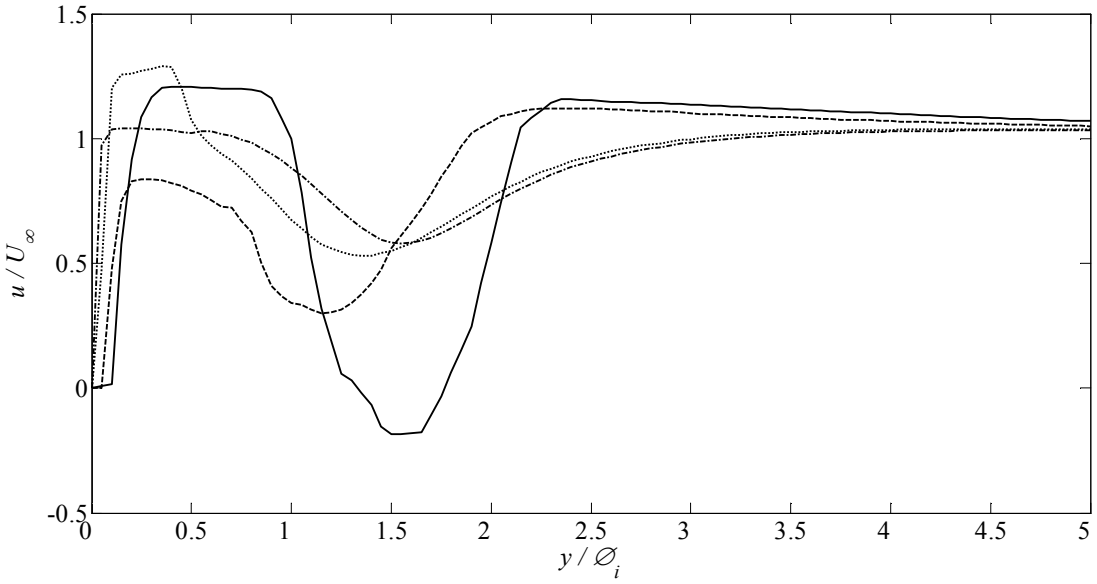


Figure 5.9. Stream-wise flow velocity profiles at cross section 4, two diameters downstream from the centre of the circular island. The model is run with no-slip boundary conditions at island and coastline. Fluidity predictions for Mesh 3 (solid line), 4 (dashed line), 5 (dotted line) and 6 (dash-dot line).

Figure 5.10 shows the unstructured mesh used to discretise the island-landmass domain, based on the mesh edge lengths detailed for Mesh 4 in Table 5.1. The mesh contains 8,027 vertices and 16,054 elements. In addition, a regular grid of 80 isosceles triangles is placed at

the narrowest section of the strait where power extraction is implemented. The width $B_f$ of the farm is equal to $s$. The length $L_f$ of the farm is equal to $h$, which is of same order of size as the element mesh edge length used to discretise the island and the strait. The length of the farm used is also in agreement with the expected footprint of a staggered two row tidal array.

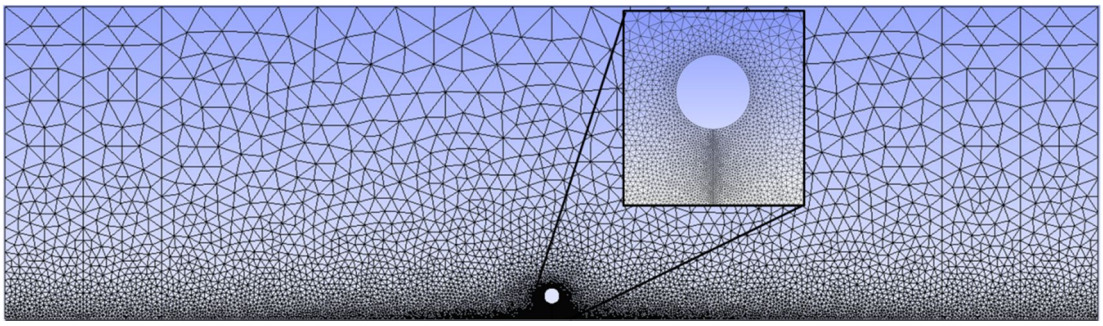

Figure 5.10. Unstructured spatial discretisation of the island landmass domain, with a regular biased right isosceles triangles grid used to delineate the tidal farm at the strait.

## 5.3. Dynamic analysis

This section presents results from the dynamic sensitivity analysis of the resource in the island-landmass coastal site. In all cases, simulations are run for seven tidal periods, with the first two tidal periods corresponding to the ramp-up of the system (Eq. 5.2). The following two tidal periods correspond to spin-up of the system to obtain a stable flow dynamic response. The final three tidal periods are used in the resource assessment of the strait.

### 5.3.1 Island in the proximity of a semi-infinite landmass

This section presents tidal power resource assessments for an island of dimensions $L_i = B_i = \emptyset_i = 50h = 0.0023\lambda$ and a landmass. Here, $\lambda$ is the wavelength of the $M_2$ tide in shallow water of depth $h$. The strait width $s$ is equal to $\emptyset_i$. Unless otherwise stated, the domain length $L = 0.1581\lambda$ and width $B = 0.0452\lambda$. From now on, this domain is referred to as an island-landmass baseline system. To understand the influence of choice of boundary conditions on power extracted, three scenarios are considered: a free-slip condition at the solid boundaries of the island and landmass; a no-slip condition at the island and landmass boundaries; and a domain with a non-uniform bathymetry in the strait region (Figure 5.11), referred to as the non-uniform seabed scenario. In this scenario, water depth is increased

linearly from $h$ = 5 m at the island and landmass boundaries to $h$ = 40 m at a distance $0.1Ø_i$ off the boundaries.

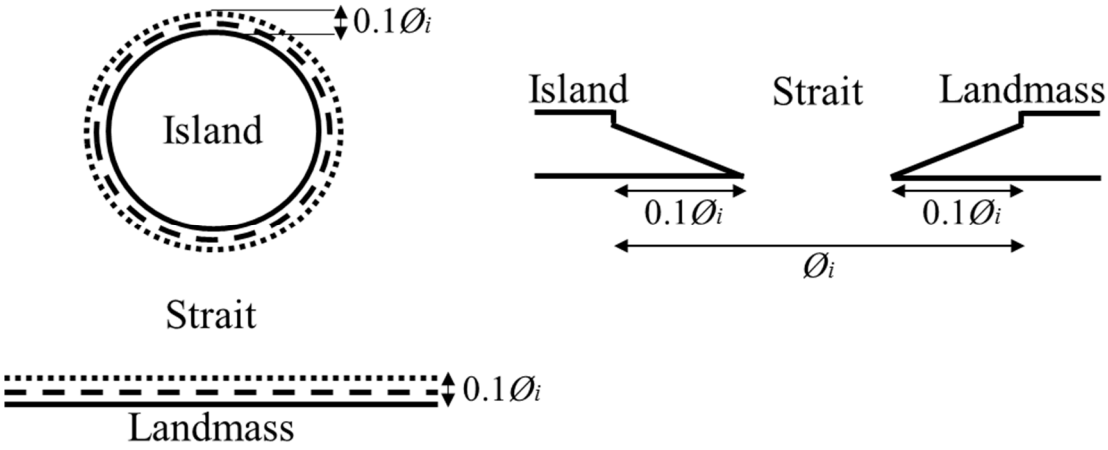


Figure 5.11. Top (left) and lateral (right) sketches of water depth profile defined in the island-landmass non-uniform seabed scenario. $h$ = 5 m (solid line), $h$ = 20 m (dashed line) and $h$ = 40 m (dotted line).

Figure 5.12 shows the tidal flow speed distributions as contour plots for the three scenarios, at times $T/4$, $T/2$, $3T/4$ and $T$. Figure 5.13 presents the vorticity contour plots for the three scenarios, at times $T/2$ and $T$. As observed in the validation test in Section 4.8, a no-slip boundary condition at the island is required to yield a wake of the vortex-shedding type. The non-uniform seabed scenario presents similar dynamic behaviour and wake type than that obtained for the no-slip scenario.

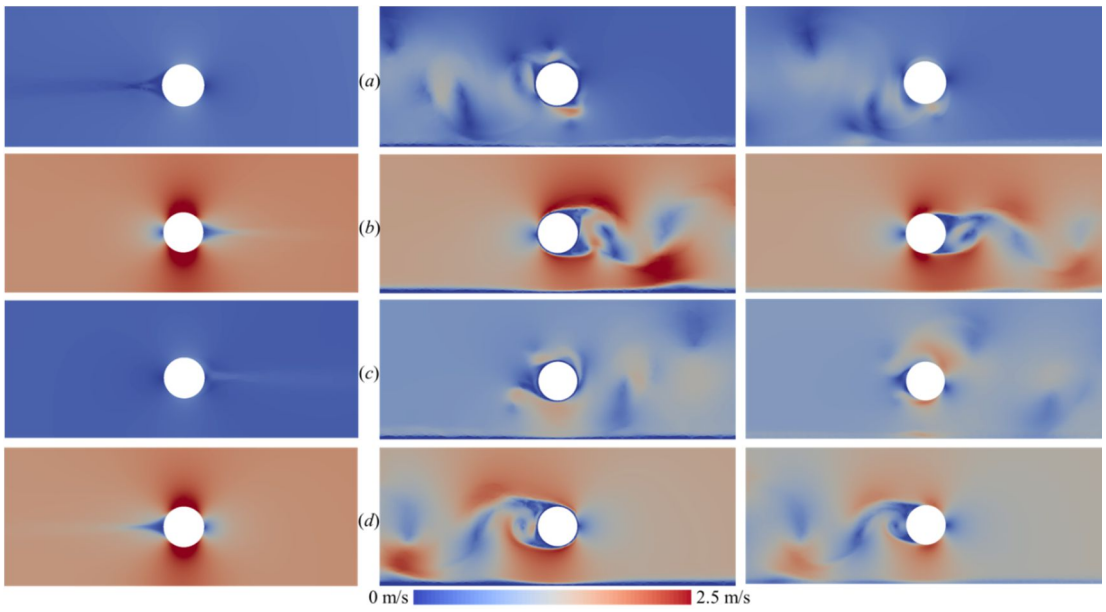


Figure 5.12. Flow speed contour plots for the free-slip (left), no-slip (centre) and non-uniform seabed (right) scenarios taken at (*a*) *T*/4, (*b*) *T*/2, (*c*) 3*T*/4 and (*d*) *T*.

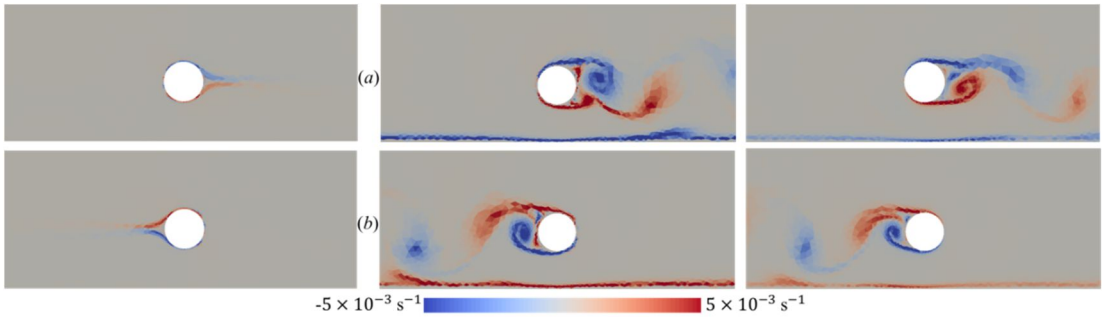


Figure 5.13. Vorticity contour plots for the free-slip (left), no-slip (centre) and non-uniform seabed (right) scenarios taken at (*a*) *T*/2 and (*b*) *T*.

Figure 5.14 shows the averaged contour plots of the speed and kinetic power over three tidal cycles obtained in the free-slip scenario. As predicted by the potential flow theory presented in Section 4.3, higher velocities and consequently kinetic power densities are obtained north and south of the island close to its limits.

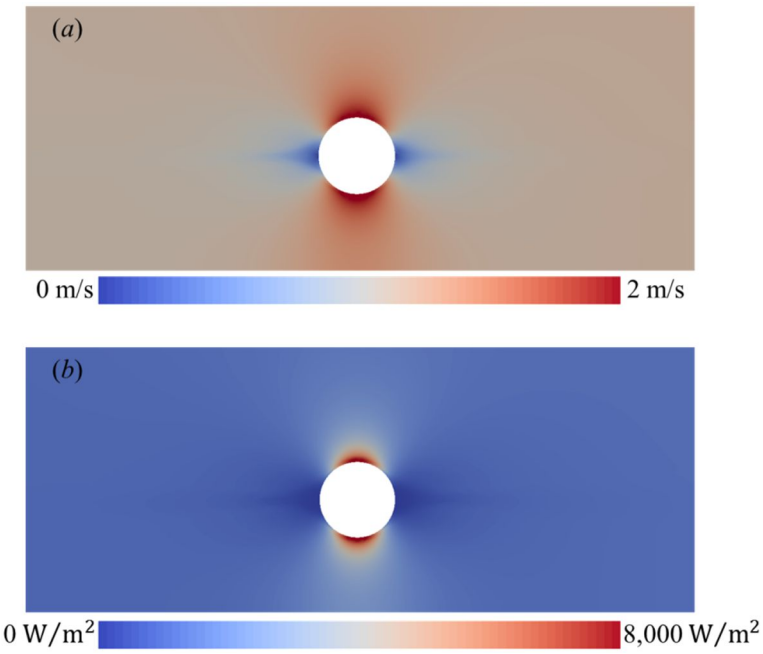


Figure 5.14. Contour plots of the three-tidal-cycle averaged speed (*a*) and kinetic power density (*b*) for the free-slip scenario.

Power extraction level in the tidal farm is characterised by a parameter $k_f$ (see Section 4.9). Power extraction levels $k_f$ between 0 and 4.5 are implemented at the farm in the strait for the three scenarios. Figure 5.15 shows three tidal period-averaged results: undisturbed kinetic power $\bar{P}_{ko}$, defined as the kinetic power in the strait with no power extraction; natural power dissipated on the seabed in the strait in the absence of power extraction $\bar{P}_s$; kinetic power in the strait $\bar{P}_k$ with the tidal farm present; and power extracted from the flow by the tidal farm $\bar{P}_e$. As denoted by [35], $\bar{P}_e$ represents an upper limit to power extractable by tidal turbines and it is referred as the potential of the strait because the power extraction methodology does not account for losses due to mixing behind tidal turbines and the turbine array [149]. There is a clear disparity in the kinetic and extracted power figures between the three scenarios. In terms of power extracted, free-slip and no-slip scenarios represent lower and upper bounds. The difference in power extracted between the two scenarios can be explained by flow separation occurring at the island in the no-slip case, in agreement with results from Section 4.8. The maximum power extracted for the non-uniform seabed scenario lies between that obtained for the free-slip and no-slip scenarios.

From Figure 5.15, there is no clear relationship between the maximum extracted power and the natural power dissipated in the strait in any of the three scenarios. Results from the no-slip scenario may indicate a link between maximum extracted power and undisturbed kinetic

power. However, the undisturbed kinetic power is not a good indicator of the maximum power extracted in the free-slip and non-uniform seabed scenarios. Kinetic power in the strait also behaves differently for the three scenarios. For low extraction levels $k_f < 0.5$, the rate of decrease in the free-slip and non-uniform seabed scenarios is higher than in the no-slip scenario, but it is approximately the same for $k_f > 0.5$.

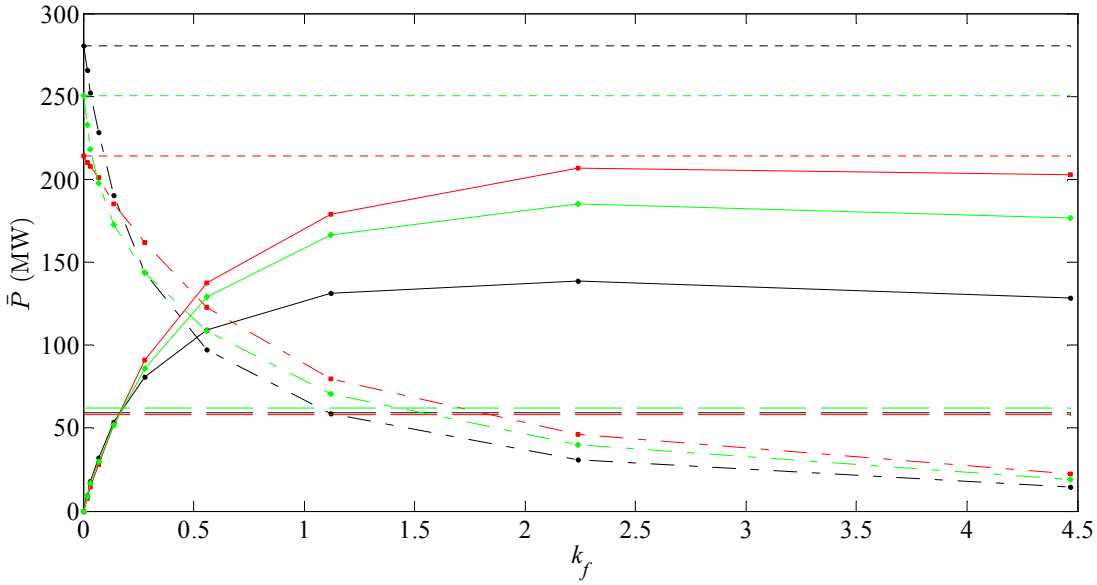


Figure 5.15. Power profiles as functions of $k_f$ for a strait between an island and landmass: free-slip (black), no-slip (red) and non-uniform seabed (green) scenarios. Extracted power for a tidal farm located in the strait (solid line); kinetic power for the strait with the tidal farm present (dash-dot line); kinetic power for undisturbed conditions in the strait (dotted line); and natural power dissipated on the seabed at the strait (dashed line). Markers indicate output data from the numerical model.

During the pre-feasibility stages of a tidal project, developers may only have access to velocity data from which to derive an estimate of the undisturbed kinetic power $\bar{P}_{ko}$. For this reason, it is interesting to investigate the ratio of the power extracted $\bar{P}_e$ to the undisturbed kinetic power $\bar{P}_{ko}$, $\hat{P}$. For maximum power extraction $\bar{P}_e$ obtained in all three scenarios for $k_f > 2$, the power ratios are $\hat{P}$ = 0.49, 0.96, and 0.74 for the free-slip, no-slip, and non-uniform seabed scenarios respectively. The value of $\hat{P}$ for the non-uniform seabed scenario is close to the mean of the free-slip and no-slip values.

Consequent flow reductions at maximum $\hat{P}$ will make tidal projects commercially unfeasible in addition to bringing about possibly unacceptable changes to the local environment. For instance, when $\bar{P}_e$ is one-third maximum $\bar{P}_e$, the percentage decreases in $\bar{P}_k$ compared to $\bar{P}_{ko}$ are approximately 30 %, 20 % and 34 % for the free-slip, no-slip and non-uniform seabed scenarios.

The extraction levels $k_f$ can be converted into an approximate equivalent number of turbines $N_T$ (Section 3.2.2.1) to give a more realistic idea as to what are the orders of magnitude analysed. Consider a 1 MW power rated $P_R$ turbine of 20 m rotor diameter $\emptyset_T$ with cut-in speed $U_C$ of 1m/s and rated speed $U_R$ of 2.5 m/s. The following $C_P$ function defines the power output of the turbine (Figure 5.16):

$$C_P = \begin{cases} 0 & \text{if} \quad U < U_C \\ 0.4 & \text{if} \quad U_C \leq U \leq U_R \\ \dfrac{2P_R}{\rho A_T U^3} & \text{if} \quad U > U_R \end{cases} \tag{5.3}$$

where $A_T$ is the rotor swept area.

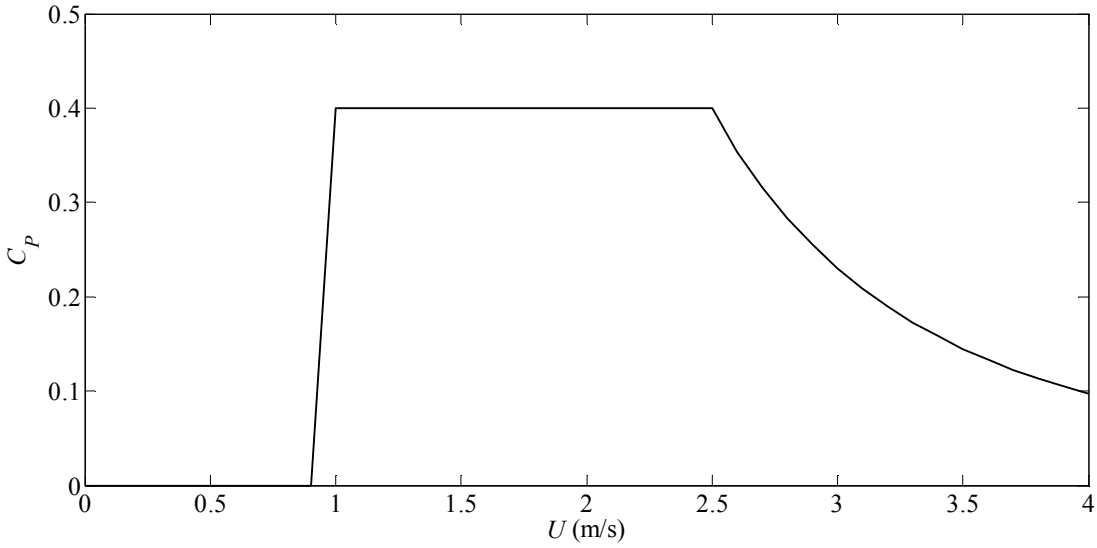


Figure 5.16. Turbine power coefficient $C_p$ as a function of incident flow speed between 0 and 4 m/s.

The above power curve is valid for an isolated turbine or for a limited number of turbines. However, site dynamics and tidal array arrangement will impact the overall power coefficient $C_P$ experienced by turbines in large arrays [150]. Due to the dependency between $C_P$, power extracted by turbines, and flow reduction in the site, an iterative turbine design procedure will be required to maximise power output from the array [46].

The projected area of the turbine's support structure $A_S$ is considered to be equivalent to 10 % of the turbine rotor swept area. Herein, both thrust $C_T$ and support structure drag $C_D$ coefficients are assumed constant and set equal to 0.8 and 0.9 respectively [49]. Thus, the equivalent number of turbines may be computed as:

$$N_T = \frac{2k_f A_f}{A_S C_D + A_T C_T} \tag{5.4}$$

where $A_f$ is the area through which power is extracted from the flow, in this case it is equal to the area of the tidal farm (i.e. $L_f B_f$).

Table 5.2 includes the equivalent number of turbines $N_T$ for extraction levels $k_f$ between 0 and 1.12. The period-averaged power $\bar{P}_T$ generated by the tidal array is computed from $N_T$, $C_P$ curve, and velocity field at the farm over a duration of three tidal cycles. The capacity factor $CF$ of the tidal farm during the three tidal cycles is computed based on $\bar{P}_T$, $N_T$ and $P_R$ as:

$$CF = \frac{\bar{P}_T}{N_T P_R} \tag{5.5}$$

Finally, Table 5.2 shows the percentage decrease in mean strait velocity $\bar{U}_o^*$ and mean kinetic power in the strait $\bar{P}_k^*$ over three tidal periods against the case with no power extraction in the strait.

| $k_f$ | 0.02 | 0.03 | 0.07 | 0.14 | 0.28 | 0.56 | 1.12 |
|---|---|---|---|---|---|---|---|
| $N_T$ | 10 | 20 | 40 | 80 | 160 | 320 | 640 |
| $\bar{P}_T$ [MW] | 3.7 | 7.2 | 13.4 | 23.2 | 35.5 | 47.2 | 54.2 |
| $CF$ [%] | 37.2 | 35.9 | 33.5 | 29.0 | 22.2 | 14.8 | 8.5 |
| $\bar{U}_o^*$ [%] | 1.6 | 3.1 | 5.9 | 10.7 | 17.7 | 26.9 | 37.6 |
| $\bar{P}_k^*$ [%] | 5.4 | 10.2 | 18.8 | 32.1 | 48.6 | 65.3 | 79.1 |

Table 5.2. Extraction levels and equivalent number of turbines in the strait. Period-averaged tidal farm power generated, tidal farm capacity factor, percentage decrease in mean strait velocity, and percentage decrease in mean kinetic power; in each case, the averaging is over three tidal periods.

The power generated and capacity factor figures in Table 5.2, together with an economic model, will help developers to identify the optimal economic number of turbines in the tidal farm. As mentioned earlier, this economic optimum $N_T$ is likely to be a small fraction of the $N_T$ at maximum power extracted. In addition, the flow reduction at the economic optimum point may be unacceptable from an environmental point of view. In this case, $N_T$ may be set by environmental constraints and be below the economic optimum.

Unlike a channel connecting two infinite basins, where there is only one path for the flow, in the island-landmass system there are two routes for the flow: through the strait and the offshore side of the island. The two paths exert an identical resistance to flow under equal water depths and bottom friction conditions. Because of the existence of an alternative flow path, it is interesting to understand the effects of power extraction on the system flow dynamics. To do this the volumetric flow rate, $\bar{Q} = uhl$, is considered along two cross-sections of length $l$; one across the shortest distance between the landmass and the island, and the second of equal length but spanning offshore of the island. The choice of offshore cross-section length is in accordance with the results from Section 4.4 which showed that at a distance equal to the island diameter, the stream-wise velocity attains a value close to the free-stream velocity. For each scenario the volumetric flow rate is normalised by the volumetric flow rate in the absence of power extraction, $\bar{Q}_o$; the results are presented in Figure 5.17. The trends of the volumetric flow rate across the strait are in agreement with the diminishing rates in kinetic power across the strait shown in Figure 5.15. Figure 5.17 also reveals that the reduction in volumetric flow rate through the strait does not convert into an equivalent increase of flow rate through the analysed section at the offshore side of the island. This implies that the fraction of power lost by the system due to power extraction at the strait is not recovered.

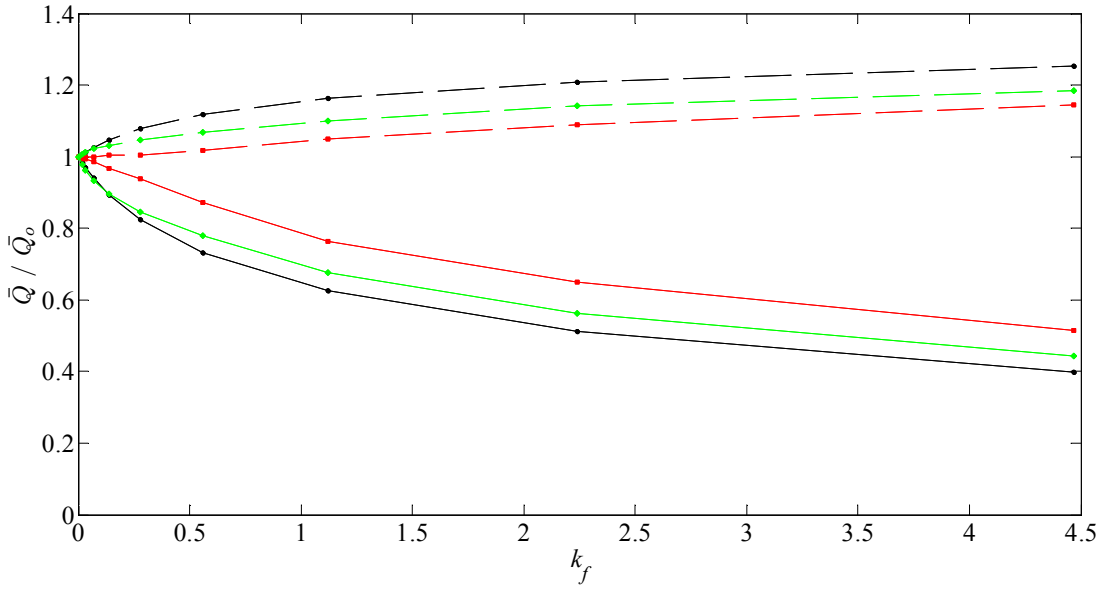


Figure 5.17. Changes in the ratio of actual to undisturbed volumetric flow rate for free-slip (black), no-slip (red), and non-uniform seabed (green) scenarios at different levels of power extraction. Volumetric flow rates are calculated across the tidal farm (solid line) and through a cross-section of identical length at the offshore side of the island (dashed line). Markers indicate discrete points computed using the numerical model.

Comparison of Figure 5.17 with Figure 5.15 reveals that the maximum power extracted may be reached when flow through the strait is in the 60-40 % range of the volumetric flow rate in the absence of power extraction (Figure 5.18). Similar to a channel, numerical tests showed that maximum power extracted in a strait may be reached when flow is reduced to 57.7 % of the flow in the absence of power extraction, in agreement with the work from GC2005 [11] and Bryden and Couch [43]. At maximum $\bar{P}_e$, the resulting bypass volumetric flow rate to flow in undisturbed conditions is 1.21, 1.09 and 1.14 for the free-slip, no-slip and non-uniform seabed scenarios respectively.

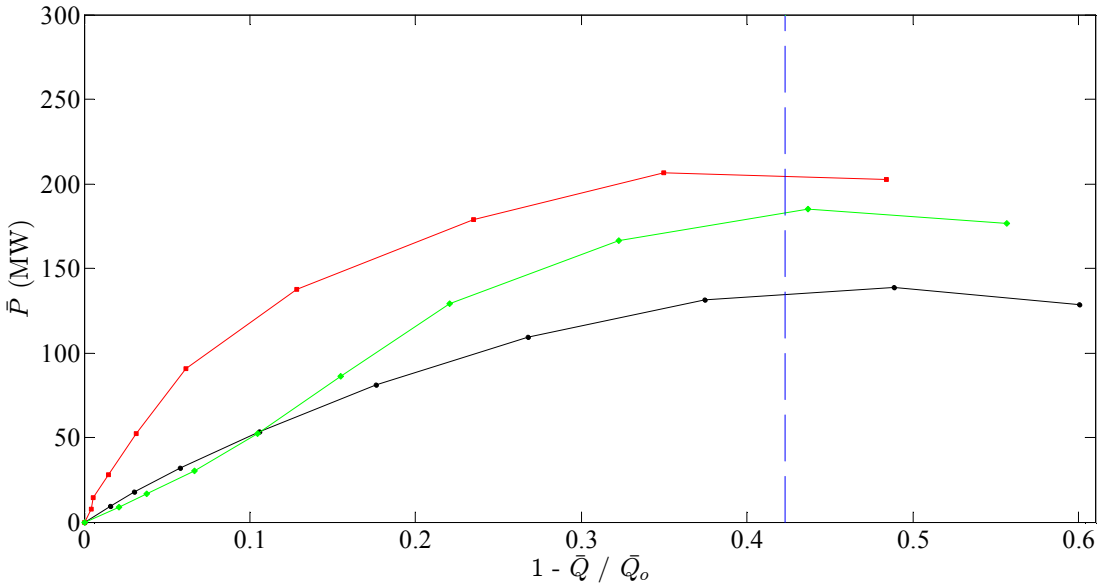


Figure 5.18. Power profiles against changes in normalised volumetric flow rate for a strait between an island and landmass: free-slip (black), no-slip (red) and non-uniform seabed (green) scenarios. Markers indicate output data from the numerical model. Vertical blue dashed line indicates a volumetric flow rate in the strait equal to 57.7 % of the undisturbed conditions.

To understand better the relationship between levels of power extraction and bypass flow, the velocity streamlines are visualised for the free slip scenario. Figure 5.19 and Figure 5.20 show respectively the velocity streamlines without power extraction and with high power extraction where $k_f = 2.24$. The large resistance in the strait caused by the power extraction leads to flow being diverted to the offshore side of the island where resistance is lower.

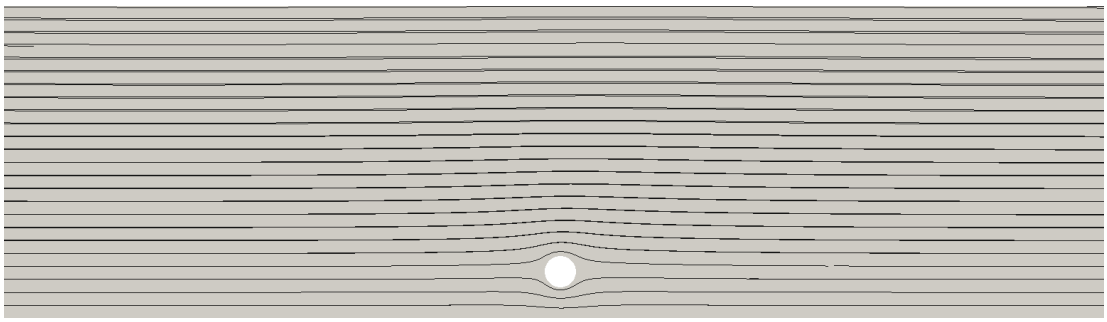

Figure 5.19. Steady-state velocity streamlines for the free-slip island-landmass scenario in the absence of power extraction at the strait.

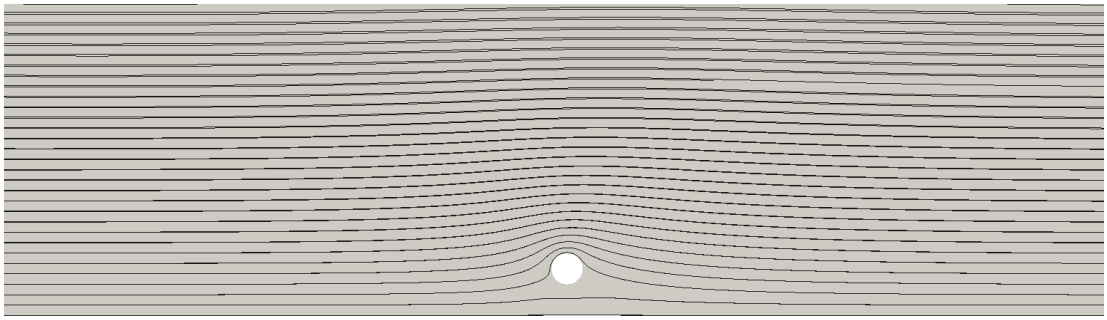

Figure 5.20. Steady-state velocity streamlines for the free-slip island-landmass scenario with power extraction in the strait corresponding to $k_f = 2.24$.

Draper [13] analysed the extracted power at a strait between an island with a high width to length ratio and a landmass representing the Pentland Firth. He found that the increase of driving head along the strait produced by the power extraction was the main cause of discrepancy with results from the model of a channel connecting two infinite ocean basins proposed by GC2005. Allowing for this difference, Draper concluded that the GC2005 channel model provided a satisfactory representation of the basic physics in the strait. This conclusion was only valid at the scale of island assessed, where there was negligible bypass flow. However, as Figure 5.17 indicates, the bypass flow is not negligible in the island-landmass system analysed herein. Figure 5.21 and Figure 5.22 show the effects of power extraction levels on the head driving the flow in the strait $\delta_{wi} - \delta_{ei}$ (Figure 5.1) throughout three tidal periods in the free-slip and no-slip scenarios respectively for zero, low ($k_f = 0.14$) and high ($k_f = 2.24$) power extraction levels. As observed by Draper, the increase in power extraction yields to an increase in the amplitude of the head driving the flow in the two scenarios. The higher head driving amplitudes observed in the no-slip scenario are in agreement with the higher power extracted figures shown in Figure 5.15.

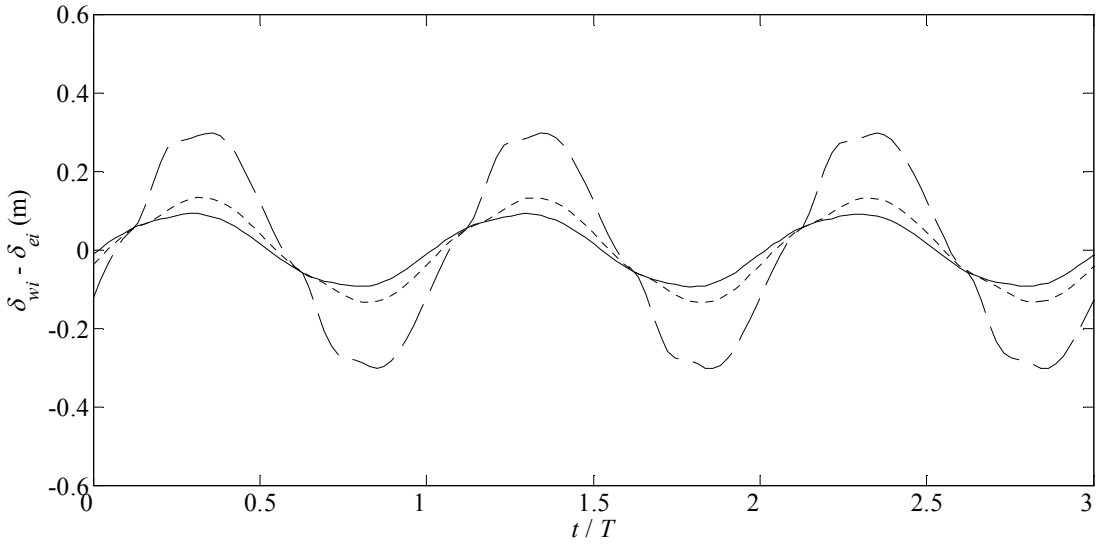


Figure 5.21. Flow driving head between entrance and exit of the strait for the free-slip scenario: no power extraction (solid line); low extraction $k_f$ = 0.14 (dotted line); and very high extraction $k_f$ = 2.24 (dashed line).

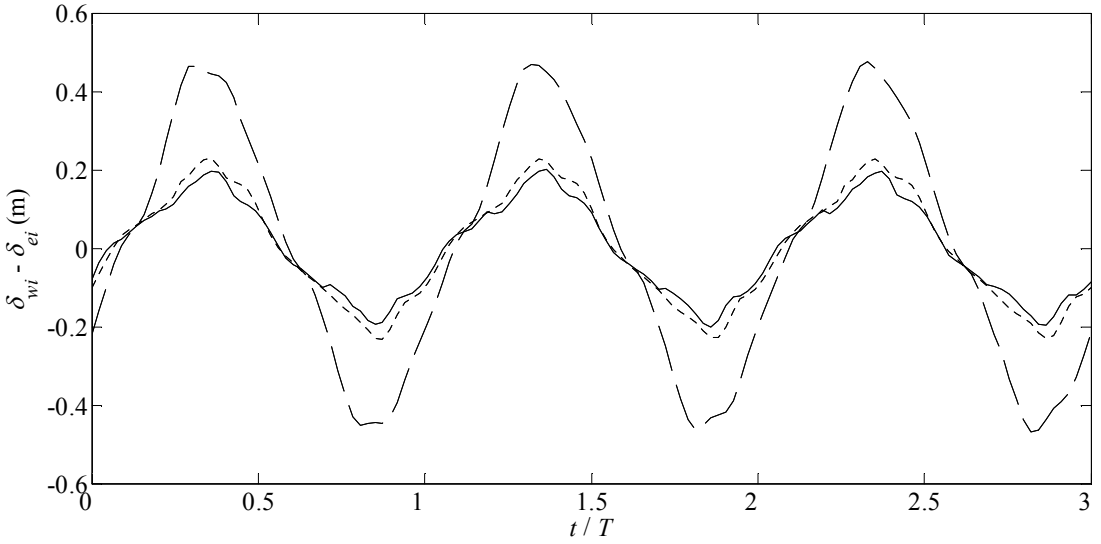


Figure 5.22. Flow driving head between entrance and exit of the strait for the no-slip scenario: no power extraction (solid line); low extraction $k_f$ = 0.14 (dotted line); and very high extraction $k_f$ = 2.24 (dashed line).

In the free-slip scenario, based on the amplitude of the head driving the flow in undisturbed conditions shown in Figure 5.21, the GC2005 channel model with $\gamma$ = 0.22 (Section 4.9.2) predicts a maximum extracted power in the order of about 45 MW. The peak flow lags the peak head drop along the strait by 35º, and so according to GC2005 $\gamma$ can be approximated by 0.2, which leads to a predicted maximum power extracted of 40.7 MW. These values are 67.7 % and 78.3 % lower than the numerically computed values in the free-slip case. For the

no-slip scenario, the peak flow lags 5º the peak head drop, leading to $\gamma = 0.21$. The values of maximum power extracted for $\gamma = 0.22$ and 0.21 are 81.6 and 77.9 MW respectively, which are 60.5 % and 62.3 % lower than the numerical estimates of maximum power extracted. Consequently, the GC2005 model may not apply to this case, where the island geometry scale does not prevent bypass flow effects, and the head driving the flow increases with extraction rate.

#### 5.3.1.1 Viscous environment

In numerical models of actual coastal sites, the eddy viscosity is occasionally used as a calibration parameter [89]. It is important to understand the sensitivity of the power extracted in the strait to the way viscosity is defined in the model. For model and flow conditions, the values of eddy viscosity coefficient from Eq. (3.23) are in the range $10^{-1}$-1 $m^2s^{-1}$ in the vicinity of the island. Sensitivity to choice of value of the eddy viscosity coefficient is assessed by comparing results obtained with Eq. (3.23) against those for constant kinematic viscosity values of $\nu = 10^{-6}$, 1, and 100 $m^2s^{-1}$, which correspond to the molecular kinematic viscosity, and two typical eddy viscosity values used in calibration of numerical models [89].

Table 5.3 and Table 5.4 show the effect on kinetic power in the strait and extracted power due to the choice of eddy viscosity coefficient at three extraction levels, for the free-slip and no-slip scenarios respectively. In each free-slip and no-slip scenarios, the empirical depth-averaged parabolic and constant ($\nu = 10^{-6}$ and 1 $m^2s^{-1}$) depth-averaged viscosity cases yield very similar kinetic and extracted power results. The case with $\nu = 100$ $m^2s^{-1}$ yields different kinetic and extracted power results, and the difference is greater in the no-slip scenario than in the free-slip scenario. Interestingly, for the no-slip scenario with $\nu = 100$ $m^2s^{-1}$, the ratio of $\bar{P}_e$ to kinetic flux in the absence of turbines is 95.1 %, which is almost identical to ratios obtained for the other three viscosity cases assessed. In the free-slip scenario, this ratio at $\nu = 100$ $m^2s^{-1}$ is 66.0 % which is higher than the 49.5 % obtained in the other three viscosity cases assessed.

| Eddy viscosity ($m^2s^{-1}$) | Depth-averaged Parabolic | | $10^{-6}$ | | 1 | | 100 | |
|---|---|---|---|---|---|---|---|---|
| $k_f$ | $\bar{P}_k$ (MW) | $\bar{P}_e$ (MW) | $\bar{P}_k$ (MW) | $\bar{P}_e$ (MW) | $\bar{P}_k$ (MW) | $\bar{P}_e$ (MW) | $\bar{P}_k$ (MW) | $\bar{P}_e$ (MW) |
| 0 | 280.9 | n.a. | 280.5 | n.a. | 279.8 | n.a. | 250.4 | n.a. |
| 0.14 | 190.7 | 53.6 | 190.6 | 53.5 | 190.0 | 53.4 | 191.0 | 53.6 |
| 2.24 | 31.0 | 138.7 | 30.9 | 138.4 | 31.0 | 139.0 | 36.9 | 165.2 |

Table 5.3. Kinetic power in the strait and extracted power for a tidal farm located in a strait for the free-slip scenario with prescribed extraction levels $k_f$ = 0, 0.14 and 2.24. Eddy viscosity is defined using a depth-averaged parabolic eddy viscosity formula or using constant viscosity coefficient values of $10^{-6}$, 1 and 100 $m^2s^{-1}$.

| Eddy viscosity ($m^2s^{-1}$) | Depth-averaged Parabolic | | $10^{-6}$ | | 1 | | 100 | |
|---|---|---|---|---|---|---|---|---|
| $k_f$ | $\bar{P}_k$ (MW) | $\bar{P}_e$ (MW) | $\bar{P}_k$ (MW) | $\bar{P}_e$ (MW) | $\bar{P}_k$ (MW) | $\bar{P}_e$ (MW) | $\bar{P}_k$ (MW) | $\bar{P}_e$ (MW) |
| 0 | 213.9 | n.a. | 214.3 | n.a. | 214.2 | n.a. | 115.8 | n.a. |
| 0.14 | 185.2 | 52.0 | 185.9 | 52.2 | 183.9 | 51.6 | 96.4 | 27.0 |
| 2.24 | 46.1 | 206.5 | 46.0 | 206.0 | 45.3 | 202.9 | 24.6 | 110.1 |

Table 5.4. Kinetic power in the strait and extracted power for a tidal farm located in a strait for the no-slip scenario with prescribed extraction levels $k_f$ = 0, 0.14 and 2.24. Eddy viscosity is defined using a depth-averaged parabolic eddy viscosity formula or using constant viscosity coefficient values of $10^{-6}$, 1 and 100 $m^2s^{-1}$.

#### 5.3.1.2 Frictional environment

In a similar fashion to viscosity, bottom friction is used as a calibration parameter when modelling real coastal sites [51] [94] [151]. Based on the range of bottom drag coefficients shown in Table 3.1 (Section 3.2.1.1), the sensitivity of the power extracted in the strait to bottom friction is tested using three dimensionless friction coefficients $C_d$ = 0.00125, 0.0025 and 0.005. Figure 5.23 plots the tidal period-averaged results (over three tidal cycles) of $\bar{P}_{ko}, \bar{P}_s$ , $\bar{P}_k$ and $\bar{P}_e$ for the three assessed $C_d$ values. Given that the head driving the amplitude is kept constant, it is not surprising that the lowest $C_d$ yields the highest $\bar{P}_{ko}$. $\bar{P}_s$ behaves different to $\bar{P}_{ko}$, and more power is dissipated from the bottom when $C_d$ increases. The percentage decrease in $\bar{P}_k$ compared to $\bar{P}_{ko}$ when power extraction is a third of the

maximum $\bar{P}_e$ is in the order of 32 % for $C_d$ = 0.0025 and approximately 23 % for $C_d$ = 0.00125 and 0.005. The increasing difference in resistance between the strait and the offshore path for increasing $k_f$ leads to higher bypass flows for lower bottom frictions (Figure 5.24). The ratios of bypass volumetric flow rate to the flow in undisturbed conditions at maximum $\bar{P}_e$ are 1.25, 1.21 and 1.17 for $C_d$ equal to 0.00125, 0.0025 and 0.005 respectively. From these results, it is clear that lower $C_d$ yields higher bypass flow rates as would be expected. Finally, the results show that lower $C_d$ leads to higher $\bar{P}_e$ as less power is naturally dissipated by the bottom and there is more power available for the tidal farm.

The change in bottom friction is consistent with earlier conclusions, and the maximum power extracted does not seem to relate to the undisturbed kinetic power or the power naturally dissipated by the bottom. However, the results confirm the sensitivity of the resource assessment to the frictional environment characterisation of the domain. This sensitivity requires further analysis and, in the particular case of the Pentland Firth in the U.K., has led to some discrepancies in the assessment of the resource [51] [152].

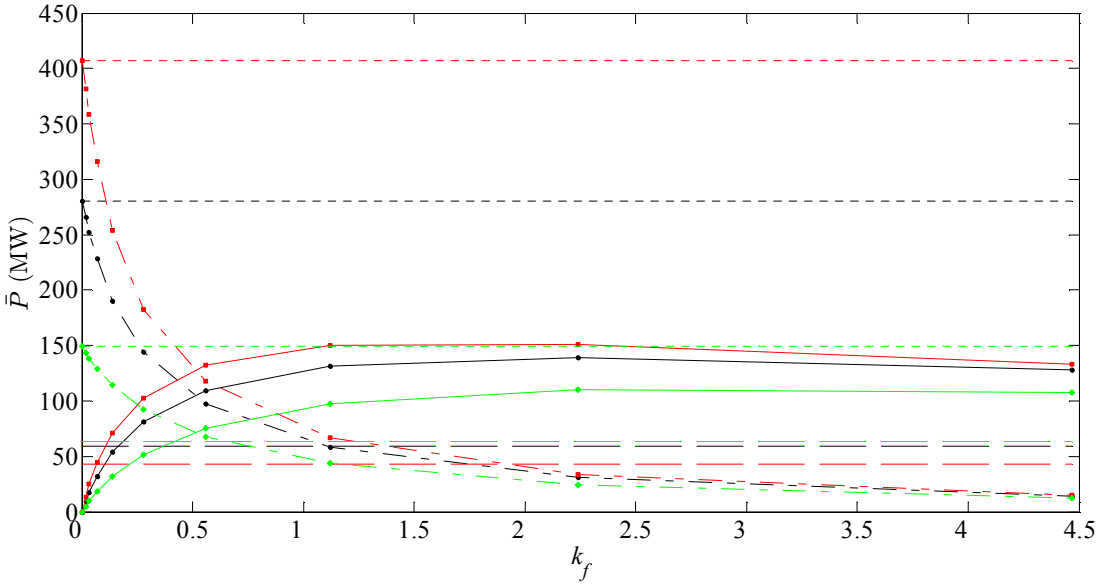


Figure 5.23. Power profiles as functions of $k_f$ for a strait between an island and landmass: $C_d$ = 0.0025 (black), $C_d$ = 0.00125 (red) and $C_d$ = 0.005 (green) scenarios. Extracted power for tidal farm located in the strait (solid line); kinetic power for the strait with the tidal farm present (dash-dot line); kinetic power for undisturbed conditions in the strait (dotted line); and natural power dissipated on the seabed at the strait (dashed line).

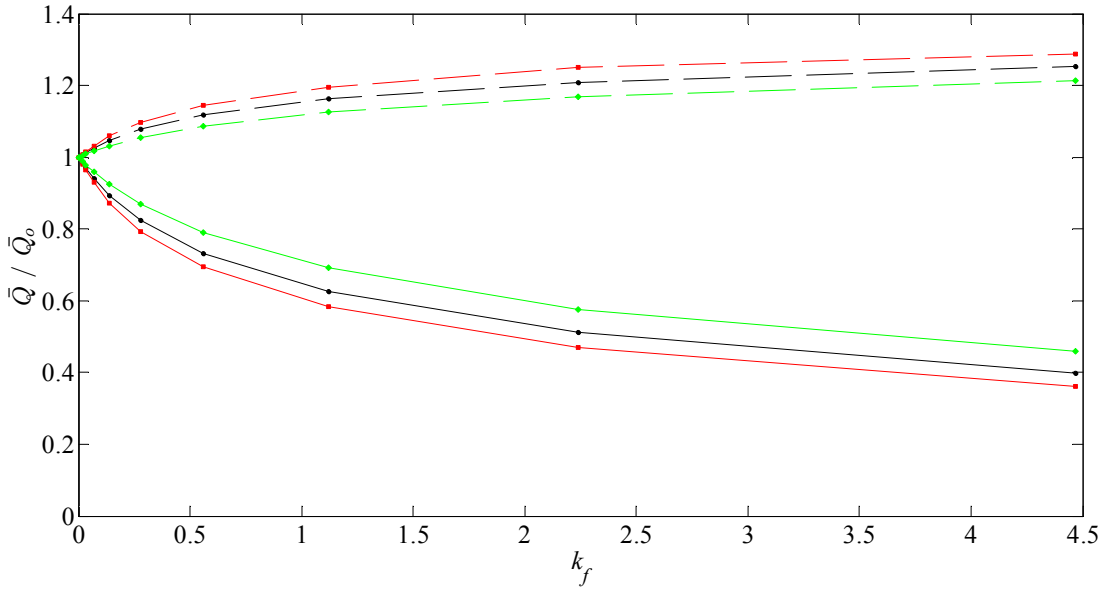


Figure 5.24. Changes in the ratio of actual volumetric flow rate to that in undisturbed conditions for $C_d$ = 0.0025 (black), $C_d$ = 0.00125 (red) and $C_d$ = 0.005 (green) scenarios at different levels of power extraction. Volumetric flow rate across the tidal farm (solid line) and through a cross-section of identical length at the offshore side of the island (dashed line).

#### 5.3.1.3 Water depth

The results of the free-slip and no-slip scenarios were previously compared to the non-uniform seabed scenario emulating a realistic bathymetry in the island-landmass system. Here, the sensitivity of the power extracted in the strait to water depth is assessed. The first part analyses the free-slip scenario where water depth is increased from $h$ to $4h$ in the continental shelf. The second part modifies the non-uniform seabed scenario, increasing the water depth at the offshore side of the island from $h$ to $4h$.

Figure 5.25 shows the effects of increasing extraction levels in the strait on $\bar{P}_{ko}$, $\bar{P}_s$ , $\bar{P}_k$ and $\bar{P}_e$ when water depth in the domain is set to $4h$. An increase of water depth to $4h$ leads to a rise of $\bar{P}_{ko}$ by a factor of six compared to the case where the water depth is $h$ (Figure 5.15). As the bottom friction is kept constant, any increase in water depth results effectively in a lower resistance to the flow by the system, and thus higher kinetic power at the strait. This is also observed in $\bar{P}_e$, where the relatively lower power rates naturally extracted by the system lead to higher extracted power by the farm in the strait. Unlike previous cases analysed, here the maximum power extracted is observed to be between $k_f$ = 4.47 and 8.95. Trends observed for increasing water depths are similar to those observed when reducing $C_d$. There

is a reduction of about 24 % in $\bar{P}_k$ compared to $\bar{P}_{ko}$ when a third of the maximum $\bar{P}_e$ is extracted from the strait; this is slightly lower than the 30 % reduction in the free-slip scenario with depth equal to $h$. Figure 5.26 exhibits the changes in flow through the strait and the offshore side of the island. Flow ratios through the strait and offshore side of the island are similar to those obtained when the water depth is equal to $h$ (Figure 5.17). The rate of actual bypass volumetric flow rate to that in undisturbed conditions for maximum $\bar{P}_e$ is equal to 1.21, which is identical to the ratio found in the free-slip scenario with water depth equal to $h$.

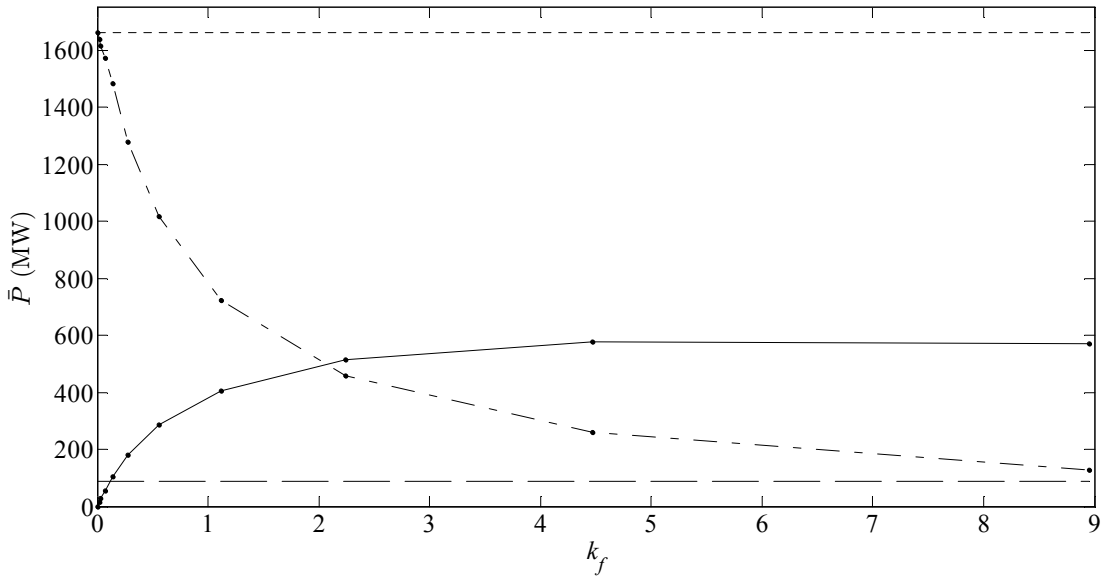


Figure 5.25. Power profiles as functions of $k_f$ for a strait between an island and landmass for a domain of water depth 4$h$. Extracted power for tidal farm located in the strait (solid line); kinetic power for the strait with the tidal farm present (dash-dot line); kinetic power for undisturbed conditions in the strait (dotted line); and natural power dissipated on the seabed at the strait (dashed line).

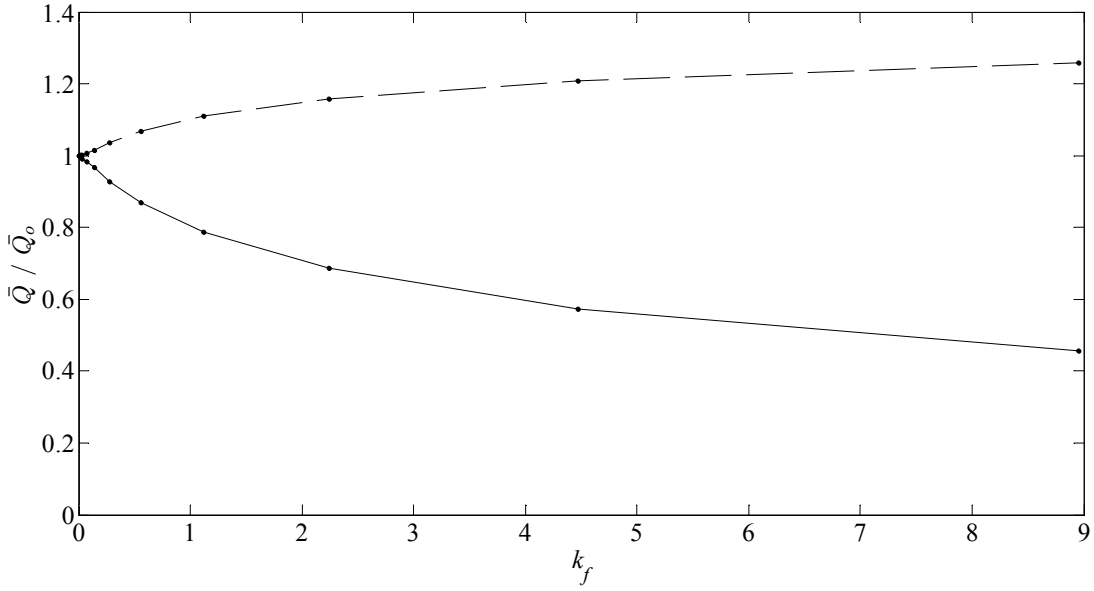


Figure 5.26. Changes in the volumetric flow rate to flow in undisturbed conditions ratio for the island-landmass system of water depth 4$h$ for different levels of power extraction. Volumetric flow rate across the tidal farm (solid line) and through a cross-section of identical length at the offshore side of the island (dashed line).

Figure 5.27 sketches a bird's eye view of the island-landmass domain from above, where the water depth increases linearly northwards from the island (from 0.125$h$ at the island to 4$h$ at a distance 0.4$Ø_i$ north of the island). The water depth also linearly increases from $h$ to 4$h$ west and east of the island along the landmass throughout the continental shelf limits. Power extraction is implemented across the entire cross-section of the strait following the methodology used in the non-uniform seabed scenario.

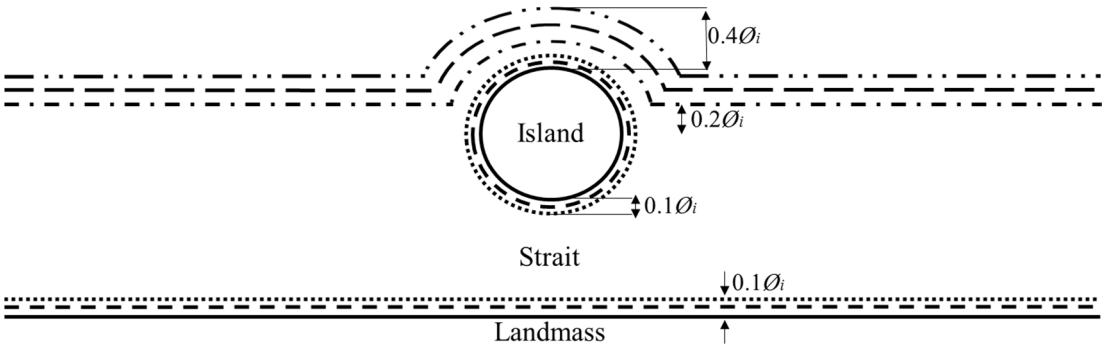


Figure 5.27. Plan view of water depth contours defined in the island-landmass system: depth 0.125$h$ (solid line); 0.5$h$ (dashed line); $h$ (dotted line); 2$h$ (dash dot line); 3$h$ (long dash); and 4$h$ (long dash dot dot line).

Figure 5.28 compares the (three-tide) period-averaged power coefficients, $\bar{P}_{ko}$, $\bar{P}_s$, $\bar{P}_k$ and $\bar{P}_e$, for the non-uniform seabed scenario with water depth $h$ offshore against corresponding values for the case where the water depth offshore is $4h$. In both cases $\bar{P}_{ko}$ and $\bar{P}_s$ are identical, which means that the increase of depth offshore of the island does not have any direct effect on the flow dynamics in the strait in undisturbed conditions. There is a percentage decrease of 41 % in $\bar{P}_k$ when a third of the maximum $\bar{P}_e$ is extracted in the strait. This figure is higher than the 34 % decrease in $\bar{P}_k$ obtained in the non-uniform seabed scenario where water depth was equal to $h$ both in the strait and offshore side of the island. Maximum $\bar{P}_e$ decreases from 180 MW to 130 MW when water depth offshore of the island is increased from $h$ to $4h$. This decrease in maximum $\bar{P}_e$ has direct implications for tidal resource assessment and highlights the need for tidal site developers to be aware of the effect of far-field bathymetry.

Due to the increase of water depth offshore of the island, there is a reduction in resistance to the flow in the offshore direction, which leads to higher bypass flow rates as the extraction level increases in the strait. This trend in volumetric flow rate ratios is shown in Figure 5.29, where volumetric flow rate ratios through the strait are lower for equal extraction levels when the depth is $4h$ offshore than when the depth is equal to $h$. The use of flow ratios leads to counterintuitive bypass flow figures because deeper offshore depths decrease volumetric flow rate ratios offshore. Figure 5.30 shows the absolute difference between the actual to undisturbed volumetric flow in the strait and offshore of the island. For power extraction levels below 2.24, the offshore bypass flow is more predominant for water depth $4h$ than water depth $h$. However, for $k_f$ above 2.24 this trend is inversed, which may be explained by the increase in complexity of the fluid dynamics at the site induced by the differences in water depth between the strait and offshore sides of the island.

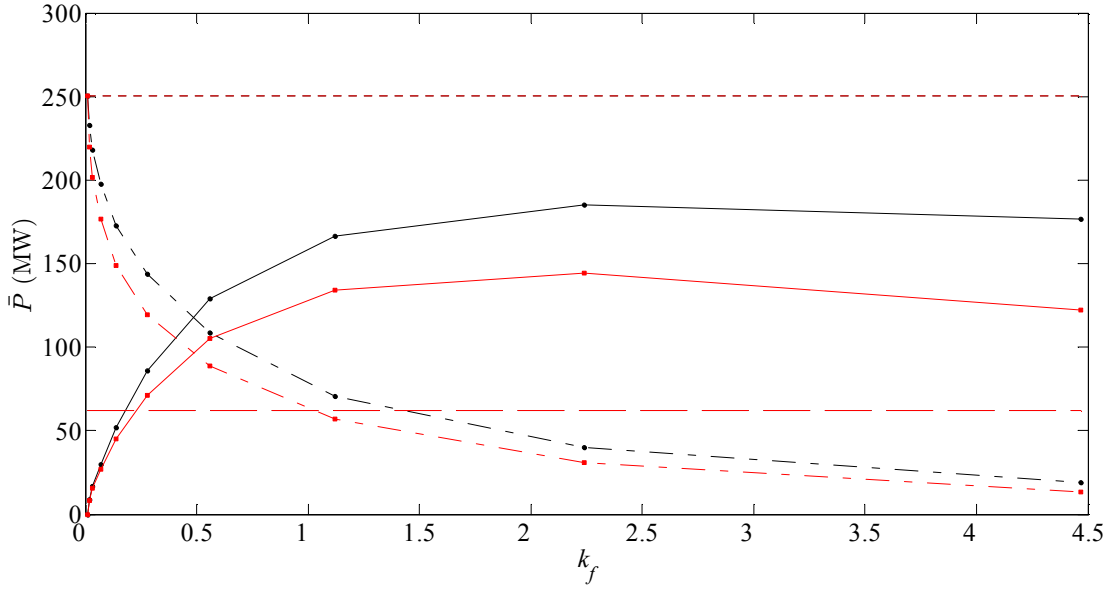


Figure 5.28. Power profiles as functions of $k_f$ for a strait between an island and landmass: depth $h$ offshore (black) and depth $4h$ offshore (red). Extracted power for tidal farm located in the strait (solid line); kinetic power for the strait with the tidal farm present (dash-dot line); kinetic power for undisturbed conditions in the strait (dotted line); and natural power dissipated on the seabed at the strait (dashed line).

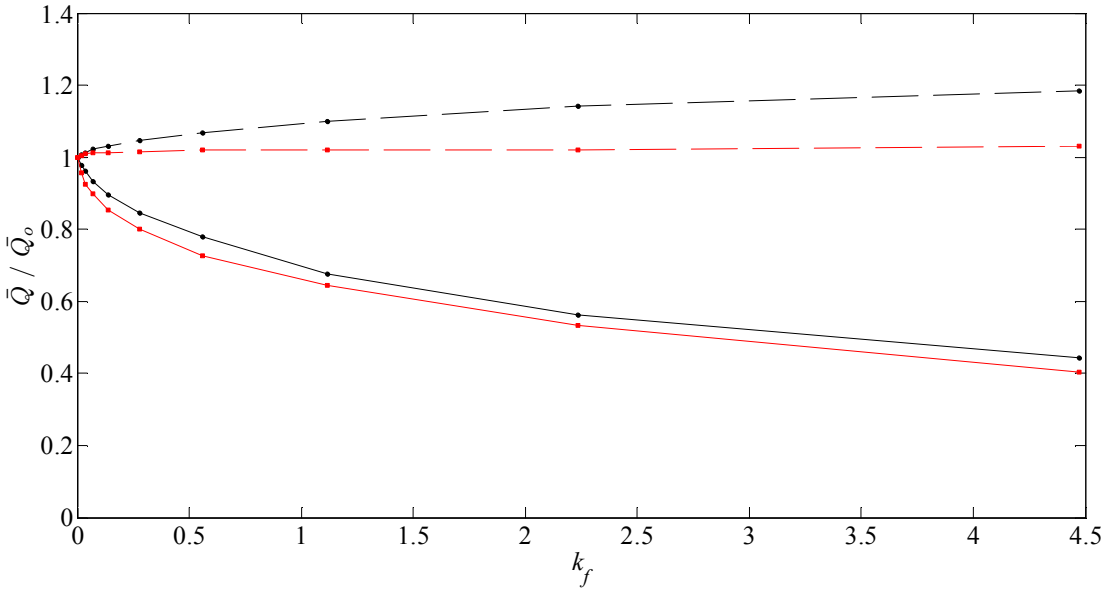


Figure 5.29. Variations in the ratio of actual to undisturbed volumetric flow for different levels of power extraction: depth $h$ offshore (black); and depth $4h$ offshore (red). Volumetric flow rate across the tidal farm (solid line) and through a cross-section of identical length at the offshore side of the island (dashed line).

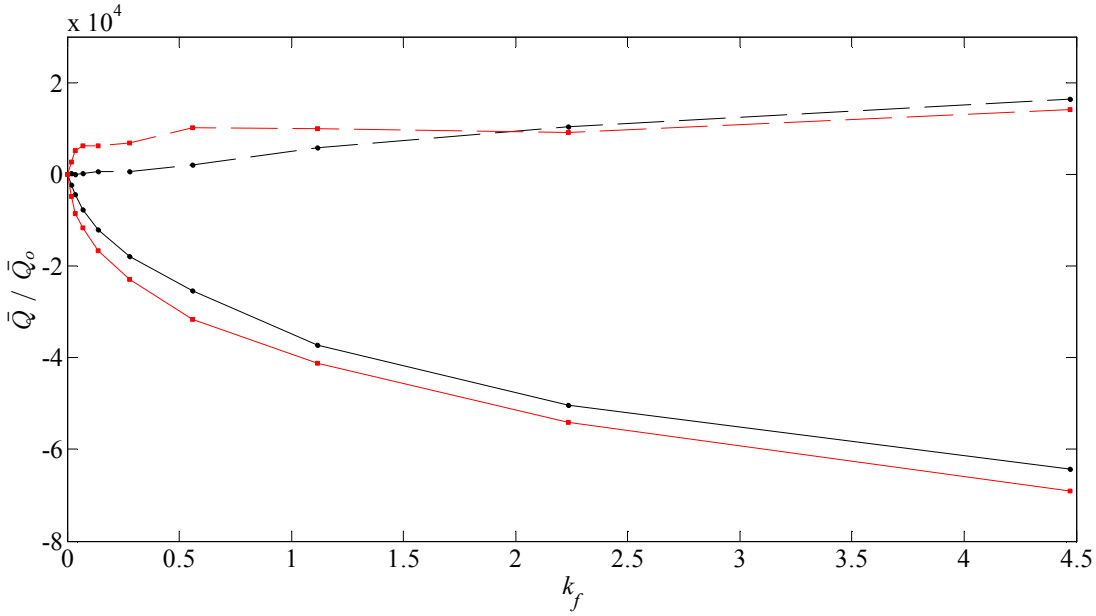


Figure 5.30. Absolute difference between the actual to undisturbed volumetric flow in the strait and offshore of the island for different levels of power extraction: depth $h$ offshore (black) and depth $4h$ offshore (red). Volumetric flow rate across the tidal farm (solid line) and through a cross-section of identical length at the offshore side of the island (dashed line).

#### 5.3.1.4 Tidal farm area

This section analyses the sensitivity of the power extracted from the flow in the strait against the area over which power extraction is implemented. The tidal farm configuration (plan area and shape) may affect the results when carrying out a resource assessment. This is obviously important when the method employed to account for power extraction in the numerical model is based on uniform force acting on the flow smeared across an area. As discussed in Section 2, there is currently no agreement on the choice of the area of the farm when using this methodology of power extraction in a numerical model. In order to understand better the effects of the choice of farm area and shape on the resource assessment in the strait, the free-slip scenario presented in Section 5.3.1 is run for three farm layouts (Figure 5.31): (*a*) thin strip of dimensions $h$ x $\varnothing_i$ (where $\varnothing_i = s$)[1]; (*b*) rectangular farm of dimensions ($\varnothing_i + h$) x $\varnothing_i$ and area 51 times bigger than the thin strip farm; and (*c*) almost rectangular farm of side length $\varnothing_i / 2$ adapted to the circular shape of the island on the north side of the farm (which allows it to fill the entire strait and have a total area 26 times bigger than the thin strip farm).

[1] Note this is the farm layout that has been used in the results prior to this section.

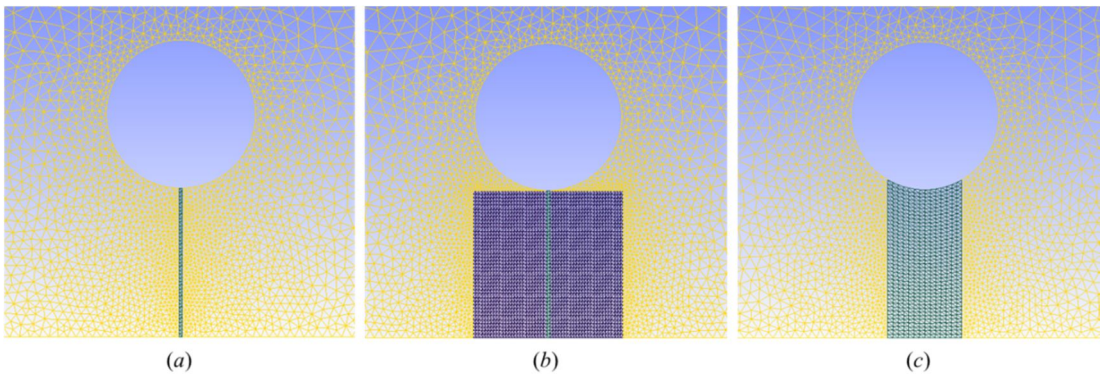


Figure 5.31. Assessed areas where power is extracted from flow in the strait: (*a*) rectangular farm of dimensions $h$ x $\emptyset_i$; (*b*) rectangular farm of dimensions ($\emptyset_i + h$) x $\emptyset_i$; and (*c*) almost rectangular farm with length equal to $\emptyset_i$ / 2 implemented along the circular contour of the island and filling the entire strait.

Figure 5.32 plots the (three-tide) period-averaged power coefficients, $\bar{P}_{ko}$, $\bar{P}_s$ , $\bar{P}_k$ and $\bar{P}_e$, for the three tidal farm layout cases as functions of the equivalent number of turbines $N_T$ in the farm (Section 5.3.1). Power extraction and kinetic power curves for cases (*a*) and (*c*) are very similar. Results show that case (*b*) yields a higher maximum $\bar{P}_e$ in the strait than cases (*a*) and (*c*). Case (*b*) also yields higher $\bar{P}_k$ than cases (*a*) and (*c*) due to high local velocities experienced at the low resistance area between the island and farm. This occurs because in case (*b*) no extraction is implemented in the area between the rectangular farm and the circular island.

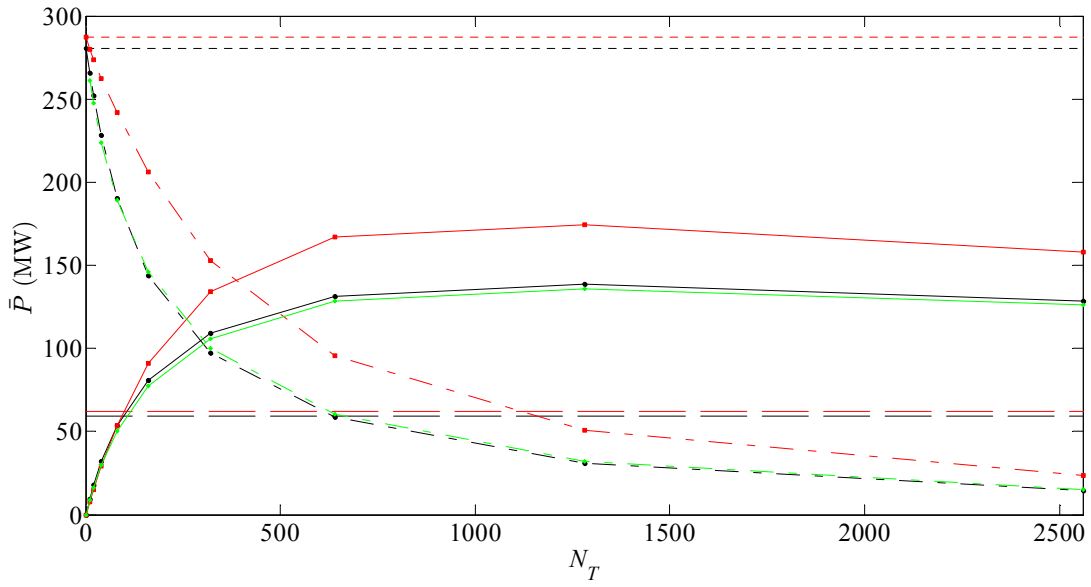


Figure 5.32. Power profiles as functions of $N_T$ for a strait between an island and landmass: rectangular farm of dimensions $h$ x $\varnothing_i$ (black); rectangular farm of dimensions ($\varnothing_i$ + $h$) x $\varnothing_i$ (red); rectangular farm with length equal to $\varnothing_i$ / 2 implemented along the circular contour of the island and filling the entire strait (green). Extracted power for tidal farm located in the strait (solid line), kinetic power for the strait with the tidal farm present (dash-dot line), kinetic power for undisturbed conditions in the strait (dotted line) and natural power dissipated on the seabed at the strait (dashed line).

The area between island and farm represents a low resistance path to the flow, which combined with geometry effects due to the circular shape of the island, increases local velocities (Figure 5.33*b*). The cubed relationship between velocity and power extracted explains the higher power extracted figures observed in case (*b*). Farm layouts (*a*) and (*c*) ensure a uniform resistance distribution to the flow across the entire strait cross-section (Figure 5.33*a* and *c*), thus excluding the presence of a low resistance flow path. This is confirmed as both cases (*a*) and (*c*) yield a similar maximum $\bar{P}_e$.

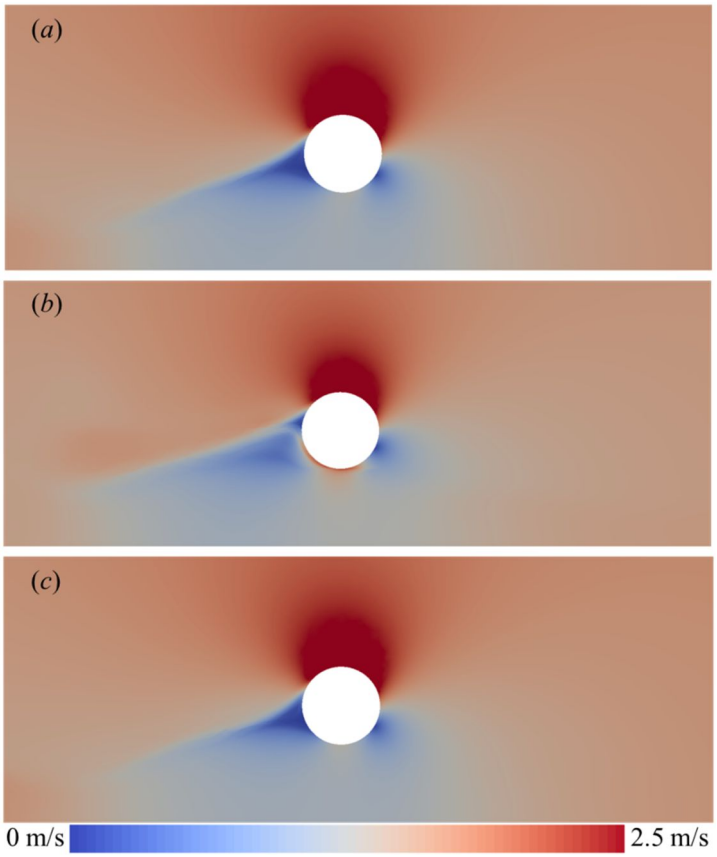


Figure 5.33. Contour flow speed plots obtained for farm cases (*a*), (*b*) and (*c*) with an equivalent number of turbines $N_T$ = 1,280 turbines at peak flow propagating from east to west of the domain.

The near independence of the power extracted at the strait to the choice of the area of the farm observed in cases (*a*) and (*c*) agrees with the results from the sensitivity analysis of the influence of farm area carried out in a channel connecting two infinite ocean basins in Section 4.9. In both strait and channel examples the flow is constrained by the presence of the island-landmass and channel sides respectively. This conclusion may vary if power extraction is implemented at the offshore side of the island, where flow is only partially constrained by the island [13].

#### 5.3.1.5 Strait blockage by tidal farm

In actual sites, the area where turbines can be installed may be constrained due to technical (e.g. minimum water depth needed for turbine technology), commercial (e.g. shipping routes), environmental (e.g. mammal migratory routes) and social (e.g. local community acceptance) factors. Consequently, the design of the original farm layout may have to be modified to comply with these limitations and the final farm layout may differ from the

optimum from a power generation point of view. This section analyses the effects on the power extracted at the strait when tidal farms cannot block the entire cross section of the strait. Nishino and Wilden [153] explored the efficiency of turbines of an array of tidal turbines partially blocking a wide channel. For small blockage ratios Nishino and Wilden found an increase in turbine efficiency with a reduction in the intra-turbine spacing until there was a reduction of flow through the entire array. For high blockage ratios the efficiency of turbines increases monotonically with the reduction of intra-turbine spacing.

The analysis is carried out using the non-uniform seabed scenario analysed in Section 5.3.1 (Figure 5.11). Here, three cases of array to strait width ratios are analysed (Figure 5.34): (*a*) turbines are installed across the entire cross-section of the strait, independent of water depth; (*b*) turbines are only installed where depths are equal or greater to $h$, representing an effective 80 % blockage of the strait; and (*c*) turbine installation is constrained by minimum water depth and for environmental reasons there is a minimum clearance between farm and island and farm and landmass of $0.2\emptyset_i$, leading to an effective strait blockage of 60 %.

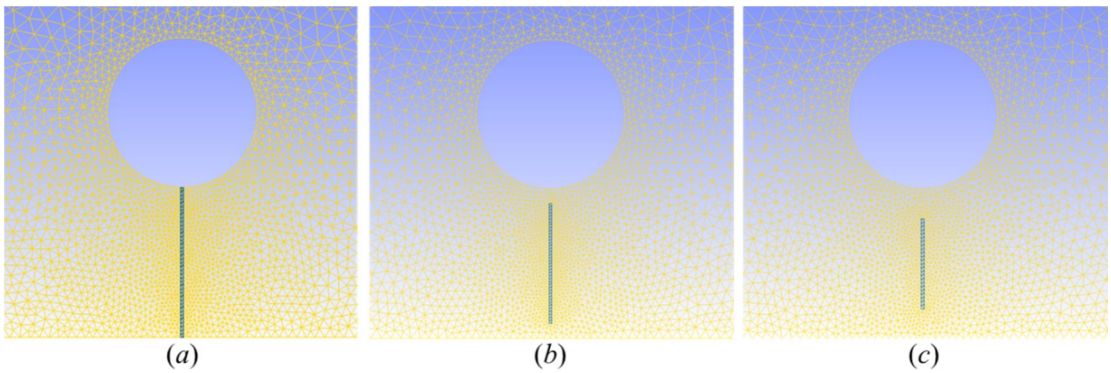


Figure 5.34. Grids used in the assessment of three blockage ratios in a strait with power extraction: (*a*) 100 % blockage; (*b*) 80 % blockage; and (*c*) 60 % blockage.

Figure 5.35 plots the (three-tide) period-averaged power coefficients, $\bar{P}_{ko}$, $\bar{P}_s$ , $\bar{P}_k$ and $\bar{P}_e$, for the three strait blockage ratio cases analysed, against the equivalent number of turbines in the farm. The reduction in blockage ratio leads to alternative low resistance flow paths within the strait, which are then translated into three effective bypass flow paths in the system island-landmass (Figure 5.36): the route between the farm and the landmass; the route between the farm and the island; and the route through the offshore side of island. The 60 % blockage ratio case leads to lower maximum $\bar{P}_e$ at the strait than the other two cases. The 80 % blockage ratio yields a maximum $\bar{P}_e$ in the same range as in the 100 % blockage ratio case but for a lower number of turbines and consequently lower $k_f$. The reduction of water depth between farm and island and farm and landmass increases frictional resistance, which limits

the bypass flow and explains why the 80 % and 100 % blockage ratio cases yield similar results. In addition, higher $\bar{P}_e$ values are achieved in the 80 % blockage ratio case than in the 100 % case when the number of turbines is below 1280. This has important implications for site selection and tidal array design as it shows that it is not critical to implement power extraction at shallow regions of the strait (e.g. by using turbines of smaller size and power rating) to reduce or prevent bypass flow. Interestingly, for a number of turbines fewer than 200, which as discussed in Section 5.3.1 is likely to be commercially viable, the 60 % blockage ratio case yields similar $\bar{P}_e$ to the 100 % blockage case. The results agree with Nishino and Wilden [153] as in the 60 % blockage ratio case power increases with array density until flow through the farm starts to diminish, but power extraction continues to increase with array density in the 100 % blockage ratio case. The rates of decrease in $\bar{P}_k$ are lower as strait blockage ratio is decreased because the flow velocity reduction in the farm area is counterbalanced by an increase of flow velocity in the bypass regions of the strait. However, high levels of power extraction with partial blockage could lead to significant increases in flow velocity in the bypass regions, leading to local seabed erosion.

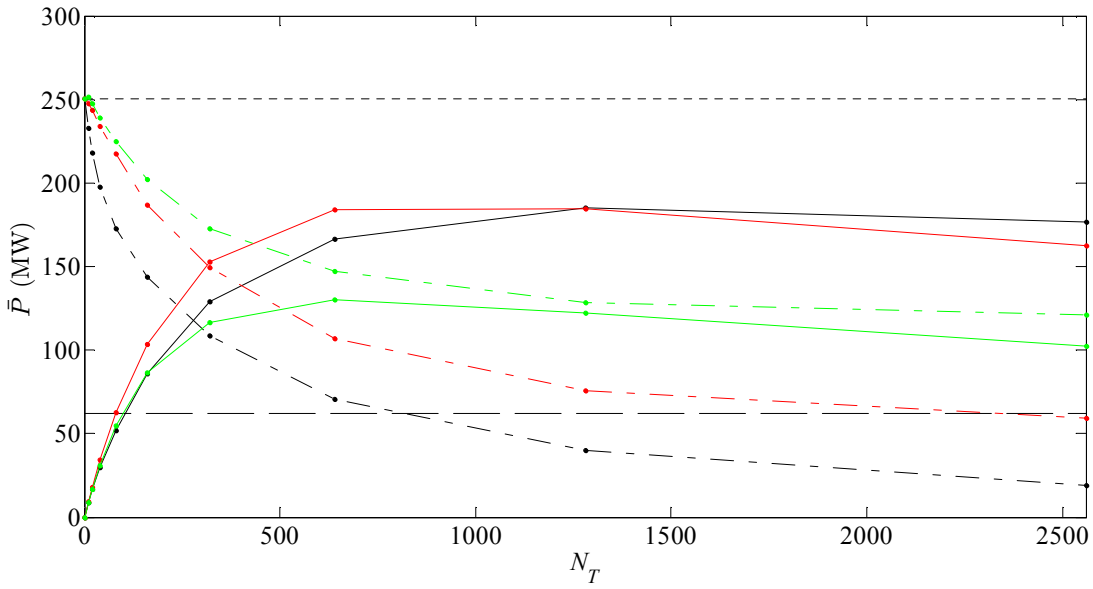


Figure 5.35. Power profiles as functions of $N_T$ for a strait between an island and landmass for three extraction blockage ratios in the strait: 100 % (black); 80 % (red); and 60 % (green). Extracted power for tidal farm located in the strait (solid line); kinetic power for the strait with the tidal farm present (dash-dot line); kinetic power for undisturbed conditions in the strait (dotted line); and natural power dissipated on the seabed at the strait (dashed line).

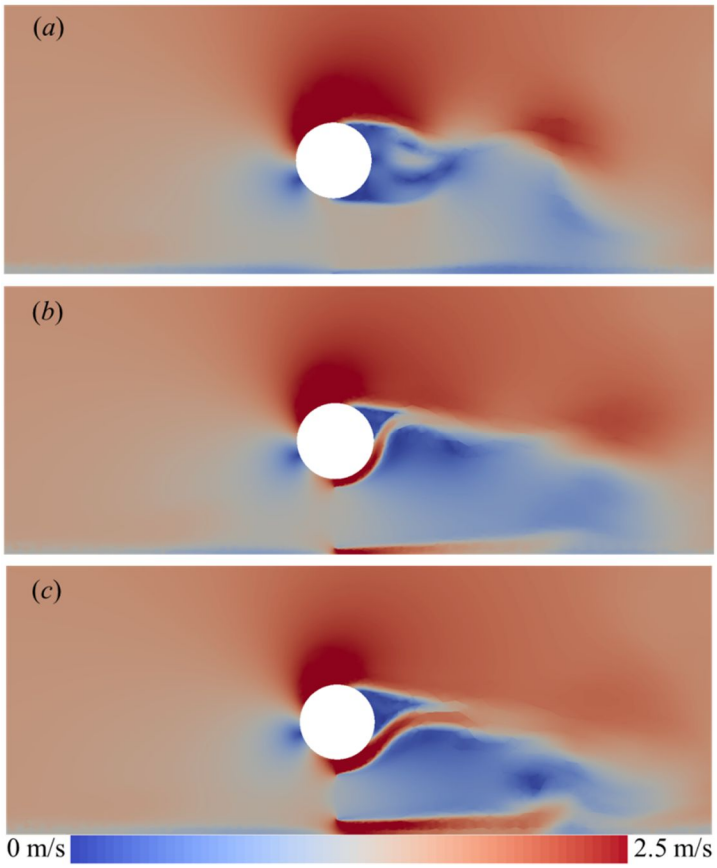


Figure 5.36. Contour flow speed plots for $N_T$ = 1,280 turbines, flow from west to east, and strait blockage ratios: (*a*) 100 %; (*b*) 80 %; and (*c*) 60 %.

Figure 5.37 shows volumetric flow rate ratios obtained for the three blockage ratios in the strait. It can be seen that the volumetric flow rate through the strait exhibits a similar trend to $\bar{P}_k$, with lower strait blockage ratios having a lower impact on the flow through the strait. The increase in power extraction leads to similar decay rates in the flow through the farm in both the 60 % and 80 % blockage ratio cases. The decrease in volumetric flow rate through the farm is balanced by an increase in the flow through the bypass routes in the strait, and this increase is higher in the 60 % than in the 80 % blockage ratio case. Half of the bypass routes in the 60 % blockage ratio case occur for a water depth $h$, indicating why this may present higher rates of increase in the bypass flow. It appears that higher bypass flow rates offshore of the island are achieved in the 60 % and 80 % blockage ratio cases. These results may be explained by complex flow dynamic interactions between power extraction, and farm and island geometries (Figure 5.36) which require further analysis.

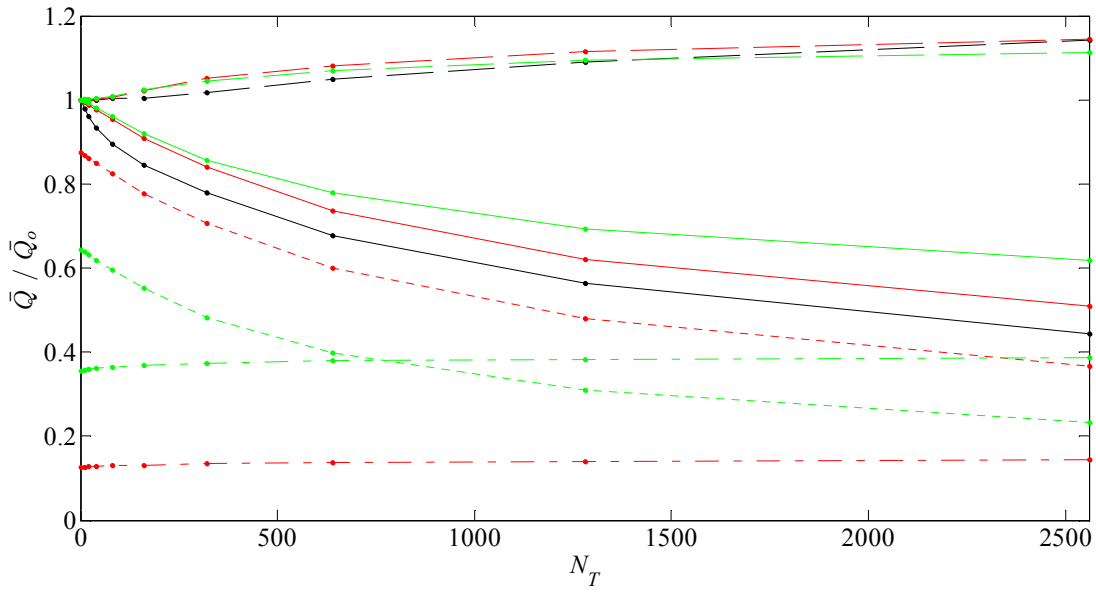


Figure 5.37. Variation in ratio of volumetric to undisturbed flow rates as a function of the number of turbines for three extraction blockage ratios in the strait: 100 % (black); 80 % (red); and 60 % (green). Volumetric flow rate across the strait (solid line); through the farm in the strait (dotted line); bypassing the farm at the strait (dash-dot line); and through a cross-section of identical length as the strait at the offshore side of the island (dashed line).

#### 5.3.1.6 Power extraction capping

The conversion of $k_f$ into an equivalent number of turbines in the farm applied in previous sections assumed a constant value for the supporting structure drag $C_D$ and rotor thrust $C_T$. However, in reality the parameter $C_D$ is a function of local flow velocity and may change with time with increasing bio-fouling growing on the supporting structure. Moreover, the value of $C_T$ varies with local flow speeds and angle of attack of flow experienced by the turbine blades. Turbine blades can be pitched to reduce power output to rated power above rated flow speeds. If the ratio between the power coefficient $C_P$ and thrust coefficient $C_T$ is constant, the $C_T$ curve can be parameterised as follows [49] (Figure 5.38):

$$C_T = \begin{cases} 0 & \text{if} \quad U < U_C \\ C_{T0} & \text{if} \quad U_C \leq U \leq U_R \\ \dfrac{C_{T0}}{C_{P0}} \dfrac{2P_R}{\rho A_T U^3} & \text{if} \quad U > U_R \end{cases} \tag{5.6}$$

For current speeds between $U_C$ and $U_R$, the suggested design values $C_{P0}$ = 0.45 and $C_{T0}$ = 0.80 from Bahaj *et al*. [154] are used.

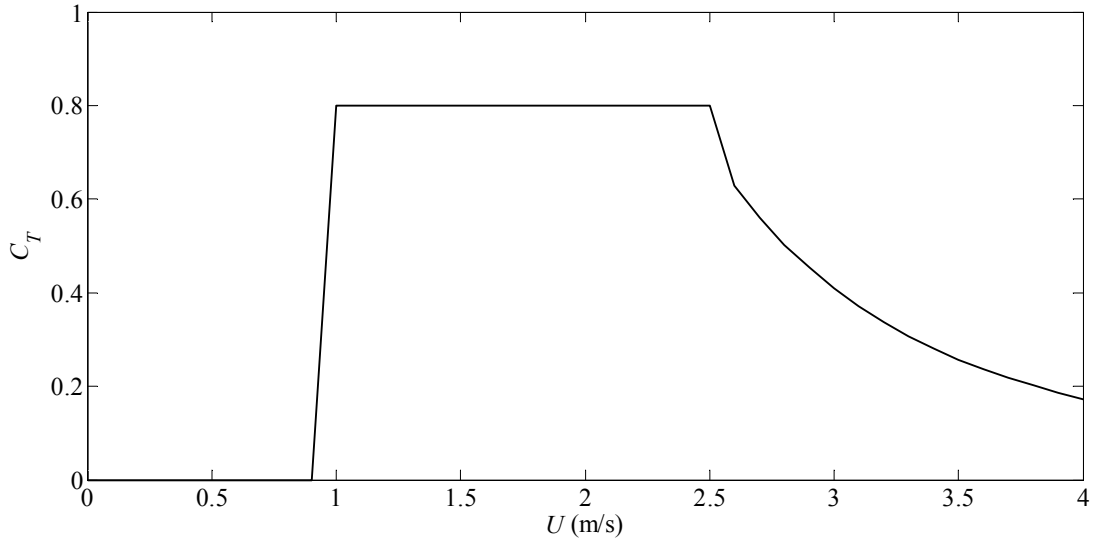


Figure 5.38. Turbine $C_T$ curve based on incident flow speed between 0 and 4 m/s [49].

Figure 5.39 shows the (three-tide) period-averaged power coefficients, $\bar{P}_{ko}$, $\bar{P}_s$ , $\bar{P}_k$ and $\bar{P}_e$, obtained for constant and variable thrust cases as functions of the equivalent number of turbines in the farm. Here the number of turbines is kept below 320, where, according to Table 5.2, the resulting capacity factor of the farm may be still economically viable. $\bar{P}_e$ is similar for both constant and variable $C_T$, with the most obvious difference below 160 turbines; as expected, the reduction in $\bar{P}_k$ for the variable $C_T$ is lower than when $C_T$ is constant because turbines with variable $C_T$ exert lower forces on the flow and thus lead to lower reductions in the flow momentum.

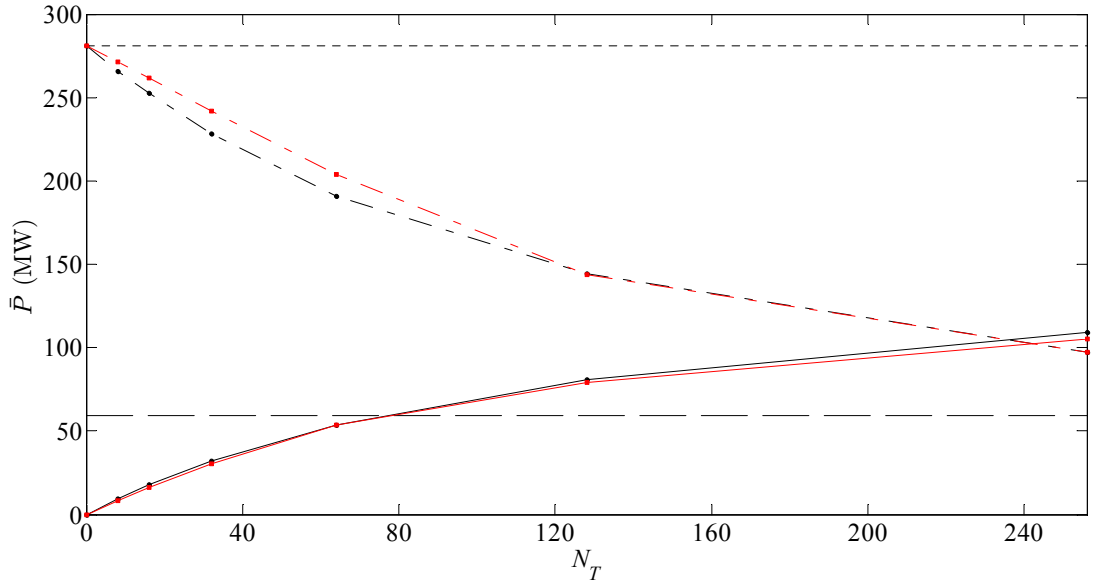


Figure 5.39. Power profiles as functions of $N_T$ for a strait between an island and landmass: tidal turbines implemented with constant $C_T$ (black); and local flow speed dependent $C_T$ (red). Extracted power for tidal farm located in the strait (solid line); kinetic power for the strait with the tidal farm present (dash-dot line); kinetic power for undisturbed conditions in the strait (dotted line); and natural power dissipated on the seabed at the strait (dashed line).

Table 5.5 lists the (three-tide) period-averaged power coefficients $\bar{P}_T$ generated by the tidal array, the array capacity factor *CF*, the cross-sectional velocity deficit $\bar{U}_o^*$, and the kinetic power deficit $\bar{P}_k^*$ values for an equivalent number of turbines between 10 and 320 with constant and velocity-dependent $C_T$. For $N_T \leq 80$, the velocity-dependent $C_T$ has a lower impact on $\bar{U}_o^*$ and $\bar{P}_k^*$ and thus it leads to higher $\bar{P}_T$ and *CF* than for the case with constant $C_T$. For $N_t > 80$, the flow speeds within the farm lie between $U_C$ and $U_D$, and $C_T$ is constant and equal to 0.8. Consequently, at these levels of extraction both constant and velocity-dependent $C_T$ scenarios display very similar results. Although the characterisation of tidal turbines with a constant thrust coefficient simplifies the complexity of the system, Table 5.5 highlights that this methodology underestimates the resource available and increases the effects on the environment as opposed to modelling the turbines with a realistic thrust curve. The ability to adapt rotor thrust to incoming flow velocity (e.g. via blade pitching or stall-regulated blades) reduces the turbine loading while also controlling turbine output power. This enables turbines to generate power more efficiently with less impact on the ambient flow field.

| $N_T$ | 10 | | 20 | | 40 | | 80 | | 160 | | 320 | |
|---|---|---|---|---|---|---|---|---|---|---|---|---|
| $C_T$ | Ct | f ($U$) | Ct | f ($U$) | Ct | f ($U$) | Ct | f ($U$) | Ct | f ($U$) | Ct | f ($U$) |
| $\bar{P}_T$ [MW] | 3.7 | 3.8 | 7.2 | 7.3 | 13.4 | 13.9 | 23.2 | 24.3 | 35.5 | 35.4 | 47.2 | 47.0 |
| $CF$ [%] | 37.2 | 37.7 | 35.9 | 36.7 | 33.5 | 34.6 | 29.0 | 30.3 | 22.2 | 22.1 | 14.8 | 14.7 |
| $\bar{U}_o^*$ [%] | 1.6 | 1.1 | 3.1 | 2.1 | 5.9 | 4.4 | 10.7 | 9.1 | 17.7 | 17.7 | 26.9 | 26.7 |
| $\bar{P}_k^*$ [%] | 5.4 | 3.4 | 10.2 | 6.8 | 18.8 | 13.9 | 32.1 | 27.5 | 48.6 | 48.8 | 65.3 | 65.3 |

Table 5.5. Three-tide period-averaged tidal farm power generated, tidal farm capacity factor, percentage decrease in mean strait velocity and percentage decrease in mean kinetic power according to the equivalent number of turbines in the strait, when turbines are represented with a $C_T$ constant or function of velocity.

#### 5.3.1.7 Offshore power extraction

The previous sections have examined the sensitivity of power extraction in the strait to changes in several model parameters. It has been found that power extraction at the strait affects the flow pattern around the island and increases the bypass flow through the offshore side of the island. Atwater and Lawrence [52] studied the effects of power extraction on the relative flows in a split tidal channel. Atwater and Lawrence concluded that although small levels of extraction may not alter the total flow through the channel, they can drastically affect the relative flows in sub-channels and thus power extraction levels from the channel. This has been also considered by Cummins [40], Draper et al. [39], Polagye and Malte [53] and Woolf [155] who approximated the multiple flow path problem by an analogue electric circuit (Section 2.2.2). The offshore side of the island is usually associated with deeper water but not necessarily slower flow regimes (e.g. the Outer Sound in the Pentland Firth [51]). However, as tidal turbine technology advances into deeper waters, it is worth investigating the limits of extraction on the offshore side of the island-landmass system [62] [81]. In the future, this would become a two-path island-landmass system, whereby extraction levels at each side of the island may be interconnected [156] (e.g. Inner Sound, Section 2.3.4).

The two methodologies highlight that power extraction at both sides of the island could be designed to maximise the total power generated from the site. Power extraction is

implemented in the offshore side of the island of the free-slip scenario model over a rectangular area of dimensions $L_f$ x $B_f$, of equal area to that used in the strait of the island-landmass system. The farm extends towards the north of the domain from the northern edge of the island and it is located at the same stream-wise coordinates in the domain as the farm in the strait. Although inclusion of power extraction north of the island increases net blockage of the domain by 50 %, no effect on the resource assessment is expected because the width of the domain is sufficiently large. Table 5.6 lists the (three-tide) period-averaged power coefficient $\bar{P}_T$, farm *CF*, $\overline{U}_o^*$ and $\bar{P}_k^*$ deficit for seven power extraction scenarios at strait and offshore side of the island. Similar $\bar{P}_T$ and *CF* are obtained when identical $k_f$ are applied in the strait or offshore side of island. With regard to changes in $\overline{U}_o^*$ and $\bar{P}_k^*$ due to power extraction, a slightly higher percentage decrease is experienced when power is extracted in the strait than offshore of the island. Moreover, the increase in $\overline{U}_o^*$ and $\bar{P}_k^*$ on the side of the island where there is no extraction is significantly higher when extraction is implemented at the offshore side of the island than when extraction is in the strait. In Scenario 5, when extraction rates $k_f$ = 0.14 are applied both in the strait and offshore of the island, there is a 50 % increase in $\bar{P}_T$ compared to Scenarios 1 and 3 where an extraction rate of $k_f$ = 0.28 is applied solely at one side of the island. In Scenario 6, $k_f$ is increased to 0.28 at both sides of the island and a comparison of $\overline{U}_o^*$ and $\bar{P}_k^*$ against the corresponding results from Scenario 1 reveals that the reductions in velocity and kinetic power at both sides of the island decrease when equal extraction levels are implemented both sides of the island. This can be also seen when comparing Scenario 7 to Scenarios 2 and 4.

| *Scenario* | Island Side | $k_f$ | $N_T$ | $\bar{P}_T$ [MW] | $CF$ [%] | $\bar{U}_o^*$ [%] | $\bar{P}_k^*$ [%] |
|---|---|---|---|---|---|---|---|
| *1* | S | 0.28 | 160 | 35.5 | 22.2 | -17.7 | -48.6 |
| | O | 0 | 0 | n.a. | n.a. | +3.6 | +30.0 |
| *2* | S | 0.56 | 320 | 47.2 | 14.8 | -26.9 | -65.3 |
| | O | 0 | 0 | n.a. | n.a. | +7.5 | +46.0 |
| *3* | S | 0 | 0 | n.a. | n.a. | +12.3 | +46.9 |
| | O | 0.28 | 160 | 35.3 | 22.0 | -14.4 | -42.8 |
| *4* | S | 0 | 0 | n.a. | n.a. | +17.4 | +68.6 |
| | O | 0.56 | 320 | 48.5 | 15.1 | -23.2 | -60.1 |
| *5* | S | 0.14 | 80 | 27.9 | 34.8 | -4.5 | -15.3 |
| | O | 0.14 | 80 | 25.8 | 32.3 | -3.2 | -12.3 |
| *6* | S | 0.28 | 160 | 50.0 | 31.3 | -8.4 | -26.7 |
| | O | 0.28 | 160 | 46.9 | 29.3 | -6.2 | -23.1 |
| *7* | S | 0.56 | 320 | 79.2 | 24.7 | -15.0 | -43.0 |
| | O | 0.56 | 320 | 75.2 | 23.5 | -12.0 | -39.2 |

Table 5.6. Extraction levels and equivalent number of turbines in the strait (S) and offshore side (O) of the island. The table lists values for the (three-tide) period-averaged array power generated, tidal farm capacity factor, percentage decrease in mean strait velocity, and percentage decrease in mean kinetic power.

Table 5.6 reveals that tidal extraction at an island-landmass can be optimised for power generation considering the system as a two flow path problem. Addition of power extraction to the north of the island displaces the bypass flow path even further north and this is likely to affect extraction at the strait. As mentioned earlier, one way to investigate this problem further could be through the use the electrical analogy theory (Section 2.2.2).

However, power extraction at both sides of an island may not be always technically feasible. Sites that fall into the category of island-landmass, such as the Inner Sound in north of Scotland [94], have water depths up to 80m offshore of the island (Outer Sound). First-generation tidal turbines are limited to relatively shallow waters ($h$ < 50m) [157]. However, this technical limitation may be overtaken in coming years with the development of second- and third-generation tidal turbines designed to operate in deeper waters [148].

### 5.3.2 Isolated offshore island

This section assesses the resource in the vicinity of an island located sufficiently far from the coast that the effect of the landmass is negligible. The distance between island and landmass $s$ is set to $9.5Ø_i$, and the system is considered as an isolated offshore island. Power extraction is implemented in the south side of the island over a rectangular area of dimensions $L_f$ x $B_f$. The spatial discretisation of the model follows that of Mesh 4 presented in Table 5.1. The mesh contains 7,341 nodes and 14,682 elements (Figure 5.40). A regular grid of 80 isosceles triangles is used at both sides of the island. Power extraction is set up only in the south side of the island.

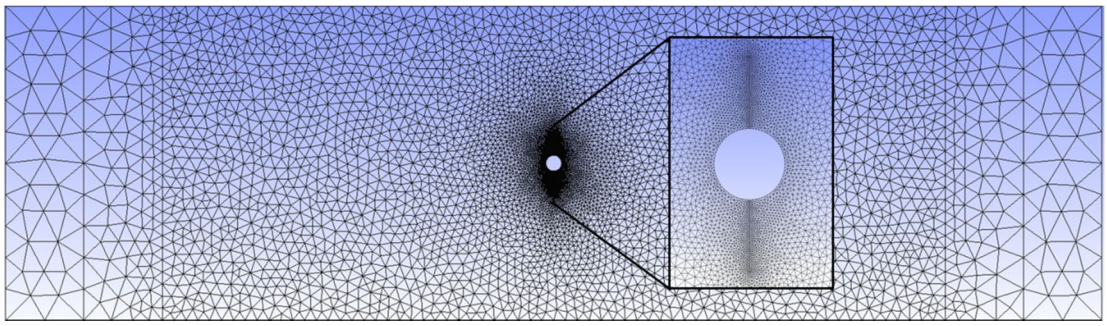

Figure 5.40. Unstructured spatial discretisation of the isolated offshore island domain, with a regular grid used at both sides of the island.

As in the island-landmass baseline system, both free-slip and no-slip boundary conditions are used to delineate the island. This enables analysis of the effect of the landmass on resource assessment for the two types of island wall boundary condition. Free-slip conditions are applied to the south and north lateral limits of the domain. Considering the analysis of the island-landmass baseline system (Section 5.3.1), from Figure 5.41 it can be seen that the free-slip and no-slip scenarios may also represent lower and upper bounds for the (three-tide) period-averaged $\bar{P}_e$ for the isolated offshore island. From Figure 5.41 it is evident that there is no clear relationship between the maximum $\bar{P}_e$ and the $\bar{P}_s$. In addition, $\bar{P}_{ko}$ measured at a cross sectional transect (of width equal to $B_f$) south of the island does not provide a useful measure by which to estimate the maximum power extracted. As in the island-landmass baseline system, the rate of decrease of $\bar{P}_k$ at low extraction levels ($k_f < 0.14$) is considerably higher for the free-slip condition than the no-slip condition.

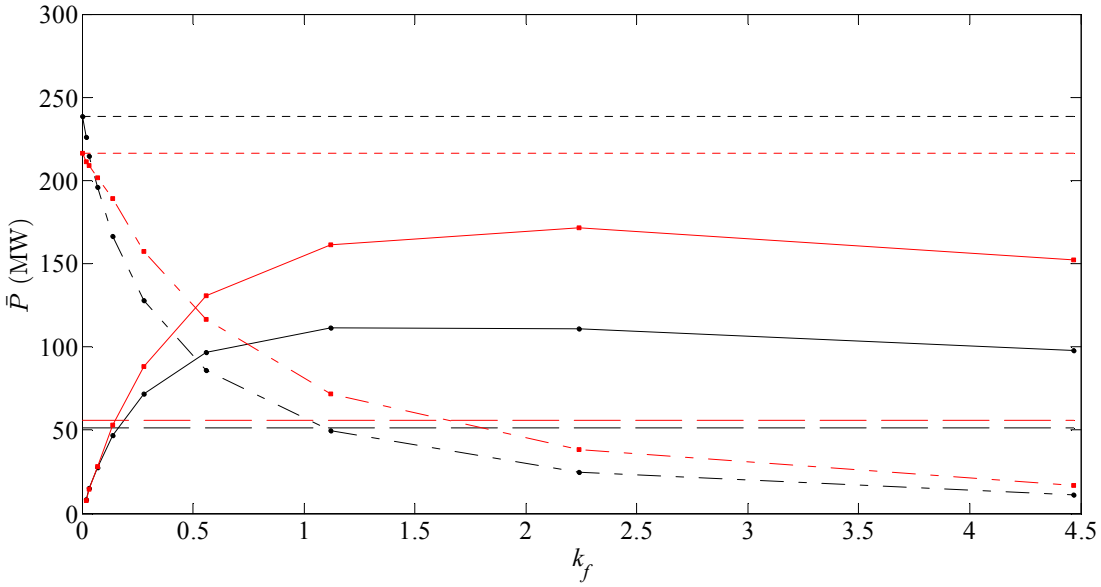


Figure 5.41. Power profiles as functions of $k_f$ for a tidal farm located south of an isolated offshore island: free-slip (black); and no-slip (red) solid boundaries. Power extracted at farm located south of the island (solid line); kinetic power measured across the tidal farm (dash-dot line); kinetic power measured across the tidal farm in undisturbed conditions (dotted line); and natural power dissipated on the seabed south of the island (dashed line).

The ratios of extracted power to the undisturbed kinetic power $\hat{P}$ for the free-slip and no-slip scenarios are 0.47 and 0.79 respectively. Compared to the island-landmass baseline system, there is an 18 % decrease for the no-slip scenario, while the free-slip values remain similar. Under the same tidal conditions, there is an increase in kinetic power available in the strait in the island-landmass baseline system compared to an isolated island because the landmass acts to constrain the flow. However, this effect is diminished when considering the ratio of power extracted to the undisturbed kinetic power, and the rates of decay of kinetic power at low levels of power extraction.

Figure 5.42 presents the non-dimensional volumetric flow rates through cross-sectional transects of width $B_f$ at the south and north sides of the island. Comparison between Figure 5.42 and the variation in volumetric flow rate in the island-landmass baseline system (see Figure 5.17) show that the rates of decrease of flow due to power extraction and consequent increase of bypass flow in the island system are very similar to those computed for the island-landmass baseline system.

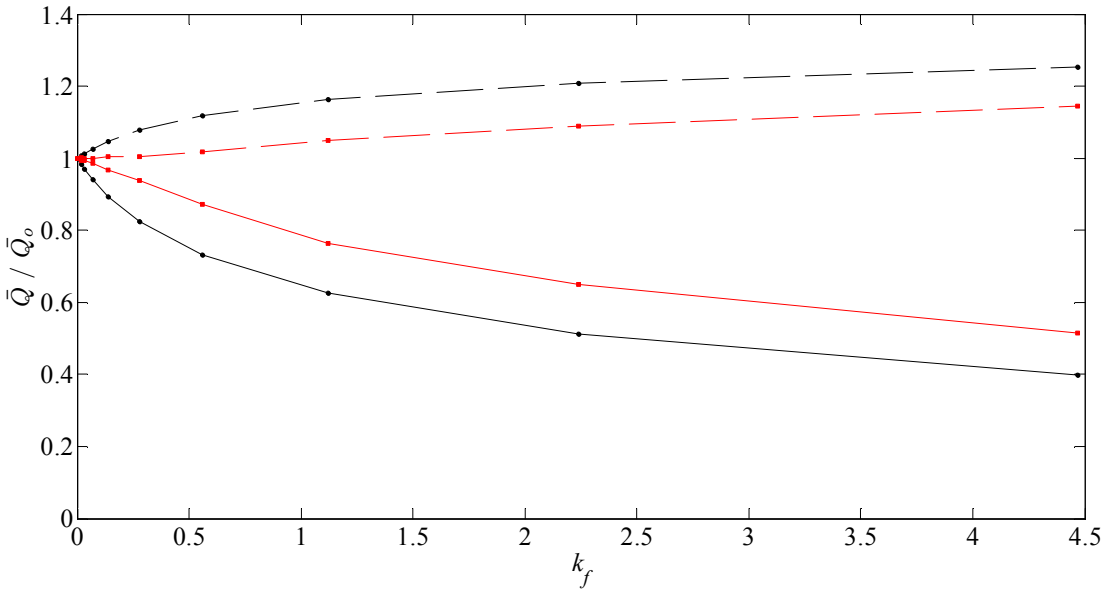


Figure 5.42. Variation of ratio of predicted to undisturbed volumetric flow rate for the free-slip (black) and no-slip (red) island boundary conditions at different levels of power extraction: volumetric flow rate across the tidal farm (solid line); and scale flow through a cross-section of identical length at the north side of the island (dashed line).

### 5.3.3 Geometrically long island

This section analyses the sensitivity of the tidal resource at the strait to the length of the island. The length of the island is equal to $L_i = 800h = 0.0362\lambda$ while the width of the island and strait remain $B_i = s = 50h = 0.00226\lambda$. The tidal farm is located at the narrowest part of the strait with a geometry length $L_f = h$ and width $B_f = s$ midway along the island in the stream-wise direction. The model is spatially discretised following the criteria used for Mesh 4 shown in Table 5.1. A regular grid containing 80 isosceles triangles is used to define the tidal farm. The resulting mesh contains 19,335 vertices and 38,670 elements (Figure 5.43).

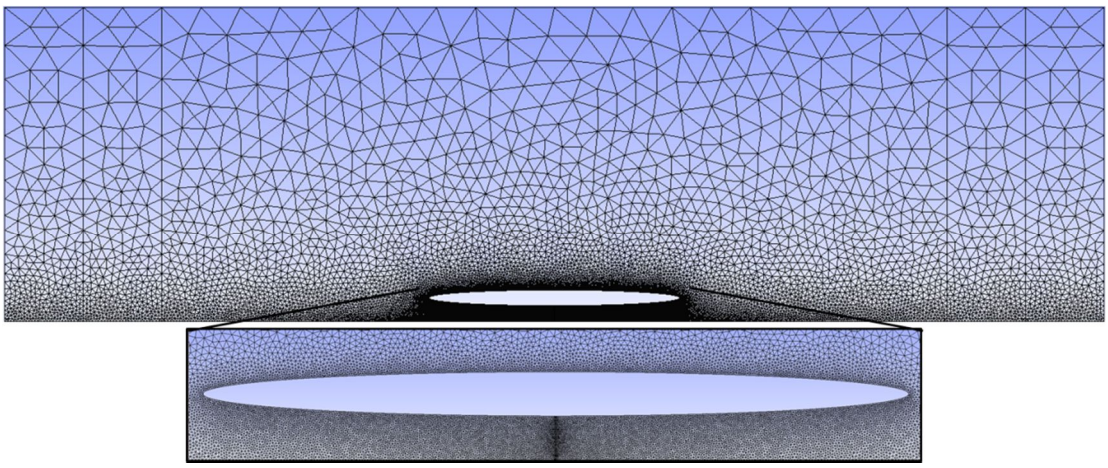

Figure 5.43. Unstructured spatial discretisation of the domain with an island with high length to width ratio, with a regular grid in the strait used to define the tidal farm.

Free-slip and no-slip scenarios are used to analyse the effects on extracted power arising from the boundary conditions defined at the island and landmass. The predictions are compared against results previously obtained for the island-landmass system in Section 5.3.1. Figure 5.44 shows the contour flow speed plots at peak west-east flow through the channel for the free-slip and no-slip scenarios. Unlike the bluff-body circular island-landmass case with no-slip condition (Figure 5.12), the present elliptic geometry appears streamlined, and does not generate any vortical structures through vortex shedding from the island.

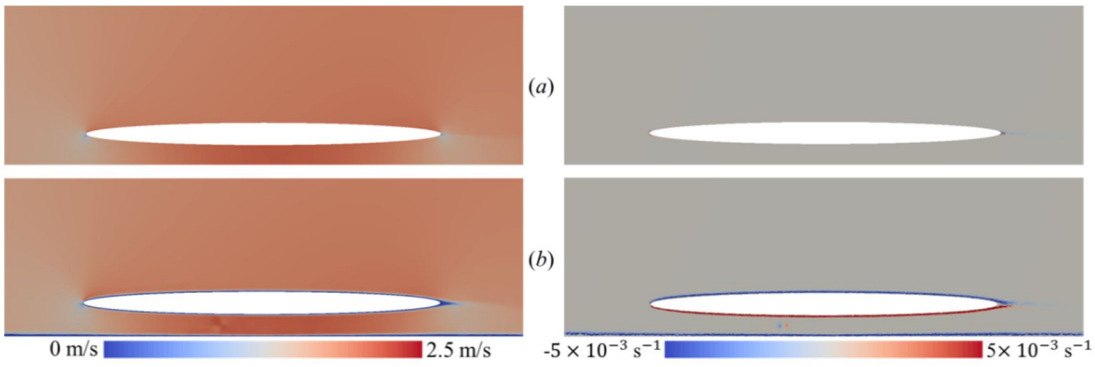


Figure 5.44. Contour flow speed (left) and vorticity (right) plots for flow travelling from west to east past a geometrically long island: (*a*) free-slip; and (*b*) no-slip boundary conditions.

Figure 5.45 plots the resulting (three-tide) period-averaged power coefficients, $\bar{P}_{ko}$, $\bar{P}_s$ , $\bar{P}_k$ and $\bar{P}_e$, obtained for the free-slip and no-slip scenarios over a range $k_f$ values between 0 and 18. Compared to the circular island-landmass baseline system, here $\bar{P}_s$ is of the order of three times larger than $\bar{P}_{ko}$, which is in agreement with the larger seabed footprint of the

extended elliptical island in the strait. Unlike the circular island-landmass baseline system, here the free-slip scenario yields a higher maximum $\bar{P}_e$ than for the no-slip scenario. Vortex shedding is not observed behind the island in either case (Figure 5.44). The free-slip case presents less dynamic resistance to the flow than the no-slip case, and so this is converted into a higher $\bar{P}_e$. Based on the island-landmass system analysis in Section 5.3.1, the differences between both scenarios may set an upper and lower bound for power extraction in the strait. The maximum $\bar{P}_e$ values are 9.6 % and 17.5 % lower compared to $\bar{P}_s$ in the free-slip and no-slip scenarios respectively. From the results, it appears that power naturally dissipated at the seabed may be a good indicator of maximum power extracted in the strait. Rates of decay of $\bar{P}_k$ are very similar in both free-slip and no-slip scenarios. Maximum $\bar{P}_e$ is achieved at a higher $k_f$ than in the island-landmass baseline system.

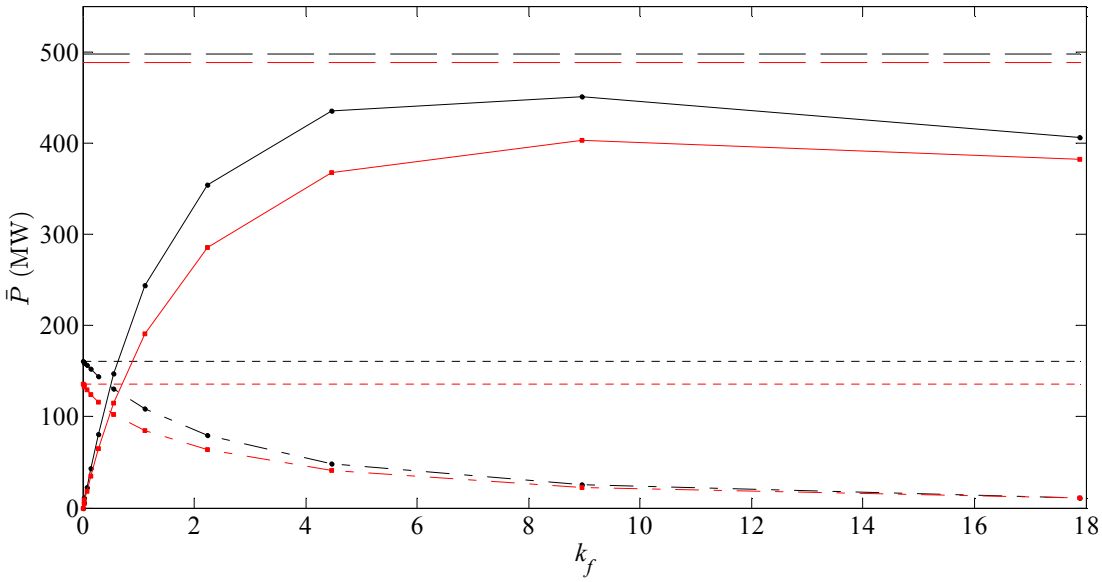


Figure 5.45. Power profiles as functions of $k_f$ for a tidal farm located in a strait between a long elliptical island and a landmass: free-slip (black); and no-slip (red) solid boundaries. Power extracted at farm located south of the island (solid line); kinetic power measured across the tidal farm (dash-dot line); kinetic power measured across the tidal farm in undisturbed conditions (dotted line); and natural power dissipated on the seabed south of the island (dashed line).

Figure 5.46 shows the variation in ratio of volumetric flow rate to that of the undisturbed flow with increasing extraction levels in the strait and offshore of the island calculated along a transect of equal width to the width of the strait. There is a lower reduction in the volumetric flow rate ratio for the no-slip scenario than the free-slip scenario. The bypass flow ratios are very similar in the free-slip and no-slip scenarios. The ratio of bypass to undisturbed volumetric flow rate for maximum $\bar{P}_e$ is equal to 1.03 and 1.02 for the free-slip

and no-slip scenarios respectively. These figures of bypass flow ratios are considerably lower than those obtained for the island-landmass baseline system (1.21 and 1.09 respectively).

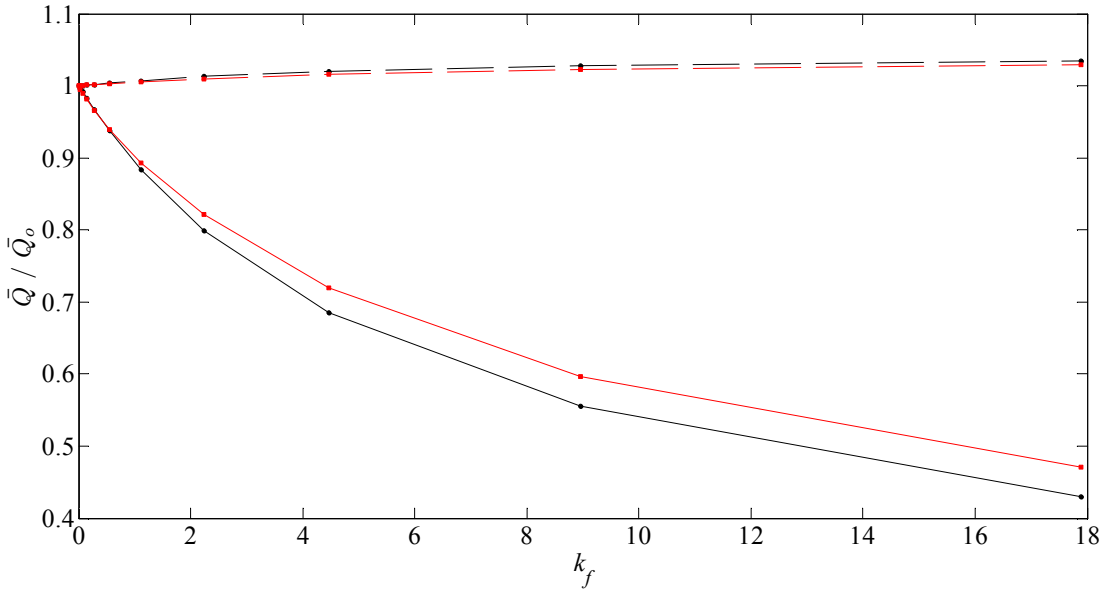


Figure 5.46. Variation in ratio of predicted to undisturbed volumetric flow rates for free-slip (black) and no-slip (red) scenarios for different levels of power extraction in the strait between the long elliptical island and landmass. Volumetric flow rate across the tidal farm (solid line) and through a cross-section of identical length at the offshore side of the island (dashed line).

Figure 5.47 plots the head driving the flow in the strait and offshore of the island for a case of no extraction and a case of extraction level $k_f$ = 8.95 in the free-slip scenario. The increase in head driving the flow due to power extraction is higher in the strait than offshore of the island.

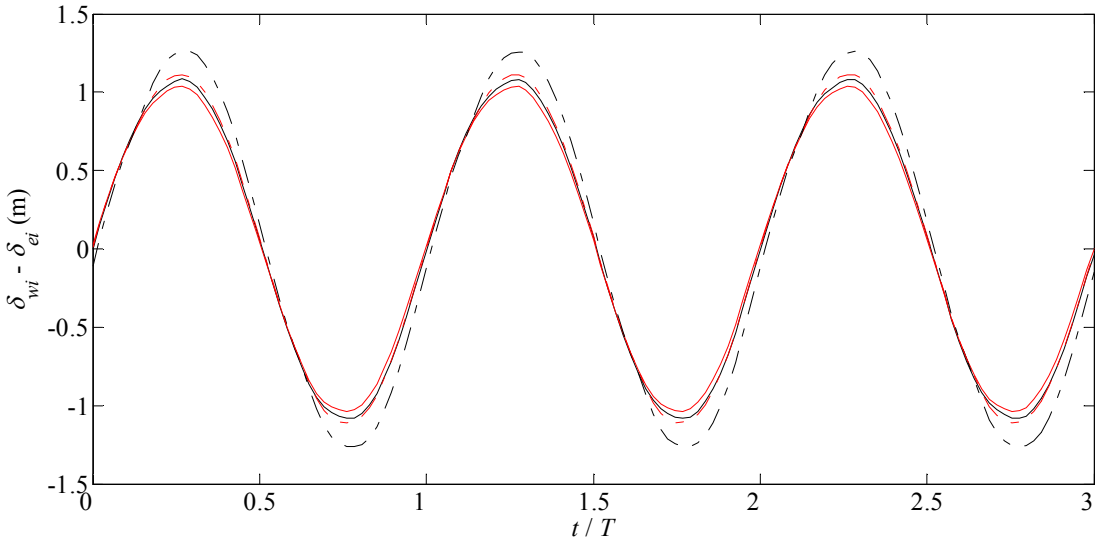


Figure 5.47. Flow-driving head between entrance and exit of the strait (black) and offshore of island (red) for the free-slip scenario: no power extraction (solid line) and very high extraction level $k_f$ = 8.95 (dash-dot line) in the strait.

In order to understand better the effects of power extraction on the head driving the flow in the strait and offshore of the island, Figure 5.48 presents a snapshot of the free surface contours when there is no extraction and when an extraction level $k_f$ = 8.95 is set in the strait. When there is no power extracted in the strait, the presence of the island leads to a slight change of phase in the free surface contours in the strait and offshore of the island. When there is high power extracted from the strait, there is a substantial change in phase and amplitude between free surface contours in the strait and offshore of the island. As shown in Figure 5.48, free surface contours offshore of the island appear not to be highly affected by power extraction in the strait. Free surface contours in the strait are highly influenced by power extraction and it can be seen that there is an increase in head driving the flow.

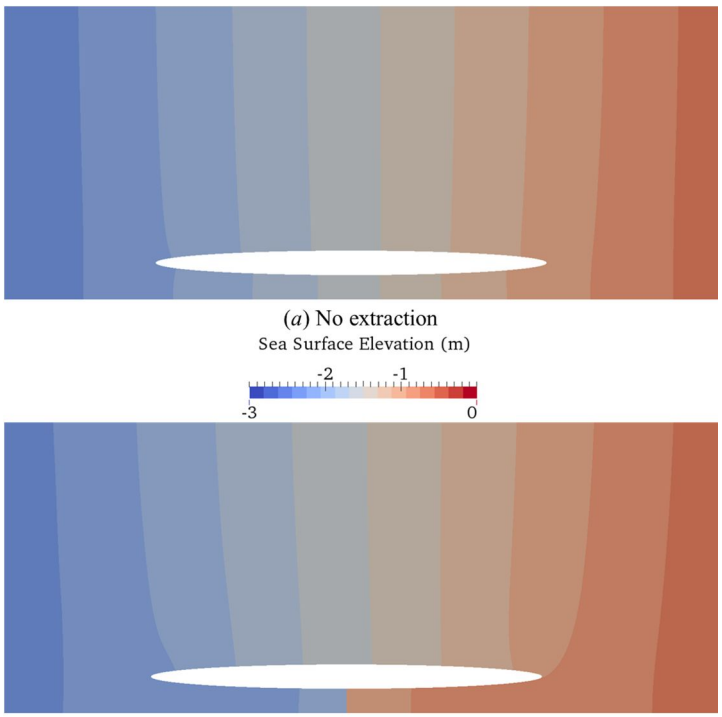


Figure 5.48. Sea surface elevation contour plots: (*a*) for no extraction at the strait; and (*b*) when maximum power is extracted from the flow at the strait for extraction level $k_f$ = 8.95.

Based on the undisturbed flow conditions and head driving the flow between the two ends of the strait in the free-slip scenario, the GC2005 channel model predicts a maximum power extracted of 411.4 MW using $\gamma = 0.22$, which is 8.6 % lower than the numerical results. If $\gamma = 0.2$ is used, derived from the phase difference between peak driving head and flow, the maximum power extracted predicted by GC2005 is equal to 374.0 MW, which represents a 16.9 % lower figure than the numerical results. The no-slip scenario yields percentage differences with the GC2005 model similar to those obtained in the free-slip scenario. From these results, it appears that the GC2005 model provides an underestimate of resource in the strait. However, comparison between these estimates and those obtained for the island-landmass baseline system demonstrates enhanced agreement between the two approaches, indicating that the strait starts behaving more like a channel as the island length increases along the coastline.

The increase in the accuracy of the resource estimates provided by GC2005 for elongated islands along the coastline agrees with findings by Sutherland *et al*. [31] in a study of the Johnstone strait at the west coast of Canada for a single open channel scenario (Section 2.3.4).

### 5.3.4 Geometrically wide island

This section analyses the sensitivity of the resource in the strait to the width of the island. The geometry of the domain used in Section 5.3.1 is modified as follows: island width is set to $B_i = 200h = 0.00904\lambda$; island length and strait width are set to $L_i = s = 50h = 0.00226\lambda$; domain length $L$ is not modified and width $B$ is increased by a factor of 4 in order to retain the same domain blockage ratio as used previously. The model is spatially discretised using the criteria for Mesh 4 in Table 5.1. A regular grid of 80 isosceles triangles defines the tidal farm in the narrowest part of the strait, filling the entire strait transect. The resulting mesh contains 10,465 vertices and 20,930 elements (Figure 5.49). The model is run with a free-slip condition applied at both island and landmass boundaries. A solution using a no-slip boundary condition was not tested because, due to the island geometry employed, the free-slip scenario already led to vorticity structures shedding from the island (Figure 5.50).

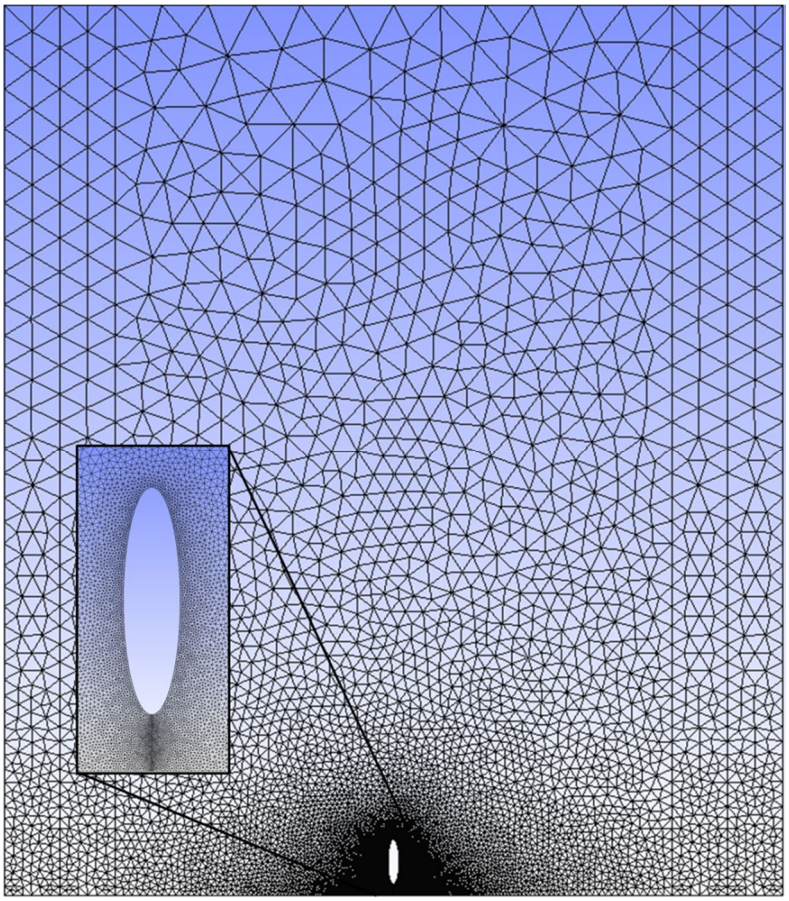

Figure 5.49. Unstructured spatial discretisation of domain containing an island of high width to length ratio, with a regular grid in the strait used to define the tidal farm.

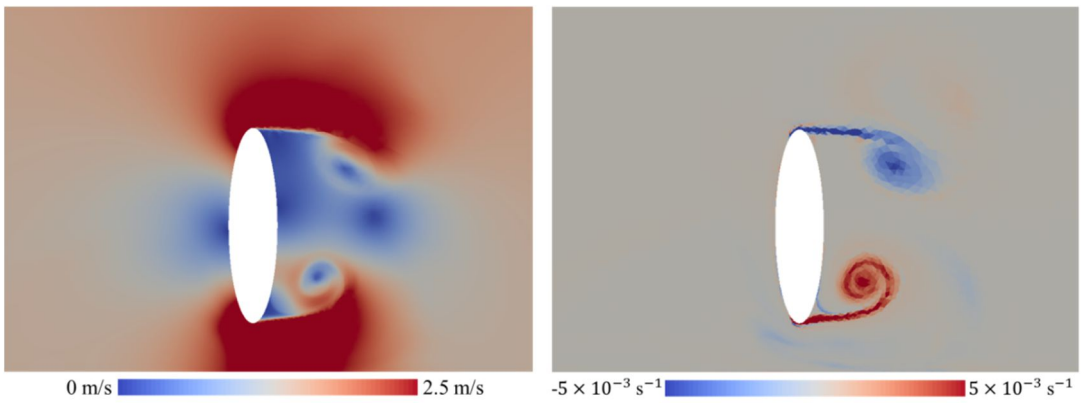


Figure 5.50. Contour plots of flow speed (left) and vorticity (right) distribution throughout domain at peak flow, with flow travelling from west to east, and free-slip boundary scenario for a geometrically wide island.

Figure 5.51 plots the resulting (three-tide) period-averaged power coefficients, $\bar{P}_{ko}$, $\bar{P}_s$ , $\bar{P}_k$ and $\bar{P}_e$, for a range of $k_f$ values between 0 and 4.5. As in previous cases analysed, neither $\bar{P}_{ko}$ nor $\bar{P}_s$ are good indicators of the maximum power extracted in the strait, with $\bar{P}_s$ providing a better estimate of the maximum power extracted than $\bar{P}_{ko}$. The maximum value of $\bar{P}_e$ is 256 % higher than the average maximum $\bar{P}_e$ obtained for the circular island-landmass baseline system (for both the free-slip and no-slip boundary scenarios). The increase in width of the island is translated into an increase in resistance of the bypass path and higher power extracted from the strait. Regarding the effect of extraction on the stream power resource in the strait, there is approximately a 38 % decrease in $\bar{P}_k$ compared to $\bar{P}_{ko}$ when $\bar{P}_e$ is one-third of the maximum value of $\bar{P}_e$. This figure is considerably higher than the rates of decrease obtained for the circular island-landmass baseline system, which are 30 % and 20 % for the free-slip and no-slip scenarios respectively.

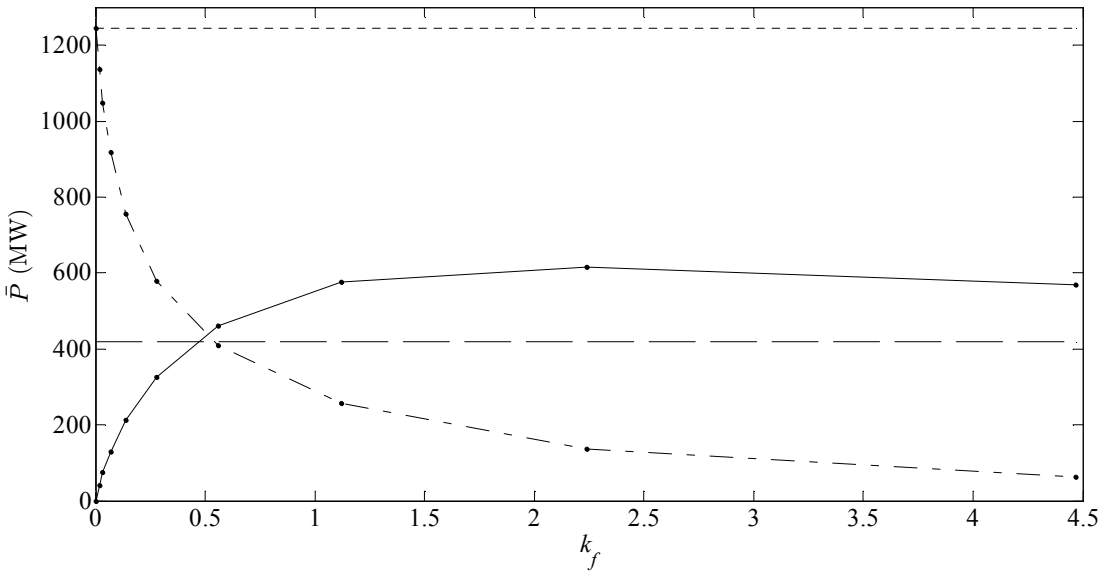


Figure 5.51. Power profiles as functions of $k_f$ for a strait between an island with high width to length ratio and landmass. Extracted power for tidal farm located in the strait (solid line); kinetic power for the strait with the tidal farm present (dash-dot line); kinetic power for undisturbed conditions in the strait (dotted line); and natural power dissipated on the seabed at the strait (dashed line).

Figure 5.52 plots the ratios of predicted to undisturbed flow for the strait and offshore of the island. As mentioned above, the bypass flow ratios obtained for an island with high width to length ratio are relatively lower than those obtained for the circular island-landmass baseline system (for both the free-slip and no-slip scenarios). At the $k_f$ level which yields maximum $\bar{P}_e$ the ratio of bypass to undisturbed volumetric flow rate is equal to 1.08. This value is lower than those values found for the island-landmass system (Figure 5.17) which are 1.21 and 1.09 for the free-slip and no-slip scenarios respectively. It appears that the geometry of the island diminishes the bypass volumetric flow rates by increasing the effective distance between the strait and the alternative flow path. This reduction in the bypass flow may be converted into an increase in extracted power from the strait.

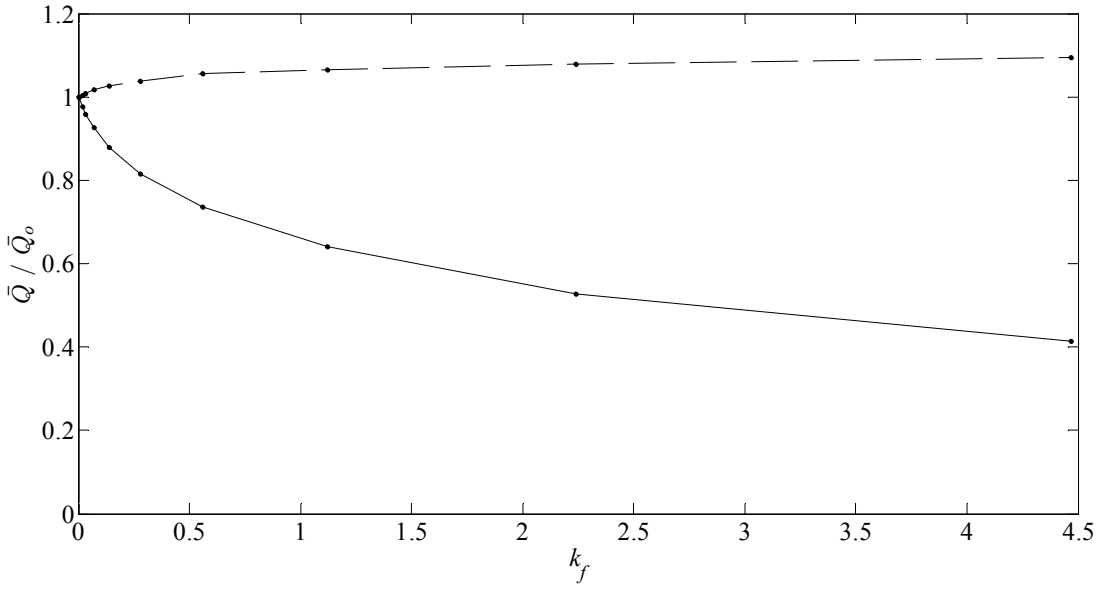


Figure 5.52. Variation in the ratio of predicted to undisturbed volumetric flow rate with power extraction level for the wide island-landmass system. Volumetric flow rate across the tidal farm (solid line) and through a cross-section of identical length at the offshore side of the island (dashed line).

Figure 5.53 plots the head driving the flow at the strait and at the offshore side of the island with no extraction and an extraction level of $k_f$ = 2.24. Eddies shedding from the island (Figure 5.50) produce local fluctuations that are superimposed on the sinusoidal signals. The head driving the flow experiences a greater increase in the strait than offshore of the island. This is in accordance with the bypass flow rates shown in Figure 5.52, and similar flow behaviour was observed in the geometrically long island case. Based on the undisturbed flow conditions at the strait and the head between the two ends of the strait, the GC2005 channel model predicts maximum power extracted of 169.5 and 161.8 MW for $\gamma$ = 0.22 and 0.21 (derived from phase difference between maximum head and flow in the strait) respectively. This value under-predicts the numerically computed results by 72.5 % and 73.7 % respectively. Based on results shown in Figure 5.52 and Figure 5.53, the differences between the numerical and analytical model results may be primarily due to increasing the head driving the flow due to power extraction and partly due to reduced bypass flow caused by power extraction.

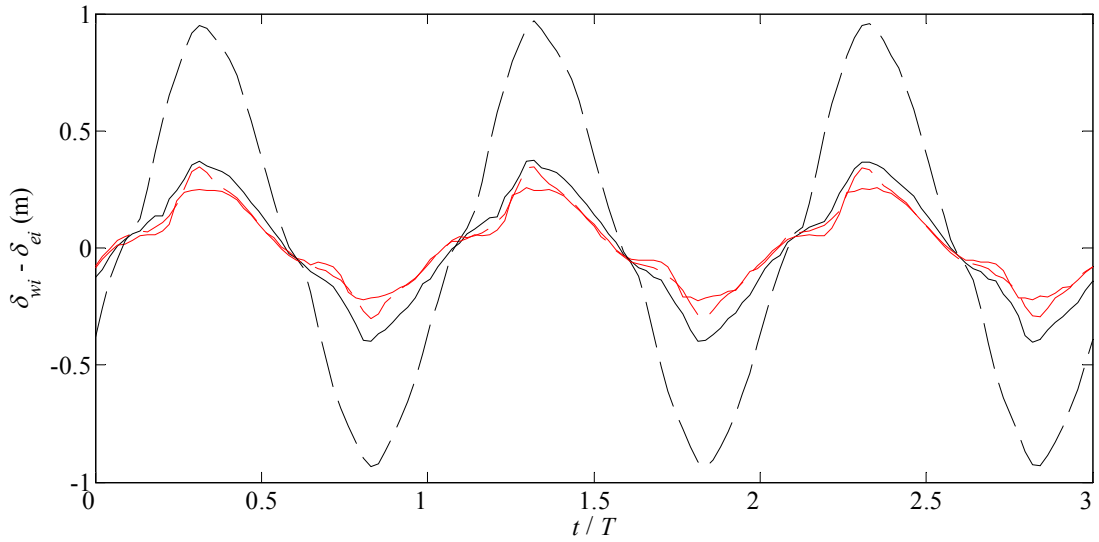


Figure 5.53. Flow driving head between the entrance and exit of the strait (black) and offshore of island (red) for the free-slip scenario: no power extraction (solid line) and high extraction level $k_f$ = 2.24 (dashed line) at the strait.

## 5.4. Summary

This chapter has presented a parametric study of resource assessment for an idealised coastal site defined by an island in the proximity of a landmass. Mesh convergence tests indicated that the flow velocities converged for a case where a free-slip condition is applied at both the island and landmass boundaries. Corresponding mesh convergence tests for a case where a no-slip condition is applied to both the island and landmass boundaries required a finer mesh resolution to capture satisfactorily the wake behind the island. Validation results obtained for flow past a surface-piercing circular cylinder in Section 4.8 have provided sufficient confidence in the capability of the mesh resolution utilised to reproduce the main flow features around the island.

No clear relationship was found between the power extracted in the strait and the power dissipated naturally on the seabed or kinetic power in the absence of the turbines. The analysis of free-slip and no-slip scenarios revealed that these conditions may provide lower and upper bounds to the power extracted in the strait. In keeping with this, the power extraction estimates for the non-uniform seabed scenario were between those obtained for the free-slip and no-slip scenarios. Bypass flow ratios when maximum power is extracted from the strait are equal to 1.21 and 1.09 for the free-slip and no-slip scenarios respectively. Comparison of power extracted in the strait against the GC2005 model with $\gamma$ = 0.22

revealed that the GC2005 model predicts values that are 67.7 % and 60.5 % lower than those from the present scheme for the free-slip and no-slip scenarios respectively. The main causes for discrepancies between the numerical and analytical results are the non-inclusion in the latter of changes to the head driving the flow due to power extraction in the strait and the flow diversion on the offshore side of the island.

The parameter test concerned with the influence of the value of eddy viscosity, used in some numerical models as a calibration parameter, on the power extracted in the strait, revealed that results only start to differ for high values of eddy viscosity (e.g. 100 $m^2 s^{-1}$). Changes in the estimates of power extracted with choice of eddy viscosity are seen in both the free-slip and no-slip scenarios.

Power extracted in the strait depended on the seabed frictional environment, highlighting the importance of the choice of bottom friction coefficient, which is commonly used in numerical models as a calibration parameter. There is an inverse relationship between bottom friction and power extracted in the strait. This occurs because as a lower bottom friction leads to less power naturally dissipated by the seabed, and with unchanged boundary conditions, more power is available in the strait to be extracted by the tidal array. Furthermore, the results showed that a reduction in bottom friction yields an increase in bypass flow rates.

The increase in water depth in the continental shelf of the domain yields higher values of extracted power from the strait, which are primarily induced by reduction in equivalent frictional forces per unit water depth. Bypass flow rates were found to be independent of changes to the domain water depth. Increasing the water depth offshore of the island leads to lower power extracted in the strait due to the reduction in the flow resistance on the path offshore of the island, which lead to a higher bypass flow rates. There is a direct implication for tidal resource assessment in that developers need to be aware of the effect of far field bathymetry.

Sensitivity of the resource estimate was also assessed against the choice of layout and area of the tidal array. It was found that the farm layout that created a low resistance flow path in the vicinities of the island led to higher rates of power extraction. However, when forces from the farm acting on the flow were uniformly distributed across the entire cross-sectional transect of the strait, the power extracted showed no dependence on the area of the tidal array, in agreement with the previous findings discussed in Section 4.9.

Analysis of the strait blockage by the array showed that reduction in strait blockage leads to a decrease in the maximum power extracted, mainly due to the availability of two additional bypass flow routes in the straits between the array and island, and array and landmass. When strait blockage is reduced to 80 % and power extraction is restricted to water depths suitable for turbine installation, maximum power extracted is similar to the case with 100 % strait blockage. Reduction of water depth in the strait bypass routes increases the resistance to the flow and appears to counteract the absence of power extraction. Reduction of strait blockage to 60 %, which includes areas with water depths suitable for tidal turbine deployment, leads to lower maximum power extracted in the strait by the array than in the 100 % and 80 % strait blockage cases.

Inclusion of turbine power capping in the extraction methodology increased the estimated power generated by the array and yielded lower cross-section velocity and kinetic power deficits compared to the results obtained with constant drag and thrust to characterise the tidal turbines. Variation of rotor thrust based on incoming flow velocity should enable turbines to increase their hydrodynamic efficiency, leading to higher rates of power generated to power extracted from the flow.

The inclusion of power extraction on the offshore of the island revealed that, for identical extraction levels, similar power is generated regardless whether extraction is implemented only in the strait or offshore of the island. However, when identical extraction levels are applied both in the strait and in the offshore side of the island, the total power generated in the strait and offshore of the island is higher than for an equivalent extraction level only applied one side of the island. Implementation of power extraction offshore of the island increases the resistance of the bypass route, leading to lower bypass flow rates and velocity deficits, which then translate into higher power outputs generated by the island-landmass system. It appears that power generation can be optimised if the system island-landmass system is considered as a two-flow path problem.

The sensitivity of the power extracted in the vicinity of the island was assessed against the relative distance of the island from the landmass. For an isolated island far from the coast, the assessment showed that neither the power dissipated by the seabed or the kinetic power in natural conditions properly approximated the maximum power extracted. The comparison against the case where the island is near the landmass shows a similar ratio of power extracted to undisturbed kinetic power for the free-slip scenario and 18 % lower for the no-slip scenario. Comparison of volumetric flow rates near the island and near the landmass

show similar rates of decay and increase of volumetric flow rate through the tidal array area and through the opposite side of the island.

The sensitivity of the power extracted in the strait was assessed against the length of the island. Free-slip and no-slip scenarios yielded different maximum powers extracted in the strait, which may indicate upper and lower limits respectively. The maximum power extracted was found to be 9.6 % and 17.5 % lower than the power naturally dissipated by the seabed for the free-slip and no-slip scenarios respectively. This indicates that for geometrically long islands, the power naturally dissipated by the seabed may be a good indicator of the maximum power extracted in the strait. When maximum power is extracted in the strait, bypass flow ratios for the free-slip and no-slip scenarios were 1.03 and 1.02 respectively, considerably lower than those obtained in the island-landmass baseline system. In addition, the ratios of increase in head driving the flow due to power extraction in the strait were found to be lower than in the island-landmass baseline system. These two factors explain why the predicted maximum power extracted by GC2005 for $\gamma = 0.22$ is only 16.9 % lower than the numerical results for a geometrically long island.

Finally, the sensitivity of the power extracted in the strait is assessed against the width of the island for the free-slip scenario. No clear relationship was found between the maximum power extracted in the strait and the undisturbed kinetic power or power naturally dissipated in the strait. The bypass flow ratio was 1.08 when the maximum power is extracted from the strait; this is lower than the values obtained for the island-landmass baseline system. The head driving the flow in the strait is significantly affected by extraction levels in the strait. The change in the head driving the flow is likely to be the main cause why the GC2005 model for $\gamma = 0.22$ under-predicts the power extracted in the strait by 72.5 %.

# 6. Tidal resource of the Rathlin Sound

## 6.1. Introduction

The previous chapter investigated the limits to power extraction for an idealised strait between an island and a landmass. It is important for site developers to understand the applicability of such idealised cases to real-world scenarios. This chapter investigates the limits to power extraction in Rathlin Sound, a strait located between Rathlin Island and the north-east coast of Northern Ireland. This analysis assesses the validity of outcomes derived from the idealised island-landmass study when applied to an actual site. The aim is to provide useful generic information on this type of coastal site to developers during the pre-feasibility stage of a tidal project, before a detailed numerical model of the site is constructed.

There have been several studies of actual sites that involve one or more strait(s) between an island and landmass. Adcock *et al*. [51] and Draper *et al.* [12] analysed the extractable tidal power from the Pentland Firth, located between the north coast of Scotland and the Orkney Islands, which could be approximated as a channel between a landmass and a geometrically long and wide island. Draper *et al.* found that their power extracted estimates agreed reasonably well with predictions using the analytical channel model derived by Garrett and Cummins [11] (GC2005). Sutherland *et al*. [31] assessed limits to power extraction in the Johnstone Strait, located between the geometrically long Vancouver Island and west coast of Canada, and found that their results also agreed well with the GC2005 analytical channel model. The conclusions from Draper *et al*. and Sutherland *et al*. are in keeping with the analysis of a geometrically long island in Chapter 5. However, studies looking at the limits to power extraction for the other categories of island and landmass analysed in Chapter 5 are not available in the literature. Turning to Rathlin Sound, the width of the strait is of the same order as the length and width of Rathlin Island, and so this site allows investigation of the validity of the outcomes of the analysis of an island in the vicinity of a landmass presented in Chapter 5.

This chapter is divided in three sections. Section 6.2 details the set-up of the numerical model of Rathlin Sound. Section 6.3 presents the results of the resource assessment of Rathlin Sound and compares them to those obtained in the island-landmass study in Chapter

5. Section 6.4 summarises the conclusions derived from the analysis of the results obtained for Rathlin Sound.

## 6.2. Set-up of Rathlin Sound numerical model

### 6.2.1 Rathlin Sound

Rathlin Sound is defined by Rathlin Island and the north-east coast of Northern Ireland (Figure 6.1). The length of the strait is defined by the geometry of Rathlin Island which is approximately 7.5 km long. The width of the strait is defined by the distance between Rathlin Island and the north-east coast of Northern Ireland, which ranges from 4 km to 10 km. The width of the Rathlin Island is approximately 2 km at its centre and west side and expands 6 km south at the east side, forming a tip called Rue Point. Mean water depths in the strait and offshore of the Rathlin Island are 60 m and 180 m respectively. There are three headlands along the Northern Ireland coast that influence the flow dynamics in Rathlin Sound: Fair Head, located east of the Rathlin Sound, which together with Rue Point defines the narrowest section of the strait; Torr Head, located approximately 8 km south-east of the east end of Rathlin Sound; and Kimbane Head, located west of Rathlin Sound.

The primary flow dynamics within the Rathlin Sound are generated by the interaction between two tides, one progressing north from the Irish Sea through the North Channel east of Rathlin Sound and a second tide progressing east from the Atlantic. As a result, during flood tide the currents flow from west to east and from east to west during ebb tide.

Rathlin Sound has been chosen for this study for two reasons: the first relates to the domain geometry, Rathlin Island has similar width to length dimensions and its strait is also of similar breadth, meaning that the overall configuration can be simplified as an island in the proximity of a semi-infinite landmass (Section 5.3.1); the second relates to the tidal resource which is potentially one of the largest of Ireland, when taken together with the coastal sites of Fair Head and Torr Head [158].

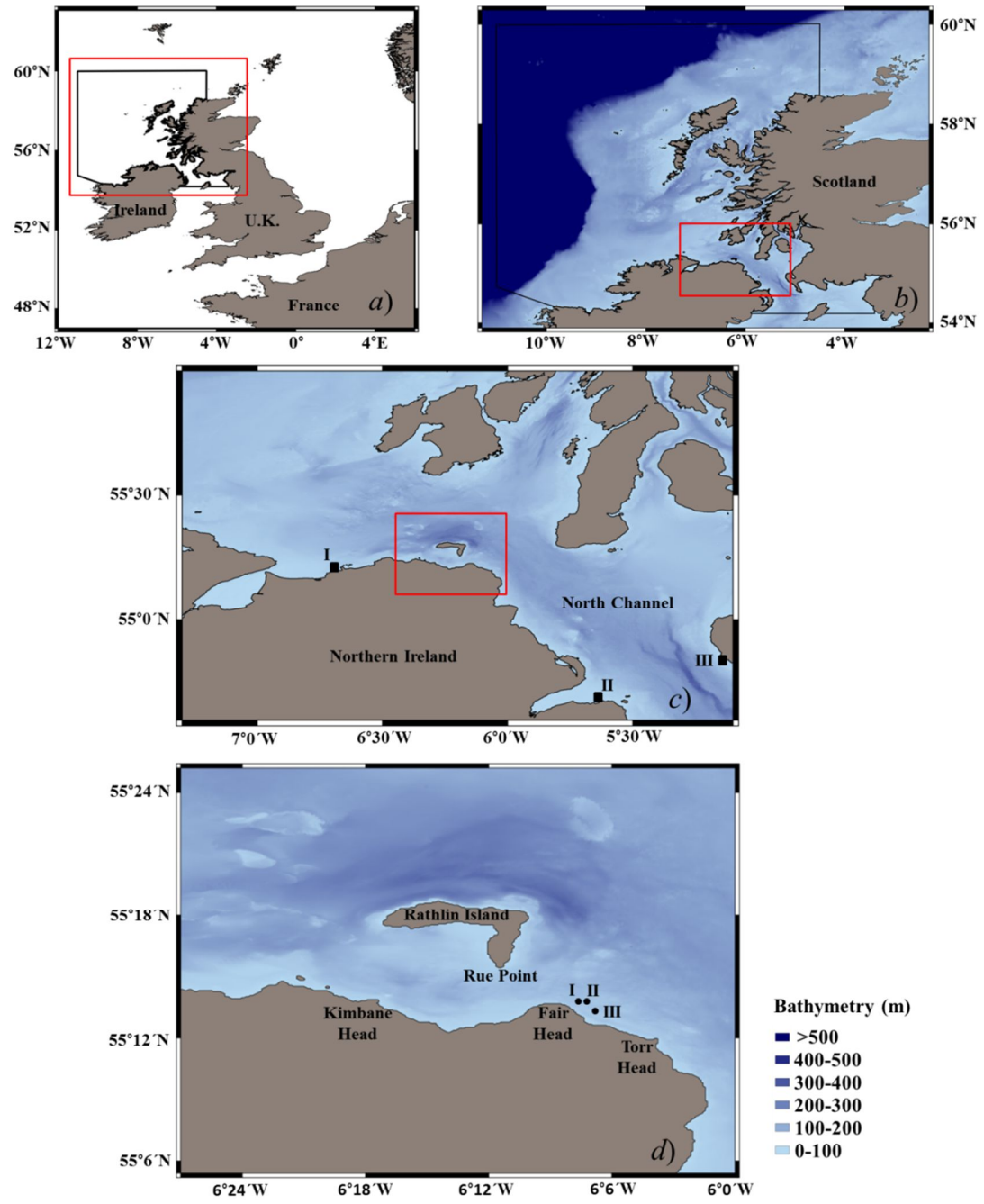


Figure 6.1. (a) Overview of Rathlin domain with respect to the British Isles; (b) bathymetry expressed with respect to mean sea level vertical reference for the Rathlin domain and its surroundings; and bathymetry and coastal features at the Rathlin Sound and surrounding areas (c) (d) [159]. Red squares indicate the domain area zoomed in. Tidal gauge location (square): I) Portrush; II) Bangor; and III) Portpatrick. ADCP location (circle): I) ADCP 1; II) ADCP 2; and III) ADCP 3.

### 6.2.2 Bathymetry and domain

Bathymetry data were obtained from the HydroSpatial One Gridded Bathymetry dataset via the Digimap online database [159]. After referencing to the Lowest Astronomical Tide (LAT) vertical datum, the data were presented at two resolutions of 1 and 6 arcsec for British territorial waters. The bathymetry data were then converted from LAT to Mean Sea Level (MSL) vertical datum using the local solution provided by the Vertical Offshore Reference Frame (VORF) model available for British and Irish waters [160]. As the resolution provided by VORF is of 28.8 arcsec, a nearest point interpolation was used to alter the vertical reference of the bathymetry data. All datasets were in WGS84 geographic horizontal datum.

Figure 6.1 shows the bathymetry in MSL vertical datum used in the numerical model. The bathymetry presents two regions, linked to the mesh resolution requirements of Section 6.2.4:

- Near-field region. A 1 arcsec resolution bathymetry is used in the region containing the Rathlin Sound and surrounding areas contained within longitude and latitude coordinates 4-8W and 54-56N respectively.
- Far-field region. A 6 arcsec resolution bathymetry is employed throughout the rest of the domain.

Figure 6.2 depicts the limits and coastline of the domain, which extends over longitudes 3.5W to 11W and latitudes 54.2N to 60N. The size of the domain was chosen so that it extended to the edge of the continental shelf [135], for the reasons detailed in Section 3.3.5. In the near-field region the coastlines were derived from the zero-depth contour of the bathymetry. In the far-field region, precision of coastline was not likely to affect the hydrodynamics of the site and consequently, the coastline was obtained from the GSSHG NOAA database [159], which provided approximately a 100 m spatial resolution in MSL vertical datum. The use of low-resolution coastline in the far-field limited the coastal features represented (e.g. islands of small size) which simplified the pre-processing of the coastal domain.

The coastline from GSSHG NOAA and derived from the bathymetry was merged and pre-processed to obtain the coastline shown in Figure 6.2. Pre-processing of the far-field region coastlines comprised two parts: closure of certain small shallow bays, due to Fluidity not accounting for wetting and drying (Section 3.3.5); and the deletion of islands, which, due to

their size and location, are not expected to influence the hydrodynamics of the Rathlin Sound. Figure 6.3 shows the pre-processed results obtained for the coastline north of the Republic of Ireland. It should be noted that the coastline pre-processing and mesh generation was undertaken iteratively because the mesh edge length defined during the mesh generation process (Section 6.2.4) determined the minimum size of the islands that could be spatially represented by the grid.

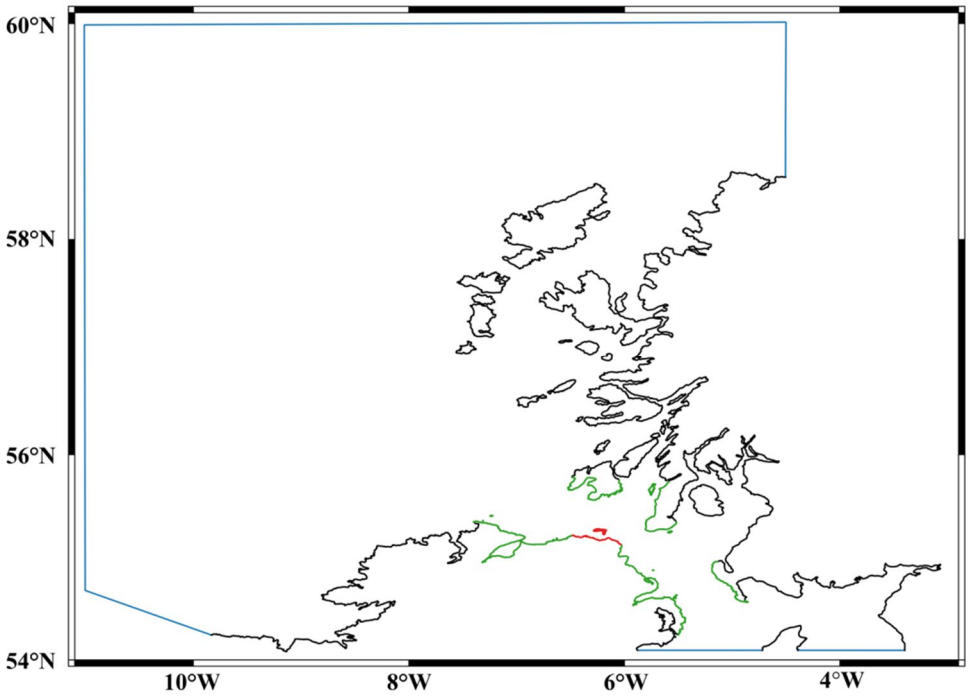


Figure 6.2. Domain boundaries, coastlines and mesh regions: open boundaries (blue); mesh regions 1 (red); 2 (green); and 3 (black).

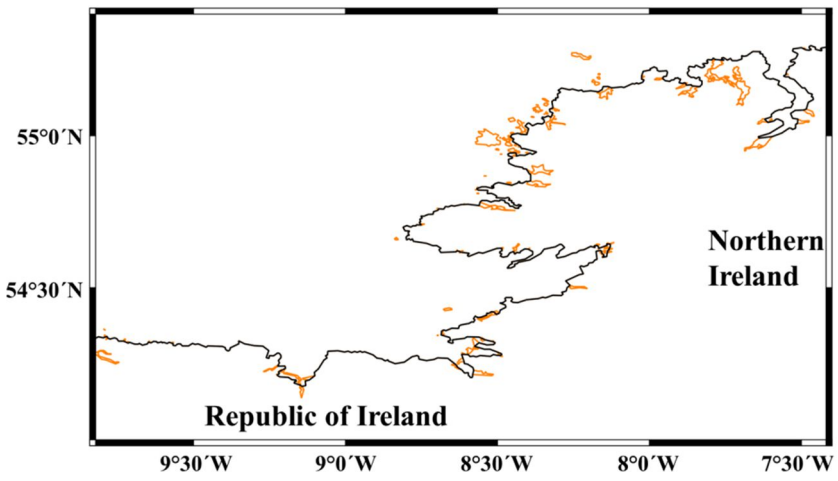


Figure 6.3. Original GSHHG NOAA coastline (orange) and coastline after pre-processing (black).

### 6.2.3 Model parameterisation

The domain presented in Figure 6.2 essentially has four boundaries: two solid boundaries defined respectively by the coastlines of the Republic of Ireland and the United Kingdom; an open boundary extending from the north of Scotland to the north-west coast of Ireland; and an open boundary across the Irish Sea split into two sections by the Isle of Man (minimising numerical distortions at the boundary induced by generated wake or reflections from the Isle of Man if boundary were located north or south of it). At all solid boundaries, the normal flow is set to zero and a wall friction condition applied. Open boundary conditions are derived from the Oregon State University European shelf (ES) solution [132]. This tidal harmonic database covers the north-east of the Atlantic Ocean and contains 11 harmonic components with a spatial resolution of 1/30 degree.

As in Section 5.2.1, the tidal signal at open boundaries is ramped up during the first 24 hours of each simulation using the parameter $a_o$:

$$a_o = 0.5\left(1 - \cos\left(\frac{\omega_t t}{4}\right)\right) \tag{6.1}$$

where $\omega_t$ is equal to 7.27 x $10^{-5}$ rad/s.

A spin-up time period of 48 hours after ramp-up is utilised to allow the flow dynamics of the system to stabilise. The frictional environment in the domain is first parameterised by means of a non-dimensional seabed friction coefficient $C_d$ = 0.0025. Viscosity is implemented with a depth averaged parabolic eddy viscosity empirical model [92] (Section 3.2). Due to the unavailability of wetting and drying in the SWE version of Fluidity (Section 3.3.5), a minimum depth of 5 m is set in the domain. This minimum depth prevents numerical instabilities developing in regions where the tidal range is large, such as the Solway Firth, a bay located off the Irish Sea at the western boundary between England and Scotland.
Coriolis effects are computed from:

$$f = 2\Omega \sin\lambda \tag{6.2}$$

where $\Omega$ is the frequency of the earth's rotation, and $\lambda$ is the latitude of the Rathlin Sound, taken as 55.25N.

Other parameters such as wind, wave or atmospheric conditions are not included in the numerical model. A time step of 60 s is chosen to limit the *CFL* number to within O(1).

### 6.2.4 Spatial discretisation of the numerical model

Figure 6.2 depicted three regions used to discretise the domain in space. Coastlines are defined by means of the open-source Geographic Information System QGIS [161] and imported into Gmsh using the Qmesh tool developed at Imperial College London [162]. Qmesh enables the user to define mesh regions with coastlines, define mesh element edge lengths at coast and offshore boundaries, and set the gradation between the coast and offshore mesh edge lengths.

Four mesh resolutions are considered in the mesh convergence analysis (Table 6.1). Each mesh is defined by the element edge length at the coastline and offshore of each region. The element edge length defined at the coast is kept constant for a distance of 0.15 degrees off the coast. After this the element-edge length increases to the offshore value over a distance of 1 degree. In all mesh cases, the same offshore mesh edge length is set to all the mesh regions.

| | Mesh element edge length (m) | | | | |
|---|---|---|---|---|---|
| Mesh | Coast 1 | Coast 2 | Coast 3 | Offshore | Mesh elements |
| 1 | 1000 | 2000 | 10000 | 100000 | 11,708 |
| 2 | 500 | 1000 | 5000 | 50000 | 40,152 |
| 3 | 250 | 500 | 2500 | 25000 | 147,750 |
| 4 | 125 | 250 | 1250 | 12500 | 569,906 |

Table 6.1. Four spatial discretisation cases considered in the mesh convergence analysis. Element edge length used at the coastline and offshore in the three mesh regions of the model, and total number of mesh elements.

To facilitate comparison with the results of the idealised coastal site presented in Chapter 5, an $M_2$ tide obtained from the ES harmonic database is forced at the open boundaries of the domain. The model is run for 120 hours: the first 24 hours to ramp-up the boundary conditions as described by Eq. (6.1); then 48 hours to spin-up the system; and the final 48 hours to provide numerical data for analysis.

Mesh convergence assessment is undertaken by analysis of results at four transects, shown as dashed lines in Figure 6.4. Transect 2 and Transect 3 are located at the west and east limits of the island. Transect 1 and Transect 4 are located 10 km upstream and downstream respectively of Transects 2 and 3. The four transects extent north off the coast of Northern

Ireland until latitude coordinate 55.375 N is reached and so each is of different length. For example, Transect 3 is 17 km long, of which approximately one half lies between Rathlin Island and the coast of Northern Ireland and the other half extends offshore of the island.

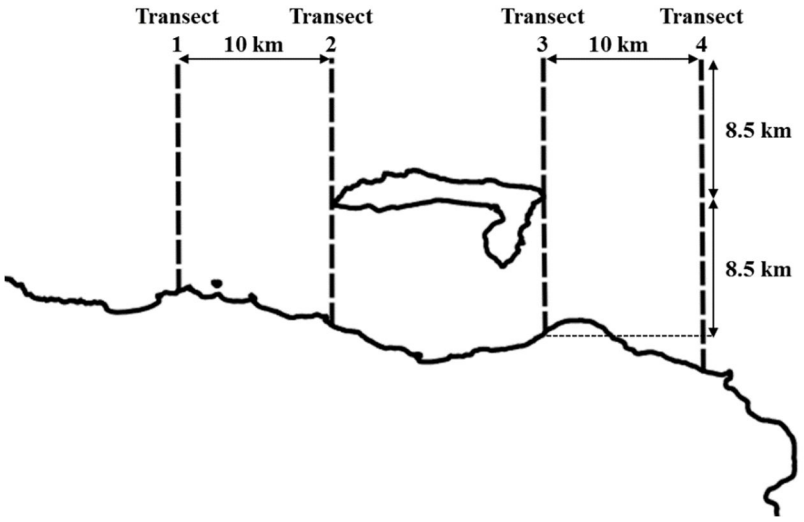


Figure 6.4. Location of simulated Transects 1-4 used in the mesh convergence analysis undertaken for the Rathlin Sound numerical model.

The norm of the depth-averaged velocity vector, referred to commonly as the flow speed, used in the mesh convergence analysis is defined as:

$$|\vec{u}| = (u^2 + v^2)^{\frac{1}{2}} \tag{6.3}$$

The flow speed profile along each transect is considered at the peak flow instants during flood and ebb tides that occur on the second $M_2$ cycle of day 4 of the simulation (Figure 6.5 to Figure 6.12). Mesh convergence appears to have been almost achieved for Mesh 3. However, Figure 6.6 and Figure 6.11 corresponding to Transect 1 at ebb tide and Transect 4 at flood tide respectively, show that the solution has not fully converged, and that further refinement may be necessary to capture properly flow features advecting past the island and through the strait.

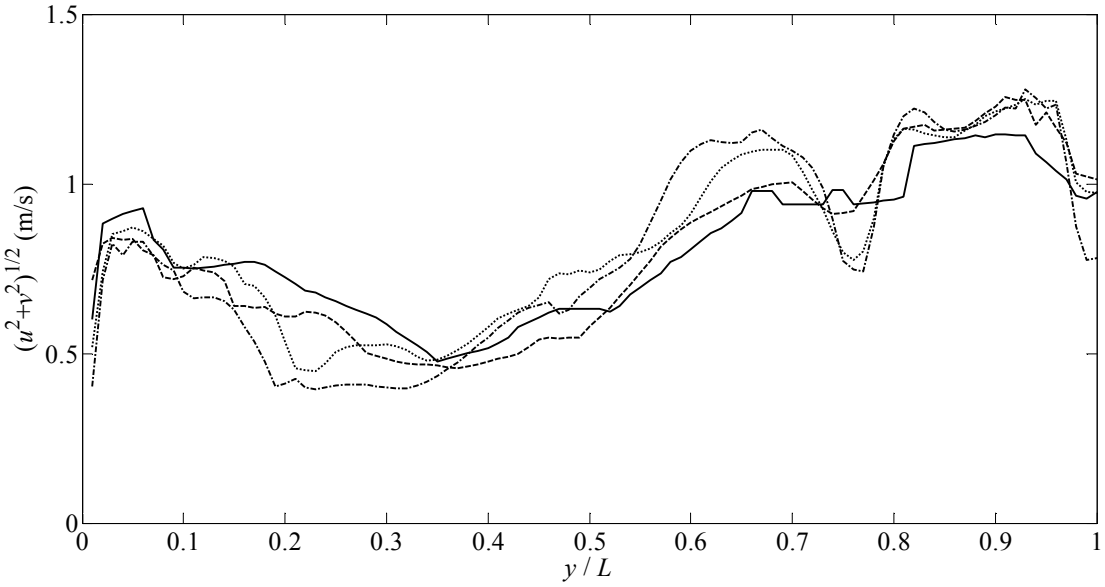


Figure 6.5. Depth-averaged flow speed at Transect 1 at peak flow during flood tide: Mesh 1 (solid line); Mesh 2 (dashed line); Mesh 3 (dotted line); and Mesh 4 (dash-dot line).

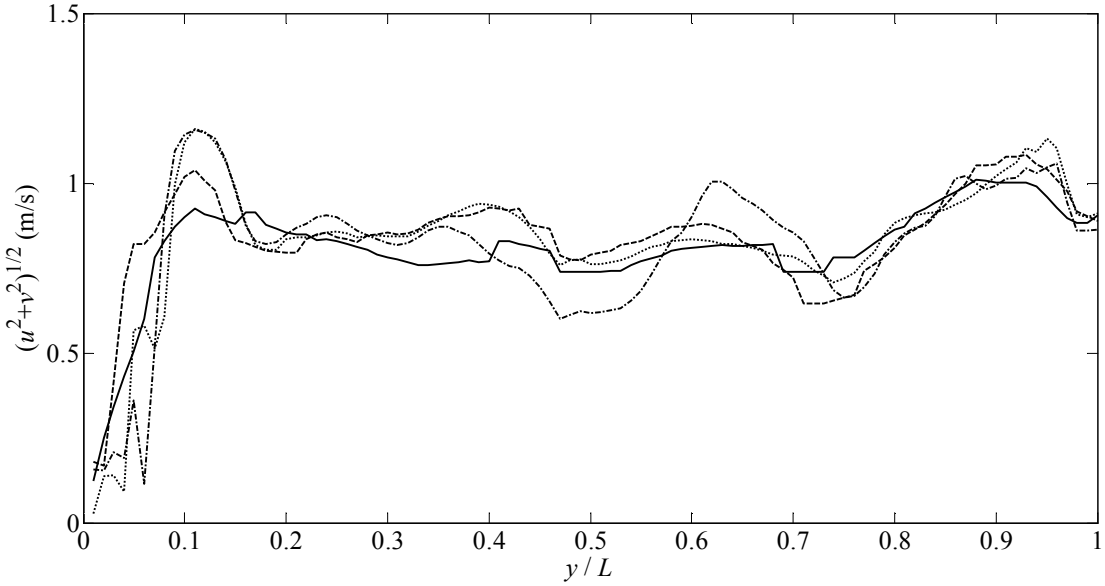


Figure 6.6. Depth-averaged flow speed at Transect 1 at peak flow during ebb tide: Mesh 1 (solid line); Mesh 2 (dashed line); Mesh 3 (dotted line); and Mesh 4 (dash-dot line).

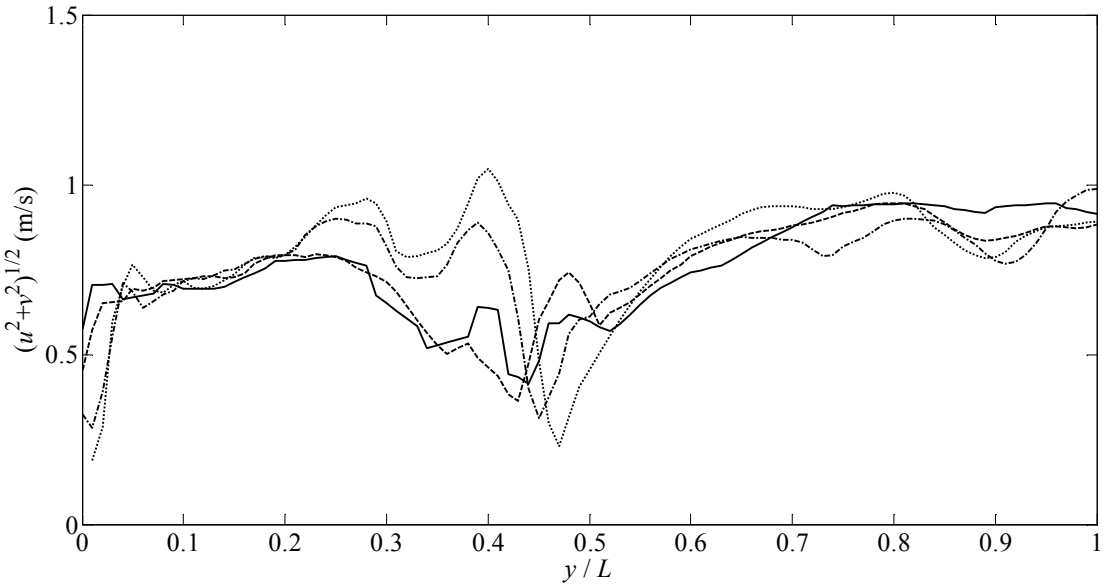


Figure 6.7. Depth-averaged flow speed at Transect 2 at peak flow during flood tide: Mesh 1 (solid line); Mesh 2 (dashed line); Mesh 3 (dotted line); and Mesh 4 (dash-dot line).

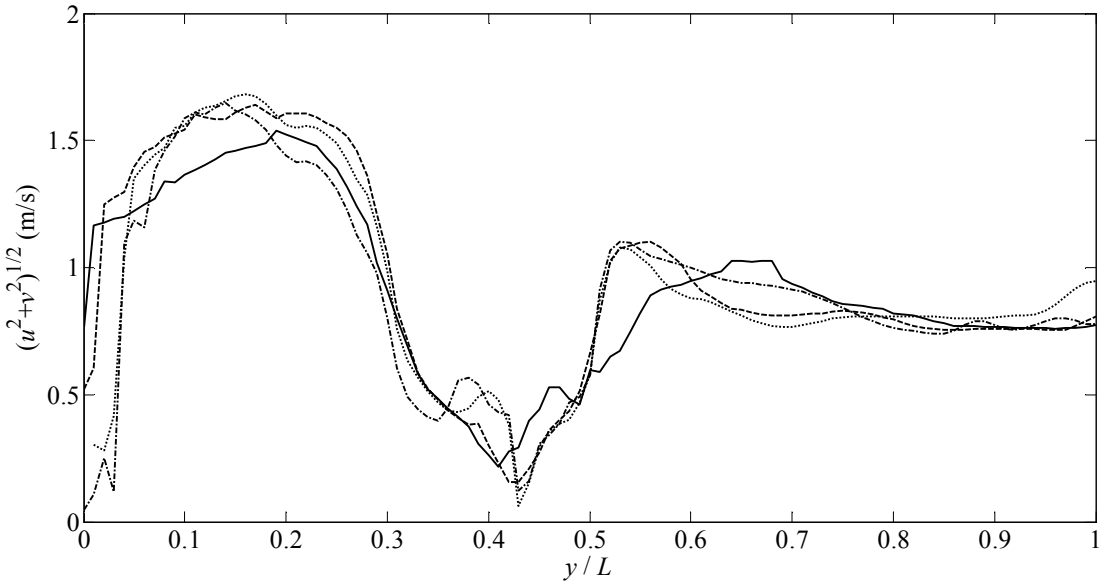


Figure 6.8. Depth-averaged flow speed at Transect 2 at peak flow during ebb tide: Mesh 1 (solid line); Mesh 2 (dashed line); Mesh 3 (dotted line); and Mesh 4 (dash-dot line).

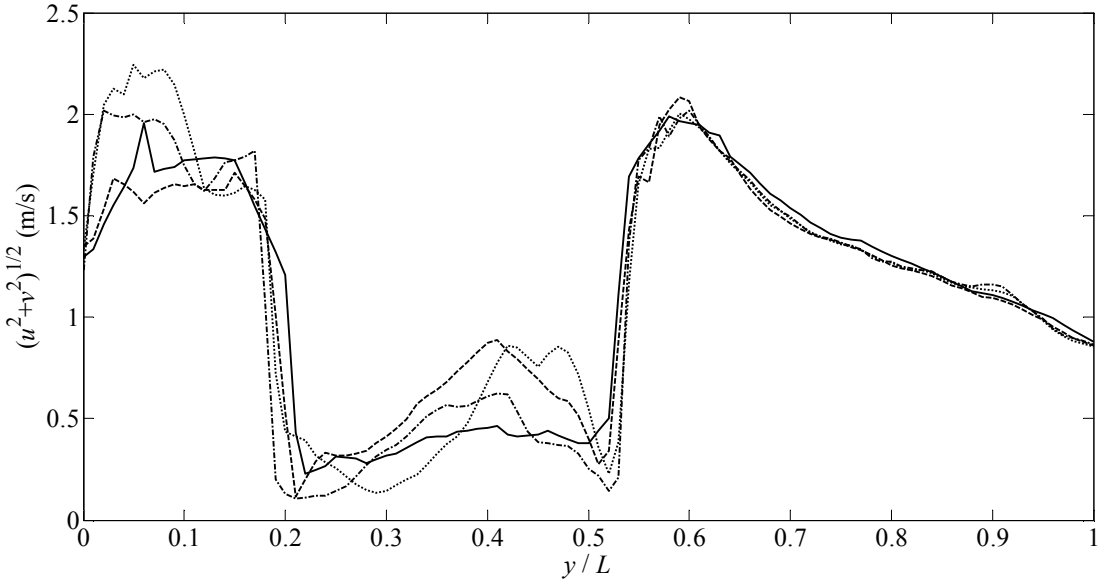


Figure 6.9. Depth-averaged flow speed at Transect 3 at peak flow during flood tide: Mesh 1 (solid line); Mesh 2 (dashed line); Mesh 3 (dotted line); and Mesh 4 (dash-dot line).

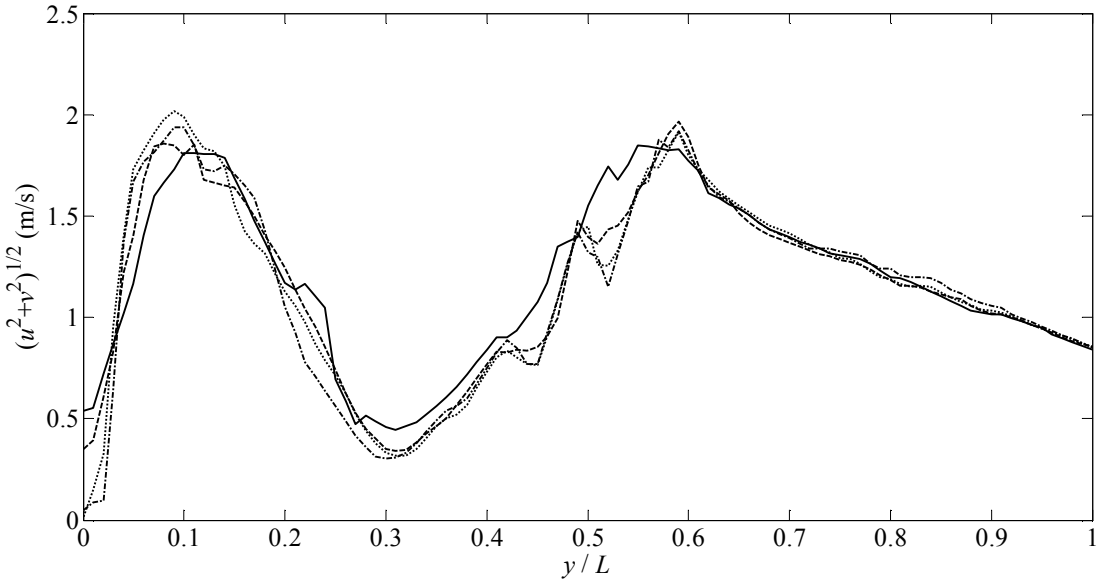


Figure 6.10. Depth-averaged flow speed at Transect 3 at peak flow during ebb tide: Mesh 1 (solid line); Mesh 2 (dashed line); Mesh 3 (dotted line); and Mesh 4 (dash-dot line).

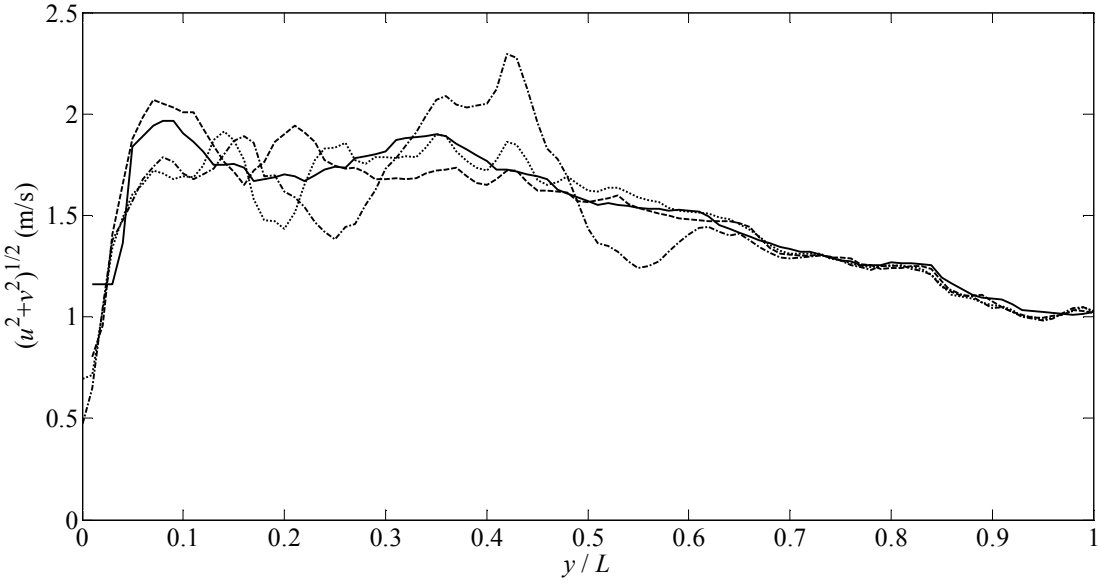


Figure 6.11. Depth-averaged flow speed at Transect 4 at peak flow during flood tide: Mesh 1 (solid line); Mesh 2 (dashed line); Mesh 3 (dotted line); and Mesh 4 (dash-dot line).

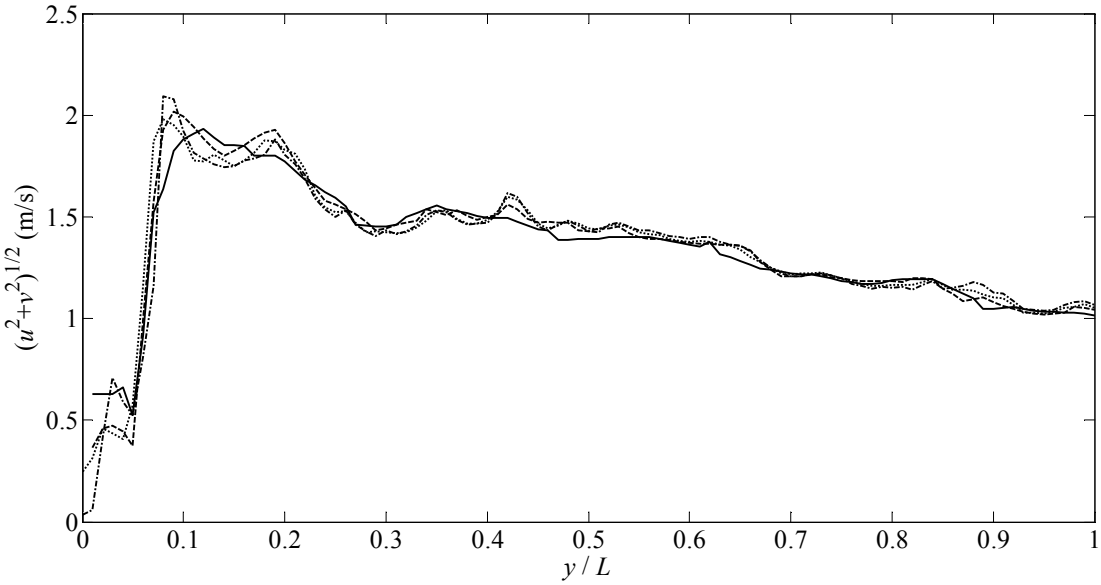


Figure 6.12. Depth-averaged flow speed at Transect 4 at peak flow during ebb tide: Mesh 1 (solid line); Mesh 2 (dashed line); Mesh 3 (dotted line); and Mesh 4 (dash-dot line).

Furthermore, the convergence in time is checked at ADCP 1 (Figure 6.1). Figure 6.13 and Figure 6.14 plot the stream-wise and transverse velocity components respectively during the first and second $M_2$ tidal cycles during the fourth day of simulation. Here, solution convergence is achieved for Mesh 3.

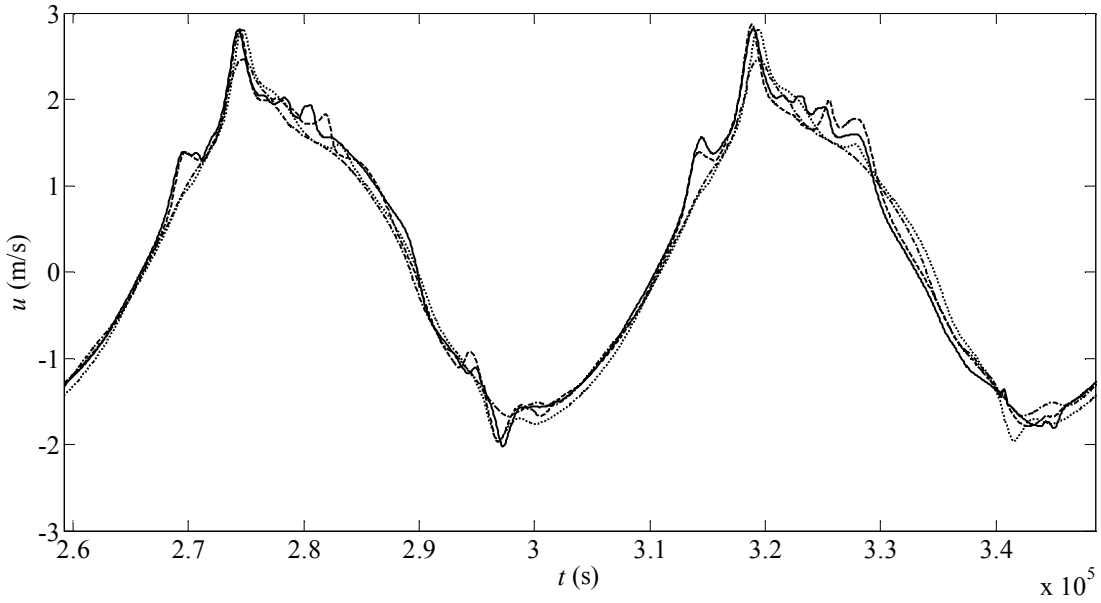


Figure 6.13. Time series of stream-wise velocity component south-east of Rathlin Island during two $M_2$ tidal cycles: Mesh 1 (solid line); Mesh 2 (dashed line); Mesh 3 (dotted line); and Mesh 4 (dash-dot line).

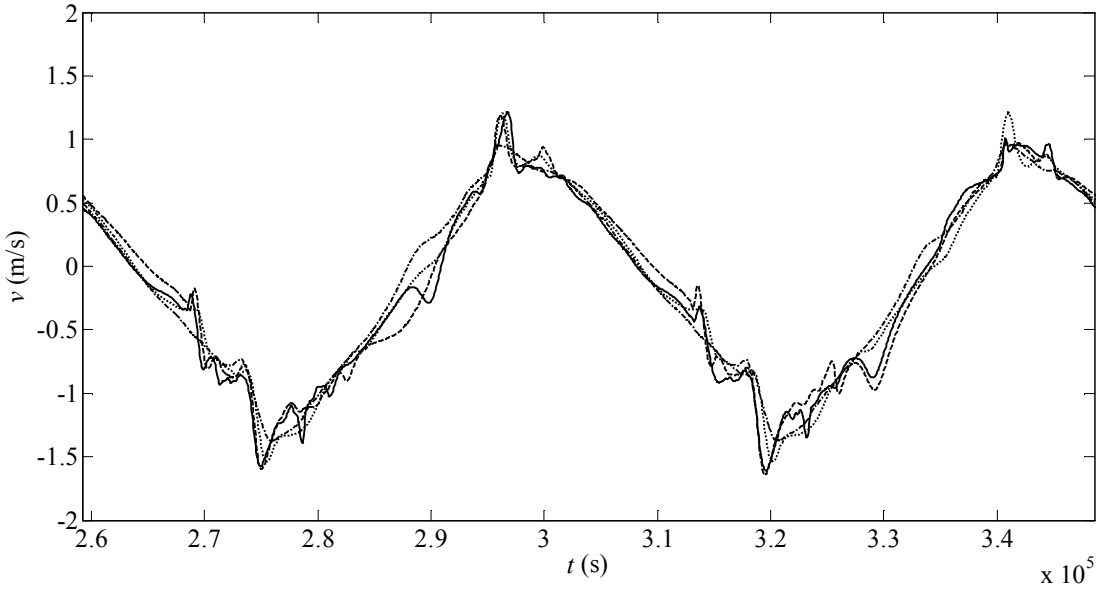


Figure 6.14. Time series of transverse velocity component south-east of Rathlin Island during two $M_2$ tidal cycles: Mesh 1 (solid line); Mesh 2 (dashed line); Mesh 3 (dotted line); and Mesh 4 (dash-dot line).

From the above analysis it can be concluded that Mesh 3 is capable of resolving the main flow features generated at the island and in the strait, thus providing sufficient accuracy for

the purposes of resource assessment in the strait. An overview of the mesh is shown in Figure 6.15 which shows the local refinement near the area of interest.

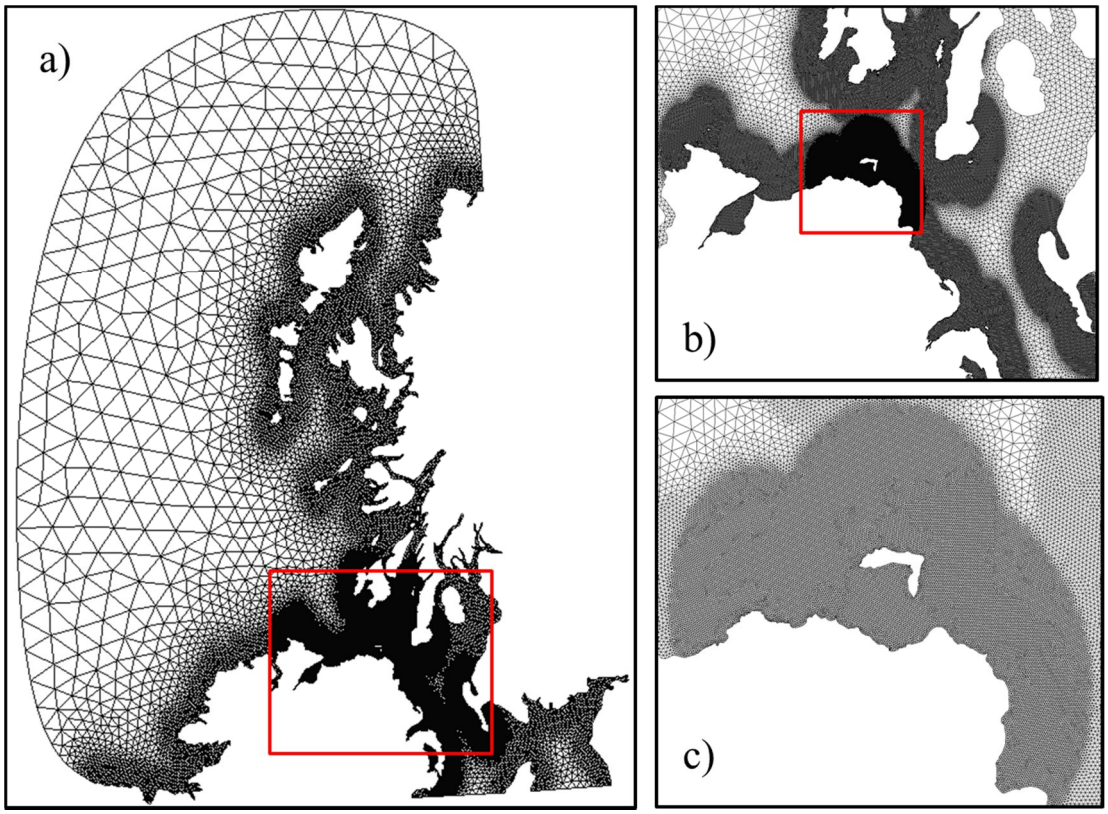


Figure 6.15. Spatial discretisation Mesh 3 of the domain, with different local mesh resolutions indicated. Red squares indicate the domain area zoomed in.

### 6.2.5 Calibration of the numerical model

This section describes calibration of the numerical model, whereby certain parameters of the model are modified to tune the model predictions so that they agree satisfactorily with observed data. As highlighted in Sections 5.3.1.1 and 5.3.1.2, the eddy viscosity and seabed friction are parameters commonly used in the calibration of SWE numerical models. The field observations used in the model calibration include measurements of free surface elevation and flow velocity components averaged over 10-minute intervals from three ADCPs deployed by Dp Marine Energy Ltd [163] south east of Rathlin Island (Figure 6.1). Table 6.2 presents latitude and longitude coordinates and total sampling periods for the three ADCPs.

| ADCP | Latitude (deg) | Longitude (deg) | Sampling time period (Start – End) |
|---|---|---|---|
| 1 | 55.230N | 6.114W | 24/04/2014 – 27/05/2014 |
| 2 | 55.228N | 6.113W | 24/04/2014 – 04/06/2014 |
| 3 | 55.222N | 6.090W | 24/04/2014 – 04/06/2014 |

Table 6.2. Latitude and longitude coordinates of deployed ADCPs, and sampling time periods [163].

The ADCP data were supplied after pre-processing, with bin values near the sea surface and sea bottom removed from the dataset. The remaining binned velocity components were depth-averaged.

Free surface elevation data according to chart datum (CD) vertical reference were also used, acquired from the UK tidal gauge network at the British Oceanographic Data Centre [164]. Table 6.3 lists the locations of three tidal gauges in the proximity of the Rathlin Sound which recorded data over the same time period as the ADCP dataset (Figure 6.1): Portrush, off the north coast of Northern Ireland, west of Rathlin Sound; Bangor, in Belfast Lough north-east of Belfast, south-east of Rathlin Sound; and Portpatrick, on the east side of the North Channel, south-west Scotland, south-east of Rathlin Sound.

| Station | Latitude (deg) | Longitude (deg) | Time period data (Start – End) |
|---|---|---|---|
| Portrush | 55.207N | 6.657N | 27/04/2014 – 28/05/2014 |
| Bangor | 54.665N | 5.669N | 27/04/2014 – 28/05/2014 |
| Portpatrick | 54.843N | 5.120N | 27/04/2014 – 28/05/2014 |

Table 6.3. Latitude and longitude coordinates and time period of data obtained from three UK tidal gauge stations in the proximity of Rathlin Sound [164].

Calibration of the numerical model is performed by modifying the value of the seabed friction coefficient $C_d$, a constant over the domain, between 0.001 and 0.005, in accordance with Section 5.3.1.2. To ensure the main flow dynamics are captured, the model is run with 8 primary harmonic constituents: $M_2$, $S_2$, $N_2$, $K_2$, $K_1$, $O_1$, $P_1$ and $Q_1$. The model is run for 18 days starting on the 24$^{th}$ of April 2014. The first three days correspond to the ramp-up and spin-up of the system, and the following 15 days are used in the calibration process covering a spring and neap tidal cycle. Iyer [22] highlighted that a minimum of 14.77 days of data are required to separate the $M_2$ and $S_2$ harmonics. The normalised amplitudes $A$ and phases $\phi$ of the $M_2$ (Table 6.4) and $S_2$ (Table 6.5) harmonic constituents are obtained with the Matlab

based tool T_Tide [24] for the measured data and Fluidity predictions at ADCP and tidal gauge locations.

The results listed in Table 6.4 show that the predicted amplitudes and phases of the $M_2$ free surface elevation obtained with $C_d$ = 0.0025 and 0.003 are in very good agreement with the measured values at the three ADCP locations. These seabed friction values yield a close approximation to the phase of the $M_2$ free surface elevation measured at Portrush, although the amplitude is better approximated for lower seabed friction coefficients. The computed $M_2$ free surface amplitude at Bangor appears to be independent of the seabed friction coefficient and the agreement in phase decreases with seabed friction coefficient. At Portpatrick, better agreement is reached in terms of amplitude when the seabed friction coefficient is increased.

The predicted $S_2$ free surface amplitude at the ADCP locations agree closely with the measured values for $C_d$ = 0.0025 and 0.003. The $S_2$ free surface phase at the ADCP locations are not so well reproduced by the numerical model. Tidal amplitude and phases at Portrush, Bangor and Portpatrick are relatively well reproduced by the numerical model but there is no clear trend between the results and the seabed friction coefficient employed.

| Location | Model Magnitude | | | | | | | | | | | |
|---|---|---|---|---|---|---|---|---|---|---|---|---|
| | $C_d = 0.001$ | | $C_d = 0.002$ | | $C_d = 0.0025$ | | $C_d = 0.003$ | | $C_d = 0.004$ | | $C_d = 0.005$ | |
| | $A^*$ | $\phi^*$ | $A^*$ | $\phi^*$ | $A^*$ | $\phi^*$ | $A^*$ | $\phi^*$ | $A^*$ | $\phi^*$ | $A^*$ | $\phi^*$ |
| ADCP 1 | 1.10 | -10.40 | 1.03 | -3.80 | 1.03 | -0.80 | 1.00 | 2.30 | 0.97 | 8.50 | 0.97 | 14.30 |
| ADCP 2 | 1.07 | -9.40 | 1.03 | -3.00 | 1.00 | 0.00 | 0.97 | 3.10 | 0.93 | 9.10 | 0.93 | 14.90 |
| ADCP 3 | 1.15 | -3.60 | 1.09 | 2.20 | 1.06 | 5.00 | 1.03 | 8.00 | 0.97 | 14.00 | 0.94 | 19.90 |
| Portrush | 1.04 | 3.60 | 0.96 | 1.60 | 0.94 | 0.20 | 0.90 | -1.20 | 0.84 | -3.90 | 0.80 | -6.50 |
| Bangor | 0.96 | -1.10 | 0.96 | 0.50 | 0.96 | 1.20 | 0.96 | 2.00 | 0.95 | 3.60 | 0.95 | 5.10 |
| Portpatrick | 0.92 | 1.00 | 0.95 | 1.20 | 0.96 | 1.30 | 0.97 | 1.50 | 0.98 | 1.80 | 0.99 | 2.10 |

Table 6.4. Comparison of normalised measured and Fluidity predicted $M_2$ free surface amplitudes $A^* = A_{computed} / A_{measured}$ and phases $\phi^* = \phi_{computed} - \phi_{measured}$ (deg) for the ADCP and tidal gauge stations for a range of seabed friction coefficients $C_d$ 0.001-0.005.

| Location | Model Magnitude | | | | | | | | | | | |
|---|---|---|---|---|---|---|---|---|---|---|---|---|
| | $C_d$ = 0.001 | | $C_d$ = 0.002 | | $C_d$ = 0.0025 | | $C_d$ = 0.003 | | $C_d$ = 0.004 | | $C_d$ = 0.005 | |
| | $A^*$ | $\phi^*$ | $A^*$ | $\phi^*$ | $A^*$ | $\phi^*$ | $A^*$ | $\phi^*$ | $A^*$ | $\phi^*$ | $A^*$ | $\phi^*$ |
| ADCP 1 | 4.00 | 64.90 | 3.00 | 58.40 | 2.00 | 50.70 | 1.00 | 31.70 | 1.00 | -32.50 | 1.00 | -75.50 |
| ADCP 2 | 4.00 | 68.40 | 2.00 | 62.70 | 2.00 | 55.20 | 1.00 | 30.60 | 1.00 | -60.10 | 2.00 | -89.70 |
| ADCP 3 | 2.33 | 9.20 | 1.67 | 14.00 | 1.33 | 18.40 | 1.00 | 26.80 | 0.33 | 65.80 | 0.67 | 116.70 |
| Portrush | 1.09 | 0.60 | 1.04 | -2.80 | 1.04 | -4.50 | 1.04 | -6.30 | 1.00 | -9.40 | 0.96 | -12.10 |
| Bangor | 1.07 | -10.00 | 1.07 | -7.50 | 1.07 | -6.30 | 1.07 | -5.10 | 1.07 | -2.70 | 1.07 | -0.40 |
| Portpatrick | 1.03 | -5.60 | 1.05 | -5.90 | 1.08 | -5.90 | 1.08 | -5.80 | 1.11 | -5.70 | 1.11 | -5.50 |

Table 6.5. Comparison of measured and Fluidity predicted $S_2$ free surface amplitudes $A^* = A_{computed} / A_{measured}$ and phases $\phi^* = \phi_{computed} - \phi_{measured}$ (deg) for the ADCP and tidal gauge stations for a range of seabed friction coefficients $C_d$ 0.001-0.005.

Figure 6.16 illustrates the major $C_{max}$ and minor $C_{min}$ ellipse parameters, phase and inclination $\theta$ used to characterise the flow velocity ellipses.

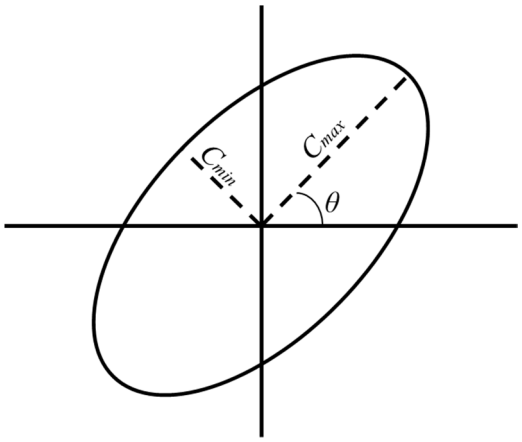


Figure 6.16. Parameterisation of flow velocities: major $C_{max}$ and minor $C_{min}$ ellipse parameters and inclination $\theta$.

Table 6.6 and Table 6.7 list the normalised characteristic parameters of the measured and predicted flow velocities obtained for the $M_2$ and $S_2$ harmonic constituents. The results show that the $M_2$ major ellipses at the three ADCP locations are best approximated by $C_d$ = 0.002. Low seabed friction coefficients yield a better $M_2$ minor ellipse. It is not possible for all the predicted values to match exactly the measured values for any single bed friction coefficient. Reasonable agreement in the $M_2$ phase is achieved for ADCP 1 and 2 using $C_d$ = 0.0025. For ADCP 3, an increased value of seabed friction coefficient leads to improved agreement with

the measured data. The $M_2$ inclination appears relatively insensitive to $C_d$ over the range considered. Although discrepancies occur between the predicted and measured results for ADCP 1 and 2, good agreement is obtained for ADCP 3. These trends observed in the $M_2$ major and minor ellipses, phase and inclination are also seen in the $S_2$ flow magnitudes.

| Location | Model magnitude | | | | | |
|---|---|---|---|---|---|---|
| | $C_d = 0.001$ | $C_d = 0.002$ | $C_d = 0.0025$ | $C_d = 0.003$ | $C_d = 0.004$ | $C_d = 0.005$ |
| Major ellipse parameter: $C_{max\_computed}$ / $C_{max\_measured}$ | | | | | | |
| ADCP 1 | 1.11 | 0.99 | 0.95 | 0.91 | 0.84 | 0.78 |
| ADCP 2 | 1.06 | 0.95 | 0.91 | 0.86 | 0.80 | 0.75 |
| ADCP 3 | 1.09 | 0.98 | 0.93 | 0.89 | 0.81 | 0.76 |
| Minor ellipse parameter: $C_{min\_computed}$ / $C_{min\_measured}$ | | | | | | |
| ADCP 1 | 0.13 | 0.20 | 0.20 | 0.20 | 0.07 | -0.07 |
| ADCP 2 | 0.22 | 0.28 | 0.22 | 0.22 | 0.11 | 0.06 |
| ADCP3 | 2.00 | 1.25 | 1.25 | 1.00 | 1.00 | 0.75 |
| Phase: $\phi_{computed}$ - $\phi_{measured}$ (deg) | | | | | | |
| ADCP 1 | -19.1 | -6.4 | -1.4 | 1.4 | 2.3 | 1.2 |
| ADCP 2 | -15.9 | -4.9 | 0.2 | 3.6 | 6.2 | 5.7 |
| ADCP3 | -45.8 | -38.2 | -31.5 | -32.1 | -33.6 | -27.7 |
| Inclination: $\theta_{computed} - \theta_{measured}$ (deg) | | | | | | |
| ADCP 1 | -9.9 | -10 | -10.1 | -10.4 | -11 | -11.5 |
| ADCP 2 | -8.1 | -8.3 | -8.5 | -8.9 | -9.6 | -10.2 |
| ADCP3 | 2.1 | 1.3 | 1.4 | 1.1 | 0.9 | 0.6 |

Table 6.6. Comparison of normalised measured and computed $M_2$ currents at the ADCP locations for a range of seabed friction coefficients 0.001-0.005.

| Location | Model magnitude | | | | | |
|---|---|---|---|---|---|---|
| | $C_d = 0.001$ | $C_d = 0.002$ | $C_d = 0.0025$ | $C_d = 0.003$ | $C_d = 0.004$ | $C_d = 0.005$ |
| Major ellipse parameter: $C_{max\_computed}$ / $C_{max\_measured}$ | | | | | | |
| ADCP 1 | 1.21 | 1.08 | 1.00 | 0.97 | 0.86 | 0.78 |
| ADCP 2 | 1.12 | 1.01 | 0.94 | 0.91 | 0.81 | 0.73 |
| ADCP 3 | 1.21 | 1.10 | 1.01 | 0.96 | 0.85 | 0.78 |
| Minor ellipse parameter: $C_{min\_computed}$ / $C_{min\_measured}$ | | | | | | |
| ADCP 1 | 0.50 | 0.42 | 0.33 | 0.25 | 0.08 | 0.08 |
| ADCP 2 | 0.54 | 0.46 | 0.38 | 0.31 | 0.15 | 0.08 |
| ADCP3 | 0.57 | 0.29 | 0.14 | 0.14 | 0.14 | 0.14 |
| Phase: $\phi_{computed}$ - $\phi_{measured}$ (deg) | | | | | | |
| ADCP 1 | -46 | -23.4 | -17.9 | -9 | -3.8 | -4.7 |
| ADCP 2 | -40.3 | -19.7 | -13.4 | -4.6 | 3.3 | 4 |
| ADCP3 | -97.9 | -91.8 | -98.7 | -98.9 | -106.1 | -100.7 |
| Inclination: $\theta_{computed} - \theta_{measured}$ (deg) | | | | | | |
| ADCP 1 | -8.1 | -8.3 | -8.9 | -9.1 | -10.2 | -11.2 |
| ADCP 2 | -7.2 | -7.3 | -8.1 | -8.4 | -9.8 | -10.7 |
| ADCP3 | 1.1 | 0.7 | 0.2 | 0.7 | 0.3 | 0.5 |

Table 6.7. Comparison of normalised measured and computed $S_2$ currents at the ADCP locations for a range of seabed friction coefficients 0.001-0.005.

The results show that, after calibration, the numerical model satisfactorily captures the magnitude of the stream-wise velocity component at all ADCP locations. Transverse velocity component predictions are not as accurate as those obtained for the stream-wise component; however these are of one order of magnitude lower than the stream-wise component. Phase is reasonably well captured at ADCP 1 and 2 locations and worse agreement is achieved at ADCP 3. The independence of the inclination to the choice of seabed friction coefficient reveals that this is a bathymetry dependent parameter, and as such, an increase in accuracy may only be reached by increasing the mesh refinement in the area.

Table 6.8 and Table 6.9 present the coefficient of determination $R^2$ computed at the three ADCP locations for the stream-wise and transverse velocity components respectively. For both velocity components, the increase in value of bottom friction coefficient improves the

value of $R^2$ at the three ADCP locations. The relatively low $R^2$ values obtained for the transverse velocity component at ADCP 1 and 2 are in accordance with the disagreement observed in the minor ellipse and inclination values shown in Table 6.6. Overall, the use of $C_d = 0.0025$ appears to provide a good approximation to the flow characteristics at the three ADCP locations.

| | Non-dimensional seabed friction coefficient ($C_d$) | | | | | |
|---|---|---|---|---|---|---|
| Location | 0.001 | 0.002 | 0.0025 | 0.003 | 0.004 | 0.005 |
| ADCP 1 | 0.90 | 0.92 | 0.94 | 0.94 | 0.96 | 0.97 |
| ADCP 2 | 0.91 | 0.93 | 0.94 | 0.95 | 0.96 | 0.97 |
| ADCP 3 | 0.90 | 0.93 | 0.93 | 0.94 | 0.94 | 0.95 |

Table 6.8. Coefficient of determination $R^2$ for the stream-wise velocity component $u$ at ADCP 1, 2 and 3 locations, for seabed friction coefficients between $C_d = 0.001$ and 0.005.

| | Non-dimensional seabed friction coefficient ($C_d$) | | | | | |
|---|---|---|---|---|---|---|
| Location | $C_d = 0.001$ | $C_d = 0.002$ | $C_d = 0.0025$ | $C_d = 0.003$ | $C_d = 0.004$ | $C_d = 0.005$ |
| ADCP 1 | 0.69 | 0.73 | 0.73 | 0.74 | 0.74 | 0.75 |
| ADCP 2 | 0.76 | 0.80 | 0.79 | 0.81 | 0.81 | 0.82 |
| ADCP 3 | 0.89 | 0.93 | 0.94 | 0.95 | 0.95 | 0.96 |

Table 6.9. Coefficient of determination $R^2$ for the transverse velocity component $v$ at ADCP 1, 2 and 3 locations, for seabed friction coefficients between $C_d = 0.001$ and 0.005.

From the above results it may be concluded that the numerical predictions using a seabed friction coefficient $C_d = 0.0025$ are in good agreement with the measured free surface and velocity data in the vicinity and far-field of the site. Figure 6.17 shows a contour plot of the $M_2$ tidal amplitudes predicted by Fluidity with a bottom friction $C_d = 0.0025$. An amphidromic point, where tidal amplitudes are equal to zero, can be seen to the north of the Rathlin Island. The location of the amphidromic point and spatial variation of $M_2$ amplitudes are in agreement with the three-dimensional numerical predictions by Davies and Jones in the Celtic and Irish Seas [165].

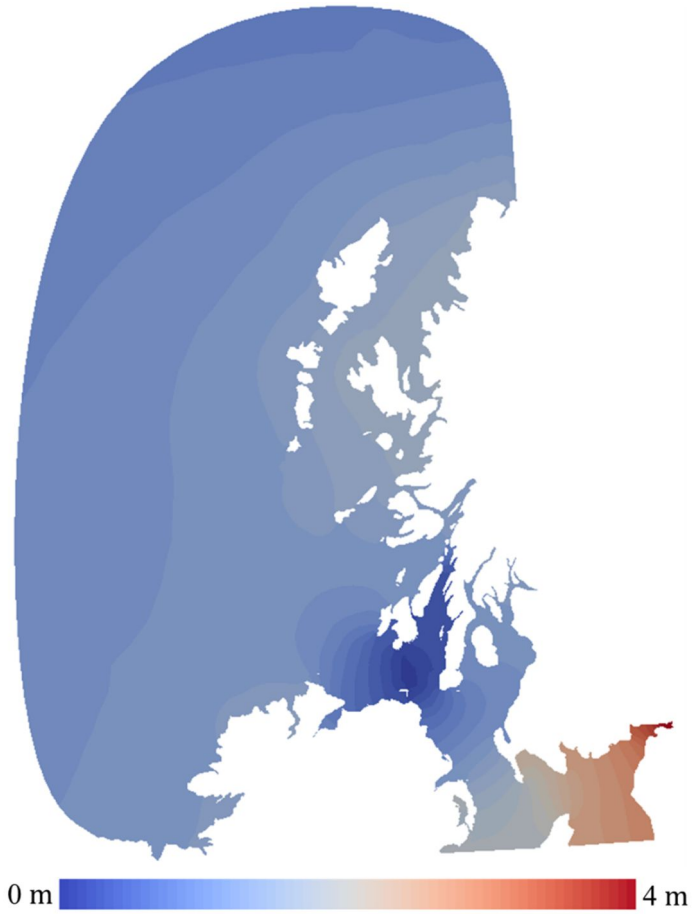


Figure 6.17. $M_2$ tidal amplitudes predicted by Fluidity with seabed friction coefficient $C_d = 0.0025$.

The results from the harmonic analysis of the free surface and velocities and the coefficient of determination of the velocities have determined that the numerical predictions are best calibrated using a seabed friction coefficient $C_d = 0.0025$. Unless otherwise stated, the results from the analysis presented in the following sections are simulated using a seabed friction coefficient $C_d = 0.0025$.

## 6.3. Analysis of the Rathlin Sound

The previous section has detailed the set-up of the Fluidity numerical model of Rathlin Sound and showed that the model satisfactorily replicates the main flow dynamics in the vicinity and in the far field of Rathlin Sound. This section presents a resource assessment for Rathlin Sound and compares the predictions to results obtained in the idealised island-landmass study in Chapter 5. In all cases, the numerical model is run for nine $M_2$ tidal cycles starting on the 24$^{th}$ of April 2014: here, two $M_2$ tidal periods correspond to the ramp-

up of the system; the following four $M_2$ tidal periods correspond to system spin-up; the final three tidal cycles are used for data analysis. In order to help the comparison process with results from Chapter 5, the boundary conditions are forced solely with an $M_2$ tide.

### 6.3.1 The natural state

It is important to understand the natural flow dynamics at the site in order to evaluate changes to the hydrodynamic environment caused by tidal power extraction. Figure 6.18 presents contour plots of the depth-averaged flow speed and vorticity during flood, ebb and slack water. During flood tide, Rue Point and Fair Head appear to constrain the flow east of the strait leading to a jet advecting south-east from Rathlin Sound. During ebb tide, the flow travels west in Rathlin Sound and is constrained by a large eddy shedding from Rue Point. This large, westward-advecting eddy increases the complexity of the flow dynamics west of the strait, and the resulting high flow rotationality will make tidal energy exploitation west of the island a challenging prospect. At slack water from ebb to flood tide, large residual eddies are released in both the strait and the near field offshore of the island. The residual eddies are smaller during slack water between flood and ebb tides. These residual eddies are responsible for the flow velocity not completely disappearing during the slack period. The location and duration of these residual eddies must be taken into account during site selection and farm design.

Figure 6.19 depicts contour plots of mean flow speeds (during three $M_2$ tidal cycles) and maximum flow speed in the natural state. High velocities are predicted at the east side of the strait and offshore east of the island, and along the coast south-east of Rathlin Sound. Averaged and maximum speeds in the order of 2 and 3 m/s are achieved respectively in the vicinity of the site, solely due to the $M_2$ tide. Based on the local flow speeds, Figure 6.20 presents the three-cycle averaged kinetic power density contour plots, which are slightly lower than 5,000 $W/m^2$ in the vicinity of the site.

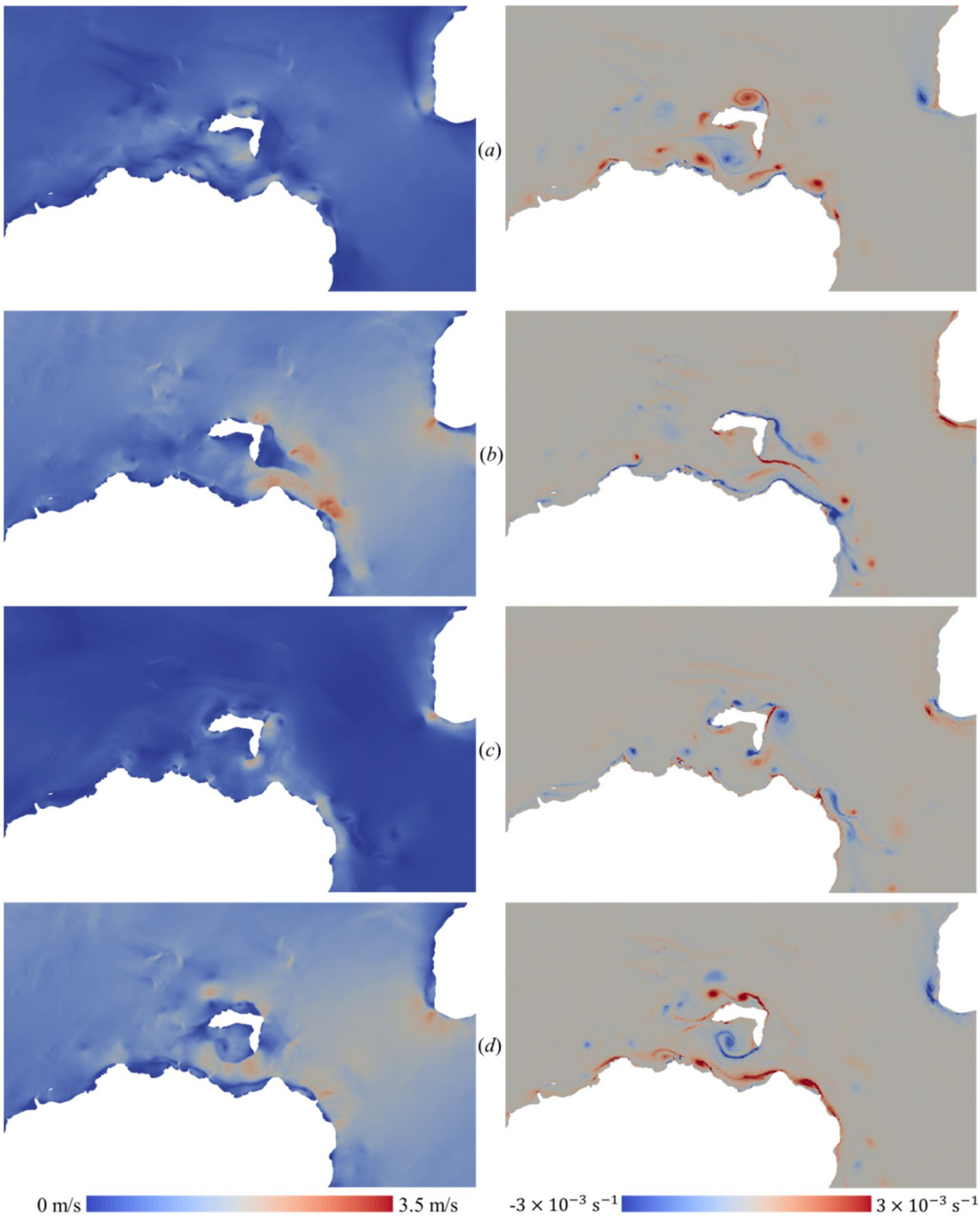


Figure 6.18. Predicted flow speed (left) and vorticity (right) contour plots for undisturbed conditions at $t$ = (*a*) $T/4$ (slack tide), (*b*) $T/2$ (flood tide), (*c*) $3T/4$ (slack tide) and (*d*) $T$ (ebb tide).

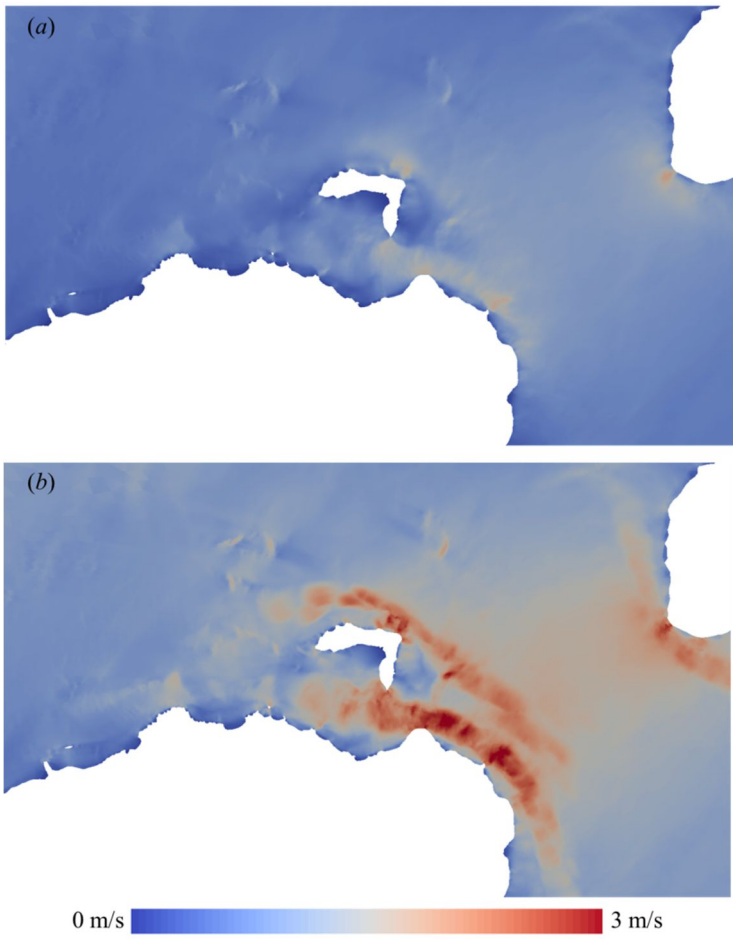


Figure 6.19. Contour plots of the three-tidal-cycle (*a*) mean and (*b*) maximum flow speeds in undisturbed conditions.

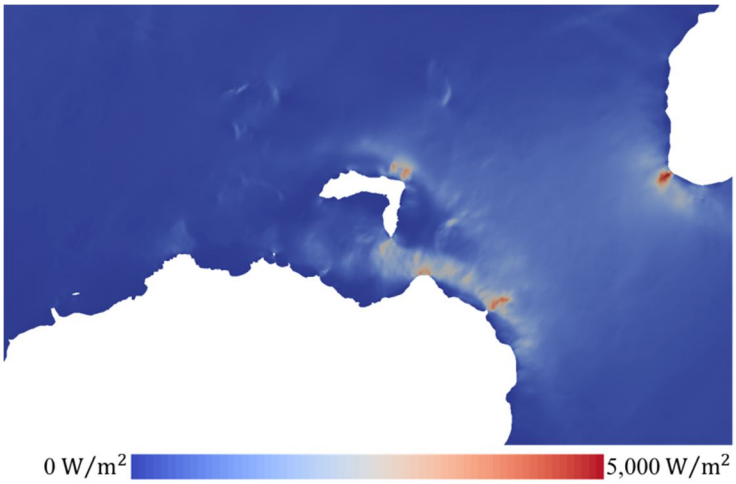


Figure 6.20. Contour plot of the three-tidal-cycle mean kinetic power density in undisturbed conditions.

Both Figure 6.19 and Figure 6.20 indicate that the area east of Rathlin Sound, between Rue Point and Fair Head, is likely to be the most energetic part of Rathlin Sound. The flow dynamics at the east of the strait are now explored further through analysis of the flow speed time series at the shortest transect of length $L_s$ = 4,020 m connecting Rue Point (55.23N / 6.15W) to Fair head (55.26N / 6.19W) (Figure 6.21).

Figure 6.21. Location of the east transect at Rathlin Sound (dashed line) connecting Rue Point with Fair Head, with the diamond symbols indicating the locations used to estimate the head driving the flow in the strait.

Figure 6.22 plots time series of the flow speeds across the transect east of the Rathlin Sound. The parameter $l$ defines the location within the transect normalised by $L_s$, where 0 and 1 refer to the Fair Head and Rue Point locations. The plot shows that the highest speeds (2.5 m/s) are achieved near Fair Head and Rue Point during flood (e.g. 0.1-0.6 $t/T$) and ebb (e.g. 0.6-1.1 $t/T$) tides respectively. The predicted maximum speed values at mid-transect are relatively uniform, with higher speeds at flood that at ebb tide.

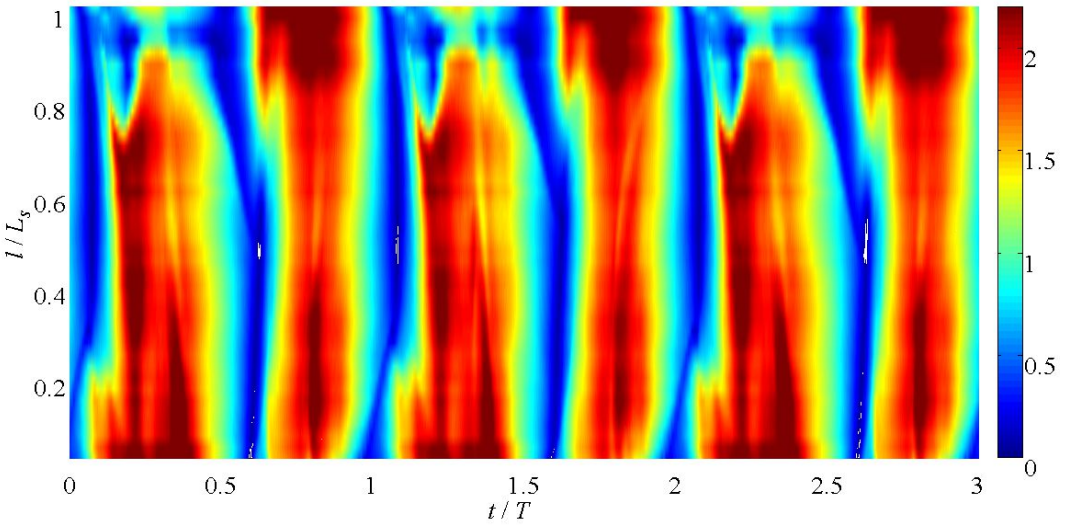


Figure 6.22. Flow speed time series across east transect of Rathlin Sound during three $M_2$ cycles.

### 6.3.2 Power extraction at the Rathlin Sound

Based on the analysis of Rathlin Sound in its natural state (Section 6.3.1), power extraction is now located at a cross-section east of Rathlin Sound highlighted in Figure 6.21. The area of power extraction, herein referred as the tidal farm, is defined as a rectangle of length $L_f$ = 100 m and width $B_f$ = 4,020 m. The tidal farm is implemented in a regular grid of 80 isosceles triangles (Figure 6.23) inserted in Mesh 3 (Figure 6.15).

Figure 6.23. Spatial discretisation of Rathlin Island and Sound with a triangular regular grid both in the strait and offshore east of the Sound.

Power extraction level in the tidal farm is characterised by a parameter $k_f$ (see Section 4.9). Figure 6.24 shows three tidal period-averaged results: undisturbed kinetic power $\bar{P}_{ko}$, defined as the kinetic power in the strait with no power extraction; power naturally dissipated at the seabed in the strait in the absence of power extraction $\bar{P}_s$; kinetic power in the strait $\bar{P}_k$ with the tidal farm present; and power extracted from the flow by the tidal farm $\bar{P}_e$, which as explained in Section 5.3.1 represents an upper limit to power extraction in the strait. The maximum power extracted in the strait is computed to be $\bar{P}_e = 298$ MW. No clear relationship is found between the maximum extracted power and either the undisturbed kinetic power or the power dissipated naturally at the seabed by friction. However, it is interesting to note that $\bar{P}_s < \bar{P}_e < \bar{P}_{ko}$ as for the non-uniform seabed and no-slip island-landmass scenarios analysed in Section 5.3.1. Rates of decrease in $\bar{P}_k$ are similar to those observed in the non-uniform seabed scenario. Analysis of the ratio of the power extracted $\bar{P}_e$ to the undisturbed kinetic power $\bar{P}_{ko}$, $\hat{P}$, shows that for the Rathlin Sound $\hat{P} = 0.79$ which is quite close to $\hat{P} = 0.74$ obtained for the non-uniform seabed island-landmass scenario. However, analysis of a case where the water depth offshore is greater than in the strait (Section 5.3.1.3) showed a negative correlation with the power extracted in the strait, with

$\hat{P} = 0.58$ when the depth was increased from $h$ in the strait to $4h$ offshore. In Rathlin Sound, the water depth offshore is around three times the depth in the strait. So the ratio $\hat{P} = 0.79$ reached in the Rathlin Sound already incorporates the offshore depth effects, and so the ratio $\hat{P}$ for Rathlin Sound differs from the island-landmass predictions.

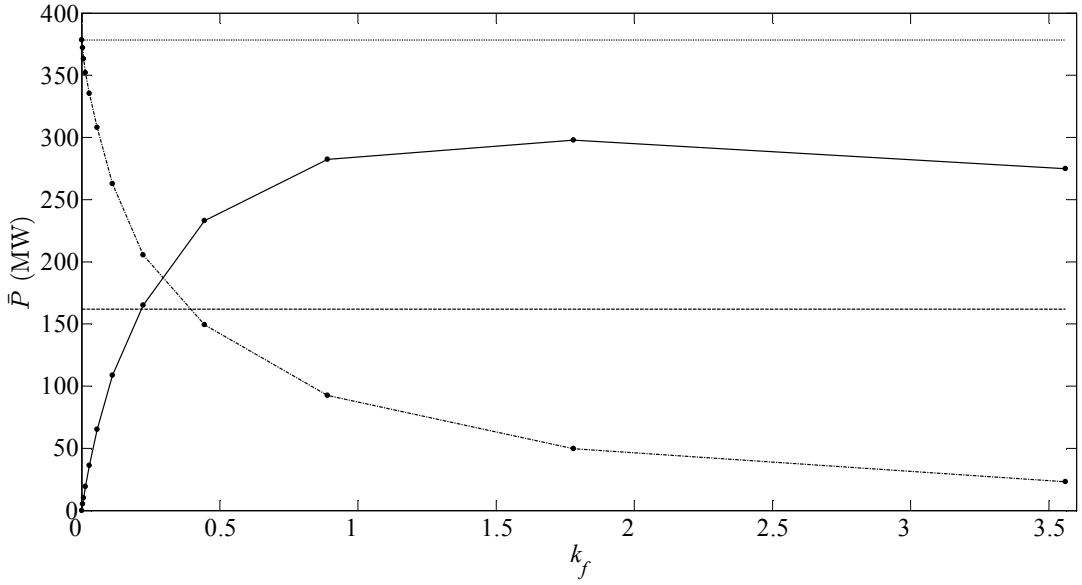


Figure 6.24. Power profiles as functions of $k_f$ in Rathlin Sound: extracted power for tidal farm located in the strait (solid line); kinetic power for the strait with the tidal farm present (dash-dot line); kinetic power for undisturbed conditions in the strait (dotted line); and power dissipated naturally at the seabed in the strait (dashed line). Markers indicate discrete points computed using the numerical model.

The difference in water depth between the strait and offshore side of the island implies that the offshore path exerts lower resistance on the flow than the path through the strait, thus affecting volumetric flow rate trends. The changes in the volumetric flow rate with power extraction are assessed at two sections: at the strait cross-section where power extraction is implemented, and at a section of equal length spanning offshore of the east side of the island (Figure 6.23). Figure 6.25 shows the volumetric flow rate in the strait $\bar{Q}$ and offshore normalised by the volumetric flow rate in the absence of power extraction $\bar{Q}_o$. When the difference in water depth between the strait and offshore sides of the island is accounted for, the trends observed in the volumetric flow rate at both sides of the island agree with those observed in the non-uniform seabed island-landmass scenario.

Figure 6.26 plots the power extracted in the strait $\bar{P}_e$ against the volumetric flow rate across the strait. The results indicate that the peak in $\bar{P}_e$ may be reached for values of flow

reduction slightly higher than 57.7 % of the flow in the absence of power extraction derived by GC2005 and Bryden and Couch [43] for a channel linking two infinite ocean basins.

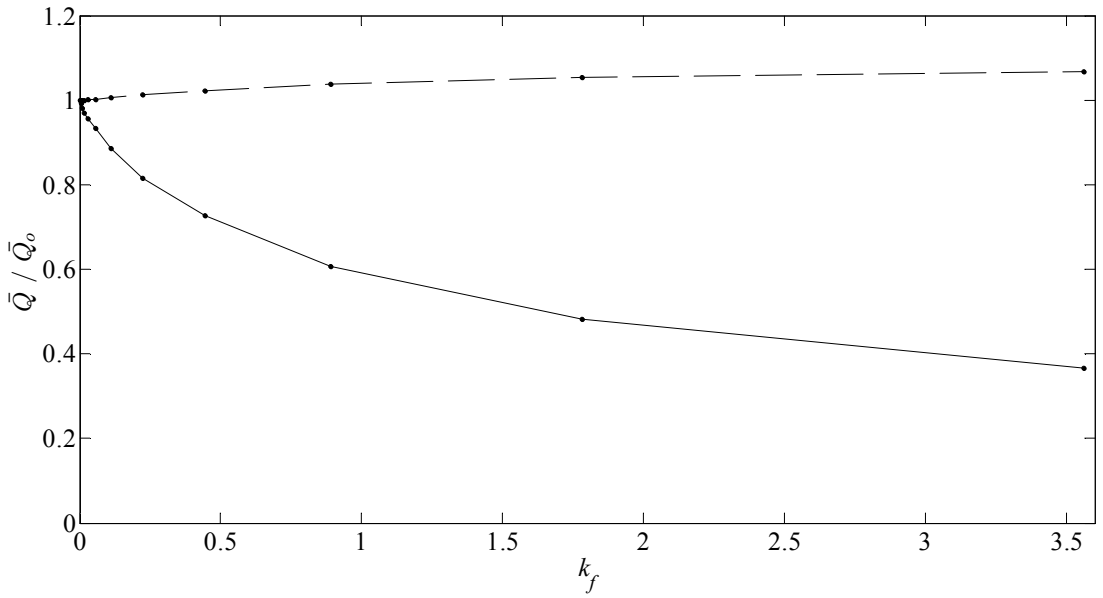


Figure 6.25. Changes in the ratio of actual to undisturbed volumetric flow rate across the tidal farm (solid line) and through a cross-section of identical length at the offshore side of the island (dashed line). Markers indicate discrete points computed using the numerical model.

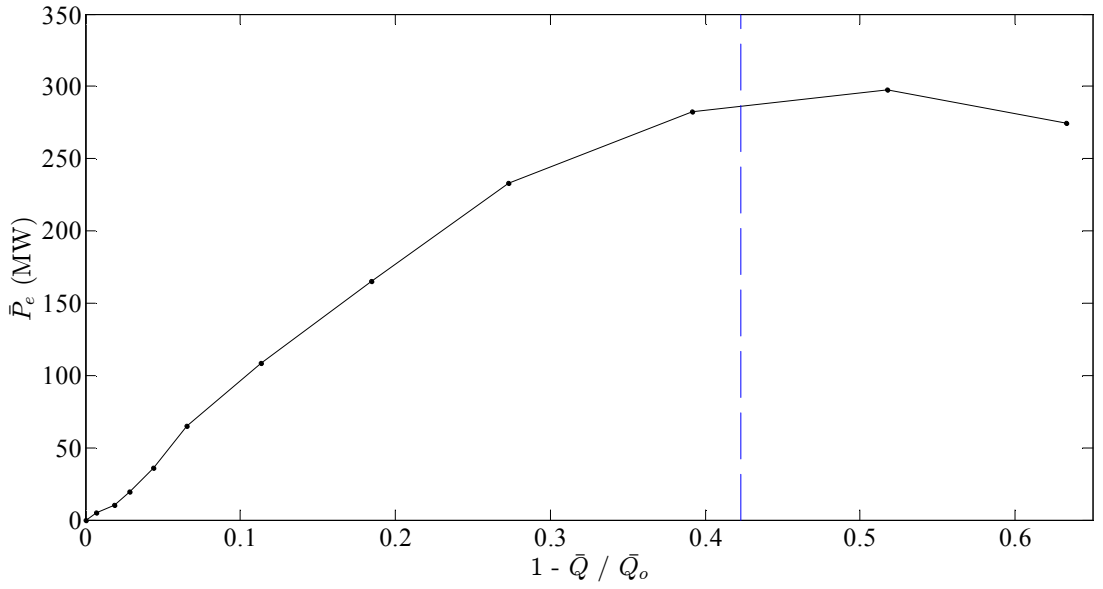


Figure 6.26. Power extracted against changes in normalised volumetric flow rate in the Rathlin Sound. Markers indicate output data from the numerical model. Vertical blue dashed line indicates a volumetric flow rate in the strait equal to 57.7% of the undisturbed conditions.

Changes in the head driving the flow through the strait are assessed at the east (55.25N / 6.16W) and west (55.25N / 6.31W) (Figure 6.21). Figure 6.27 plots the head driving the flow in Rathlin Sound with no power extraction, low extraction $k_f = 0.11$ and high extraction $k_f = 1.78$. In the natural state, the peak in the driving head at ebb is higher than at flood. During the ebb tide the head drop almost doubles during an hour, most likely induced by the large eddy detaching from Rathlin Island west of Rue Point (Figure 6.18d). With the addition of power extraction east of the strait, the head driving the flow at flood tide increases as observed in the no-slip island-landmass scenario in Section 5.3.1. During the ebb tide, the presence of power extraction produces an increase in head during most of the ebb tide while attenuating the temporary increase observed in the natural state.

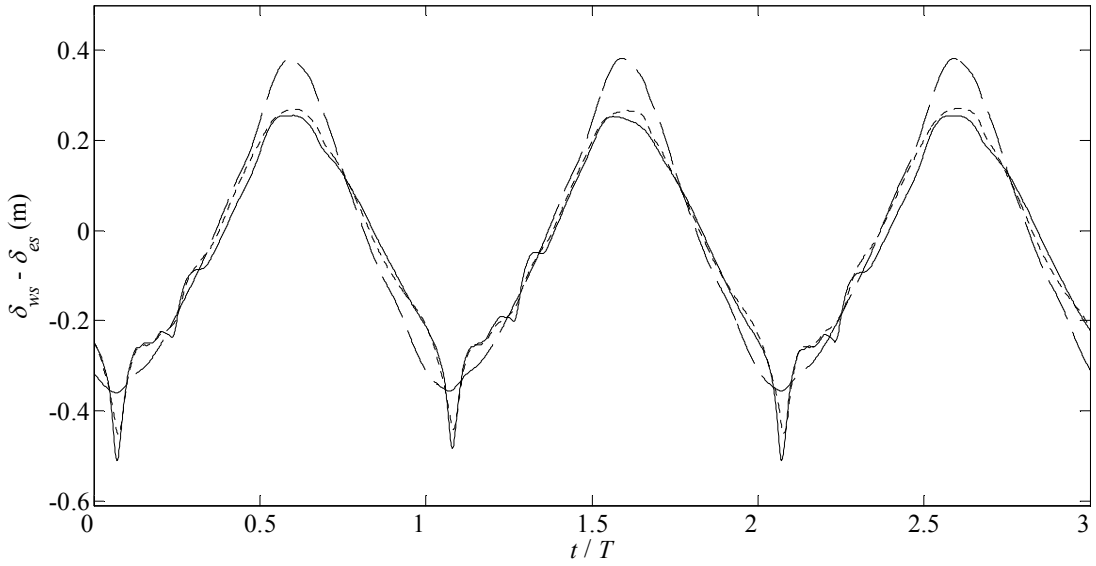


Figure 6.27. Flow-driving head between west and east of Rathlin Sound: no power extraction (solid line); low extraction $k_f = 0.11$ (dotted line); and high extraction $k_f = 1.78$ (dashed line).

Figure 6.27 indicates that the choice of location for analysis can affect the head amplitude estimates. This problem is mitigated by computing the head driving the flow based on the average strait cross-section free surface elevations east and west of Rathlin Sound (Figure 6.28). It can be seen that after the averaging process there is no longer a temporary increase in the head during ebb tide. By using an amplitude of the head driving the flow in undisturbed conditions of 0.22 m (Figure 6.28), it is possible to approximate the potential of the Rathlin Sound using the GC2005 channel model (Section 4.9.2). Based on $\gamma = 0.22$, the average power extracted is 162 MW, which is 46 % lower than the numerical predictions. Using $\gamma = 0.2$ based on the phase lag between head drop and volumetric flow rate peaks, the

analytical results are 51 % lower than the numerical predictions. These figures are of the same order as those obtained for the island-landmass no-slip scenario in Section 5.3.1.

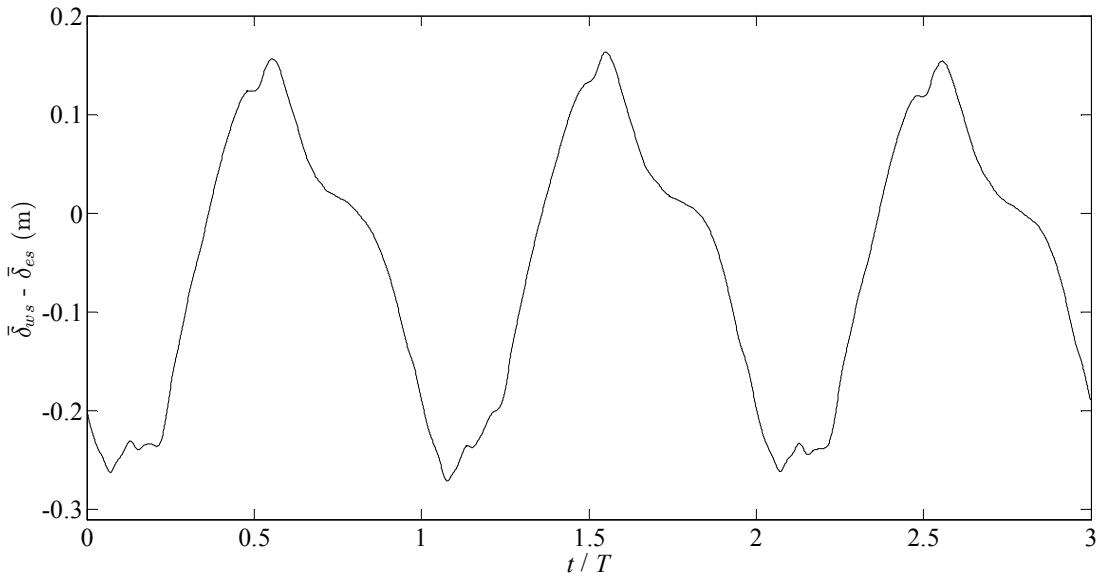


Figure 6.28. Flow-driving head between west and east of Rathlin Sound based on the cross-section averaged values of free surface.

During the pre-feasibility stage of a tidal project, data available for the site may be limited. In the case of Rathlin Sound, if free surface datasets are only available at the locations shown in Figure 6.21, the head amplitude may be taken equal to 0.38 m provided the temporary increase during ebb tide is accounted for (Figure 6.27). Based on this amplitude and assuming $\gamma = 0.22$, the GC2005 model underpredicts the maximum extracted power by only 5.4 %. However, as shown in Figure 6.28, the results vary depending on where data are available. This highlights the difficulty of applying analytical models to real coastal sites of complicated seabed topography where data available are scarce.

As highlighted in Section 5.3.1, environmental regulations may set limits to power extraction to limit the effects on local flow speeds and tidal ranges. Figure 6.29 compares contour plots of mean flow speeds (during three $M_2$ tidal cycles) at the site in undisturbed conditions against those at maximum power extraction in the strait. A substantial reduction in mean speed is observed in the strait, especially in the east, and along the coast of Northern Ireland south-east of the sound. The flow jet advecting south-east from Rathlin Sound during flood tide is diminished by the power extracted in the strait. This speed reduction is very significant near the mouth of the sound and appears to recover partly further downstream at Torr Head due to mixing with the surrounding flow field. From observations, it appears that

there is a slight increase in flow speed north of the island due to the increase in volumetric flow rates.

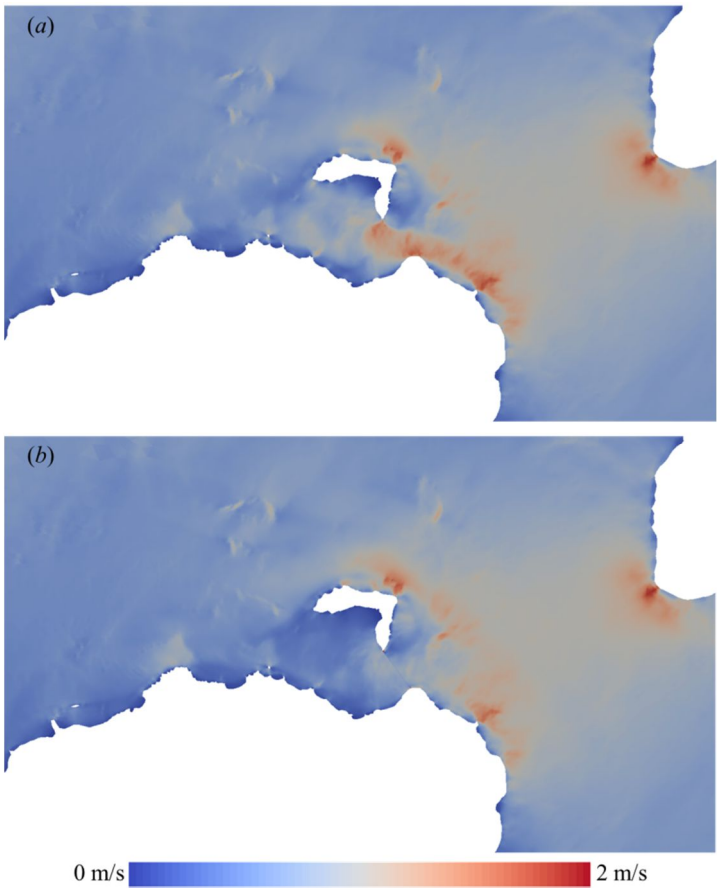


Figure 6.29. Contour plots of the three-tidal-cycle mean flow speeds: (*a*) no power extraction; and (*b)* extraction for $k_f = 1.78$.

To provide better understanding of changes to the site flow dynamics due to power extraction, Figure 6.30 presents the vorticity contour plots at peak flood and ebb tides with no extraction and maximum power extracted in the strait. At flood tide, there is an obvious reduction in the magnitude of the flow features advecting south-east of the sound in agreement with Figure 6.29. This reduction is less important further south-east of the site. During ebb tide, power extraction appears to diminish the eddy shedding from Rue Point and Fair Head. In addition, there appear to be flow changes north of the island which may be explained by the increase in local flow velocity.

Figure 6.31 shows the effect of power extraction from Rathlin Sound on sea surface elevation time histories at ADCP 3, Portrush and Bangor. As expected, ADCP 3 experiences the biggest change in the free surface time history, with a mean difference in the sea-surface

elevation during the three tidal cycles of about 10 %; at Portrush and Bangor the mean differences are found to be less than 1 %.

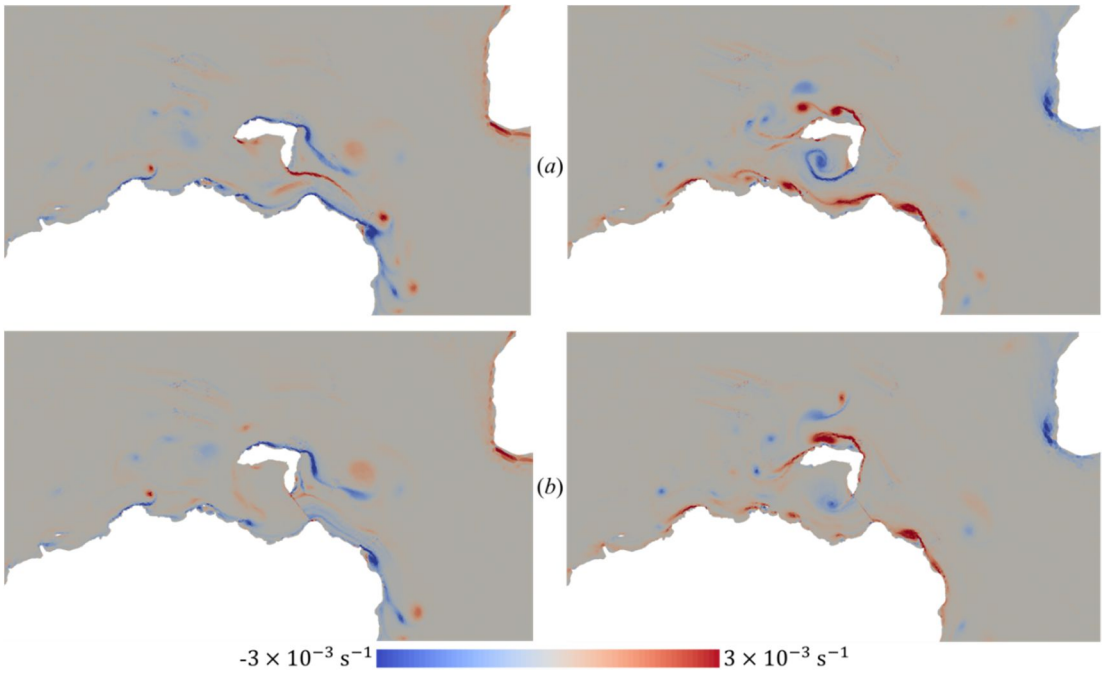


Figure 6.30. Vorticity contour plots with (*a*) no extraction and (*b*) $k_f$ = 1.78 at peak flood (left) and ebb (right) tides.

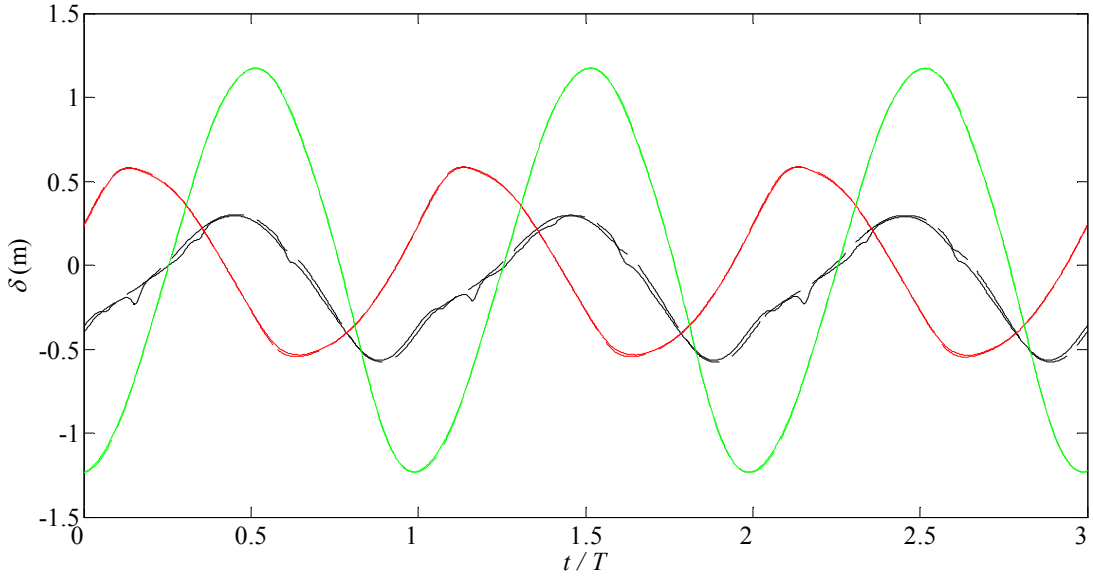


Figure 6.31. Time series of free surface elevation at locations ADCP 3 (black), Portrush (red) and Bangor (green) for the cases with no power extraction (solid) and maximum power extracted at $k_f$ = 1.78 (dashed).

### 6.3.3 Frictional environment

In the numerical model calibration presented in Section 6.2.5, the accuracy of the velocity predictions was measured by means of the coefficient of determination (see Table 6.8 and Table 6.9). The results indicated that for the three locations assessed, an increased seabed friction coefficient (within the range of values considered) improved the coefficient of determination of the stream-wise and transverse velocity components. If no further analysis had been performed on the data (e.g. harmonic analysis), the value of seabed friction coefficient $C_d$ = 0.005 may have been chosen to approximate the flow dynamics at the site. Choice of seabed friction coefficient affects power extraction estimates, as discussed by Adcock *et al*. [51] in their analysis of the Pentland Firth. Adcock *et al*. found that when $C_d$ was increased from 0.0025 to 0.005 there was a 29 % and 15 % reduction in the available power for a single row of low blockage turbines and four rows of highly blocked turbines respectively. Noting this, the present section analyses the sensitivity of power extraction in the Rathlin Sound to the choice of seabed friction coefficient.

Figure 6.32 presents the mean flow speed contour plots (during three $M_2$ tidal cycles) obtained with $C_d$ = 0.0025 and 0.005 in undisturbed conditions. The increase in seabed friction coefficient leads to a reduction in the averaged speeds at the site but it does not appear to modify the main site flow dynamics, in agreement with the conclusions from Section 6.2.5.

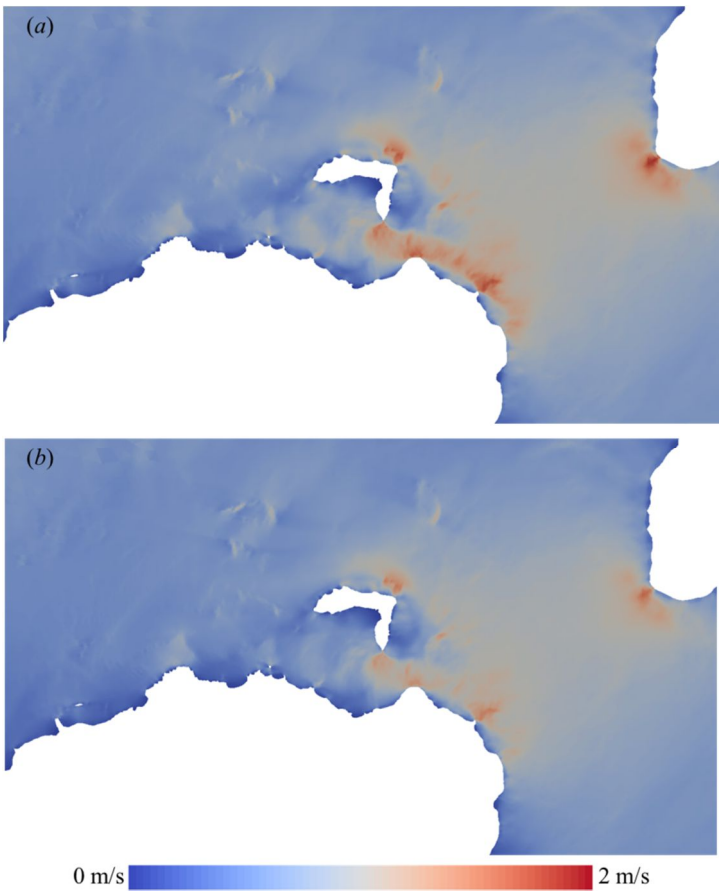


Figure 6.32. Contour plots of the three-tidal-cycle mean flow speeds in undisturbed conditions for (*a*) $C_d = 0.0025$ and (*b*) $C_d = 0.005$.

Figure 6.33 plots three-tidal-cycle averaged results of $\bar{P}_{ko}$, $\bar{P}_s$ , $\bar{P}_k$ and $\bar{P}_e$ for the two assessed seabed friction coefficients. As a result of increasing the seabed friction coefficient, the undisturbed kinetic power in the strait is reduced by 34 %, while there is a 12 % increase in the power naturally dissipated in the strait by the seabed. The increase of seabed friction coefficient yields a 15 % decrease in the maximum power extracted by the farm in the strait, although both peaks in power extraction are achieved at the same level of power extraction $k_f$. It appears that in this case the maximum power extracted in the strait is well approximated by the undisturbed kinetic power. For high levels of power extraction, both cases yield similar kinetic power values in the strait.

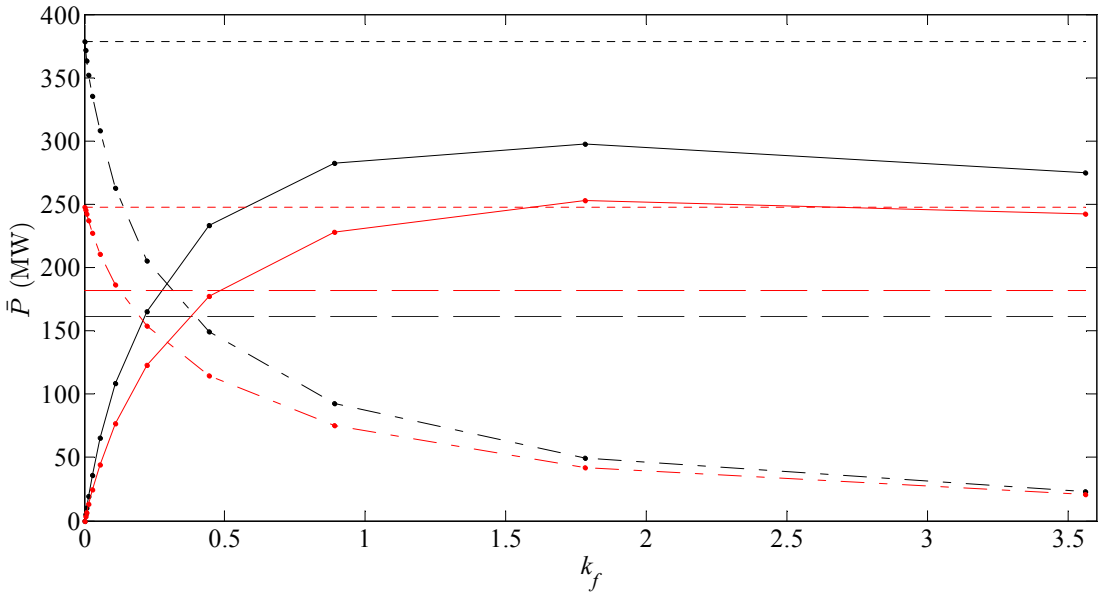


Figure 6.33. Power profiles as functions of $k_f$ in the Rathlin Sound: $C_d$ = 0.0025 (black) and $C_d$ = 0.005 (red). Extracted power for tidal farm located in the strait (solid line); kinetic power for the strait with the tidal farm present (dash-dot line); kinetic power for undisturbed conditions in the strait (dotted line); and power dissipated naturally at the seabed in the strait (dashed line).

From Figure 6.33, it can be concluded that the choice of seabed friction coefficient as input to the numerical model affects power extraction estimates; in this case doubling the seabed friction coefficient has reduced power extraction by 15 %. In the island-landmass study, a reduction in 20 % was found when doubling the seabed friction coefficient. These results are in accordance with the previously mentioned findings of Adcock *et al.* [51] for the Pentland Firth. Likewise, the island-landmass study showed that when the seabed friction coefficient was halved, there was an increase of 8 % in the maximum power extracted from the strait. These results highlight the uncertainty involved in the numerical predictions associated with the choice of seabed friction coefficient and the use of seabed friction dependent parameters (undisturbed kinetic power and power dissipated naturally at the seabed) to assess the potential of a strait.

### 6.3.4 Location of power extraction in the strait

This section explores the sensitivity of the maximum power extracted to the location of power extraction within the strait. Figure 6.20 showed that lower power densities are obtained at the west limit of the Rathlin Sound than at the east of the strait. The tidal farm is implemented in a regular grid filling the entire cross-section west of the strait (Figure 6.34), with dimensions $L_f$ = 100 m and $B_f$ = 6,860 m, and inserted in Mesh 3 (Figure 6.15).

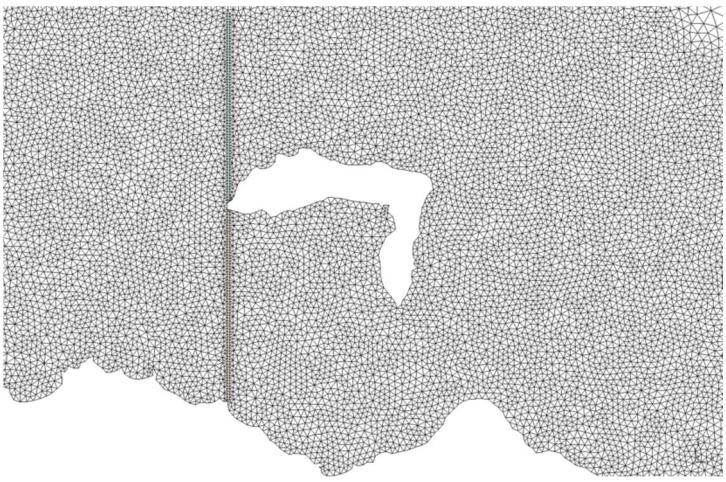

Figure 6.34. Spatial discretisation of Rathlin Island and Rathlin Sound with a triangular regular grid both in the strait and offshore west of the Sound.

Figure 6.35 plots three-tidal-cycle averaged values of $\bar{P}_{ko}, \bar{P}_s$ , $\bar{P}_k$ and $\bar{P}_e$ as functions of $k_f$ obtained to the west and east of the strait. There is a 15 % reduction in maximum power extracted when turbines are inserted west of the strait. The predicted value of maximum power extracted is higher than the undisturbed kinetic power west of the strait. This highlights the uncertainty associated with the use of this parameter to assess the potential of a strait of variable breadth and hence non-uniform undisturbed kinetic power distributions. Due to the lower velocity distribution achieved west of the strait, maximum power extracted is achieved at a higher extraction level than at the east of the strait. In order to extract the same amount of power, turbines installed west of the strait will require larger rotors to produce higher drag, compared to turbines installed east of the strait. The analysis of the island-landmass free-slip scenario in Section 5.3.1.4 concluded that when the strait is completely blocked by the array, the maximum power extracted is independent of the footprint area over which the tidal array is implemented, from which it might be conjectured that perhaps maximum power extraction is not influenced by the location of the array within the strait. However, Figure 6.35 shows that the position of the array in the Rathlin Sound does influence the maximum extracted power estimates. This apparent anomaly may be explained by the complex flow dynamics of the Rathlin Sound, with a large eddy shedding west from Rue Point during ebb tide (Figure 6.18).

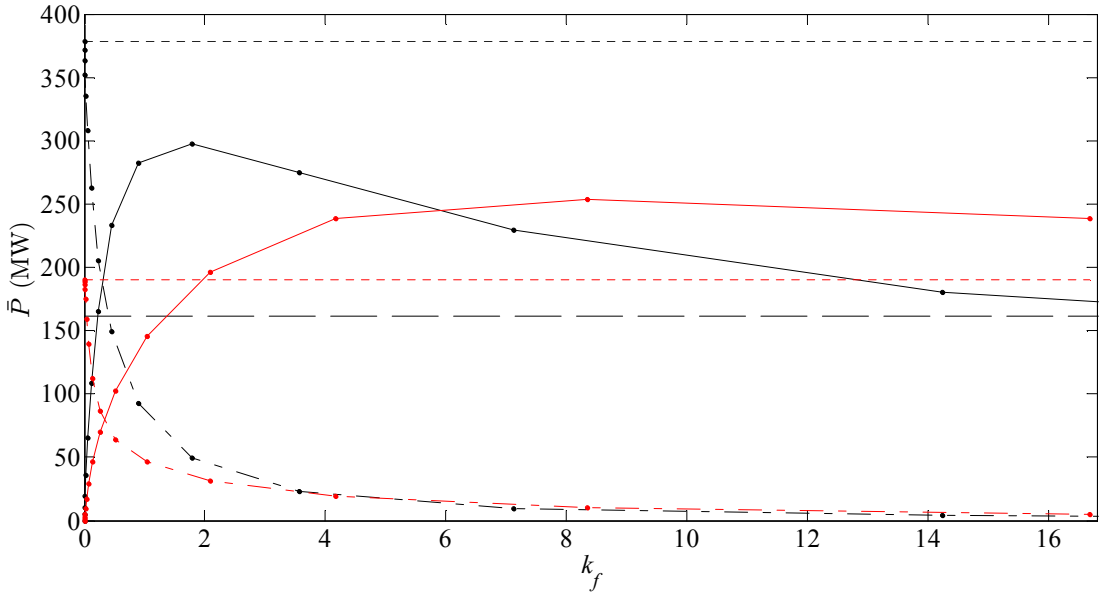


Figure 6.35. Power profiles as functions of $k_f$ in the Rathlin Sound: extraction east (black) and west (red) of Rathlin Sound. Extracted power for tidal farm located in the strait (solid line); kinetic power for the strait with the tidal farm present (dash-dot line); kinetic power for undisturbed conditions in the strait (dotted line); and power dissipated naturally at the seabed in the strait (dashed line).

Figure 6.36 plots the changes in volumetric flow rates in the strait and offshore when power extraction is implemented west and east of the strait. The volumetric flow rate offshore west of the strait is measured at a cross-section of similar breadth than the west strait cross-section (Figure 6.34). Similar flow rates are achieved in the strait and offshore in both cases when maximum power is extracted in the strait. Below a certain limit, further reductions in volumetric flow through the strait appear not to produce increases in volumetric flow offshore of the island.

Figure 6.37 shows the flow speed contour plots (averaged over three $M_2$ tidal cycles) for the value of $k_f$ which yields maximum power extracted at the east and west of the strait respectively. Similar velocity distributions are achieved in the far-field in both cases, with slightly higher velocities achieved south-east of the strait when power is extracted west of the strait. This may be explained by the increase of the distance to the array allowing further flow recovery.

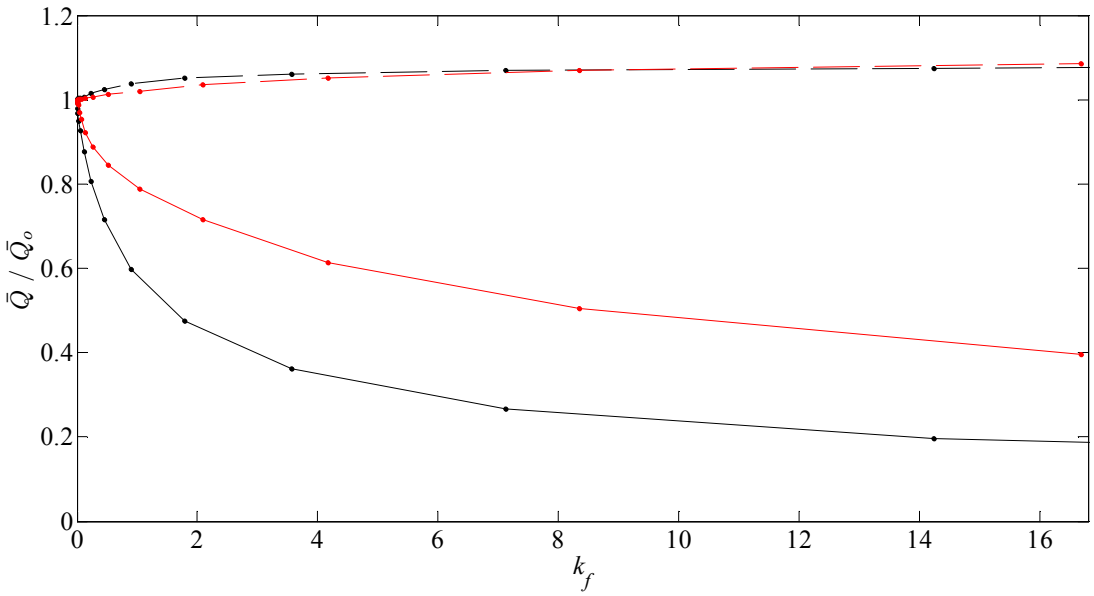


Figure 6.36. Variation in ratio of disturbed to undisturbed volumetric flow rate as function of power extraction $k_f$ when power extraction is implemented east (black) and west (red) of Rathlin Sound. Volumetric flow rate across the farm in the strait (solid line) and through a cross-section of similar length at the offshore side of the Rathlin Island (dashed line).

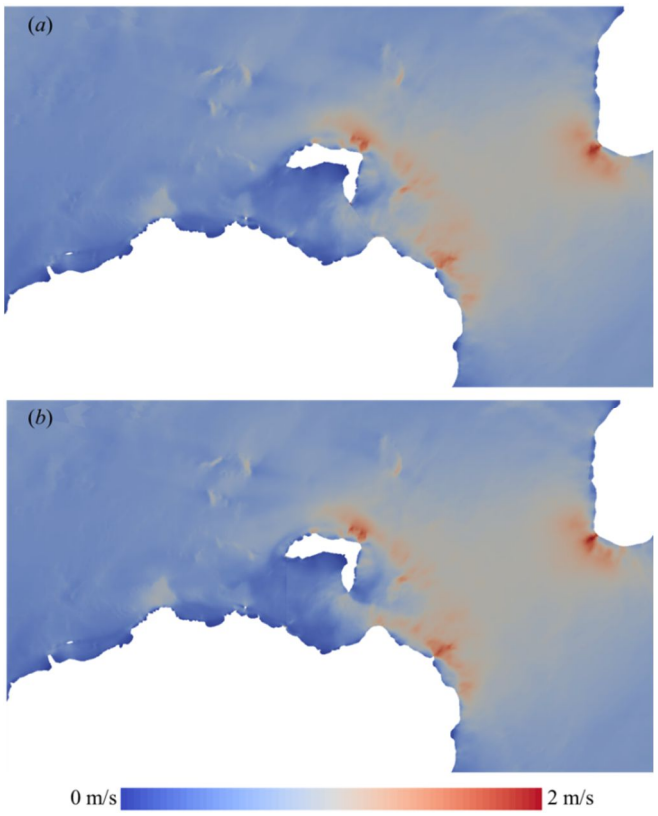


Figure 6.37. Contour plots of the three-tidal-cycle mean flow speeds when maximum power is extracted (*a*) east and (*b*) west of the strait.

### 6.3.5 Strait blockage

Sections 6.3.2 to 6.3.4 assessed the maximum power extracted in Rathlin Sound for an array that blocked the entire strait cross-section. In practice however, power extraction will not be implemented in certain parts of the strait due to technical and environmental constraints. This section investigates the influence of partial strait blockage on power extraction estimates for the array located east of the Rathlin strait in Section 6.3.2. Here, the array width is shortened equally from both ends, to 80 % and 60 % of the original width. Figure 6.38 plots the three tidal period-averaged results of $\bar{P}_{ko}$, $\bar{P}_s$, $\bar{P}_k$ and $\bar{P}_e$ obtained for the different array-blockage ratios against the equivalent number of turbines (defined in Section 5.3.1). At blockage ratios of 80 % and 60 % the maximum power extracted from Rathlin Sound decreases by 14 % and 36 %, compared to the fully blocked case. In the non-uniform seabed island-landmass scenario 80 % and 60 % blockage ratios lead to reductions in power extracted of 0.4% and 30%. Agreement between the Rathlin Sound and idealised cases is satisfactory for 60 % array blockage ratio. Discrepancies for 80 % blockage ratio arise from the island-landmass bathymetry, which increases resistance and restricts the bypass flow. The three blockage ratios yield similar power extraction estimates for a low number of turbines ($N_T \leq 200$), but the estimates diverge when the turbine density is increased and flow through the farm reduces at low blockage ratios. This accords with results from the idealised island-landmass and Nishino and Willden [153] discussed in Section 5.3.1.5. The reduction of kinetic power in the strait is smaller as array to strait ratio is reduced, because the area is increased within the strait where flow is permitted to bypass the array.

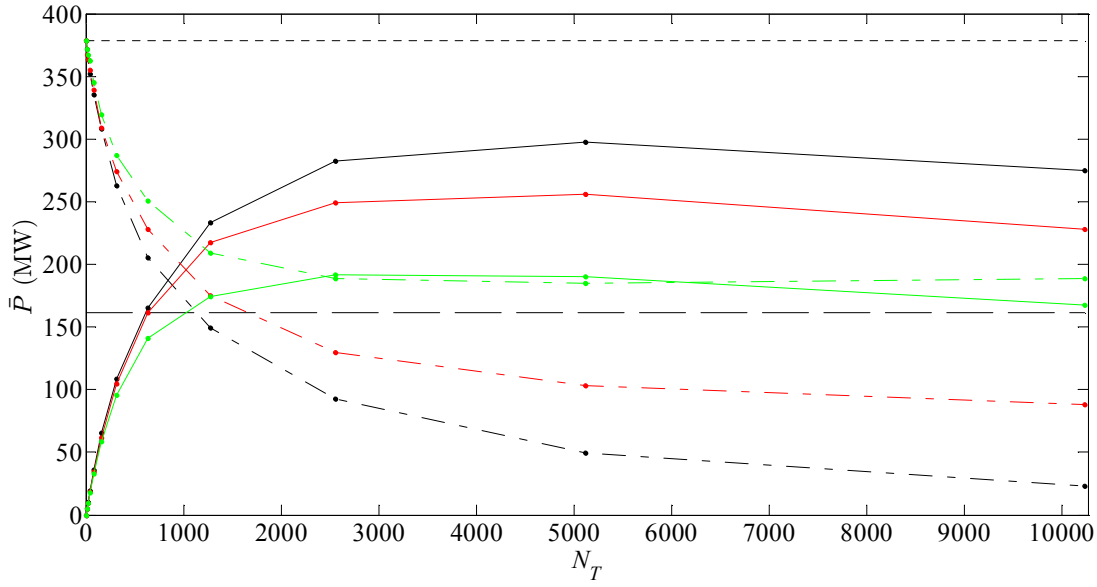


Figure 6.38. Power profiles as functions of number of turbines $N_T$ in Rathlin Sound for three blockage ratios: 100 % (black); 80 % (red); and 60 % (green). Extracted power for tidal farm located in the strait (solid line); kinetic power for the strait with the tidal farm present (dash-dot line); kinetic power for undisturbed conditions in the strait (dotted line); and power dissipated naturally at the seabed in the strait (dashed line).

Figure 6.39 plots the volumetric flow rate ratios through the strait, offshore, through the array and through the strait bypass sections for the different array blockage ratios. Farm and strait bypass volumetric flow rates are normalised by the undisturbed volumetric flow rate through the strait. Volumetric flow rate through the strait is less affected by power extraction as blockage ratio is reduced. Similar rates of change in volumetric flow through the farm are observed for the 80 % and 60 % blockage ratios. A higher rate of change in the strait bypass section volumetric flow rate is observed for the 60 % blockage ratio than for the 80 %, leading to higher volumetric flow rates through the strait for equal numbers of turbines in the array. When maximum power is extracted from the strait, an increase in strait blockage yields an increase in offshore volumetric flow rates.

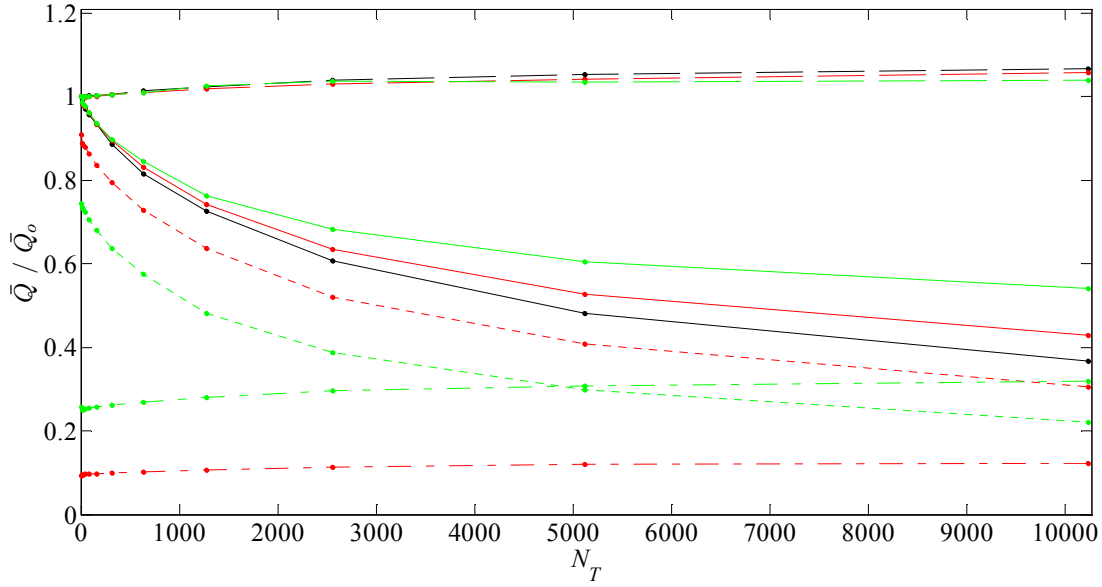


Figure 6.39. Variation in ratio of disturbed to undisturbed volumetric flow rates in Rathlin Sound as a function of number of turbines for three extraction blockage ratios: 100 % (black); 80 % (red); and 60 % (green). Volumetric flow rate across the strait (solid line); through the farm in the strait (dotted line); bypassing the farm at the strait (dash-dot line); and through a cross-section of almost identical length as the strait at the offshore side of the island (dashed line).

Figure 6.40 presents contour plots of mean flow speeds (during three tidal cycles) at maximum power extracted from the strait for three blockage ratios. For both the 80 % and 60 % cases, there is a local increase in flow speed in the strait bypass sections where power extraction is not implemented. The average increases of mean flow speed in the strait bypass sections over the three tidal cycles are 20 % and 14 % for the 80 % and 60 % blockage ratios respectively. If the seabed is erodible, this increased change in the local flow speed might accelerate sediment erosion in the bypass zones whereas the reduction in mean flow speed at the centre of the strait might increase sediment deposition, thus altering the overall sediment transport processes and seabed morphodynamics during the project life.

Changes in the site flow dynamics at maximum power extraction for the three blockage ratios can be discerned from the vorticity plots in Figure 6.41. At flood tide, vortical structures are generated from the ends of the array, which then advect south-east off the strait, and increase in size as strait blockage is reduced. At ebb tide, the magnitude of the eddy generated at Rue Point increases as strait blockage reduces. Interestingly, it appears that the vortical structures generated from the north tip of the array merge with those generated at Rue Point. As the mean flow speed increases at the south of the strait, the

strength of the vortical structures advecting west of the strait also increases. No significant changes are observed in the far-field flow site dynamics.

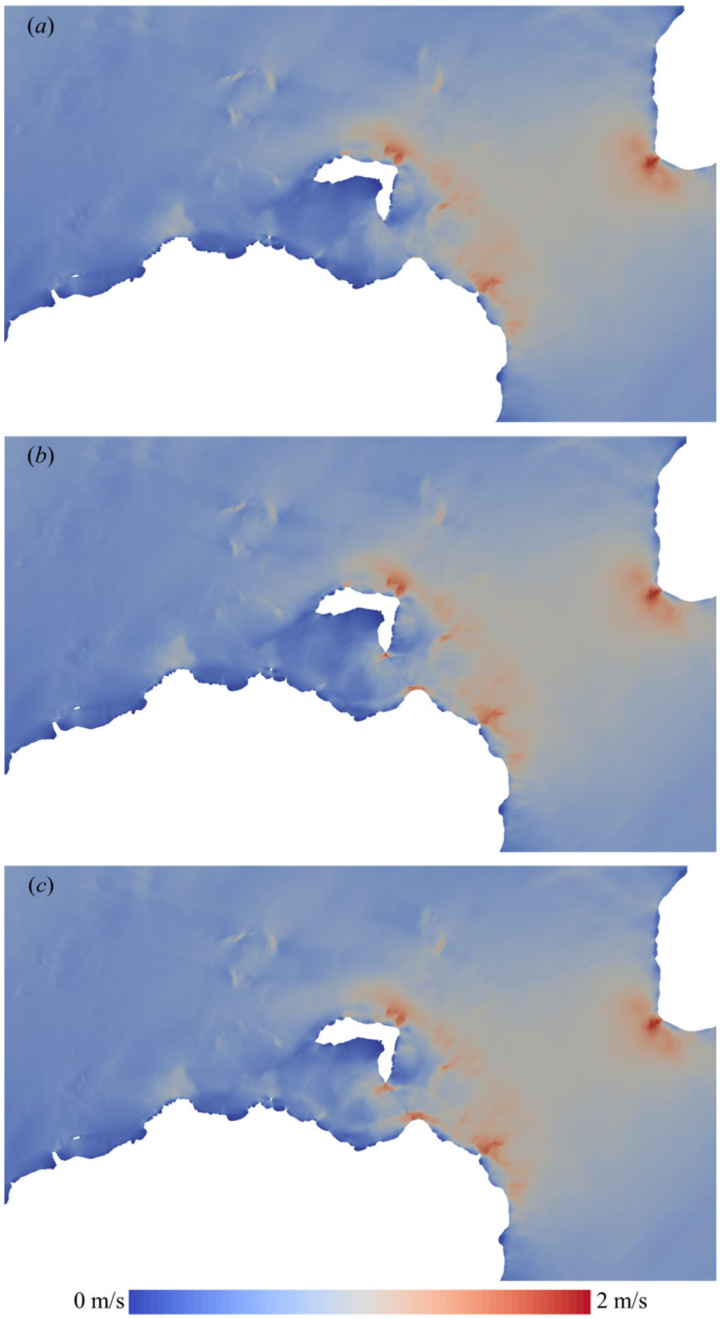


Figure 6.40. Contour plots of the three-tidal-cycle mean flow speeds at maximum power extraction for array to strait width ratios of: (*a*) 100 %; (*b*) 80 %; and (*c*) 60 %.

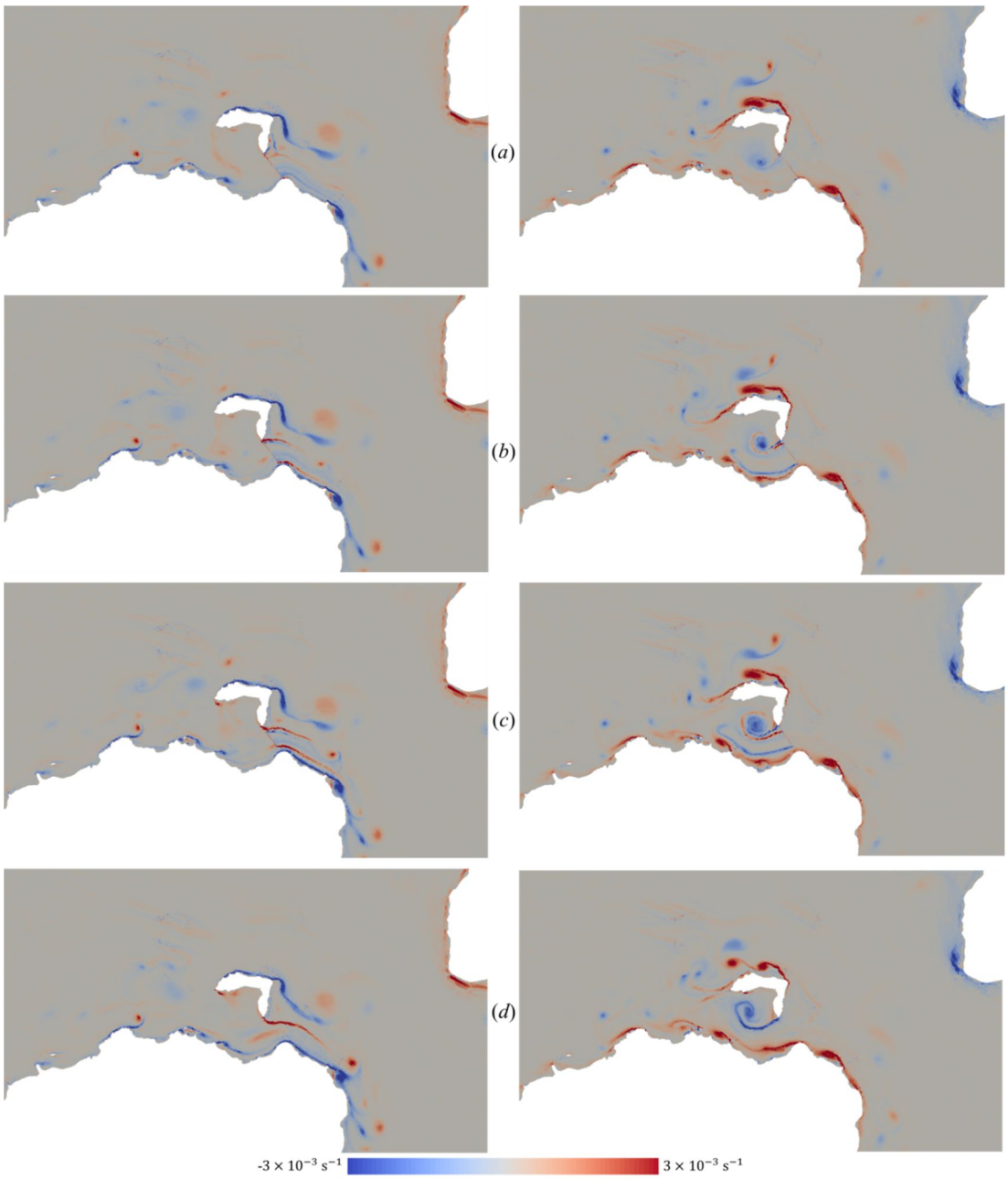


Figure 6.41. Vorticity contour plots at maximum power extraction for array to strait width ratios: (*a*) 100 %; (*b*) 80 %; (*c*) 60 %; and (*d*) no extraction at peak flood (left) and ebb (right) tides.

### 6.3.6 Power extraction offshore of the island

Analysis of the natural state in Section 6.3.1 revealed that there is an area of high power density north-east of Rathlin Island (Figure 6.20). The present section analyses the limits to power extraction offshore of Rathlin Island and extends the analysis to consider power extraction both in the strait and offshore. Power extraction is now implemented north-east of

Rathlin Island (Figure 6.23) over a rectangular area extending north of the domain of dimensions $L_f$ x $B_f$ that are the same as those of the farm east of the strait considered in Section 6.3.2. Figure 6.42 plots the three-tidal-cycle averaged values of $\bar{P}_{ko}$, $\bar{P}_s$ , $\bar{P}_k$ and $\bar{P}_e$ as functions of power extracted $k_f$, obtained when power extraction is implemented separately in the strait and offshore of the island. There is a 134 % increase in maximum power extracted offshore of the strait compared to the peak in power extraction attained at the east side of the strait. Here, the peak in power extracted is reached at higher power extraction levels than for the strait. Maximum power extracted offshore is approximately 13 % lower than the undisturbed kinetic power offshore of the island.

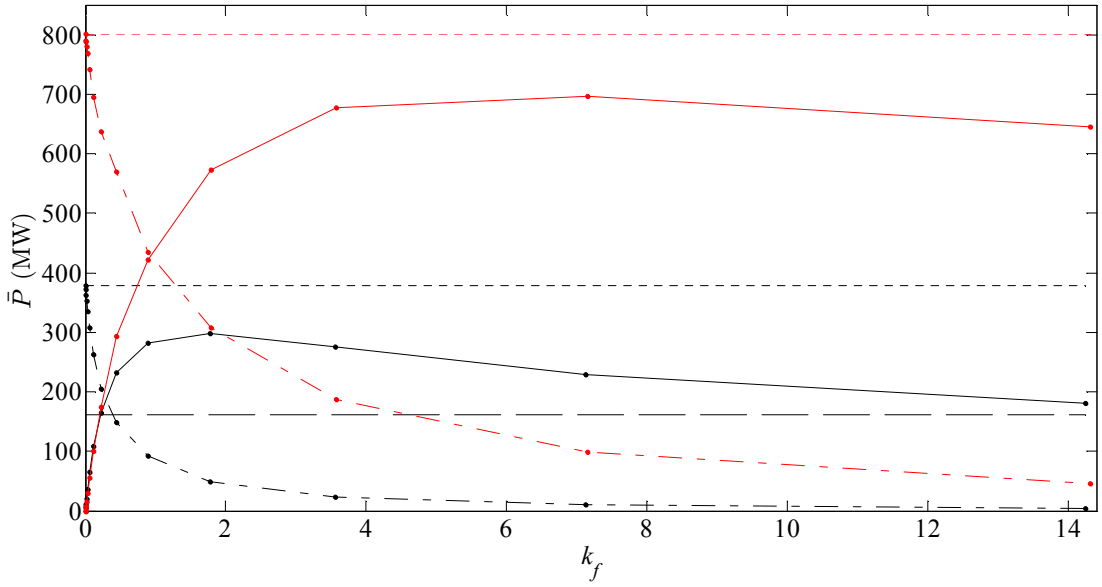


Figure 6.42. Power profiles as functions of power extracted $k_f$ for the Rathlin Sound site: extraction only at strait (black) and extraction only offshore of the island (red). Extracted power for tidal farm (solid line); kinetic power with the tidal farm present (dash-dot line); kinetic power for undisturbed conditions (dotted line); and power dissipated naturally at the seabed (dashed line).

Figure 6.43 compares changes in volumetric flow rate in the strait and offshore of the island when power is extracted separately at each side of the island. There is an increase in volumetric flow rate through the strait as the power extracted increases offshore of the island. Although the flow can divert further north from the offshore farm, the changes in the volumetric flow rates through the strait indicate that part of this flow diverts through the strait. The figure shows that there is a higher volumetric flow ratio bypassing the island through the strait when power is extracted offshore than the equivalent offshore bypass flow when power is implemented in the strait. This is directly linked to the water depths in the strait and offshore and absolute volumetric flow rates, and when the absolute difference in

volumetric flow rates is accounted for, the differences between both cases become relatively small.

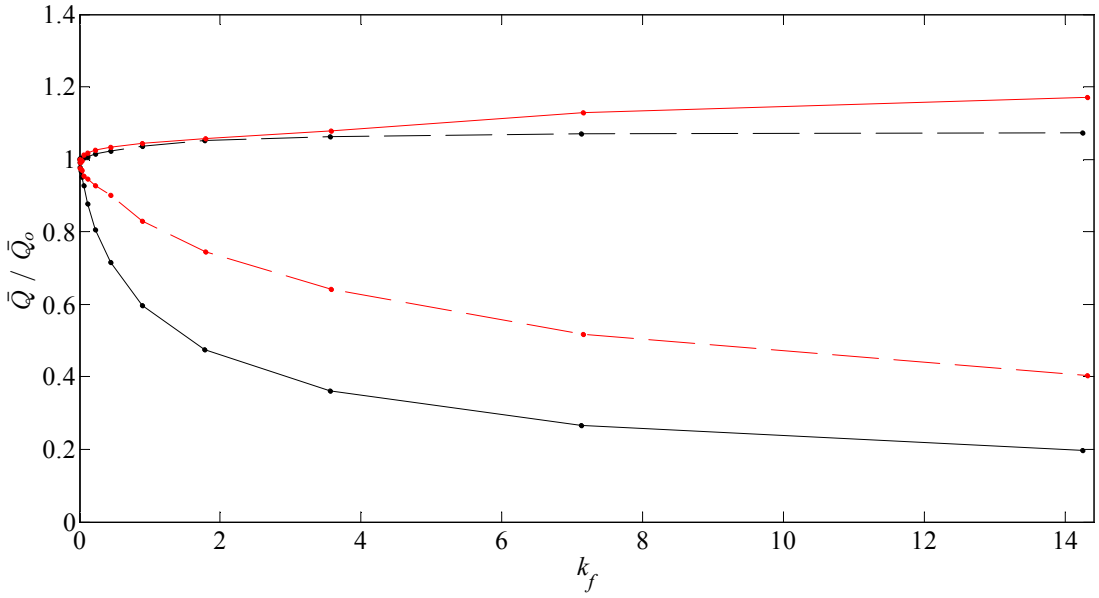


Figure 6.43. Variation in ratio of disturbed to undisturbed volumetric flow rate with power extraction for: extraction solely in the strait (black); and extraction solely offshore of the island (red). Volumetric flow rate across the tidal farm (solid line) and through a cross-section of identical length at the offshore side of the island (dashed line).

Figure 6.44 compares the contour plots of the mean flow speeds (over three $M_2$ tidal cycles) with no power extraction against those predicted when maximum power is extracted offshore of the island. The increase observed in flow speed north of the tidal array corresponds to acceleration of the flow bypassing north of the array. This increase in flow speed extends upstream and downstream of the array. The flow speeds also increase in the strait, in accordance with the increasing volumetric flow rate (Figure 6.43).

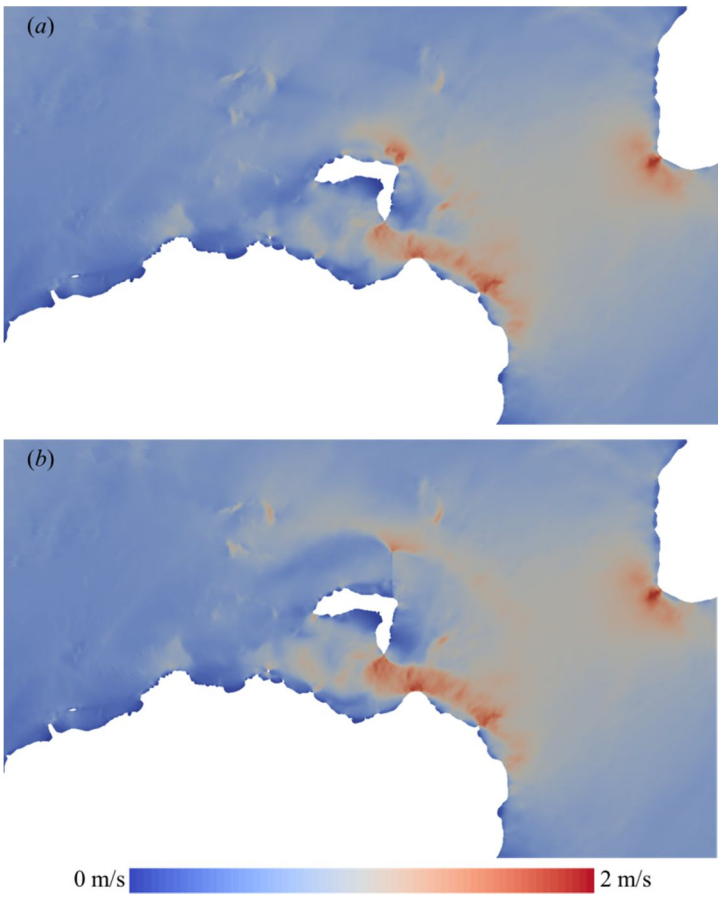


Figure 6.44. Contour plots of the three-tidal-cycle mean flow speeds: (*a*) no extraction; and (*b*) power extraction at $k_f = 7.16$ offshore of the island.

Figure 6.45 compares vorticity contour plots in the natural state against those obtained at maximum power extracted offshore at peak ebb and flood tides. The flow dynamics offshore of the island are completely changed because of the presence of the array. Eddies that would otherwise have grown and shed from the north-east end of the island at ebb and flood tides are now unable to form due to the flow reduction induced by power extraction offshore of the island. Vortical structures can be discerned advecting from the north end of the offshore array. No significant change occurs to the main strait flow dynamics at either tide for maximum power extracted offshore.

Table 6.10 indicates the benefits of combined power extraction in the strait and offshore of the island. Seven power extraction scenarios are considered: in Scenarios 1 and 2, power is extracted solely from the strait; in Scenarios 3 and 4 power is extracted solely offshore of the island; and in Scenarios 5 to 7 power is extracted from the strait and offshore of Rathlin Island. Table 6.10 lists the equivalent number of turbines $N_T$, farm average power generated $\bar{P}_T$, and capacity factor $CF$ based on the turbine description given in Section 5.3.1, the

average velocity $\overline{U}_o^*$, and kinetic power $\overline{P}_k^*$ deficit for each scenario. The results confirm that combined power extraction yields higher power production rates compared to a case where the same number of turbines are installed solely on one side of the island. However, compared to the trends observed in the island-landmass study in Section 5.3.1.7, the increase in yield is relatively small. These results confirm that combined power extraction can enhance the total power production of a tidal development, but highlights the need for a detailed assessment of multiple options in order to maximise power output from the site. One way to carry out this optimisation process is through the iterative method based on the adjoint method proposed by Funke *et al.* [101].

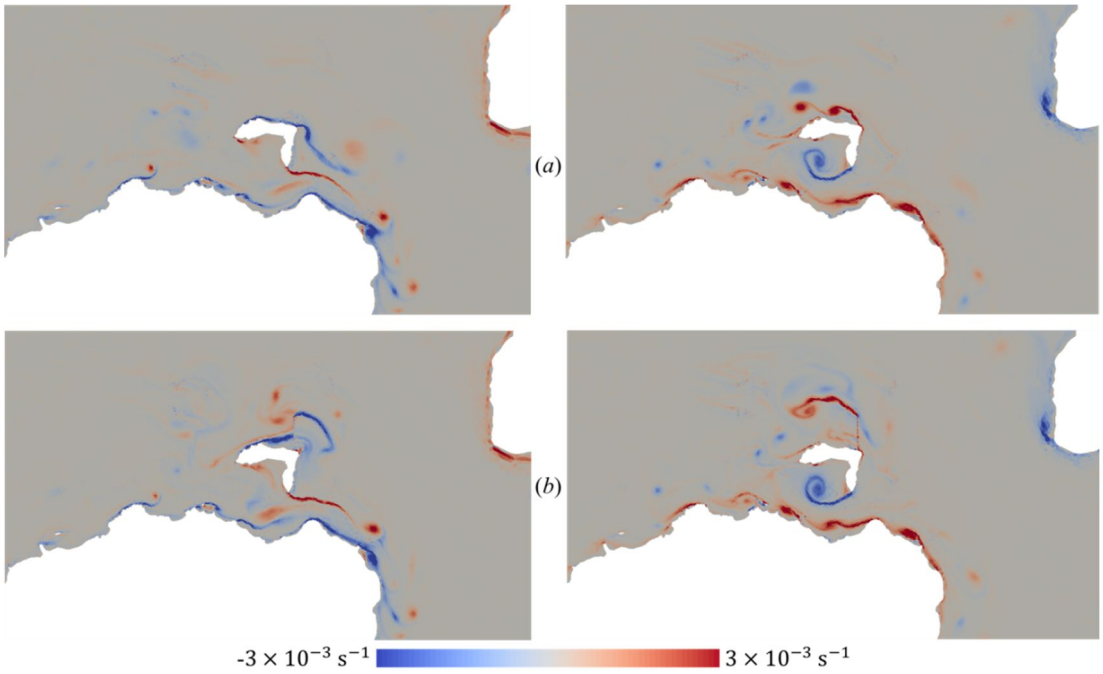


Figure 6.45. Vorticity contour plots with (*a*) no extraction and (*b*) $k_f$ = 7.16 offshore of the island at peak flood (left) and ebb (right) tides.

| *Scenario* | Island Side | $N_T$ | $\bar{P}_T$ [MW] | *CF* [%] | $\bar{U}_o^*$ [%] | $\bar{P}_k^*$ [%] |
|---|---|---|---|---|---|---|
| *1* | S | 160 | 27.9 | 17.5 | -9.4 | -18.6 |
| | O | 0 | n.a. | n.a. | +0.4 | +2.1 |
| *2* | S | 320 | 46.1 | 14.4 | -14.9 | -30.5 |
| | O | 0 | n.a. | n.a. | +0.7 | +3.2 |
| *3* | S | 0 | n.a. | n.a. | +1.7 | +2.8 |
| | O | 160 | 23.9 | 14.9 | -5.2 | -7.5 |
| *4* | S | 0 | n.a. | n.a. | +2.9 | +4.4 |
| | O | 320 | 43.2 | 13.5 | -7.6 | -13.4 |
| *5* | S | 80 | 15.7 | 19.6 | -5.8 | -10.4 |
| | O | 80 | 12.7 | 15.8 | -2.7 | -3.2 |
| *6* | S | 160 | 28.7 | 18 | -8 | -16.5 |
| | O | 160 | 24.1 | 15.1 | -4.7 | -6.1 |
| *7* | S | 320 | 47.8 | 14.9 | -13.2 | -28.3 |
| | O | 320 | 44 | 13.8 | -7.1 | -10.4 |

Table 6.10. Values of the (three-tide) period-averaged array power generated, tidal farm capacity factor, percentage decrease in mean strait velocity and percentage decrease in mean kinetic power according to equivalent numbers of turbines in the strait (S) and offshore side (O) of the Rathlin island.

## 6.4. Summary

This chapter has assessed the maximum power extracted in the Rathlin Sound and compared results with those obtained from the analysis of the island-landmass idealisation considered in Chapter 5. The mesh convergence tests showed that the flow velocities converged for flood and ebb tides at both ends of the Rathlin Sound using Mesh 3, while further refinement would be required upstream and downstream to capture the wake behind the Rathlin Island. Numerical model calibration was carried out by modifying the domain seabed friction coefficient. The numerical solution was found to approximate best observed free surface elevation and flow velocity data when using a non-dimensional seabed friction coefficient $C_d$ = 0.0025.

The numerical domain was analysed solely with an $M_2$ tide forced at the boundaries of the system. Averaged and maximum flow speeds of 2 and 3.5 m/s were achieved in the vicinity of Rathlin Sound for undisturbed tidal flows. Higher kinetic power densities were predicted east of the Rathlin Sound where analysis of the transect speeds showed that higher speeds were achieved near Fair Head and Rue Point during flood and ebb tides respectively. Power extraction at the east section of the Rathlin Sound showed no clear relationship between maximum power extracted and either the undisturbed kinetic power or the power dissipated naturally at the seabed. Similar values of ratio of power extracted to undisturbed kinetic power were obtained for the non-uniform seabed and equal depth island-landmass scenarios. However, the value diverged when water depth changes between strait and offshore were considered in the island-landmass case. Trends observed in the ratios of volumetric flow through the strait and offshore of the island were similar to those observed for the non-uniform seabed island-landmass scenario. Analysis of the head drop along the strait for increasing power extraction in the strait highlighted significant sensitivity to location selected within the strait. When the head drop along the strait was computed using transect-averaged free surface elevations to reduce the effects of the island and coastline shape, the GC2005 model under-predicted the maximum power extraction in the strait by 51 %, in accordance with the figure obtained in the equivalent idealised island-landmass study discussed in Chapter 5. The primary flow dynamics in Rathlin Sound were modified at maximum power extraction, leading to a substantial reduction in averaged flow speed in the strait and further south-east of the site. At maximum power extraction, a 10 % mean difference in the sea surface elevation was predicted east of the site, whereas this was less than 1 % in the far-field.

The sensitivity of the maximum power extracted in the Rathlin Sound to the choice of seabed friction coefficient was investigated for $C_d$ = 0.0025 and 0.005. Over the range of values considered, the increase in seabed friction coefficient reduced the maximum power extracted in the strait by 15 %, although peaks of power extracted were attained at the same levels of power extraction. The percentage reduction in the maximum power extracted obtained by doubling the seabed friction coefficient was in accordance with the 20 % decrease found in the island-landmass study, highlighting the importance of the calibration process on the results.

Further tests were conducted to analyse the sensitivity of power extraction to array location within the strait. Maximum power extracted west of the strait was found to be 15 % lower than east of the strait. The maximum power extracted was higher than the west cross-section

undisturbed kinetic power, highlighting the uncertainty associated with the use of this parameter to predict maximum power extracted at sites with variable cross-section widths. Maximum power extracted was achieved west of the strait at a higher power extraction level than east of the strait, implying that the slower currents would require turbines with bigger rotors to attain similar orders of power extraction than at cross-sections with faster flows. The disparity in the results disagreed with the conclusions from the island-landmass study, and might be explained by the specific flow dynamics generated from the island, with a large eddy shedding west from Rue Point and reaching the array during ebb tide.

Sensitivity of the maximum power extracted in the strait to the blockage ratio was assessed for three cases: 100 %, 80 % and 60 %. A reduction in the maximum power extracted of 14 % and 36% was found for the blockage ratios 80 % and 60 % compared to the 100 % case. The decrease obtained for the 60 % blockage ratio accorded with that obtained in the island-landmass study. The results from the 80 % blockage ratio differed from the island-landmass analysis, possibly due to the rapid reduction in water depth in the strait bypass sections in the island-landmass study. Similar changes in volumetric flow rates through the array were observed in the 80 % and 60 % blockage cases. At maximum power extracted, 20 % and 14% increase occurred in the average flow speed at the bypass strait sections for the 80 % and 60 % blockage ratios, which could increase seabed erosion in strait bypass sections.

Power extraction offshore of the island was investigated by inserting an array north-east of the island where high undisturbed kinetic power densities has been identified. Maximum power extracted offshore was 134 % higher than maximum power extracted east of the strait. The increase in volumetric flow rate through the strait was very similar to that offshore of the island, when power was extracted from the strait. At maximum power extracted, changes occurred to the flow dynamics offshore of the island while the hydrodynamics of the strait were not significantly altered. It was found that turbine arrays in both the strait and offshore of the island yielded higher power generation rates than sole extraction either from the strait or offshore of the island (for equivalent turbines). However, the increase in yield was smaller to that obtained in the island-landmass study.

The analysis was limited to an $M_2$ tide in order to facilitate comparison with results from the idealised island-landmass study (in Chapter 5). To obtain a more accurate estimate of the maximum extracted power and temporal variation in the Rathlin Sound, the addition of the $S_2$ and higher harmonic constituent tidal components is required. Draper *et al*. [12] found that maximum averaged power extracted in the Pentland Firth increases from 3.75 GW with solely an $M_2$ tide to 4.19 GW with an $M_2$ and $S_2$ tide. However, it is likely that the main

conclusions derived from the $M_2$ analysis will be also hold when $S_2$ and higher tidal components are added.

Although it is difficult to approximate a real coastal problem by an idealised one, the study of the Rathlin Sound has proved useful in confirming several outcomes of the idealised site study in Chapter 5. Moreover, the results have also confirmed that the use of certain parameters available to developers at the pre-feasibility stages of a project, such as undisturbed kinetic power or head along the strait driving the flow, may not be accurate indicators of the upper limit to power extraction for this type of coastal site.

# 7. Conclusions

## 7.1. Introduction

This thesis has characterised the tidal resource at coastal sites defined as an island in the vicinity of a landmass. A finite element method numerical code called Fluidity was used to solve the shallow water equations, and its appropriateness verified using standard benchmark tests before application to idealised and actual island-landmass coastal sites. A distributed drag methodology was selected to represent power extraction from the flow by tidal turbines, as this provided an effective way to assess the limits to power extraction. The methodology employed to perform a resource assessment at the coastal site was verified and validated. Resource of an idealised island-landmass was characterised by means of a sensitivity analysis to understand the effects of several geometrical and tidal parameters on the limits to power extraction. Resource assessment was performed for Rathlin Sound, and the outcomes compared against those from the idealised island-landmass analysis. This chapter summarises the main findings of the thesis and makes recommendations for further work.

## 7.2. Verification and validation of resource assessment methodology

- Fluidity was verified to account for local changes in flow depth against the analytical solution of steady flow over a submerged hump.
- Fluidity was verified to model inviscid flow past a circular cylinder in the centre of a wide channel using the potential flow theory, and flow past a circular cylinder in the vicinity of a solid wall using the method of images.
- Fluidity was validated to simulate flow past impulsively-started submerged circular cylinders at Reynolds numbers 40, 100 and 5,000 against experimental and numerical data. Results showed that Fluidity correctly modelled the mechanisms of early stage wake formation behind circular cylinders.
- Fluidity was validated to model flow past surface piercing circular cylinders in oscillatory laminar shallow flow against experimental data. The formation of vortex-

shedding wake was satisfactorily modelled with Fluidity solving the shallow water equations and the unsteady 3D Navier Stokes equations

- The distributed drag power extraction methodology implemented in Fluidity was verified for bounded flows against two one-dimensional analytical models. The verification of the power extraction methodology was extended to unbounded two-dimensional flows against analytical and numerical solutions.

## 7.3. Tidal resource in strait between island and landmass

- The analysis of an island in the vicinity of a landmass revealed no clear relationship between the maximum power extracted in the strait and the power dissipated naturally on the seabed or kinetic power in undisturbed conditions. The only exception was found to be the geometrically long island extending along the coast where the power dissipated naturally on the seabed may be a good indicator of the maximum power extracted in the strait.
- The GC2005 model underpredicts the maximum power extracted in the strait. The discrepancies between numerical and analytical results are due to the latter not able to account for changes in the head driving the flow with power extraction in the strait and flow diversion offshore of the island. These two factors appear to not be significant for the case with a geometrically long island, where the GC2005 model satisfactorily approximates the maximum power extracted.
- Definition of boundary conditions at island and landmass affects the maximum power extracted figures, where free-slip and no-slip boundary conditions may provide lower and upper bounds to the maximum power extracted in the strait, whereas results from the non-uniform seabed scenario lie between the two.
- An isolated island far from the coast presents a similar ratio of maximum power extracted to undisturbed kinetic power and changes in volumetric flow rates at the strait and offshore to those for the island in the vicinity of a landmass.
- Maximum power extracted in the strait is sensitive to the definition of the frictional and viscous environment in the numerical model. An inverse relationship is observed between bottom friction and power extracted in the strait. Both friction and viscosity parameters are commonly used to calibrate numerical models, highlighting the

importance of the correctness of the calibration process in the results from the resource assessment.

- Higher water depths offshore of the island than in the strait reduced the resistance to the flow offshore of the island, leading to an increase in bypass flow rates and a reduction in the maximum power extracted in the strait.
- The choice of array area was found to not alter the resource estimates for arrays completely blocking the strait. Results showed that a reduction in the strait blockage by the array decreases the maximum power extracted in the strait, unless bypass routes are relatively shallow in which case similar maximum power extracted rates are achieved.
- Similar power generation was found for identical extraction levels either in the strait or offshore of the island. Combined extraction at the strait and offshore of the island yielded higher power generation rates than for an equivalent extraction level only applied one side of the island. Power generation may be optimised if island-landmass is considered as a two-flow path system.

## 7.4. Tidal resource of the Rathlin Sound

- Free surface elevation and flow velocity data in the vicinity of Rathlin Sound was better approximated in the numerical model with bed friction coefficient $C_d = 0.0025$.
- The numerical model was forced with an $M_2$ tide at the boundaries, leading to undisturbed averaged and maximum flow speeds of 2 and 3.5 m/s in the vicinity of Rathlin Sound. Higher undisturbed kinetic power densities were observed east of Rathlin Sound.
- Maximum power extracted east of Rathlin Sound was not well approximated by either the undisturbed kinetic power or power dissipated naturally at the seabed. The ratio of power extracted to undisturbed kinetic power and volumetric flow rate trends were similar to those found in the non-uniform seabed and equal depth idealised island-landmass scenario. The GC2005 model underpredicted the maximum power extracted in Rathlin Sound at a similar rate as in the equivalent idealised island-landmass. At maximum power extracted east of Rathlin Sound, there was a substantial flow reduction in the strait and further south-east of the site, and 10 % and 1 % mean differences in sea surface elevation east of the site and far-field respectively.

- A 15 % reduction in the maximum power extracted was observed when seabed friction coefficient was doubled from $C_d$ = 0.0025 to 0.005; a similar decrease was found in the idealised island-landmass study.
- A decrease of 15 % in maximum power extracted was observed when extraction was implemented west of Rathlin Sound than east of the strait. Discrepancies in the results might be due to the specific flow dynamics caused by the presence of the island. Maximum power extracted west of the strait was higher than the west cross-section undisturbed kinetic power, underlining the uncertainty associated with the use of this parameter to assess the resource at this coastal site type.
- Decreases in maximum power extracted of 14 % and 36 % were found when strait blockage by the array was reduced to 80 % and 60 % respectively. The reduction observed in the 60 % blockage ratio agreed with the figure obtained in the island-landmass study. The disagreement found in the 80 % blockage ratio case may be explained by the rapid reduction in water depth in the strait bypass section set in the island-landmass study. Increases of flow speeds in the strait bypass sections of 20 % and 14 % were observed in the 80 % and 60 % blockage ratios.
- Maximum power extracted east offshore of Rathlin Island was 134 % higher than the maximum power extracted east of the strait. Power extraction offshore appeared not to alter significantly the main flow dynamics of the strait. Combined power extraction in strait and offshore of the island yielded higher power generation rates than equivalent extraction only applied at strait or offshore of the island, although this increase was smaller to that obtained in the island-landmass study.

## 7.5. The benefits of this thesis to the tidal industry

- The idealised study of the island-landmass provided certain useful conclusions specifically related to the limits to tidal power extraction at this coastal site. The study investigated the limits to power extraction and consequent effects on the environment.
- The sensitivity analysis showed the effect of certain coastal site parameters on the limits to power extraction and environmental effects, and highlighted uncertainty in the resource estimates due to the choice of the numerical parameterisation.
- The study also identified the limits of application of one-dimensional channel analytical models to the island-landmass coastal sites.

- The validity of several outcomes from the idealised island-landmass study were assessed through the study of Rathlin Sound; the results were in reasonable agreement with those from the idealised study, and sources of differences between both approaches were identified.
- The work presented in this thesis has characterised the tidal resource of typical coastal site island-landmass scenarios, which will benefit tidal stream power developers to achieve more accurate realisations of the limits to power extraction and associated environmental changes, during the pre-feasibility stages.

## 7.6. Further work

- This thesis identified six possible island-tidal system configurations that could fall into the category of island-landmass coastal site. Four different configurations have been studied and it is recommended that the analysis be extended in future to consider island configurations defined as two isolated offshore islands and an isolated offshore multi-island system. Analysis of both configurations would benefit from the development of an optimisation algorithm capable of maximising either power generation in the system or only at one of the flow paths.
- The limitations of the methodology employed to account for power extraction were highlighted in Chapter 3 and it is acknowledged that the results provided here represent an upper limit to power extraction. The use of a turbine representation that can account for blockage and mixing losses behind individual turbines and farm such as LMADT will increase the accuracy in the estimates of the limits to power extraction in island-landmass coastal sites as well as reaffirming the conclusions derived from the island-landmass study.
- The effects on the power extraction limits from the parameterisation of turbulence were assessed in Chapter 5. It is recommended to expand this analysis to include empirical turbulence model such as the $k$-$\varepsilon$ or $k$-$\omega$ models presented in Chapter 3.
- Resource characterisation of the island-landmass system has considered solely the effects of astronomical tides. The inclusion of wave conditions in the analysis will increase the understanding of wave-current interaction and the implications in the power extraction rates from the island-landmass system.

- The changes in the transport of sediments in the island-landmass system were measured based on the changes of local flow velocities. The implementation of a sediment transport model will increase the understanding of the natural sediment dynamics at the island-landmass system and the interaction with power extraction.
- It has been shown that the electric circuit analogy theory has been applied to assess the tidal resource at idealised split channels and actual coastal sites of similar type. Application of the electric circuit analogy theory to the island-landmass configurations tested would increase confidence in the outcomes of this and related studies.
- Resource assessment data from actual coastal sites available in the literature have been used, when available, to assess the validity of the outcomes from the idealised island-landmass study. Moreover, resource assessment of Rathlin Sound has assessed the validity of several outcomes from the idealised island-landmass study. It is recommended to identify and model actual coastal sites to assess the validity of further outcomes from the idealised island-landmass coastal site.
- The limitations of shallow water modelling were highlighted in Chapter 3 together with the benefits of three-dimensional modelling. If computational resources are available, three dimensional numerical modelling of the idealised island-landmass and equivalent actual coastal sites will increase the accuracy of the limits to power extraction. Use of computational resources can be optimised combining two and three-dimensional modelling (e.g. nested modelling).
- This thesis has performed a rigorous verification and validation of the methodology employed to assess the resource at the island-landmass system. However, the combination of complex topography, bathymetry and power extraction creates a complicated system whose solution might be validated through basin-scale laboratory experimentation.

# 8. Bibliography


[1] Intergovernmental Panel on Climate Change, "Climate change 2001: Synthesis summary," 2001.

[2] M. Tsoskounoglou, G. Ayerides, and E. Tritopoulou, "The end of cheap oil: Current status and prospects," *Energy Policy*, vol. 36, no. 10, pp. 3797–3806, Oct. 2008.

[3] S. Shafiee and E. Topal, "When will fossil fuel reserves be diminished?," *Energy Policy*, vol. 37, no. 1, pp. 181–189, Jan. 2009.

[4] International Energy Agency, "World energy outlook 2014," Paris, 2014.

[5] R. Charlier and C. Finkl, *Ocean energy: tide and tidal power*. Berlin: Springer, 2009.

[6] G. D. Egbert and R. D. Ray, "Estimates of M2 tidal energy dissipation from TOPEX/Poseidon altimeter data," *J. Geophys. Res.*, vol. 106, no. C10, pp. 22,475–22,502, 2001.

[7] Black and Veatch, "UK tidal current resource & economics," The Carbon Trust, London, 2011.

[8] Department of Energy and Climate Change, "Energy consumption in the U.K.," 2013.

[9] Triton Consultants Ltd., "Canada ocean energy atlas (Phase 1). Potential tidal current energy resources. Analysis background," Vancouver, Canada, 2006.

[10] Black & Veatch Consulting Ltd, "UK tidal current resource & economics : Appendix C," 2011.

[11] C. Garrett and P. Cummins, "The power potential of tidal currents in channels," *Proc. R. Soc. A Math. Phys. Eng. Sci.*, vol. 461, no. 2060, pp. 2563–2572, Aug. 2005.

[12] S. Draper, T. A. A. Adcock, A. G. L. Borthwick, and G. T. Houlsby, "Estimate of the tidal stream power resource of the Pentland Firth," *Renew. Energy*, vol. 63, pp. 650–657, Mar. 2014.

[13] S. Draper, "Tidal stream energy extraction in coastal basins," Doctoral Thesis, University of Oxford, Oxford, United Kingdom, 2011.

[14] T. Burton, D. Sharpe, N. Jenkins, and E. Bossanyi, *Wind Energy Handbook*. Chichester, UK: John Wiley & Sons, Ltd, 2008, p. 617.

[15] I. G. Bryden and S. J. Couch, "ME1—marine energy extraction: tidal resource analysis," *Renew. Energy*, vol. 31, no. 2, pp. 133–139, Feb. 2006.

[16] I. G. Bryden, S. J. Couch, A. Owen, and G. Melville, “Tidal current resource assessment,” in *Proceedings of the Institution of Mechanical Engineers, Part A: Journal of Power and Energy*, 2007, vol. 221, no. 2, pp. 125–135.

[17] J. F. Atwater and G. A. Lawrence, “Regulatory, design and methodological impacts in determining tidal-in-stream power resource potential,” *Energy Policy*, vol. 39, no. 3, pp. 1694–1698, Mar. 2011.

[18] P. Evans, M. Allmark, and T. O. Doherty, “Are Energetic Tidal Straits Suitable for Power Generation?,” in *World Renewable Energy Congress*, 2014, pp. 1–7.

[19] K. Alexander, “Offshore power production and marine stakeholders: from understanding conflict to impact mitigation,” The University of Aberdeen, 2012.

[20] Black & Veatch Consulting Ltd, “Phase I UK tidal stream energy resource assessment,” Carbon Trust, London, 2004.

[21] I. G. Bryden, T. Grinsted, and G. T. Melville, “Assessing the potential of a simple tidal channel to deliver useful energy,” *Appl. Ocean Res.*, vol. 26, no. 2004, pp. 198–204, 2005.

[22] A. S. Iyer, “New methodologies and scenarios for evaluating tidal current energy potential,” Doctoral Thesis, The University of Edinburgh, Edinburgh, United Kingdom, 2012.

[23] J. D. Boon, *Secrets of the tide. Tide and tidal current analysis and predictions, storm surges and sea level trends*. Chichester, UK: Horwood Publishing Limited, 2004, p. 212.

[24] R. Pawlowicz, B. Beardsley, and S. Lentz, “Classical tidal harmonic analysis including error estimates in MATLAB using T_TIDE,” *Comput. Geosci.*, vol. 28, no. 8, pp. 929–937, Oct. 2002.

[25] D. L. Codiga, “Unified tidal analysis and prediction using the UTide Matlab functions,” Graduate School of Oceanography, University of Rhode Island, Narragansett, 2011.

[26] J. Hardisty, *The analysis of tidal stream power*. Chichester, UK: John Wiley & Sons, Ltd, 2009.

[27] P. E. Robins, S. P. Neill, M. J. Lewis, and S. L. Ward, “Characterising the spatial and temporal variability of the tidal-stream energy resource over the northwest European shelf seas,” *Appl. Energy*, vol. 147, pp. 510–522, Jun. 2015.

[28] S. P. Neill, M. R. Hashemi, and M. J. Lewis, “The role of tidal asymmetry in characterizing the tidal energy resource of Orkney,” *Renew. Energy*, vol. 68, pp. 337–350, Aug. 2014.

[29] S. P. Neill, E. J. Litt, S. J. Couch, and A. G. Davies, “The impact of tidal stream turbines on large-scale sediment dynamics,” *Renew. Energy*, vol. 34, no. 12, pp. 2803–2812, Dec. 2009.

[30] J. Blanchfield, C. Garrett, P. Wild, and A. Rowe, “The extractable power from a channel linking a bay to the open ocean,” *Proc. Inst. Mech. Eng. Part A J. Power Energy*, vol. 222, no. 3, pp. 289–297, May 2008.

[31] G. Sutherland, M. Foreman, and C. Garrett, “Tidal current energy assessment for Johnstone Strait, Vancouver Island,” *Proc. Inst. Mech. Eng. Part A J. Power Energy*, vol. 221, no. 2, pp. 147–157, Jan. 2007.

[32] I. Walkington and R. Burrows, “Modelling tidal stream power potential,” *Appl. Ocean Res.*, vol. 31, no. 4, pp. 239–245, Oct. 2009.

[33] G. I. Shapiro, “Effect of tidal stream power generation on the region-wide circulation in a shallow sea,” *Ocean Sci.*, vol. 7, no. 1, pp. 165–174, Feb. 2011.

[34] T. A. A. Adcock, S. Draper, and T. Nishino, “Tidal power generation - A review of hydrodynamic modelling,” *Proc. Inst. Mech. Eng. Part A J. Power Energy*, vol. 229, no. 7, pp. 755–771, Feb. 2015.

[35] R. Vennell, S. W. Funke, S. Draper, C. Stevens, and T. Divett, “Designing large arrays of tidal turbines: A synthesis and review,” *Renew. Sustain. Energy Rev.*, vol. 41, pp. 454–472, Jan. 2015.

[36] M. J. Lewis, S. P. Neill, M. R. Hashemi, and M. Reza, “Realistic wave conditions and their influence on quantifying the tidal stream energy resource,” *Appl. Energy*, vol. 136, pp. 495–508, Dec. 2014.

[37] M. R. Hashemi, S. P. Neill, P. E. Robins, A. G. Davies, and M. J. Lewis, “Effect of waves on the tidal energy resource at a planned tidal stream array,” *Renew. Energy*, vol. 75, pp. 626–639, Mar. 2015.

[38] D. Haverson, J. Bacon, H. Smith, V. Venugopal, and Q. Xiao, “Cumulative impact assessment of tidal energy in the Irish Sea,” in *Proceedings of the 11th European Wave and Tidal Energy Conference*, 2015, pp. 1–6.

[39] S. Draper, T. A. A. Adcock, A. G. L. Borthwick, and G. T. Houlsby, “An electrical analogy for the Pentland Firth tidal stream power resource,” *Proc. R. Soc. A Math. Phys. Eng. Sci.*, no. 470, p. 20, 2014.

[40] P. F. Cummins, “The extractable power from a split tidal channel: An equivalent circuit analysis,” *Renew. Energy*, vol. 50, pp. 395–401, Feb. 2013.

[41] S. Draper, A. G. L. Borthwick, and G. T. Houlsby, “Energy potential of a tidal fence deployed near a coastal headland,” *Philos. Trans. R. Soc. A Math. Phys. Eng. Sci.*, vol. 371, no. January, 2013.

[42] L. S. Blunden and A. S. Bahaj, “Initial evaluation of tidal stream energy resources at Portland Bill, UK,” *Renew. Energy*, vol. 31, no. 2, pp. 121–132, Feb. 2006.

[43] I. G. Bryden and S. J. Couch, “How much energy can be extracted from moving water with a free surface: A question of importance in the field of tidal current energy?,” *Renew. Energy*, vol. 32, no. 11, pp. 1961–1966, Sep. 2007.

[44] C. Garrett and P. Cummins, “The efficiency of a turbine in a tidal channel,” *J. Fluid Mech.*, vol. 588, pp. 243–251, Sep. 2007.

[45] C. Garrett and P. Cummins, “Limits to tidal current power,” *Renew. Energy*, vol. 33, no. 11, pp. 2485–2490, Nov. 2008.

[46] R. Vennell, “Tuning turbines in a tidal channel,” *J. Fluid Mech.*, vol. 663, pp. 253–267, Oct. 2010.

[47] R. Vennell, “Tuning tidal turbines in-concert to maximise farm efficiency,” *J. Fluid Mech.*, vol. 671, no. March 2011, pp. 587–604, Mar. 2011.

[48] R. Vennell, “Estimating the power potential of tidal currents and the impact of power extraction on flow speeds,” *Renew. Energy*, vol. 36, no. 12, pp. 3558–3565, Dec. 2011.

[49] D. R. Plew and C. L. Stevens, “Numerical modelling of the effect of turbines on currents in a tidal channel – Tory Channel, New Zealand,” *Renew. Energy*, vol. 57, pp. 269–282, Sep. 2013.

[50] T. A. A. Adcock and S. Draper, “Power extraction from tidal channels – Multiple tidal constituents, compound tides and overtides,” *Renew. Energy*, vol. 63, pp. 797–806, Mar. 2014.

[51] T. A. A. Adcock, S. Draper, G. T. Houlsby, A. G. L. Borthwick, and S. Serhadlıoğlu, “The available power from tidal stream turbines in the Pentland Firth,” *Proc. R. Soc. A Math. Phys. Eng. Sci*, vol. 469, 2013.

[52] J. F. Atwater and G. A. Lawrence, “Power potential of a split tidal channel,” *Renew. Energy*, vol. 35, no. 2, pp. 329–332, Feb. 2010.

[53] B. L. Polagye and P. C. Malte, “Far-field dynamics of tidal energy extraction in channel networks,” *Renew. Energy*, vol. 36, no. 1, pp. 222–234, Jan. 2011.

[54] C. Garrett and P. Cummins, “Generating Power from Tidal Currents,” *J. Waterw. Port, Coast. Ocean Eng.*, no. June, pp. 114–118, 2004.

[55] B. L. Polagye, P. C. Malte, M. Kawase, and D. Durran, “Effect of large-scale kinetic power extraction on time-dependent estuaries,” in *Proceedings of the Institution of Mechanical Engineers, Part A: Journal of Power and Energy*, 2008, vol. 222, pp. 471–484.

[56] R. H. Karsten, J. M. McMillan, M. J. Lickley, and R. D. Haynes, “Assessment of tidal current energy in the Minas Passage, Bay of Fundy,” *Proc. Inst. Mech. Eng. Part A J. Power Energy*, vol. 222, no. 5, pp. 493–507, Aug. 2008.

[57] J. Blanchfield, C. Garrett, a Rowe, and P. Wild, “Tidal stream power resource assessment for Masset Sound, Haida Gwaii,” *Proc. Inst. Mech. Eng. Part A J. Power Energy*, vol. 222, no. 5, pp. 485–492, Aug. 2008.

[58] M. Kawase and M. Gedney, “Tidal energy extraction in an idealized ocean-fjord tidal model with astronomical forcing,” in *10th European Wave and Tidal Energy Conference*, 2013, p. 10.

[59] R. Ahmadian and R. Falconer, “Assessment of array shape of tidal stream turbines on hydro-environmental impacts and power output,” *Renew. Energy*, vol. 44, pp. 318–327, 2012.

[60] R. Ahmadian, R. Falconer, and B. Bockelmann-Evans, “Far-field modelling of the hydro-environmental impact of tidal stream turbines,” *Renew. Energy*, vol. 38, no. 1, pp. 107–116, Feb. 2012.

[61] T. Adcock, “The available power obtainable from tidal stream turbines from a flow around an idealised headland,” *3rd Int. Assoc. hydro-environment …*, no. 1, 2013.

[62] S. Serhadlıoğlu, T. A. A. Adcock, G. T. Houlsby, S. Draper, and A. G. L. Borthwick, “Tidal stream energy resource assessment of the Anglesey Skerries,” *Int. J. Mar. Energy*, vol. 3–4, pp. e98–e111, Dec. 2013.

[63] S. P. Neill, J. R. Jordan, and S. J. Couch, “Impact of tidal energy converter (TEC) arrays on the dynamics of headland sand banks,” *Renew. Energy*, vol. 37, no. 1, pp. 387–397, Jan. 2012.

[64] R. Vennell, “Oscillating Barotropic Currents along Short Channels,” *J. Phys. Oceanogr.*, vol. 28, pp. 1561–1569, 1998.

[65] R. Vennell, “Observations of the phase of tidal currents along a strait,” *J. Phys. Oceanogr.*, no. 1994, pp. 1570–1577, 1998.

[66] R. Ingram and V. Chu, “Flow around islands in Rupert Bay: An investigation of the bottom friction effect,” *J. Geophys. Res. …*, vol. 92, no. 7, 1987.

[67] E. Wolanski, J. Imberger, and M. L. Heron, “Island Wakes in Shallow Coastal Waters,” *J. Geophys. Res.*, vol. 89, no. C6, pp. 553–569, 1984.

[68] K. Furukawa and E. Wolanski, “Shallow-water frictional effects in island wakes,” *Estuar. Coast. Shelf Sci.*, no. 46, pp. 599–607, 1998.

[69] P. M. Lloyd, P. K. Stansby, and D. Chen, “Wake formation around islands in oscillatory laminar shallow-water flows. Part 1. Experimental investigation,” *J. Fluid Mech.*, vol. 429, pp. 217–238, Feb. 2001.

[70] P. M. Lloyd and P. K. Stansby, “Shallow-water flow around model conical islands of small side slope. I: Surface piercing,” *J. Hydraul. Eng.*, vol. 123, no. 12, pp. 1057–1067, 1997.

[71] R. Pingree and L. Maddock, “Tidal flow around an island with a regularly sloping bottom topography,” *J. Mar. Biol. …*, vol. 59, pp. 699–710, 1979.

[72] R. Pingree and L. Maddock, “Tidally induced residual flows around an island due to both frictional and rotational effects,” *Geophys. J. Int.*, vol. 63, pp. 533–546, 1980.

[73] S. Couch, “Numerical modelling of tidal flows around headlands and islands.,” Doctoral Thesis, University of Strathclyde, Glasgow, United Kingdom, 2001.

[74] A. Pérez-Ortiz, A. G. L. Borthwick, H. Smith, P. Vigars, and Q. Xiao, “Tidal Resource in Strait between Island and Landmass,” in *Proceedings of the 11th European Wave and Tidal Energy Conference*, 2015, pp. 1–10.

[75] R. Martin-Short, J. Hill, S. C. Kramer, A. Avdis, P. A. Allison, and M. D. Piggott, “Tidal resource extraction in the Pentland Firth, UK: Potential impacts on flow regime and sediment transport in the Inner Sound of Stroma,” *Renew. Energy*, vol. 76, pp. 596–607, Apr. 2015.

[76] L. Myers and a. S. Bahaj, “Simulated electrical power potential harnessed by marine current turbine arrays in the Alderney Race,” *Renew. Energy*, vol. 30, no. 11, pp. 1713–1731, Sep. 2005.

[77] A. S. Bahaj and L. Myers, “Analytical estimates of the energy yield potential from the Alderney Race (Channel Islands) using marine current energy converters,” *Renew. Energy*, vol. 29, no. 12, pp. 1931–1945, Oct. 2004.

[78] D. Coles, L. Blunden, and A. Bahaj, “Energy extraction potential from the Alderney Race,” in *Proceedings of the 11th European Wave and Tidal Energy Conference*, 2015, pp. 1–9.

[79] J. Thiébot, P. Bailly du Bois, and S. Guillou, “Numerical modeling of the effect of tidal stream turbines on the hydrodynamics and the sediment transport – Application to the Alderney Race (Raz Blanchard), France,” *Renew. Energy*, vol. 75, pp. 356–365, Mar. 2015.

[80] L. S. Blunden, A. S. Bahaj, and N. S. Aziz, “Tidal current power for Indonesia? An initial resource estimation for the Alas Strait,” *Renew. Energy*, pp. 1–6, Feb. 2012.

[81] Y. Chen, B. Lin, J. Lin, and S. Wang, “Effects of stream turbine array configuration on tidal current energy extraction near an island,” *Comput. Geosci.*, vol. 77, pp. 20–28, Apr. 2015.

[82] C. Bailey, “Mathematical modelling of shallow water flows with application to Moreton Bay, Brisbane,” Doctoral Thesis, Loughborough University, Loughborough, United Kingdom, 2010.

[83] C. J. Hearn, *The dynamics of coastal models*, First. New York, United States of America: Cambridge University Press, 2008, p. 488.

[84] G. K. Vallis, *Atmospheric and oceanic fluid dynamics. Fundamentals and large-scale circulation*, First. New York, United States of America: Cambridge University Press, 2006, p. 745.

[85] O. Reynolds, “On the Dynamical Theory of Incompressible Viscous Fluids and the Determination of the Criterion.,” *Proc. R. Soc. London*, vol. 56, no. 336–339, pp. 40–45, Jan. 1894.

[86] J.-M. Hervouet, *Hydrodynamics of Free Surface FLows. Modelling with the Finite Element Method*. Wiltshire, United Kingdom: John Wiley & Sons, Ltd, 2007, p. 341.

[87] J. Lagrange, "Mémoire sur la théorie du mouvement des fluides," *Nouv. Mem. Acad. Berlin*, vol. 151–198, no. 4, pp. 695–748, 1781.

[88] A. Pérez-Ortiz, J. Pescatore, and I. Bryden, "A systematic approach to undertake tidal energy resource assessment with TELEMAC-2D," in *10th European Wave and Tidal Energy Conference*, 2013, p. 9.

[89] V. Ramos and G. Iglesias, "Performance assessment of tidal stream turbines: a parametric approach," *Energy Convers. Manag.*, vol. 69, pp. 49–57, May 2013.

[90] C. Wilson, P. Bates, and J. Hervouet, "Comparison of turbulence models for stage-discharge rating curve prediction in reach-scale compound channel flows using two-dimensional finite element methods," *J. Hydrol.*, vol. 257, pp. 42–58, 2002.

[91] L. Cea, J. Puertas, and M.-E. Vázquez-Cendón, "Depth Averaged Modelling of Turbulent Shallow Water Flow with Wet-Dry Fronts," *Arch. Comput. Methods Eng.*, vol. 14, no. 3, pp. 303–341, Aug. 2007.

[92] W. Rodi, *Turbulence Models and their Appliation in Hydraulics*, 2nd ed. International Association for Hydraulic Research, Delft, The Netherlands, 1984.

[93] W. Wu, P. Wang, and N. Chiba, "Comparison of five depth-averaged 2-D turbulence models for river flows," *Arch. Hydroengineering ...*, vol. 51, no. 2, pp. 183–200, 2004.

[94] S. Baston and R. Harris, "Modelling the hydrodynamic characteristics of tidal flow in the Pentland Firth," in *9th European Wave and Tidal Energy Conference*, 2011, p. 7.

[95] R. Soulsby, *Dynamics of Marine Sands: A Manual for Practical Applications*. Thomas Telford, 1997.

[96] R. Flather, "Results from a storm surge prediction model of the north-west European continental shelf for April, November and December, 1973," Institute of Oceanographic Sciences. Natural Environment Research Council. Birkenhead. United Kingdom, 1976.

[97] D. Coles, L. S. Blunden, and A. S. Bahaj, "2 dimensional depth averaged numerical modeling of large marine current turbine arrays," in *2nd Asian Wave and Tidal Energy Conference*, 2014, p. 4.

[98] "Fluidity Manual," Applied Modelling and Computation Group, Department of Earth Science and Engineering, South Kensington Campus, Imperial College London, London, United Kingdom, Version 4.1.10, 2014.

[99] Z. Yang and T. Wang, "Assessment of tidal energy removal impacts on physical systems: Development of MHK module and analysis of effects on hydrodynamics," Richland, Washington, U.S, 2011.

[100] S. Baston, S. Waldman, and J. Side, “Modelling energy extraction in tidal flows,” TeraWatt Consortium, 2014.

[101] S. W. Funke, P. E. Farrell, and M. D. Piggott, “Tidal turbine array optimisation using the adjoint approach q,” *Renew. Energy*, vol. 63, pp. 658–673, 2014.

[102] T. Divett, “Optimising design of large tidal energy arrays in channels: layout and turbine tuning for maximum power capture using large eddy simulations with adaptive mesh,” Doctoral Thesis, University of Otago, Dunedin, New Zealand, 2014.

[103] C. Peyrard, C. Buvat, F. Lafon, and C. Abonnel, “Investigations of the wake effects in marine current farms, through numerical modelling with the TELEMAC system,” in *Proceedings of the 1st International Conference on Ocean Energy*, 2006, no. 1.

[104] S. C. Kramer, M. D. Piggott, and J. Hill, “The modelling of tidal turbine farms using multi-scale, unstructured mesh models,” in *Proceedings of the 2nd International Conference on Environmental Interactions of Marine Renewable Energy Technologies (EIMR 2014)*, 2014.

[105] J. I. Whelan, J. M. R. Graham, and J. Peiró, “A free-surface and blockage correction for tidal turbines,” *J. Fluid Mech.*, vol. 624, p. 281, Mar. 2009.

[106] G. Houlsby, S. Draper, and M. L. G. Oldfield, “Application of linear momentum actuator disc theory to open channel flow,” *Tech. Rep. 2296-08, OUEL*, 2008.

[107] S. Draper, G. T. Houlsby, M. L. G. Oldfield, and A. G. L. Borthwick, “Modelling tidal energy extraction in a depth-averaged coastal domain,” *IET Renew. Power Gener.*, vol. 4, no. 6, p. 545, 2010.

[108] S. Draper, G. Houlsby, M. L. G. Oldfield, and A. G. L. Borthwick, “Modelling tidal energy extraction in a depth-averaged coastal domain,” in *Proceedings of the 8th European Wave and Tidal Energy Conference*, 2009, pp. 1045–1052.

[109] P. K. Stansby, “Limitations of depth-averaged modeling for shallow wakes,” *J. Hydraul. Eng.*, vol. 132, no. 7, pp. 737–740, Jul. 2006.

[110] X. Sun, J. P. Chick, and I. G. Bryden, “Laboratory-scale simulation of energy extraction from tidal currents,” *Renew. Energy*, vol. 33, no. 6, pp. 1267–1274, Jun. 2008.

[111] M. Piggott and G. Gorman, “A new computational framework for multi-scale ocean modelling based on adapting unstructured meshes,” ... *Methods Fluids*, no. December 2007, pp. 1003–1015, 2008.

[112] C. C. Pain, M. D. Piggott, A. J. H. Goddard, F. Fang, G. J. Gorman, D. P. Marshall, M. D. Eaton, P. W. Power, and C. R. E. de Oliveira, “Three-dimensional unstructured mesh ocean modelling,” *Ocean Model.*, vol. 10, no. 1–2, pp. 5–33, Jan. 2005.

[113] R. Ford and C. Pain, “A nonhydrostatic finite-element model for three-dimensional stratified oceanic flows. Part I: model formulation,” *Mon. Weather ...*, pp. 2816–2831, 2004.

[114] J.-C. Galland, N. Goutal, and J.-M. Hervouet, "TELEMAC: A new numerical model for solving shallow water equations," *Adv. Water Resour.*, vol. 14, no. 3, pp. 138–148, Jun. 1991.

[115] R. A. Luettich, J. J. Westerink, and N. W. Scheffner, "Adcirc: an advanced three-dimensional circulation model for shelves, coasts, and estuaries," Washington, DC, 1992.

[116] Hydraulics Delft, "Delft3D-FLOW. Simulation of multi-dimensional hydrodynamic flows and transport phenomena, including sediments. User Manual." The Netherlands, 2011.

[117] A. F. Shchepetkin and J. C. McWilliams, "The regional oceanic modeling system (ROMS): a split-explicit, free-surface, topography-following-coordinate oceanic model," *Ocean Model.*, vol. 9, no. 4, pp. 347–404, Jan. 2005.

[118] I. R. Warren and H. K. Bach, "MIKE 21: a modelling system for estuaries, coastal waters and seas," *Environ. Softw.*, vol. 7, no. 4, pp. 229–240, Jan. 1992.

[119] C. Chen, R. C. Beardsley, and G. Cowles, "An unstructured-grid, finite-volume coastal ocean model (FVCOM) system," *Adv. Comput. Oceanogr.*, vol. 19, no. 1, pp. 78–89, 2006.

[120] D. H. I. Mike, "& MIKE 3 flow model, hydrodynamic and transport module, scientific documentation." Hørsholm, Denmark: DHI Water Environment Health, 2010.

[121] T. Petrila and D. Trif, *Basics of fluid mechanics and introduction to computational fluid dynamics*. Springer Science & Business Media, 2005.

[122] P. K. Kundu and I. M. Cohen, *Fluid Mechanics*, Second. Academic Press, 1990, p. 638.

[123] K. Erleben, "Finite Element Method. A short introduction to principles and ideas," Department of Computer Science. University of Copenhagen, 2010.

[124] P. Houston and E. S. Uli, "hp-adaptive discontinuous galerkin finite element methods for first-order hyperbolic problems," *SIAM J. Numer. Anal.*, vol. 23, no. 4, pp. 1226–1252, 2001.

[125] C. J. Cotter, D. A. Ham, and C. C. Pain, "A mixed discontinuous/continuous finite element pair for shallow-water ocean modelling," *Ocean Model.*, vol. 26, no. 1–2, pp. 86–90, Jan. 2009.

[126] C. J. Cotter and D. A. Ham, "Numerical wave propagation for the triangular P1DG–P2 finite element pair," *J. Comput. Phys.*, vol. 230, no. 8, pp. 2806–2820, Apr. 2011.

[127] C. Geuzaine and J. Remacle, "Gmsh: A 3D finite element mesh generator with built-in pre- and post- processing facilities," *Int. J. Numer. Methods Eng.*, vol. 0, pp. 1–24, 2009.

[128] J. Donea and A. Huerta, *Finite element methods for flow problems*. Chichester, UK: John Wiley & Sons, Ltd, 2003, p. 350.

[129] R. Courant, K. Friedrichs, and H. Lewy, "On the partial difference equations of mathematical physics," AEC Research and Development Report, NYO-7689, New York: AEC Computing and Applied Mathematics Centre, 1956.

[130] S. Balay, S. Abhyankar, M. Adams, J. Brown, P. Brune, K. Buschelman, L. Dalcin, V. Eijkhout, W. Gropp, D. Karpeyev, D. Kaushik, M. Knepley, L. Curfman McInnes, K. Rupp, B. Smith, S. Zampini, and H. Zhang, "PETSc 2.0 Users Manual," Mathematics and Computer Science Division, Argonne National Laboratory, 1996.

[131] C. B. Vreugdenhil, *Numerical methods for shallow-water flow*. Springer Science & Business Media, 1994.

[132] G. D. Egbert and L. Erofeeva, "OSU Tidal Data Inversion." [Online]. Available: http://volkov.oce.orst.edu/tides/. [Accessed: 05-Feb-2013].

[133] L. Carrère, F. Lyard, M. Cancet, A. Guillot, and L. Roblou, "FES2012: a new global tidal model taking advantage of nearly 20 years of altimetry.," in *Proceedings of meeting "20 years of Altimetry,"* 2012.

[134] G. S. Carter and M. A. Merrifield, "Open boundary conditions for regional tidal simulations," *Ocean Model.*, vol. 18, no. 3–4, pp. 194–209, Jan. 2007.

[135] C. Garrett and D. Greenberg, "Predicting changes in tidal regime: the open boundary problem," *J. Phys. Oceanogr.*, vol. 7, no. 2, pp. 171–181, 1977.

[136] T. A. A. Adcock, A. G. L. Borthwick, and G. T. Houlsby, "The open boundary problem in tidal basin modelling with energy extraction," in *Proceedings of the 9th European Wave and Tidal Energy Conference*, 2011, pp. 1–7.

[137] J. Zhou, S. Pan, and R. A. Falconer, "Effects of open boundary location on the far-field hydrodynamics of a Severn Barrage," *Ocean Model.*, vol. 73, pp. 19–29, Jan. 2014.

[138] S. Medeiros and S. Hagen, "Review of wetting and drying algorithms for numerical tidal flow models," *Int. J. Numer. ...*, no. March 2012, pp. 473–487, 2013.

[139] M. Coutanceau and R. Bouard, "Experimental determination of the main features of the viscous flow in the wake of a circular cylinder in uniform translation. Part 2. Unsteady flow," *J. Fluid Mech.*, vol. 79, no. 02, p. 257, Apr. 1977.

[140] W. M. Collins and S. C. R. Dennis, "Flow past an impulsively started circular cylinder," *J. Fluid Mech.*, vol. 60, no. 01, p. 105, Mar. 1973.

[141] R. Bouard and M. Coutanceau, "The early stage of development of the wake behind an impulsively started cylinder for 40< Re< 104," *J. Fluid Mech.*, vol. 101, 1980.

[142] C. Garrett and P. Cummins, "Maximum power from a turbine farm in shallow water," *J. Fluid Mech.*, pp. 634–643, 2013.

[143] F. M. White, *Fluid Mechanics*, 4th ed. London: McGraw-Hill, 2002, p. 826.

[144] M. Coutanceau and R. Bouard, "Experimental determination of the main features of the viscous flow in the wake of a circular cylinder in uniform translation. Part 1. Steady flow," *J. Fluid Mech.*, vol. 79, no. 02, p. 231, Apr. 1977.

[145] H. Honji and S. Taneda, "Unsteady flow past a circular cylinder," *Rep. Res. Inst. Appl. Mech. Kyushu Univ.*, vol. 19, no. 265, 1972.

[146] M. Kawaguti and P. Jain, "Numerical study of a viscous fluid flow past a circular cylinder," *J. Phys. Soc. Japan*, vol. 21, no. 10, pp. 2055–2062, 1966.

[147] G. K. Batchelor, *An introduction to fluid dynamics*. Cambridge University Press, 1967, p. 615.

[148] M. Lewis, S. P. Neill, P. E. Robins, and M. R. Hashemi, "Resource assessment for future generations of tidal-stream energy arrays," *Energy*, vol. 83, pp. 403–415, Apr. 2015.

[149] R. Vennell, "The energetics of large tidal turbine arrays," *Renew. Energy*, vol. 48, pp. 210–219, Dec. 2012.

[150] R. Vennell, "Exceeding the Betz limit with tidal turbines," *Renew. Energy*, vol. 55, pp. 277–285, Jul. 2013.

[151] M. C. Easton, D. K. Woolf, and P. a. Bowyer, "The dynamics of an energetic tidal channel, the Pentland Firth, Scotland," *Cont. Shelf Res.*, vol. 48, pp. 50–60, Oct. 2012.

[152] S. H. Salter and J. R. M. Taylor, "Vertical-axis tidal-current generators and the Pentland Firth," *Proc. Inst. Mech. Eng. Part A J. Power Energy*, vol. 221, no. 2, pp. 181–199, Jan. 2007.

[153] T. Nishino and R. H. J. Willden, "The efficiency of an array of tidal turbines partially blocking a wide channel," *J. Fluid Mech.*, pp. 1–11, Aug. 2012.

[154] A. S. Bahaj, A. F. Molland, J. R. Chaplin, and W. M. J. Batten, "Power and thrust measurements of marine current turbines under various hydrodynamic flow conditions in a cavitation tunnel and a towing tank," *Renew. Energy*, vol. 32, no. 3, pp. 407–426, Mar. 2007.

[155] D. Woolf, "The strength and phase of the tidal stream," *Int. J. Mar. Energy*, vol. 3–4, no. 2, pp. 3–13, 2013.

[156] B. Polagye, M. Kawase, and P. Malte, "In-stream tidal energy potential of Puget Sound, Washington," *Proc. Inst. Mech. Eng. Part A J. Power Energy*, vol. 223, no. 5, pp. 571–587, Aug. 2009.

[157] A. S. Iyer, S. J. Couch, G. P. Harrison, and A. R. Wallace, "Variability and phasing of tidal current energy around the United Kingdom," *Renew. Energy*, vol. 51, pp. 343–357, Mar. 2013.

[158] F. O'Rourke, F. Boyle, and A. Reynolds, "Tidal current energy resource assessment in Ireland: Current status and future update," *Renew. Sustain. Energy Rev.*, vol. 14, no. 9, pp. 3206–3212, Dec. 2010.

[159] "Edina Digimap Service. Hydrospatial one, gridded bathymetry. 2014.," 2015. [Online]. Available: http://edina.ac.uk/digimap/.

[160] J. C. Iliffe, M. K. Ziebart, J. F. Turner, A. J. Talbot, and A. P. Lessnoff, "Accuracy of vertical datum surfaces in coastal and offshore zones," *Surv. Rev.*, vol. 45, no. 331, pp. 254–262, Jul. 2013.

[161] "QGIS Geographic Information System," *QGIS Development Team. Open Source Geospatial Foundation Project.*, 2015. [Online]. Available: http://qgis.osgeo.org.

[162] A. Avdis, J. Hill, C. T. Jacobs, A. Candy, M. Piggott, and G. J. Gorman, "QMesh: Efficient unstructured mesh generation for renewable tidal energy using Geographical Information Systems." In preparation, 2015.

[163] Dp Marine Energy Ltd, "Fairhead Tidal ADCP Campaign." Personal communication, 2014.

[164] British Oceanographic Data Centre, "UK Tidal Gauge Network," 2015. [Online]. Available: https://www.bodc.ac.uk/data/online_delivery/ntslf/. [Accessed: 10-Jul-2015].

[165] A. M. Davies and J. E. Jones, "A three dimensional model of the M2, S2, N2, K1 and O1 tides in the Celtic and Irish Seas," *Prog. Ocean.*, vol. 29, pp. 197–234, 1992.

# Appendix - Publications

The following papers were produced during the EngD:

Pérez-Ortiz *et al*. (2013): Pérez-Ortiz, A., Pescatore, J., Bryden, I. (2013). A Systematic Approach to Undertake Tidal Energy Resource Assessment with TELEMAC-2D. Proceedings Tenth European Wave and Tidal Energy Conference (EWTEC). Aalborg, Denmark.

Pérez-Ortiz *et al*. (2014): Pérez-Ortiz, A., Borthwick, A.G.L., McNaughton, J., Pescatore, J., Smith, H., Vigars, P., Xiao, Q. (2014). Verification and Validation of Tidal Resource Assessment Model for a Strait betwen an Island and a Landmass. Proceedings Second Asian Wave and Tidal Energy Conference (AWTEC). Tokyo, Japan.

Pérez-Ortiz *et al*. (2015): Pérez-Ortiz, A., Borthwick, A.G.L., Smith, H., Vigars, P., Xiao, Q. (2015). Tidal Resource in Strait between Island and Landmass. Proceedings Eleventh European Wave and Tidal Energy Conference (EWTEC). Nantes, France